THE NATURE AND ORIGIN OF WESTERN AUSTRALIAN TOURMALINE NODULES; A PETROLOGIC, GEOCHEMICAL AND ISOTOPIC STUDY

A Thesis Submitted to the
College of
Graduate Studies and Research
in Partial Fulfillment of the Requirements
for the Degree of
Master of Science
in the
Department of Geological Sciences
University of Saskatchewan
Saskatoon

by
Debbie Amy Shewfelt

PERMISSION TO USE

In presenting this thesis in partial fulfillment of the requirements for a Postgraduate degree from the University of Saskatchewan, I agree that the Libraries of this University may make it freely available for inspection. I further agree that permission for copying of this thesis in any manner, in whole or in part, for scholarly purposes may be granted by the professor or professors who supervised my thesis work or, in their absence, by the Head of the Department or the Dean of the College in which my thesis work was done. It is understood that any copying, publication, or use of this thesis or parts thereof for financial gain shall not be allowed without my written permission. It is also understood that due recognition shall be given to me and to the University of Saskatchewan in any scholarly use which may be made of any material in my thesis.

Requests for permission to copy or to make other use of material in this thesis in whole or part should be addressed to:

Head of the Department of Geological Sciences
University of Saskatchewan
Saskatoon, Saskatchewan
S7N 0W0

ABSTRACT

The origin of tourmaline nodules, bizarre spherical to irregular textures documented worldwide, remains a geologic mystery. Although previously described by numerous researchers, the physical and chemical parameters that govern their formation have yet to be resolved. Commonly containing tourmaline, quartz, and occasionally feldspar, nodules are surrounded by a halo of leucocratic host rock, and are typically eight to ten centimeters in diameter. Tourmaline nodules of the present study are contained within the Paleoproterozoic Scrubber Granite of the southern Gascoyne Complex in Western Australia.

This study integrated field observations, nodule petrography, tourmaline crystal chemistry, tourmaline fluid inclusion analyses, whole rock chemistry of nodule cores, leucocratic halo zones and host granite zones, stable and radiogenic isotope signatures of tourmaline separates as well as comparisons with other tourmaline nodule studies to propose the most scientifically sound theory for the formation of tourmaline nodules in the Scrubber Granite.

Numerous nodule morphologies, including spherical and C-shaped nodules, along with other features such as tube-like nodules and tourmaline veins occur in massive, porphyritic, foliated and sheared phases of the Scrubber Granite. Microscopically, tourmaline displays prismatic, sub-rounded and massive textures. Microthermometric studies completed on tourmaline fluid inclusions revealed that the nodule-forming fluid contained 14 to 15 weight percent NaCl + $CaCl_2$. Based on stable isotope studies and homogenization temperatures, fluid temperatures were constrained between 450 and 700˚C. The $\delta^{18}O$ and δD concentrations of the nodule-forming fluid at this temperature range plot above the typical magmatic water field. Epsilon Nd values indicate that the tourmaline nodules of the Scrubber Granite may have been disturbed by a later metamorphic event.

Tourmaline nodules of the Scrubber Granite are herein proposed to have formed from the exsolution and rise of buoyant pockets or bubbles of volatile fluid derived from the crystallizing Scrubber Granite magma.

ACKNOWLEDGEMENTS

As this was a joint project between the Department of Geological Sciences at the University of Saskatchewan and the Geological Survey of Western Australia (GSWA), many people were involved in the development of this thesis. First, I owe my sincere gratitude and thanks to my advisor, Dr. Kevin Ansdell, for his encouragement and expertise over these last 2 years. Thanks also to the members of my U of S advisory committee: Drs. Butler, Holmden, Pan, and Pratt. I am also grateful for the technical support I received from Blaine Novakovski, Jianzhong Fan, Jim Rosen, Tom Bonli, Bruce Eglington and Daphne Cordiero at the U of S. Financial support for the project was provided by the GSWA and an NSERC Discovery Grant held by Kevin Ansdell. Additionally, I am grateful to the U of S for the receipt of a graduate scholarship for my stipend.

Thanks to Dr. Steve Sheppard at the GSWA for his stimulating conversations, both in Australia and via email, and to Dr. Mike Donaldson and his wife Lyn who provided lodging and companionship while in Perth. Also thanks to Dr. Hugh Smithies for inspiring discussions and sharing nodule photos from other locales and to Dean Clark for his help with the sampling process. Thanks to the Saskatchewan Research Council (SRC) for their help with printing and binding of numerous copies of this thesis. A special thanks to Dr. Irvine Annesley, who was encouraging and understanding during my transition period between being a student and a full-time employee at SRC.

A huge thank you to my family, in-laws and friends who always demonstrated love and encouragement through my many years of university. Special thanks to my husband Trevor for his help as my field assistant while in Australia, and for his endless love and support throughout my academic career. I most certainly could not have done this without you.

TABLE OF CONTENTS

LIST OF TABLES

LIST OF FIGURES

CHAPTER 1
INTRODUCTION AND SCOPE

1.1 GENERAL STATEMENTS

Tourmaline nodules have long been regarded as a geologic curiosity. Distinctive in appearance, tourmaline nodules consist of tourmaline and quartz (± feldspar) clots surrounded by a halo of leucocratic granitoid rock. Although most commonly documented as spherical entities, other nodule morphologies have been observed, including tube-like or irregular nodules. The origin of these textures has eluded many investigators, who chose to tackle this problem with a site-specific approach (e.g. Nemec, 1975; LeFort, 1991; Rozendaal et al., 1995). Thus, existing theories regarding nodule genesis are based on individual nodule occurrences. A unifying hypothesis describing the formation of nodules documented around the world has yet to be prepared.

This study strives to be more encompassing, as it discusses a variety of nodule morphologies, compares the nodules of the current study to those in other locations, and is firmly based on detailed mapping as well as comprehensive textural, mineralogical, and chemical analyses of tourmaline nodules. These factors will allow for the development of a more complete model that may be used to explain other nodule occurrences.

At the heart of the "tourmaline nodule problem" is the puzzling occurrence of tourmaline as discrete pocket-like entities in granitoid host rocks. Tourmaline is a hydrous borosilicate mineral that forms over a large range of temperatures and pressures in diverse geologic environments (Benard et al., 1985; Taylor et al., 1992; London, 1999). In granitic rocks, tourmaline typically belongs to the schorl-elbaite series and is commonly disseminated homogeneously throughout the host granite. In these cases, tourmaline is thought to have crystallized directly from the magma. However, when

tourmaline occurs as discrete clots, such as the tourmaline nodules examined in this study, the task of unraveling their petrogenesis becomes more complex.

Tourmaline nodules are a distinctive feature of the massive to foliated Paleoproterozoic Scrubber Granite of the Gascoyne Complex, Western Australia (Figure 1.1). This pluton was chosen for study as it had been the focus of recent mapping by the Geological Survey of Western Australia; although the extent and nature of the granite was documented, no detailed observations on nodule morphology or distribution were made (Occhipinti and Sheppard, 2001; Occhipinti et al., 2001). Composed mostly of tourmaline, quartz and feldspar, nodules are morphologically diverse, and do not have a uniform distribution throughout the granitic host. They are fine- to coarse-grained, and range from <2 to >30 cm in diameter. Tourmaline crystals are restricted to the nodule core, and are not present in the halo or host granite. Conversely, other dark, iron-rich minerals, including biotite, are present in the granite and occasionally in the halo, but are absent in nodule cores. Tourmaline nodules are not confined to a particular granitic phase, occurring in massive, porphyritic, weakly to moderately foliated and sheared granite. Tourmaline veins, also encompassed by leucocratic halos, are sparse, and are texturally and mineralogically similar to tourmaline nodules. Pegmatites are also sparsely distributed throughout the granite as small pod-like entities.

The 1800 Ma Scrubber Granite is part of the Moorarie Supersuite, a group of granitoids intruded into the Gascoyne Complex during the Capricorn Orogeny (Occhipinti and Sheppard, 2001; Occhipinti et al., 2001). The intrusion of these granitoids is an integral part of the much-debated geologic and tectonic history of the Capricorn Orogen (Tyler and Thorne, 1990; Myers et al., 1996; Occhipinti et al., 1998; Sheppard et al., 2003; Evans et al., 2003; Cawood and Tyler, 2004).

1.2 PREVIOUS NODULE THEORIES

1.2.1 Introduction

Tourmaline nodules, also termed ovoids, clots, clusters, orbicles and spots, have been documented in numerous localities around the world, including North America, South Africa, and New Zealand. Therefore, although nodules are odd, they are not uncommon

Figure 1.1: Tourmaline nodules of the Scrubber Granite; nodules comprise dark tourmaline-rich cores surrounded by leucocratic halos (stop 108a).

and are worthy of scientific inquiry. Investigations into these bizarre textures date back to the early 1800's; the majority of the literature has focused on nodule mineralogy and texture (e.g. Sinclair and Richardson, 1992), and in some cases, spatial association with tin-tungsten deposits (Rozendaal and Bruwer, 1995; Rozendaal et al., 1995). Few papers deal with the subject of origin; those delving into this problem briefly suggest how nodule textures observed at that locale may have formed, without consideration of nodule occurrences elsewhere.

The majority of nodules described in the literature have been documented as spherical entities. Theories regarding the origin of these nodules are based on their globular appearance, leading some investigators to speculate that they are the result of solid-state replacement of a discrete entity (e.g. Nemec, 1975). However, the Scrubber Granite contains a range of nodule morphologies, including irregular, doughnut-shaped

and starburst nodules, making the application of previous morphology-based theories problematic.

Two major schools of thought have emerged in the literature concerning the origin of tourmaline nodules: 1) post-crystallization replacement theories, and 2) magmatic-hydrothermal theories. The ideals behind each school of thought are summarized in the following sections; a thorough consideration of these hypotheses is presented in Chapter 7.

1.2.2 Post-magmatic replacement theories

Proponents of post-magmatic replacement theories suggest that nodules are features of replacement related to hydrothermal alteration of previously crystallized granite (e.g. Nemec, 1975). Tourmaline nodules in leucocratic Czechoslovakian granites of Nemec's (1975) study were thought to have developed by a metasomatic replacement of the granite initiated by boron-rich fluids brought into the rock in association with pegmatite injection. According to Nemec (1975), several features are indicative of this process, including: 1) all biotite flakes in halos and cores are replaced, with the exception of biotite armored by quartz crystals in halos and tourmaline cores; and 2) the abrupt change of mineral composition at the boundaries of individual zones and the progressive simplification of mineral assemblages in the direction from the host rock through the halo to the nodule core.

Rozendaal and Bruwer (1995) and Rozendaal et al. (1995) believe that tourmaline nodules of the Cape Granite Suite, South Africa are features of post-magmatic replacement. The distribution of these nodules, which are typically spatially associated with tin-tungsten deposits, is thought to be controlled by fluid movement along micro-fractures and diffusion along grain boundaries.

1.2.3 Magmatic-hydrothermal theories

Conversely, other researchers believe that nodules are magmatic-hydrothermal features related to the separation and entrapment of immiscible boron-rich fluids within coexisting granitic magma (e.g. Sinclair and Richardson, 1992). According to Sinclair and Richardson (1992), several features of the tourmaline 'orbicles' of the Seagull

Batholith, Northwest Territories, are consistent with the separation and entrapment of aqueous, B-rich fluid in the roof zone of a crystallizing magma, including: 1) the orbicles are concentrated within the granite at the top of the batholith, and decrease in abundance and tourmaline content with depth; 2) the orbicles are typically spherical in shape and occasionally contain miarolitic cavities; and 3) there is an absence of structural features related to orbicle form or distribution. Samson and Sinclair (1992) suggest that the Seagull Batholith orbicles represent a transition from magmatic to hydrothermal processes, based on fluid inclusion studies on quartz and tourmaline crystals.

LeFort's (1991) study of tourmaline nodules in Himalayan leucogranites concluded that nodules are the result of metasomatic circulation of fluids formed during the crystallization of the boron-rich magma.

1.3 OBJECTIVES

The present study endeavors to incorporate field and analytical data to propose a theory describing the origin of tourmaline nodules in the Scrubber Granite. Also critical to this endeavor is the comparison of these nodules with those in the literature, as this will aid in the development of an all-encompassing theory.

1.4 LOCATION, ACCESS AND METHODS

The study area is located in the Gascoyne Region about 300 km east of Carnarvon, Western Australia, along the western limit of the Australian Outback (Figure 1.2). Following the main highway inland from Carnarvon to Gascoyne Junction, access to the Scrubber Granite is obtained via a network of unsealed, maintained public roads and off-road trails south of the Mooloo Downs homestead (Occhipinti et al., 2001).

The Scrubber Granite is exposed in three locations throughout the Gascoyne Complex, stretching over 75 km in an east-west direction (Occhipinti and Sheppard, 2001). The largest outcrop of this unit occurs 60 km east of Mooloo Downs station (see Figure 2.1 in Chapter 2). A relatively smaller outcrop is located 2 km southeast of Middle Well where the granite intrudes the Halfway Gneiss and Dumbie Granodiorite

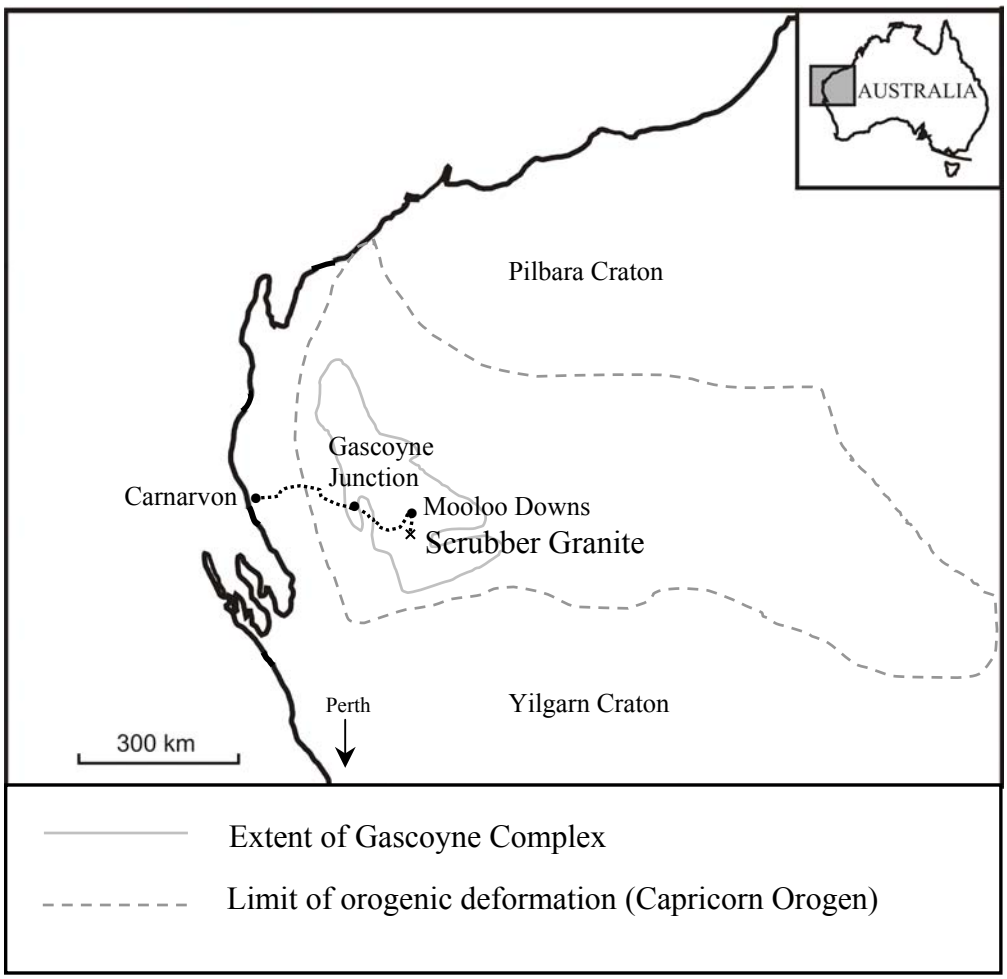

Figure 1.2: Generalized map showing the location of the study area in the Western Australian Outback (modified from Sheppard, 2004).

of the Glenburgh Terrane (see Figure 2.2). Gaining access to this outcrop of the granite requires entry through the Mooloo Downs station, located along the Dairy Creek road. Finally, a 3.5 km long intrusion of the Scrubber Granite occurs roughly 2 km southwest of the 2 Mile Well. Access to this exposure is obtained via an abandoned trail off the Dairy Creek road, west of the turn-off to Mooloo Downs homestead. This outcropping of the Scrubber Granite was chosen as the focus of the present study, as it comprises abundant nodules of various morphologies contained within excellent outcrop exposures. Additionally, it was a reasonable size to map given the time constraints of the project.

The landscape in the southern Gascoyne consists of variably rugged terrain, with incised dendritic creeks dividing the land. The main drainage area along the Gascoyne River is characterized by floodplains, sheetwash plains, and eroding outcrop (Occhipinti and Sheppard, 2001). Red soils dominate the landscape, coating most outcrop surfaces and unsealed roadways (Figure 1.3). Vegetation is sparse, and foliage diversity depends on proximity to drainage systems, condition of pastoral land, and rock type.

The nature, abundance and distribution of nodules, as well as the nature of the host granite were documented in a representative nodule-rich exposure of the Scrubber Granite. Subsequent to mapping and delineation of principal nodule types, representative samples of the various nodule morphologies were extracted from the Scrubber Granite. Seven locations were blasted, resulting in the attainment of fresh samples. Of the nodules obtained from Western Australia, those showing the most representative features were chosen for analysis.

Petrographic analyses were carried out to identify all mineral phases present and to examine textural relationships between mineral phases within the Scrubber Granite. Whole rock major and trace element analyses of the granite, leucocratic halo and nodule core zones were completed, and mass balance calculations were carried out to determine which elements were concentrated in each of the three mineralogic zones. Electron microprobe analyses were completed on tourmaline crystals to determine their chemistry and chemical formulae and to classify the tourmalines on an Al-Fe-Mg plot. Using these parameters, tourmalines of the Scrubber Granite can be compared to tourmalines in other environments, aiding in the constraint of possible fluid sources.

Fluid inclusion microthermometric analyses of tourmaline crystals within a starburst nodule and a tourmaline vein were completed to constrain the temperature, salinity and general composition of the fluid reservoir from which they crystallized. Tourmaline separates from eight nodule types were analyzed for their oxygen and hydrogen isotopic signatures to further constrain the formation temperature, isotopic composition, and possible fluid sources. Samarium-neodymium isotopic analyses were also carried out on the tourmaline separates to help constrain fluid sources; tourmaline Nd isotope ratios were compared to those of possible fluid reservoirs in the surrounding area. Results of the analyses described above are presented in the appropriate chapters.

Figure 1.3: Typical scenery of the Western Australian Outback: red dirt road in the foreground and mountainous ridges in the horizon divide the landscape (field photo).

CHAPTER 2
GEOLOGIC SETTING

2.1 INTRODUCTION

The 1800 Ma nodule-bearing Scrubber Granite is exposed along the southern margin of the Gascoyne Complex (Occhipinti and Sheppard, 2001). Igneous and metamorphic rocks of the Gascoyne Complex form part of the east-southeasterly trending Proterozoic Capricorn Orogen. Extending over 1000 km, the Capricorn Orogen was initiated during Paleoproterozoic suturing events that brought together the Archean Yilgarn and Pilbara cratons to form the West Australian Craton (Tyler and Thorne, 1990; Occhipinti et al., 1998; Occhipinti et al., 2004). The orogen comprises Paleoproterozoic plutonic and medium- to high-grade metamorphic rocks of the Gascoyne Complex, Paleoproterozoic volcano-sedimentary and sedimentary basins, and the deformed margins of the Pilbara and Yilgarn cratons.

Deformation and metamorphism in the Capricorn Orogen occurred over a series of events, namely the ca. 2200 Ma Ophthalmian Orogeny, the 2000–1960 Ma Glenburgh Orogeny, the 1830–1780 Ma Capricorn Orogeny, and a 1670-1620 Ma unnamed event (Cawood and Tyler, 2004). According to Cawood and Tyler (2004), "the orogen has been the site of repeated intracratonic reactivation with renewed basin formation, magmatism and orogeny". Of interest in this study are the effects of the Capricorn Orogeny, which extend across the entire Capricorn Orogen.

The Proterozoic geology of Australia was originally thought to reflect evolution of a single portion of crust in which all tectonic and magmatic activity was intracratonic (Rutland, 1973; Gee, 1979; Williams, 1986; Etheridge et al., 1987). However, Tyler and Thorne (1990), Myers et al. (1996) and subsequent researchers including Sheppard et al. (2003) and Evans et al. (2003) believe that the Proterozoic tectonic evolution of Australia is a consequence of plate tectonic processes consistent with global

supercontinent formation. Thus, the Capricorn Orogeny is thought to correspond with a major phase of continental collision in Australia (Cawood and Tyler, 2004).

A series of granitic plutons were emplaced throughout the Gascoyne Complex during the Capricorn Orogeny, including the Scrubber Granite of the Moorarie Supersuite (Occhipinti and Sheppard, 2001). The geologic setting surrounding the Scrubber Granite in the southern Gascoyne Complex is discussed in the following sections.

2.2 REGIONAL GEOLOGY

2.2.1 Gascoyne Complex

The Paleoproterozoic Gascoyne Complex occurs along the western border of the Capricorn Orogen (Sheppard, 2004). The Gascoyne Complex contains several terranes, each bounded by east-southeasterly trending faults or shear zones. Each terrane is composed of a sedimentary package(s) and granitic supersuites that have different ages, compositions and metamorphic and structural histories relative to adjacent terranes.

The southern portion of the Gascoyne Complex is comprised of meta-igneous and metasedimentary rocks that can be divided into three main units: 1) the 2550-1970 Ma Glenburgh Terrane; 2) the ca. 2000 Ma Camel Hills Metamorphics; and 3) the 1830-1780 Ma Moorarie Supersuite. The Camel Hills Metamorphics outcrop exclusively in the Errabiddy Shear Zone, which marks the boundary between the Yilgarn Craton and the Gascoyne Complex (Occhipinti and Sheppard, 2001). The Glenburgh Terrane consists of Archean to Paleoproterozoic granitic gneisses that, along with the Camel Hill Metamorphics, were deformed and metamorphosed at low to medium grade, and were intruded by voluminous granites and pegmatites of the Moorarie Supersuite during the Capricorn Orogeny. Those units associated with the Scrubber Granite in the southern Gascoyne Complex, namely, those of the Glenburgh Terrane and the Moorarie Supersuite, are summarized in the following sections (see Figure 2.1).

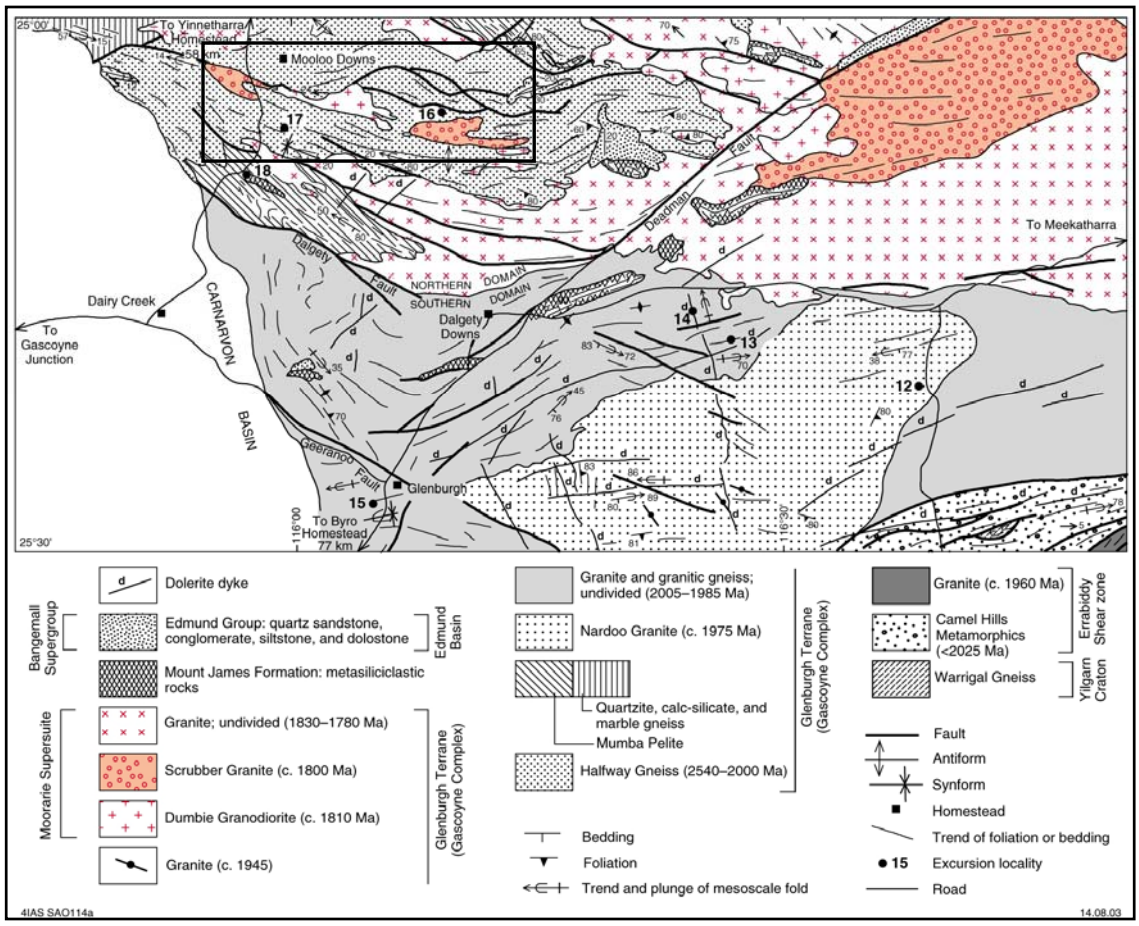

Figure 2.1: Simplified geological map of the southern Gascoyne (from Occhipinti et al., 2001). Black box indicates general area shown in Figure 2.2.

2.2.2 Glenburgh Terrane

The Glenburgh Terrane encompasses 2550-2000 Ma granitic rocks of the Halfway Gneiss, Proterozoic metasedimentary rocks of the Moogie Metamorphics, and 2005-1970 Ma granitic rocks of the Dalgaringa Supersuite (Occhipinti and Sheppard, 2001). These rock units were deformed and metamorphosed at medium to high grade during the 2000-1960 Ma Glenburgh Orogeny. A second deformation and low- to medium-grade metamorphic event, along with the intrusion of voluminous granite and pegmatite dykes, plugs, and sheets of the Moorarie Supersuite, occurred throughout the 1830-1780 Ma Capricorn Orogeny. The rocks of the Glenburgh Terrane and Moorarie Supersuite are unconformably overlain by the ca. 1800 Ma Mount James Formation and the Paleoproterozoic to Mesoproterozoic Bangemall Supergroup (Figure 2.1).

2.2.2.1 Halfway Gneiss

Augen gneiss and banded granitic gneiss comprise the upper Archean to Proterozoic Halfway Gneiss (Occhipinti et al., 2001). This unit is extensively intruded by sheets and dykes of the Dumbie Granodiorite, plutons, dykes and veins of the Scrubber Granite, and medium-grained biotite (-muscovite) granite, all of which comprise the Moorarie Supersuite.

2.2.2.2 Moogie Metamorphics

The Moogie Metamorphic suite is comprised of metasedimentary and metamorphosed mafic and ultramafic igneous rocks, including pelitic schist, quartzite, calc-silicate gneiss, marble, amphibolite, ultramafic schist, and metamorphosed banded iron-formation (Occhipinti and Sheppard, 2001). The age of the Moogie Metamorphics is poorly constrained; however, as it is intruded by granites of the Dalgaringa Supersuite, it is at least ca. 2005 Ma. Rocks of the Moogie Metamorphics are in fault contact with those of the Halfway Gneiss, and the relative ages of the two units are not known.

2.2.2.3 Dalgaringa Supersuite

The Dalgaringa Supersuite consists of 2005-1970 Ma massive, foliated, and gneissic granites (Occhipinti et al., 2001). The Supersuite is comprised of two episodes of magmatism, separated by a deformation and high-grade regional metamorphic event. Foliated to gneissic quartz diorite, tonalite, granodiorite, and monzogranite 2005-1985 Ma in age represent the first episode; the latter ca. 1975 Ma magmatic episode involved the intrusion of tonalite and granodiorite of the Nardoo Granite.

2.2.3 Moorarie Supersuite

Intermediate to silicic igneous rocks of the Moorarie Supersuite intruded Archean to Proterozoic granitic rocks of the Glenburgh Terrane during the Capricorn Orogeny (Occhipinti and Sheppard, 2001). The Supersuite is comprised of dykes, sheets, plugs and plutons of the 1810 Ma Dumbie Granodiorite, the 1800 Ma Scrubber Granite, and 1830-1780 Ma unnamed granites. Most of the intrusions are leucocratic, and pegmatites are abundant.

2.2.3.1. Dumbie Granodiorite

The fine- to medium-grained Dumbie Granodiorite forms a large massive to foliated pluton comprising numerous easterly trending sheets (Occhipinti et al., 2001). In the northeast part of the Glenburgh Terrane, this unit outcrops as boulders, tors, and scattered whalebacks. The Dumbie Granodiorite intrudes both the Halfway Gneiss and the Moogie Metamorphics and is intruded by veins and dykes of biotite (-muscovite) granite, coarse-grained granite and pegmatite, and the Scrubber Granite.

2.2.3.2 Scrubber Granite

The 1800 Ma Scrubber Granite forms an extensive unit in the Glenburgh Terrane, intruding into rocks of the Halfway Gneiss and Dumbie Granodiorite (Occhipinti and Sheppard, 2001) (Figures 2.1 and 2.2). The Scrubber Granite outcrops most extensively to the east and southeast of Mooloo Downs, where it is commonly massive, but can be locally well-foliated. Spherical and elongate tourmaline nodules are sparse to absent in this region. The outcrop of the Scrubber Granite southwest of Mooloo Downs was chosen as the focus of this study, as tourmaline nodules are most abundant and morphologically diverse in this region (see black box in Figure 2.2). This elongate intrusion is superficially divided into three lobes by overlying sedimentary rocks.

The relationship among the three separate outcrops of the Scrubber Granite that extend across the Gascoyne Complex is unclear, and the size and shape of the pluton is unknown. Perhaps laccoliths or sills of the Scrubber Granite intrude rocks of the Gascoyne Complex in several regions. The outcrop of interest in the current study could possibly represent the western margin of the Scrubber Granite pluton.

2.2.3.3 Unnamed Granites

Various 1830-1780 Ma granites of differing mineralogical characteristics are a sub-unit of the Moorarie Supersuite (Occhipinti and Sheppard, 2001). Medium-grained biotite-muscovite granite, coarse-grained granite and pegmatite, leucocratic muscovite-biotite granite, and altered granite comprise this unit. These granites tend to form large, east-southeasterly trending plutons, veins and dykes, intruding into the Camel Hills Metamorphics and rocks of the Gascoyne Complex.

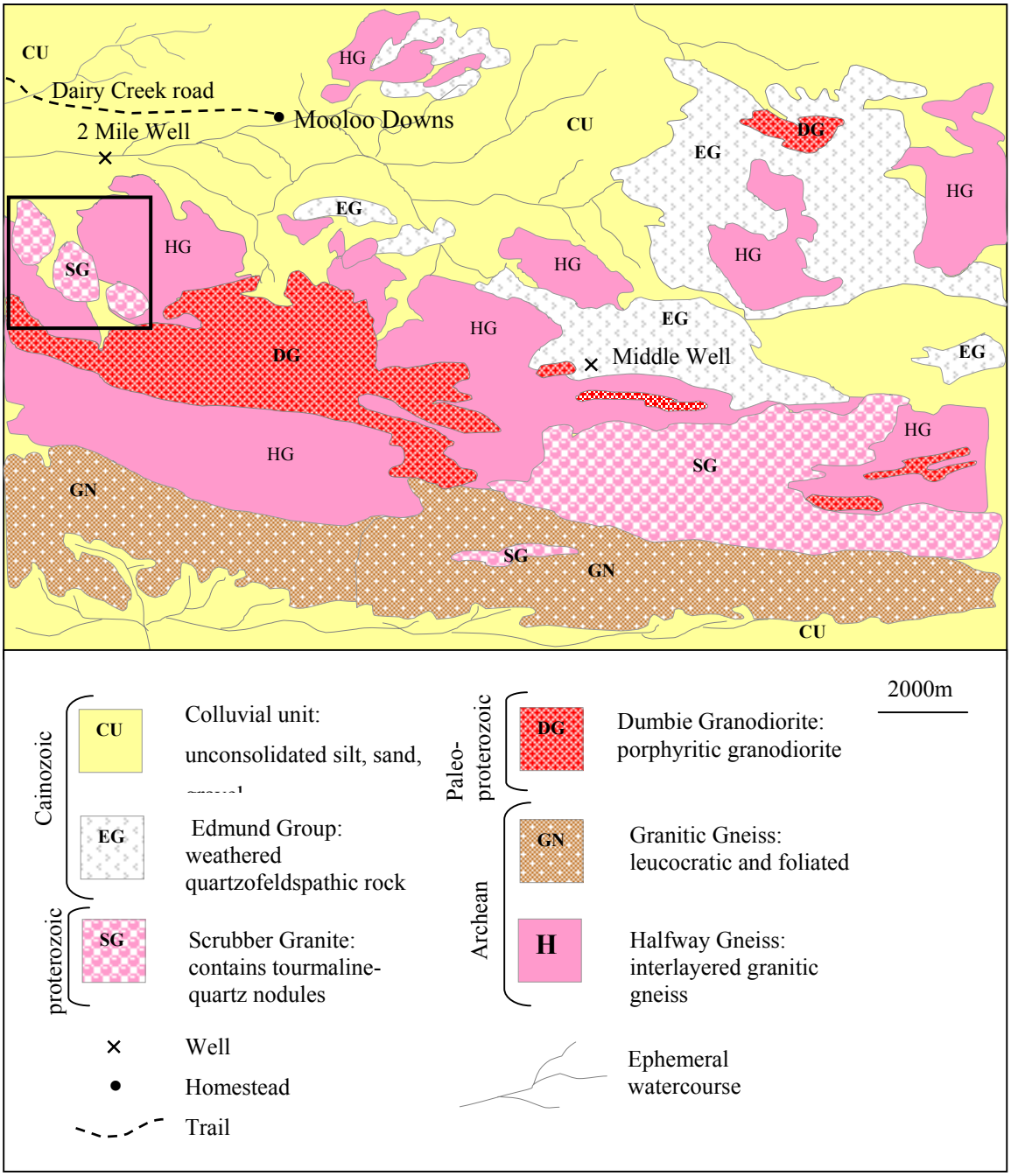

Figure 2.2: Simplified geology surrounding the Scrubber Granite study area, indicated by the black box (created from 1:100 000 map sheet in Occhipinti and Sheppard, 2001).

2.2.4 Mount James Formation

Overlaying the rocks of the Moorarie Supersuite and the Glenburgh Terrane are the ca. 1800 Ma northeasterly trending lenticular outcrops of the Mount James Formation (Occhipinti and Sheppard, 2001). This formation is comprised of deformed and metamorphosed siliciclastic sedimentary rocks, including quartzite, metamorphosed arkosic sandstone to quartz-sericite phyllite, metamorphosed quartz-pebble to cobble conglomerate, and quartz-chlorite-sericite phyllite; the degree of metamorphism is sub-greenschist to low-greenschist faces. Although the age of the Mount James Formation is not certain, SHRIMP U-Pb zircon dating gives a maximum age of ca. 1800 Ma (Occhipinti et. al., 2001). This agrees well with field observations, as granites of the Moorarie Supersuite, which can be up to 1780 Ma old, do not penetrate the Mount James Formation.

2.2.5 Bangemall Supergroup

The Paleoproterozoic to Mesoproterozoic Bangemall Supergroup consists of the Edmund and Collier Groups (Martin and Thorne, 2004). These groups comprise fine-grained siliciclastic and carbonate sedimentary rocks, which rest unconformably on granitic and supracrustal rocks of the Yilgarn Craton and ca. 1800 Ma granitic and metamorphic rocks of the Gascoyne Complex. Based on detrital zircons and mafic sills, Martin and Thorne (2004) have constrained the age of the Edmund Group to between ca. 1620 and 1465 Ma, and the age of the Collier Group to between 1400 and 1070 Ma.

2.3 DEFORMATION AND METAMORPHISM

Archean to Paleoproterozoic rocks of the Glenburgh Terrane were deformed, metamorphosed and intruded by granites of the Moorarie Supersuite during the 1830-1780 Ma Capricorn Orogeny (Occhipinti and Sheppard, 2001). Following the intrusion of the Scrubber Granite, a local deformation event associated with the Capricorn Orogeny may be responsible for structural fabrics observed in the Scrubber Granite.

2.3.1. Deformation (D_{1n})

Deformation associated with the Capricorn Orogeny (D_{1n}) has been described by Occhipinti and Sheppard (2001) as "…long-lived or continuous, rather than representing a discrete event". Upright, open to close, shallowly to moderately plunging folds and a pervasive easterly trending foliation are the most widespread D_{1n} structures in the Glenburgh Terrane. The Scrubber Granite is weakly to moderately foliated and also contains zones of intense shearing related to this event.

2.3.2 Metamorphism (M_{1n})

According to Occhipinti and Sheppard (2001), rocks of the Glenburgh Terrane, including granites of the Moorarie Supersuite, show evidence of dynamic or static recrystallization under greenschist-facies conditions. All granitic rocks in this region show similar mineralogical responses to the low-grade M_{1n} event. Igneous to high-grade metamorphic plagioclase has recrystallized to albite-oligoclase (An_{8-13}), sericite, and clinozoisite; quartz has recrystallized to fine-grained polygonal aggregates (mosaic texture); and biotite has recrystallized to fine crystals or is partly replaced by chlorite. Myrmekitic and micrographic textures are also widely developed.

2.4 CHAPTER SUMMARY

The following summary statements can be made regarding the regional geology associated with the Scrubber Granite:

1. The 1800 Ma Scrubber Granite is part of the Paleoproterozoic Moorarie Supersuite, an intermediate to silicic assemblage that was intruded into the southern Gascoyne Complex during the Capricorn Orogeny;
2. The Scrubber Granite intrudes the Dumbie Granodiorite and the Halfway Gneiss, and is overlain by Cainozoic sediments;
3. Of the three outcrops of the Scrubber Granite, a relatively small, nodule-rich outcrop southwest of Mooloo Downs was chosen as the focus of this study as it contains abundant nodules that are morphologically diverse. This outcrop is artificially divided into three lobes by younger sediments. The relationship

between this outcrop and the other two Scrubber Granite outcrops east of Mooloo Downs is unclear;

4. Deformation and metamorphic events associated with the Capricorn Orogeny that occurred after the emplacement of the Moorarie Supersuite may have affected the Scrubber Granite; and

5. The geology of the Gascoyne Complex is very complicated, and the tectonic evolution of this region is still under speculation.

CHAPTER 3
FIELD OBSERVATIONS

3.1 INTRODUCTION

The westernmost outcropping of the Scrubber Granite was chosen as the focus of this study as it displays the most abundant and diverse range of nodule types and sizes (see Figure 2.2). This northwest to southeast trending lenticular exposure is approximately 1.5 km wide and 3.5 km long, and is overlain in regions by Cainozoic sediments that superficially divide the Scrubber Granite into three lobes; namely, the western, central, and eastern lobes (see Figure B.1 in Appendix B). Throughout these regions, the Scrubber Granite outcrops as boulders, whalebacks, tors (masses of granite standing abruptly above the surroundings), and pavements (Figure 3.1). The overall topography is gently sloping to erratic, with steep tors rising up to 5m in some regions.

In order to assess the origin of the nodules, the aim of the fieldwork was to document: 1) the nature of the host granite, 2) the nature and distribution of the nodules occurring in the host granite, and 3) the nature of any structural or textural feature spatially associated with nodule formation (for more details on the fieldwork approach, see Appendix D.1). Various phases of the host granite were observed, from massive to highly sheared. Nodules were grouped into morphologic categories based on physical attributes, allowing for a systematic description of nodule characteristics; major mineralogy and textures were estimated in the field and from hand specimens. For stop location information, see Appendix A; see Figure B.1 in Appendix B and Appendix D.1 for sample locations and sampling procedures.

3.2 HOST GRANITE

Nodules are hosted by various phases of the Scrubber Granite; 1) fine- to coarse-grained massive; 2) porphyritic; 3) weakly to moderately foliated; and 4) moderately to

A

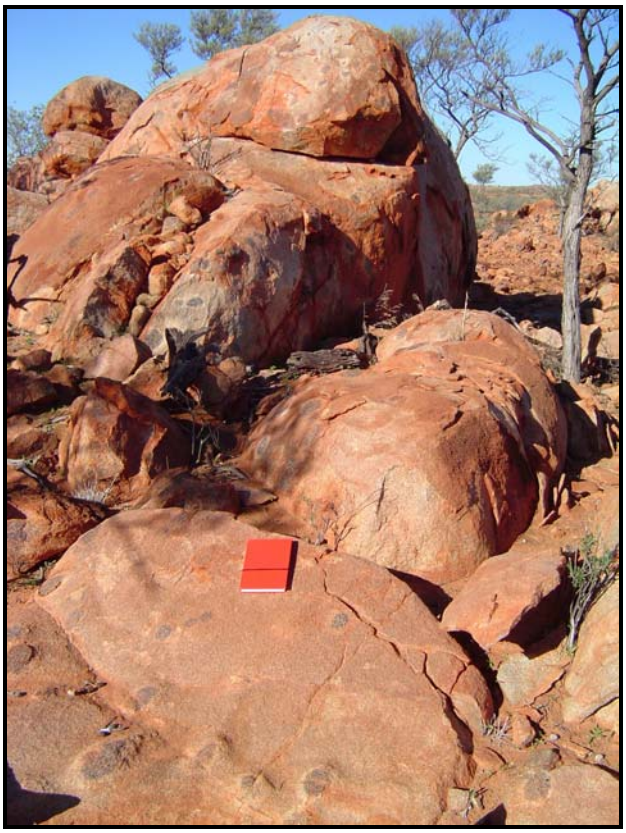

B

Figure 3.1: A) and B) Overview of whalebacks and tors of the Scrubber Granite in the western lobe; kangaroo for scale in B (field photos).

intensely sheared granite. This may indicate that the texture, mineralogy and structure of the granite were not controlling factors in the formation and distribution of nodules and that the nodules pre-date deformation. The various phases of Scrubber granite have irregular, gradational contacts and no age relationships are evident. In general, massive to porphyritic granite occurs in the central part of the pluton and foliated to sheared regions are dispersed throughout all three lobes of the Scrubber Granite.

3.2.1 Massive granite

Although the majority of the Scrubber Granite has a weak to moderate foliation, approximately 10% of the exposure is fine- to medium-grained massive granite. These regions may or may not contain tourmaline nodules, and occasionally contain biotite clots randomly disseminated throughout the groundmass.

On average, the massive granite comprises 60% quartz, 15% plagioclase feldspar, 10% alkali feldspar, 10% biotite, and 5% muscovite. Fine- to medium-grained quartz crystals are intergrown with feldspars. Biotite and muscovite occur as individual flakes, or, more commonly, may aggregate with opaque minerals to form clots up to 1mm in size, comprising ~5% of the groundmass.

3.2.2 Porphyritic granite

Approximately 10% of the Scrubber Granite is porphyritic. Plagioclase feldspar phenocrysts range from 1.5-6mm in diameter and comprise ~5% of the porphyritic granite. Nodules occurring in the porphyritic granite contain plagioclase phenocrysts in the surrounding halo material (Figure 3.2).

The fine- to medium-grained porphyritic host granite is similar to the massive granite described above, containing approximately 60% quartz, 20% plagioclase feldspar (15% in groundmass, 5% as phenocrysts), 10% alkali feldspar, 8% biotite, and 2% muscovite. Quartz, plagioclase and alkali feldspar are intergrown; plagioclase crystals occurring in the groundmass and as phenocrysts are highly included with muscovite flakes. Biotite clots, also containing muscovite and opaque minerals, occur between crystals of quartz and feldspar, defining a weak to moderate foliation in the porphyritic granite.

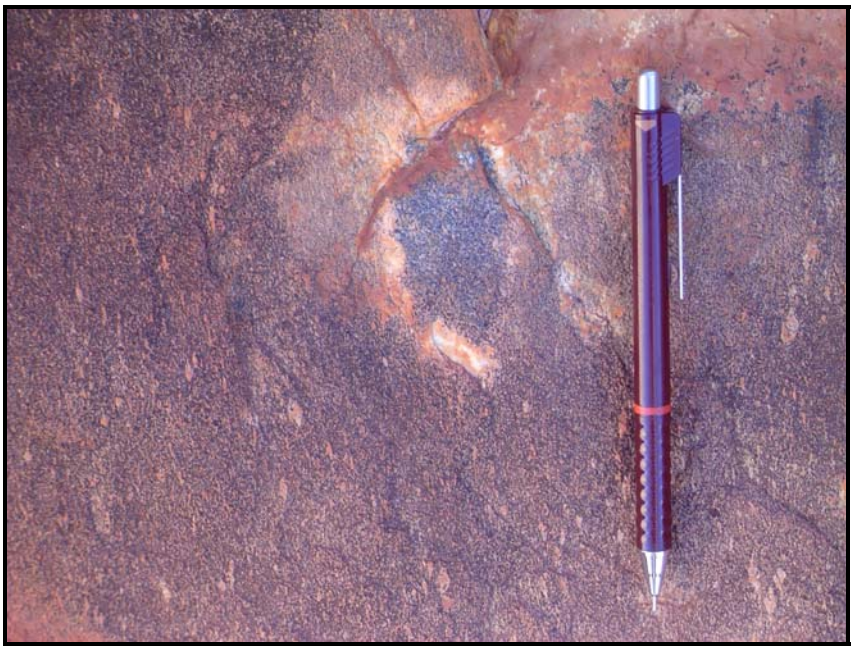

Figure 3.2: Field photo of a nodule in porphyritic granite (stop 27a). Plagioclase phenocrysts are visible in host granite.

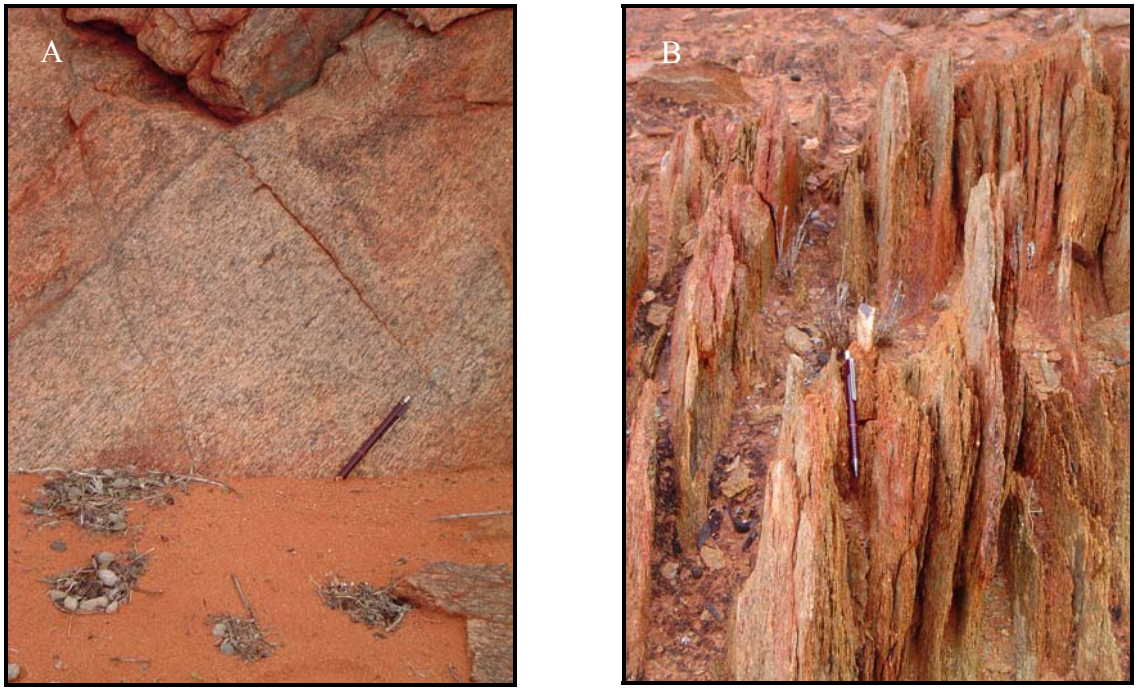

Figure 3.3: A) Strongly foliated granite defined by aligned biotite clots (parallel to pencil; stop 80b); B) Sheared granite, containing nodules (protruding above pencil; stop 36g).

3.2.3 Foliated granite

The majority of the Scrubber Granite is weakly to moderately foliated. Elongated, aligned biotite and muscovite flakes form clots along with opaque minerals to define this foliation that typically runs at 140˚/85˚SW (roughly northwest-southeast) (Figure 3.3A). Tourmaline in nodule cores present in these regions is occasionally elongated parallel to the foliation in the groundmass. Compositionally, the fine- to coarse-grained foliated granite is similar to the massive granite, containing, on average, 60% quartz, 20% plagioclase feldspar, 10% alkali feldspar, 8% biotite, and 2% muscovite. Quartz is intergrown with feldspars. Biotite/muscovite/opaque mineral clots average 1.3mm, defining the foliation throughout the groundmass.

3.2.4 Sheared granite

Approximately 10% of the Scrubber Granite is moderately to intensely sheared, with shear planes running at a similar direction to foliation observed in other localities (145˚/87˚SW). These medium- to coarse-grained areas are spatially separated from adjacent bulbous outcrops and pavements by zones of intense weathering. Some regions are so intensely sheared that it is difficult to recognize as granitic in composition. Nodules occurring in these areas are also sheared, forming jagged projections due to their resistance to weathering (Figure 3.3B). Mineral lineations in nodule cores are evident in these locations, with tourmaline crystals plunging 58˚ at 180˚. Structural features of the Scrubber Granite, including alignment of elongate nodules, veins, foliations and shear zones are summarized in Figure B.2 in Appendix B.

3.3 TOURMALINE NODULES

3.3.1 General characteristics

Fine- to coarse-grained nodules of the Scrubber Granite range from <2 to >30cm in diameter (see Figure B.3 in Appendix B). Nodules consist of two components: a leucocratic halo and a dark, tourmaline-rich core. The cores are generally more resistant to weathering, and form wart-like projections in many localities. Throughout

the Scrubber Granite, various nodule types and sizes are apparent. However, nodules commonly appear as spherical entities roughly 8 to 10cm in diameter.

On average, the 2 to 25cm-wide cores consist of 60% tourmaline, 30% quartz, and 10% plagioclase feldspar. Halos surrounding the nodules consist of leucocratic granite 0.5 to 5cm wide. There is no consistent relationship between the size of nodules and the thickness of the surrounding halo.

3.3.2 Abundance and distribution

Nodule abundance across the three lobes ranges from none (no nodules/m^2) to sparse (<4 nodules/m^2) to moderate (≥4 nodules/m^2) to abundant (>8 nodules/m^2), and is independent of nodule size or shape (see Figure B.4). Dense swarms of four or more nodules with interconnecting halos occur sporadically throughout the pluton.

Nodules do not have a uniform distribution throughout the Scrubber Granite; regions devoid of nodules are juxtaposed with regions containing abundant nodules. Variation in nodule distribution with depth in the pluton cannot be assessed with confidence, as the shape and orientation of the pluton is unclear.

3.3.3 Nodule morphologies

3.3.3.1 Spherical nodules

Spherical nodules are distributed across all three lobes and were documented at approximately 60% of all nodule-bearing stop locations (Figure B.5). Ranging from 2-20cm in diameter, the spherical nodules are encompassed by 0.5-4cm thick leucocratic halos and are fine- to coarse-grained (Figure 3.4). Three-dimensional views of nodules were observed on occasion, as in Figure 3.4B. Nodules occurring in foliated or sheared regions of the Scrubber Granite are weakly to intensely elongated, with aspect ratios up to 1:5 (Figure 3.5). This indicates that nodules pre-date deformation.

Nodule cores contain approximately 55% quartz, 30% tourmaline, 10% plagioclase feldspar, and 5% alkali feldspar. The surrounding leucocratic halo comprises 55% quartz, 20% alkali feldspar, 10% plagioclase feldspar, 10% biotite, and 5% muscovite.

A

B

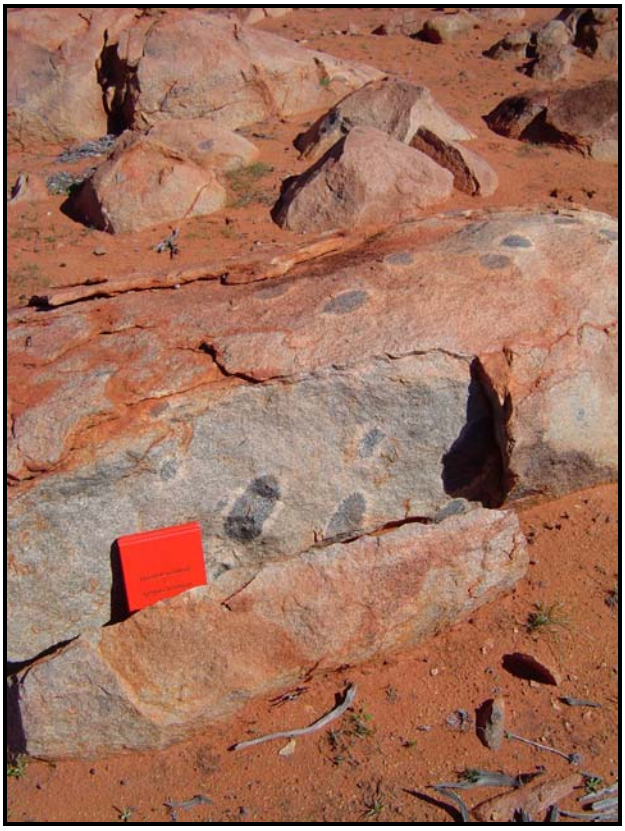

Figure 3.4 A) Spherical nodules ~7cm in diameter from stop 36k in western lobe; B) Spherical nodules ~10cm in diameter from stop 120b in central lobe.

A

B

Figure 3.5: A) Elongate nodules from stop 29a in western lobe; B) elongate nodules from stop 37a in western lobe.

3.3.3.2 Tourmaline rosette nodules

Tourmaline rosette nodules range from 4-34cm in diameter, and are surrounded by 1-2.5cm thick leucocratic halos. These medium- to coarse-grained nodules are identified by the dense "rosette" of tourmaline crystals occurring in the core region (Figure 3.6). Prismatic tourmaline crystals comprising these rosettes are thin (<2mm), and elongate, extending up to 1.5cm in length. The surrounding nodule texture and mineralogy is similar to that of the spherical and elongate nodules. The nodule core contains approximately 50% tourmaline, 35% quartz, 15% plagioclase feldspar, and trace amounts of muscovite and opaque minerals. Dense rosettes contain 95% prismatic tourmaline and 5% quartz that occurs between tourmaline crystals. On average, the halo comprises 55% quartz, 20% plagioclase feldspar, 15% alkali feldspar, 8% biotite, and 2% muscovite.

Rosettes are randomly located within nodule cores. In addition, there is no relationship between the size of the nodule and the size of the rosette; small nodules may contain large rosettes, comprising most of the nodule core, and larger nodules may have small rosettes that are difficult to identify. Tourmaline rosette nodules are found across all three lobes of the Scrubber Granite (Figure B.6).

3.3.3.3 Irregular nodules

Nodules of various shapes and sizes that do not have a specific morphologic character are termed 'irregular nodules' (Figure 3.7). These fine- to coarse-grained nodule cores comprise splays or blebs of tourmaline (95%) and quartz (5%), and are typically 5cm in diameter, although some can span over 24cm. Tourmaline occurs as bladed, prismatic crystals up to 1cm in length, and as subrounded, fractured crystals that average <1mm in diameter. Quartz crystals infill fractures within tourmaline. Halo material, comprising quartz (80%), plagioclase feldspar (20%), and trace amounts of microcline, is characteristically thinner than in other nodule morphologies, averaging 0.5cm.

Irregular nodules are located in the western and central lobes of the Scrubber Granite (Figure B.7).

A

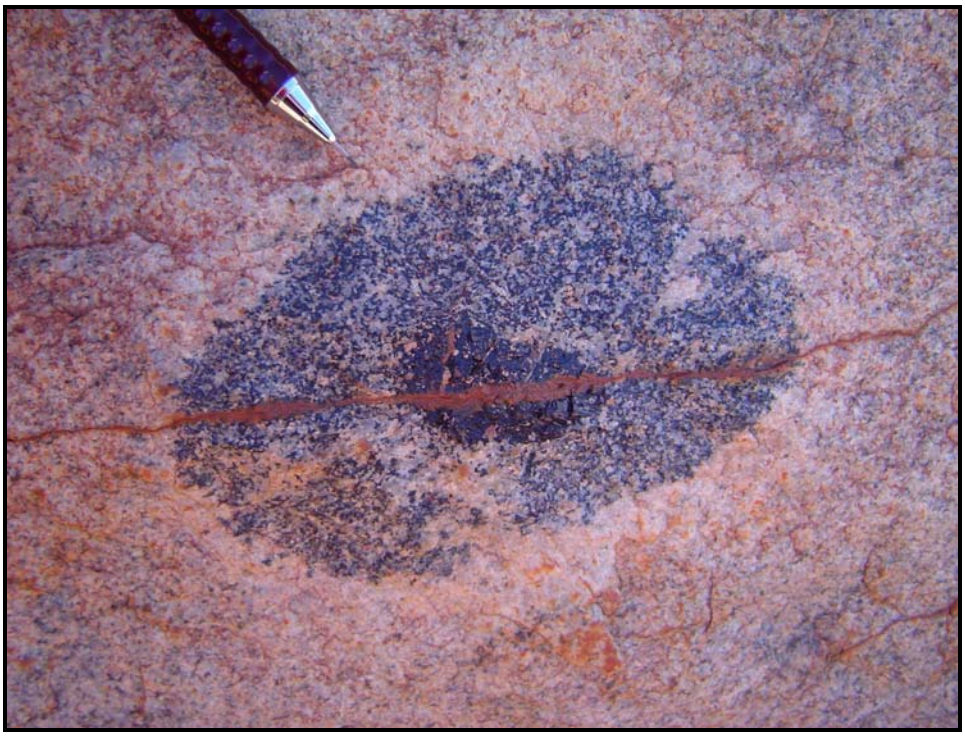

B

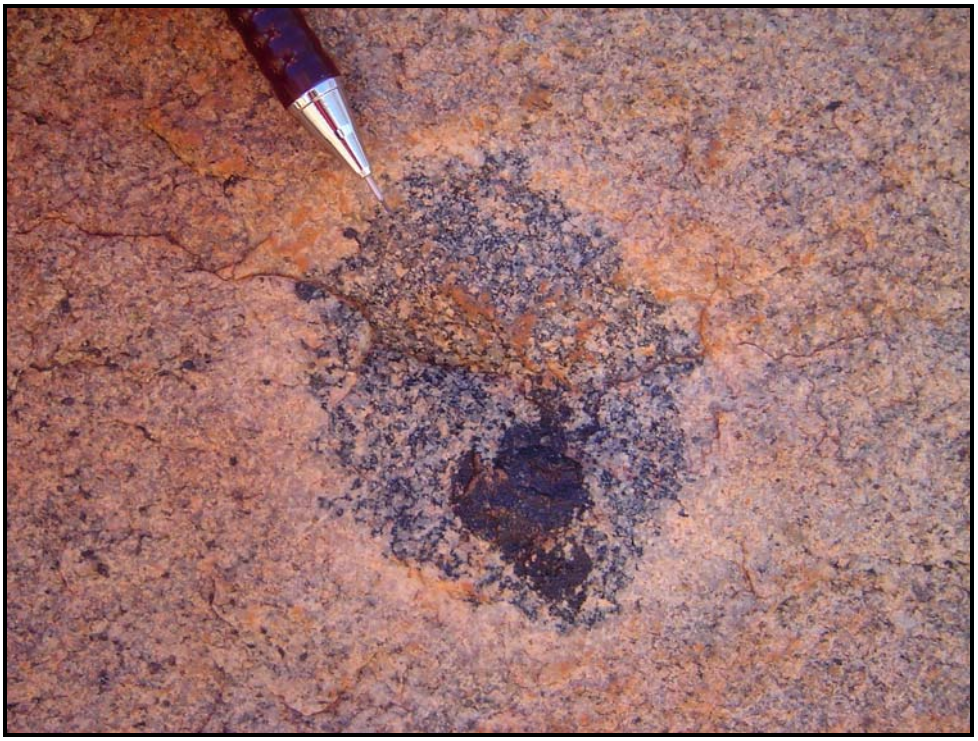

Figure 3.6: A) Nodule with a dense rosette in its core; fracture through nodule is a later feature (stop 113e); B) tourmaline rosette nodule with an off-center rosette (stop115a).

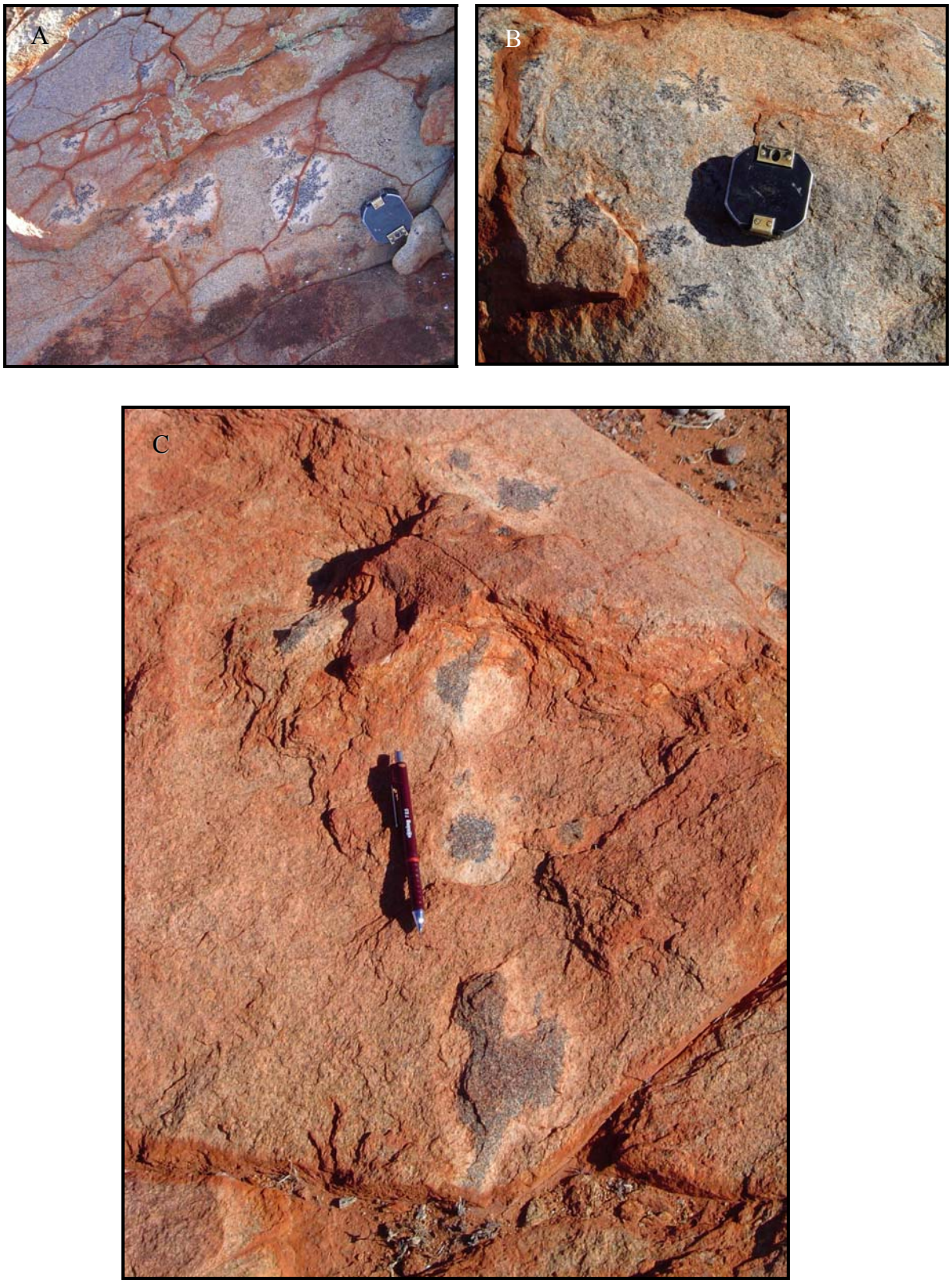

Figure 3.7: A) Irregular nodules (stop 10ae); B) Irregular, "splayed" nodules (stop 10ag); C) Irregular "blebby" nodules (stop 11c).

3.3.3.4 Flower and doughnut-shaped nodules

Nodules resembling a stylized flower or doughnut comprise this morphologic category (Figure 3.8). These two nodule types were grouped together as they are characterized by an inner zone of host granite. Ranging from 10-20cm in diameter, these medium-grained nodules contain approximately 50% tourmaline, 40% quartz, 10% plagioclase feldspar and trace amounts of biotite and muscovite. Halo material, averaging 2.5cm thick, contains approximately 65% quartz, 20% plagioclase feldspar, 10% alkali feldspar, and 5% biotite/muscovite/sericite clots. The inner granite zone is mineralogically and texturally indistinguishable from the host granite.

Flower and doughnut shaped nodules occur in the western lobe of the Scrubber Granite (Figure B.8). Irregular, spherical, and horseshoe nodules are intimately associated with these nodules, often occurring within centimeters of one another.

3.3.3.5 Horseshoe and C-shaped nodules

Horseshoe or C-shaped nodules are similar to nodules in the flower and doughnut shaped class, with the exception that they do not completely encompass the inner granitic zone (Figure 3.9). Due to their mineralogical and textural similarity to the previously outlined flower nodules, a representative sample of the horseshoe nodules was not obtained. These nodules outcrop in the western and central lobes (Figure B.9), where they are spatially associated with flower, doughnut and “telephone dial” nodules (Figure 3.10) that resemble old-fashioned telephones.

3.3.3.6 Starburst nodules

Nodules containing prismatic tourmaline crystals in the core zone that radiate outward into the halo material were termed ‘starburst’ nodules. Averaging 14cm in diameter, these nodules are generally larger and coarser grained relative to other morphologies, and contain approximately 50% tourmaline, 35% quartz, 15% plagioclase feldspar and trace amounts of muscovite in the core. Dense, bladed tourmaline crystals up to 5mm long extend out into the surrounding halo material. Quartz is associated with plagioclase feldspar, and occurs around tourmaline crystals in the core. Halo material, averaging 2cm thick, comprises 45% quartz, 25% plagioclase feldspar, 20% alkali

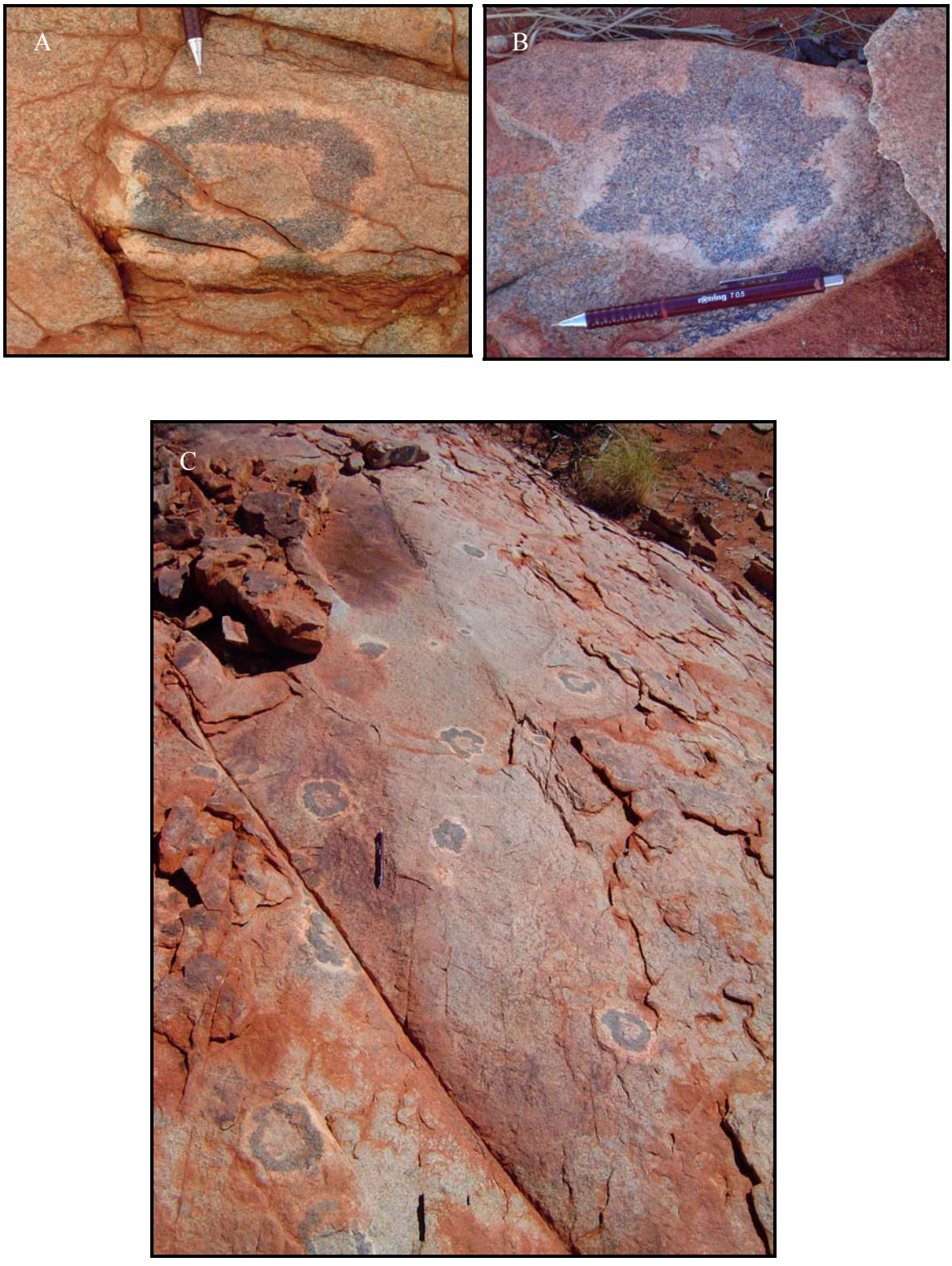

Figure 3.8: A) Doughnut shaped nodule (stop 87b); B) Flower shaped nodule (stop 65c); C) Outcrop of doughnut, flower, horseshoe and spherical shaped nodules (stop 65d).

Figure 3.9: Horseshoe or C-shaped nodule adjacent to a spherical nodule (stop 10x).

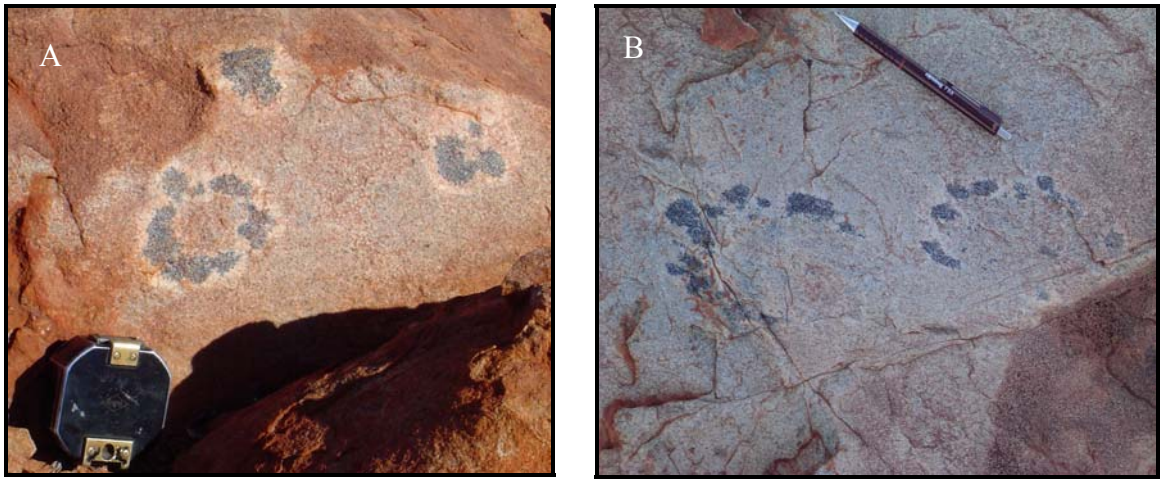

Figure 3.10: A) and B) Telephone dial nodules (stops 10d and 63a respectively).

feldspar, 6% biotite, 4% muscovite and trace amounts of opaque minerals. Quartz is associated with the feldspars. Biotite, muscovite and opaque minerals form clots that occur in the host granite and occasionally in the halo zone.

Starburst nodules occur exclusively in the southern region of the western lobe (Figure B.10). The occasional nodule core contains two or more rosettes of dense tourmaline crystals (Figure 3.11C).

3.3.3.7 Proto-nodules

Proto-nodules comprise small, 0.5-1.2cm tourmaline clots generally lacking the characteristic halo material that surrounds all other nodule morphologies (Figure 3.12). These fine- to medium-grained nodules contain 95% tourmaline crystals up to 2mm in length, and 5% quartz crystals. Biotite clots found in the host granite are in close association with tourmaline crystals of the proto-nodule.

Proto-nodules are randomly distributed throughout the western and central lobes of the Scrubber Granite, and may or may not be associated with other nodules or veins (Figure B.11). In the southern region of the western lobe, proto-nodules mimic the starburst texture of adjacent nodules.

3.4 OTHER FEATURES IN THE SCRUBBER GRANITE

3.4.1 Nodule trains, tubes and swarms

In several locations, spherical to elongate nodules are aligned parallel to each other in a train-like fashion, occasionally encompassed in the same halo material. Nodule tubes, in which halo material encloses a single pipe-like nodule, occur adjacent to other nodule morphologies in the western lobe (Figure 3.13). Running up to 3 meters in length, these tubes have rounded terminations, distinguishing them from veins. Nodule trains and tubes contain tourmaline-rich cores and leucocratic halos that are texturally and mineralogically similar to adjacent nodules and veins.

Swarms of two or more spherical to elongate nodules are sparsely located throughout the Scrubber Granite (Figure 3.14).

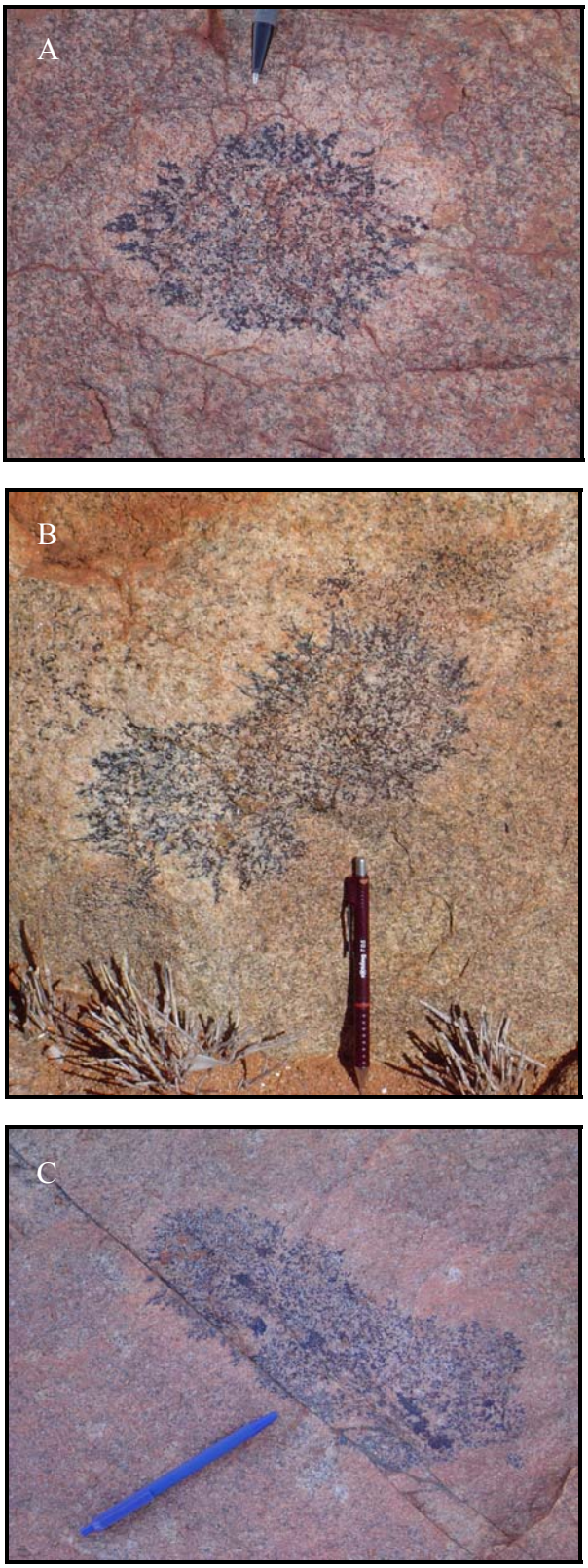

Figure 3.11: A) Starburst nodule (stop 182a); B) starburst nodule swarm (stop 35); C) starburst nodule swarm containing dense tourmaline rosettes (stop 35).

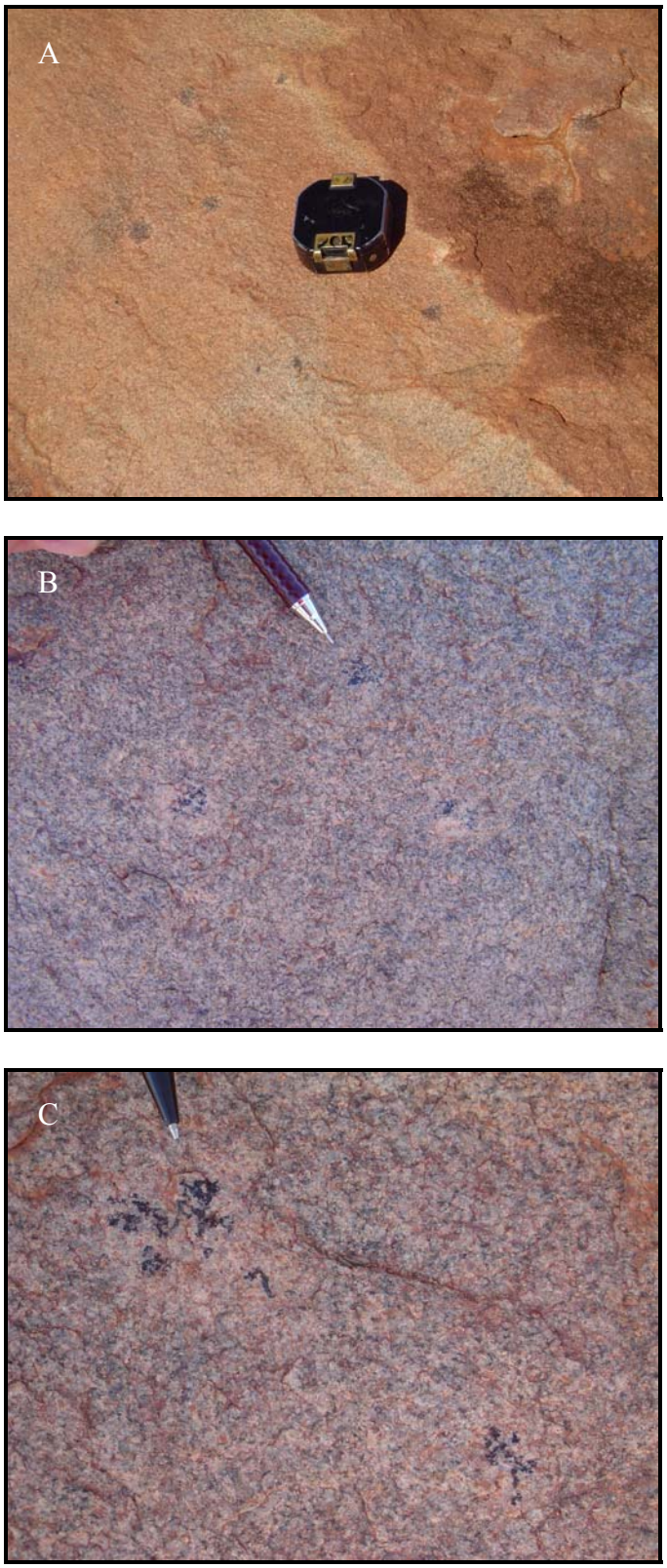

Figure 3.12: A) Proto nodules (stop 3a); B) Proto-nodules with thin halos (stop 116a); C) Proto-nodules mimicking starburst texture of adjacent nodules (stop 182c).

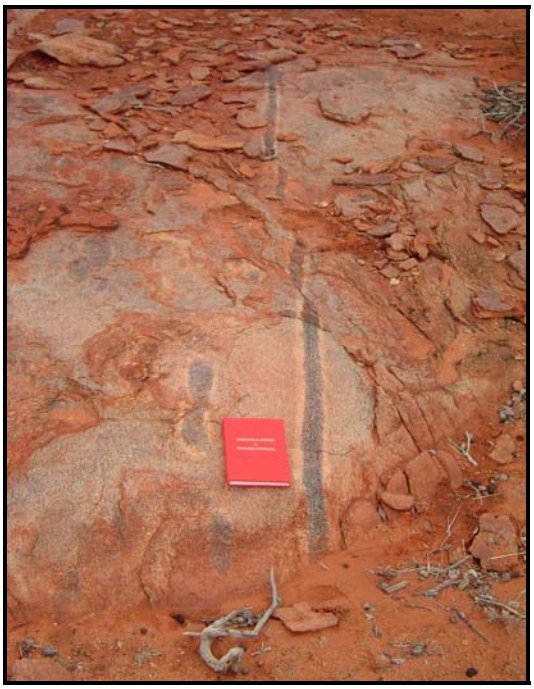

Figure 3.13: Nodule tube extending over three meters, adjacent to spherical nodules (stop 81a).

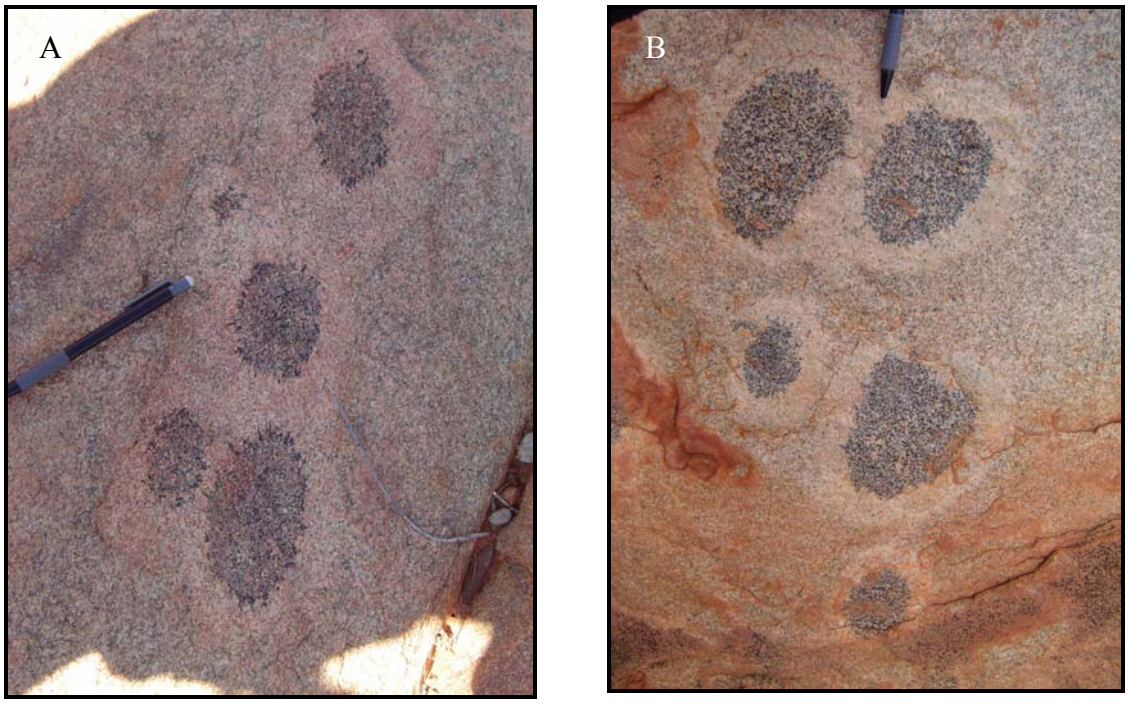

Figure 3.14: A) Swarm of five starburst nodules (stop 83g); B) Spherical nodules with adjoining halo material (stop 130b).

3.4.2 Tourmaline veins

Tourmaline veins are sparsely distributed throughout the western and central lobes of the Scrubber Granite (Figure B.12). Ranging from 0.2-2cm wide, and extending up to 8 meters long, these veins are bounded by leucocratic halos similar to those of the tourmaline nodules. Veins and veinlets (<0.5cm wide) are occasionally in close proximity to nodules; when in contact, veins crosscut nodule textures (Figure 3.15).

On average, medium- to coarse-grained veins comprise 65% tourmaline, 30% quartz and 5% plagioclase feldspar in the core region. Tourmaline crystals range from <1 to >8mm in length, with the majority occurring as elongate prisms, and some as irregular crystals. Quartz is intergrown with tourmaline and feldspar in the core. Halo material contains roughly 70% quartz, 20% alkali feldspar and 10% plagioclase feldspar.

3.4.3 Quartz-tourmaline patches

In a discrete region of the central lobe, coarse white quartz and prismatic black tourmaline crystals occur as patches in the host granite (Figure B.12). These 20 to 35cm elongate patches are similar to nodules, with the exceptions that they contain extremely coarse crystals, and lack leucocratic halos (Figure 3.16). Some patches contain multiple rosettes of dense, prismatic tourmaline needles up to 3cm in length. These patches are physically different from pegmatite pods in the Scrubber Granite.

3.4.4 Pegmatites

Pegmatites are sparsely distributed across the three lobes of the Scrubber Granite. Although mostly found as discrete pods and veins, pegmatites occasionally occur as elongate clots in the host granite. Pegmatites are recognized by their coarse crystal size, and lack of a surrounding leucocratic halo. They contain large amounts of white, cloudy quartz (85%) and lesser amounts of black tourmaline (15%).

The distribution of pegmatites appears to be random, as they are not associated with a particular granitic phase or region of the Scrubber Granite (Figure B.12). Some pegmatite pods and lenses occur in close proximity to tourmaline nodules. When in

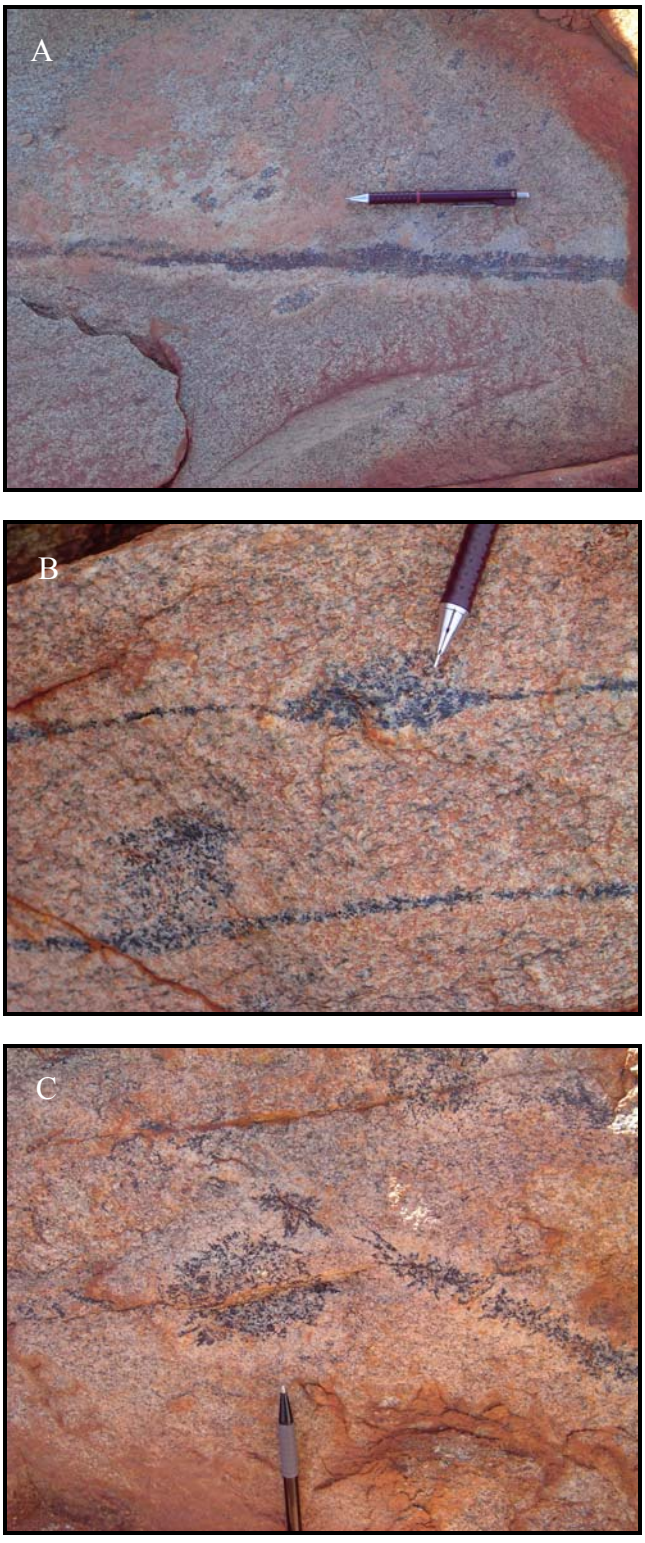

Figure 3.15: A) Tourmaline vein in close association with nodules (stop 11f); B) Veinlets overprinting nodule texture (stop 81e); C) Starburst nodule adjacent to vein with similar texture (stop 184b).

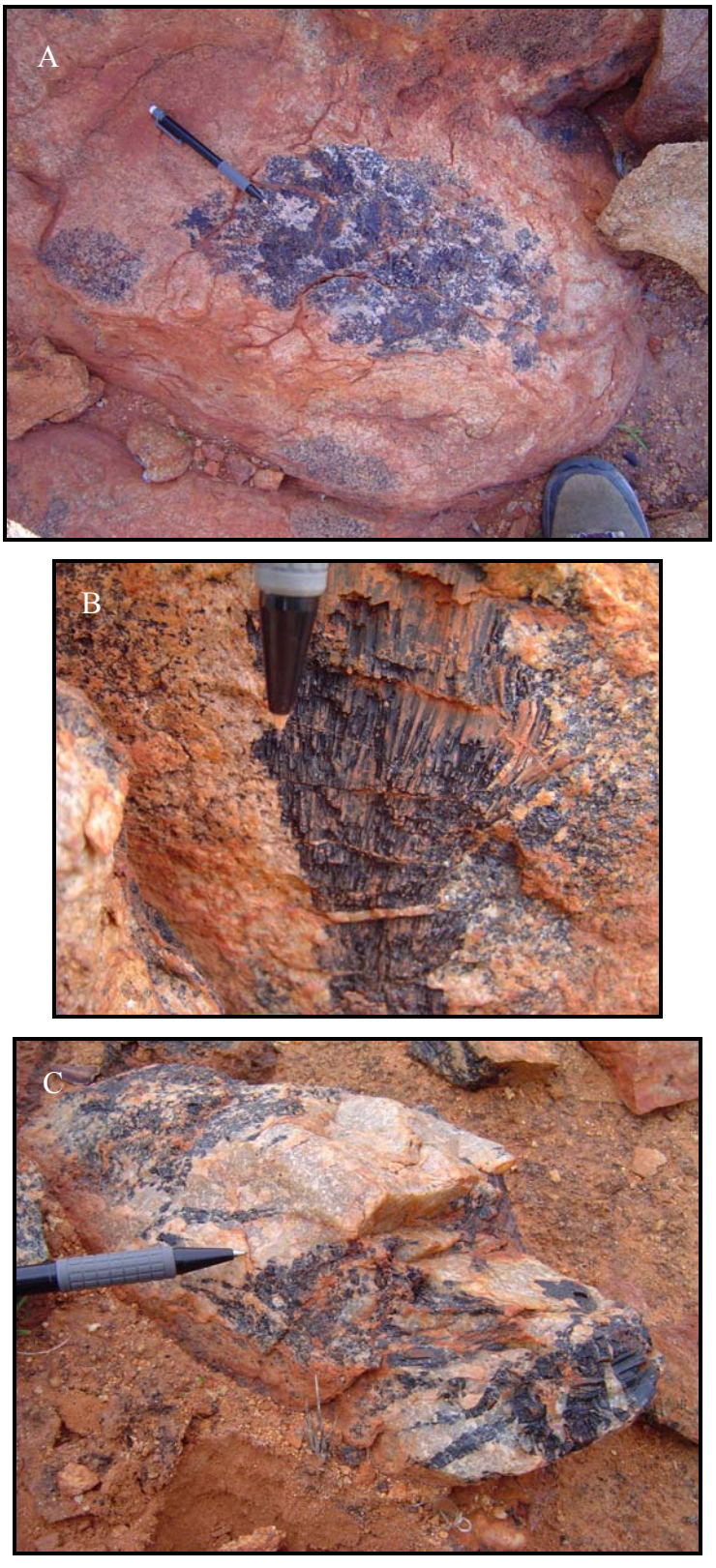

Figure 3.16: A) Quartz-tourmaline patch adjacent to nodules (stop 123a); B) Prismatic tourmaline crystals (stop 123e); C) Quartz-tourmaline patch (stop 123d).

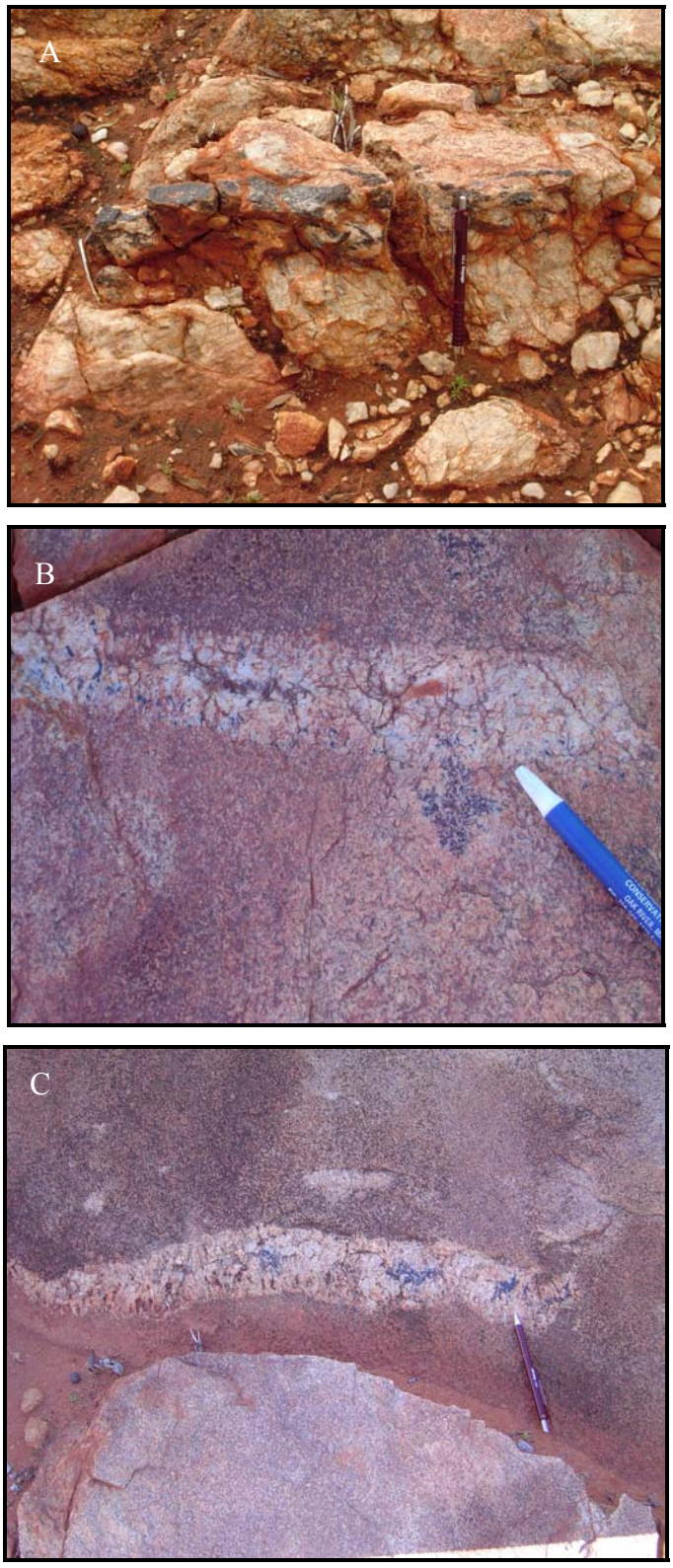

Figure 3.17: A) Pegmatite clot (stop 71a); B) pegmatite pod adjacent to tourmaline nodule (stop 10); C) pegmatite pod in groundmass of Scrubber Granite (stop 98a).

contact, pegmatites appear to overprint the nodule texture (Figure 3.17B). There are pegmatite pods and clots beyond the limits of the Scrubber Granite in surrounding rock units.

3.4.5 Inclusions in the host granite

Two inclusions of other rock types were documented in the western lobe of the Scrubber Granite; a dark, veined gneissic inclusion and a mica-rich pelitic inclusion (Figure 3.18). These inclusions do not appear to be related to nodule development, as they are not altered to tourmaline, and are not spatially associated with nodules.

3.5 CHAPTER SUMMARY

The following summary statements can be made based on field observations of the Scrubber Granite:

1. The Scrubber Granite contains various granitic phases: massive, porphyritic, foliated and sheared. Nodules, consisting of leucocratic halos and tourmaline-rich cores, are randomly distributed throughout all granitic phases;
2. Nodules were grouped into the following morphologic types: spherical, elongate, tourmaline rosette, irregular, flower/doughnut-shaped, horseshoe/C-shaped, starburst, and proto-nodules;
3. Other features observed in the Scrubber Granite include nodule trains, tubes, and swarms. Tourmaline veins and pegmatites are sparsely distributed throughout the granite; when in contact with nodules, they appear to overprint nodule textures; and
4. The host granite, halo and tourmaline-rich nodule core regions are mineralogically similar throughout the Scrubber Granite. However, there are variations in crystal size on a regional scale.

A

B

Figure 3.18: A) Gneissic inclusion in massive granitic groundmass (stop 24a); B) pelitic inclusion in granitic groundmass (stop 85a).

CHAPTER 4
MINERALOGY AND CHEMISTRY

4.1 INTRODUCTION

In order to determine the origin of nodules in the Scrubber Granite, an endeavor that intimately involves understanding the origin of tourmaline, mineralogic and textural relationships within the granite must be understood. Although these parameters have been observed macroscopically in the field and in hand specimen, the more thorough and precise details revealed through microscopic examination are essential. Field observations and petrographic studies of the Scrubber Granite resulted in the identification of three discrete mineralogic zones: 1) host granite, 2) leucocratic halo, and 3) tourmaline-rich nodule cores. Petrographic characteristics of these zones are summarized in the preliminary sections of this chapter.

Just as the change in mineralogy and texture across these zones is important for considering the genesis of nodules, so is the change in chemistry. In fact, one cannot take place without the other; a mineralogic change is essentially a chemical change. Major and trace element concentrations of each mineralogic zone in six samples were determined by x-ray fluorescence spectrometry (XRF) and inductively coupled plasma mass spectrometry (ICP-MS). Subsequent to these analyses, mass balance calculations identified fluctuations in element concentrations between mineralogical zones. Chemical variation between zones may indicate which geologic processes were involved in nodule formation.

Due to the considerable range in possible tourmaline compositions, it was necessary to chemically examine Scrubber Granite tourmaline crystals in order to categorize them. Electron microprobe analysis of zoned and unzoned tourmaline crystals are presented in section 4.6. The composition of the tourmaline aids in constraining the elements present in the nodule-forming fluid.

4.2 OVERVIEW OF MINERALOGIC ZONES

4.2.1 Macroscopic characteristics

The host granite, halo, and tourmaline-rich core zones are readily observable in the field and in hand specimen (Figure 4.1). In all mineralogic descriptions, the "host" zone represents the massive, porphyritic, foliated or sheared granite surrounding the nodule or vein. The "halo" zone consists of leucocratic granite that is commonly devoid of ferromagnesian constituents, and immediately encompasses the tourmaline-rich core region. The "core" zone is the inner region of the nodule or vein that contains tourmaline.

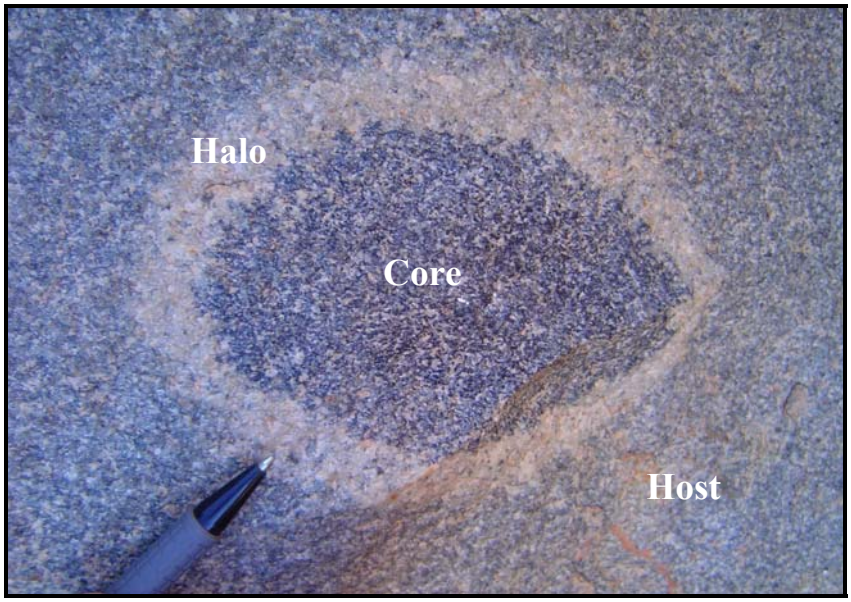

Figure 4.1: A spherical nodule (stop 162a) showing the host granite (Host), leucocratic halo (Halo) and tourmaline-rich core (Core) zones.

Although the overall texture and crystal size of the Scrubber Granite is similar across all mineralogic zones on a local (nodule) scale, regional variations in crystal size occur. Macroscopically, crystal sizes across the three lobes of the study area range from approximately 0.2 to 1cm in length. An example of crystal size variation between nodules is shown in Figure 4.2. The starburst nodule, a hand sample from stop 183 in the western lobe, is coarse grained (0.5-4mm) throughout all zones. The spherical nodule, a hand sample from stop 27, also in the western lobe, is quite fine grained throughout (0.2-0.4mm). This demonstrates that while there is variation in crystal size

from one locality to another, even within the same lobe of the Scrubber Granite, the textural characteristics are similar throughout the mineralogic zones on a nodule scale.

Also of relevance in Figure 4.2 is the marked difference in the texture of tourmaline in these two hand samples. The starburst nodule contains long, prismatic tourmaline crystals in the core region that radiate into the halo material. Conversely, the fine-grained tourmaline of the spherical nodule is irregular to blebby, and does not form prismatic crystals. The range of textures observed in tourmaline crystals through the various nodule types in the Scrubber Granite is discussed in section 4.3.3.

Figure 4.2: Starburst nodule (top) and spherical nodule (bottom) showing crystal size differences between nodules from spatially separate areas of the Scrubber Granite. However, crystal size is constant throughout the mineralogic zones in each of these nodules.

4.2.2 Microscopic characteristics

Typical major mineral assemblages and textures of the mineralogic zones in the Scrubber Granite are summarized in Table 4.1 (full petrographic descriptions of samples 130315-130324 are provided in Appendix C). Typical major mineral abundances are summed to 100%. Accessory phases (zircon, apatite, allanite and monazite) are present throughout all mineralogic zones, comprising trace to 1% volume of the Scrubber Granite. Rare earth element carbonates (bastnasite, (Ce, La, Y) CO_3F and synchysite, Ca (Ce, La, Nd, Y)$(CO_3)_2$ F; see Pan et al., 1994), detected during electron microprobe analyses, occur along fractures between tourmaline, quartz, and feldspar crystals in the core zone, and between quartz and feldspars in the halo and host granite.

Table 4.1: Typical major mineralogy and texture of the various zones in the Scrubber Granite.

Zone	Mineral Phase	Range %	Typical %	Occurrence/ Textures
Host Granite	Quartz	55-65	60	Mosaic texture
	Albite	10-20	15	Intercrystalline texture with microcline and quartz
	Microcline	2-20	10	Intercrystalline texture with albite and quartz
	Biotite	7-15	10	Disseminated throughout groundmass as clots
	Muscovite	2-8	5	Isolated flakes or in biotite clots
Halo	Quartz	45-75	60	Mosaic texture
	Albite	10-25	20	Intercrystalline texture with microcline and quartz
	Microcline	2-20	12	Intercrystalline texture with albite and quartz
	Biotite	2-8	5	Disseminated throughout groundmass as clots
	Muscovite	2-5	3	Isolated flakes or in biotite clots
Core	Tourmaline	30-95	60	Irregular to prismatic
	Quartz	5-55	28	Mosaic texture
	Albite	5-16	10	Intercrystalline texture with microcline and quartz
	Microcline	2-5	2	Intercrystalline texture with albite and quartz

The typical major mineralogy of the three zones outlined in Table 4.1 is appropriate for the spherical, elongate, irregular, horseshoe/C-shaped, and starburst nodules, as well as tourmaline veins and tubes. However, there are additional mineralogic zones present in the tourmaline rosette nodules (dense rosette) (Figure 4.3),

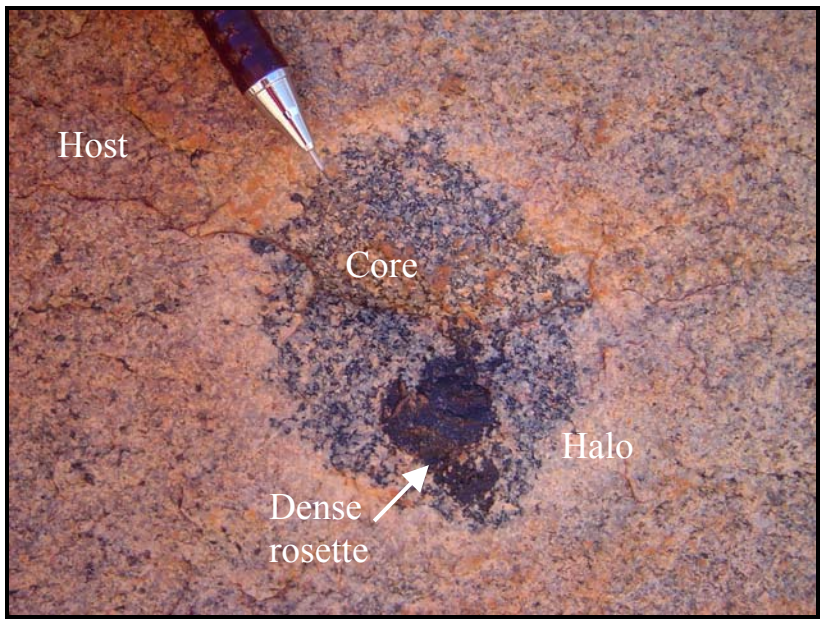

Figure 4.3: Field photo of tourmaline rosette nodule (stop 115a) displaying four mineralogic zones: 1) Host; 2) Halo; 3) Core; and 4) Dense rosette.

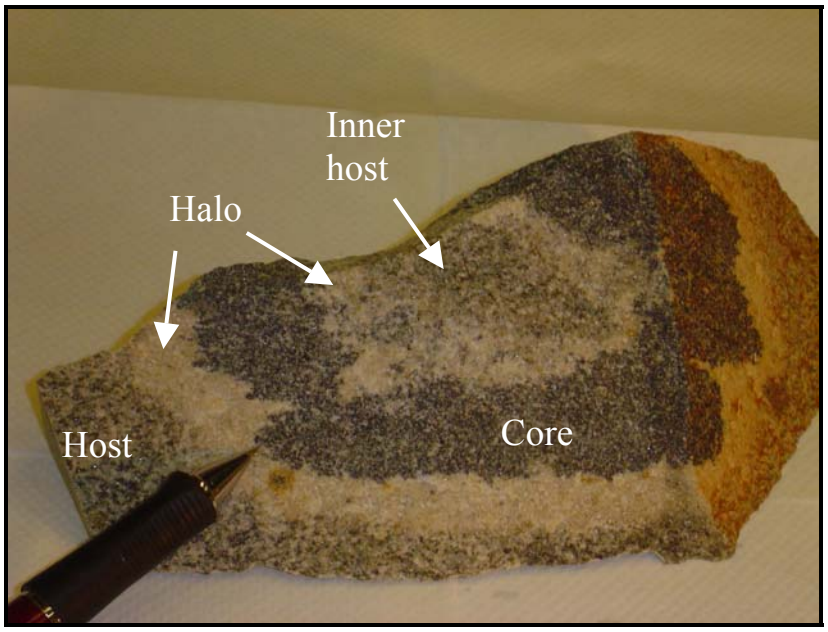

Figure 4.4: Hand sample of flower-shaped nodule (from stop 65) comprising five mineralogic zones: 1) Host; 2) Halo; 3) Core; 4) Halo; and 5) Inner host.

and in the flower/doughnut-shaped nodules (inner granitic zone and an additional halo zone) (Figure 4.4). Proto-nodules are commonly devoid of the leucocratic halo zone.

4.3 MINERALOGIC ZONES IN DETAIL

The host granite, halo and tourmaline-rich zones are obvious in hand specimen, and it is easy to pinpoint where one zone ends and another begins. However, the microscopic transition from one mineralogic zone to another is quite ambiguous. There is no distinct transition from host granite to halo, with the exception of the absence of biotite (excluding those halos that contain biotite clots), and no distinct transition from halo to core, excluding the presence of tourmaline (Figure 4.5; sample 130318, stop 65). Textural relationships (grain size and the nature of grain contacts) between the major mineral constituents are similar through all mineralogical zones. Typical petrographic characteristics of the three zones are presented in the following sections.

4.3.1 Host granite zone

The host granite may be massive, porphyritic, foliated or highly sheared, and may or may not contain nodules. The host commonly contains abundant biotite clots, although some regions do not contain any. Microscopic analyses of the host granite have revealed that the host granite is texturally and mineralogically similar to the halo and core zones, with the exceptions that it is more melanocratic than the halo due to higher concentrations of biotite clots, and it does not contain tourmaline (Figure 4.6).

The host granite typically contains 60% quartz, 15% albite, 10% microcline, 10% biotite, and 5% muscovite. Quartz crystals range from 0.1-1.2mm in diameter, forming interlocking polycrystalline aggregates that display a mosaic texture between grains. Aggregates are commonly parallel to any foliation in the rock, and are intergrown with feldspar crystals. Quartz commonly contains trace to moderate amounts of apatite, zircon and monazite crystals ranging from 0.01-0.02mm in diameter.

Sub-rounded to tabular microcline crystals range from 0.2-3.10mm in length, and are randomly distributed throughout the groundmass. Crystals are intergrown with albite and quartz, and are moderately included with muscovite flakes 0.03-0.2mm in

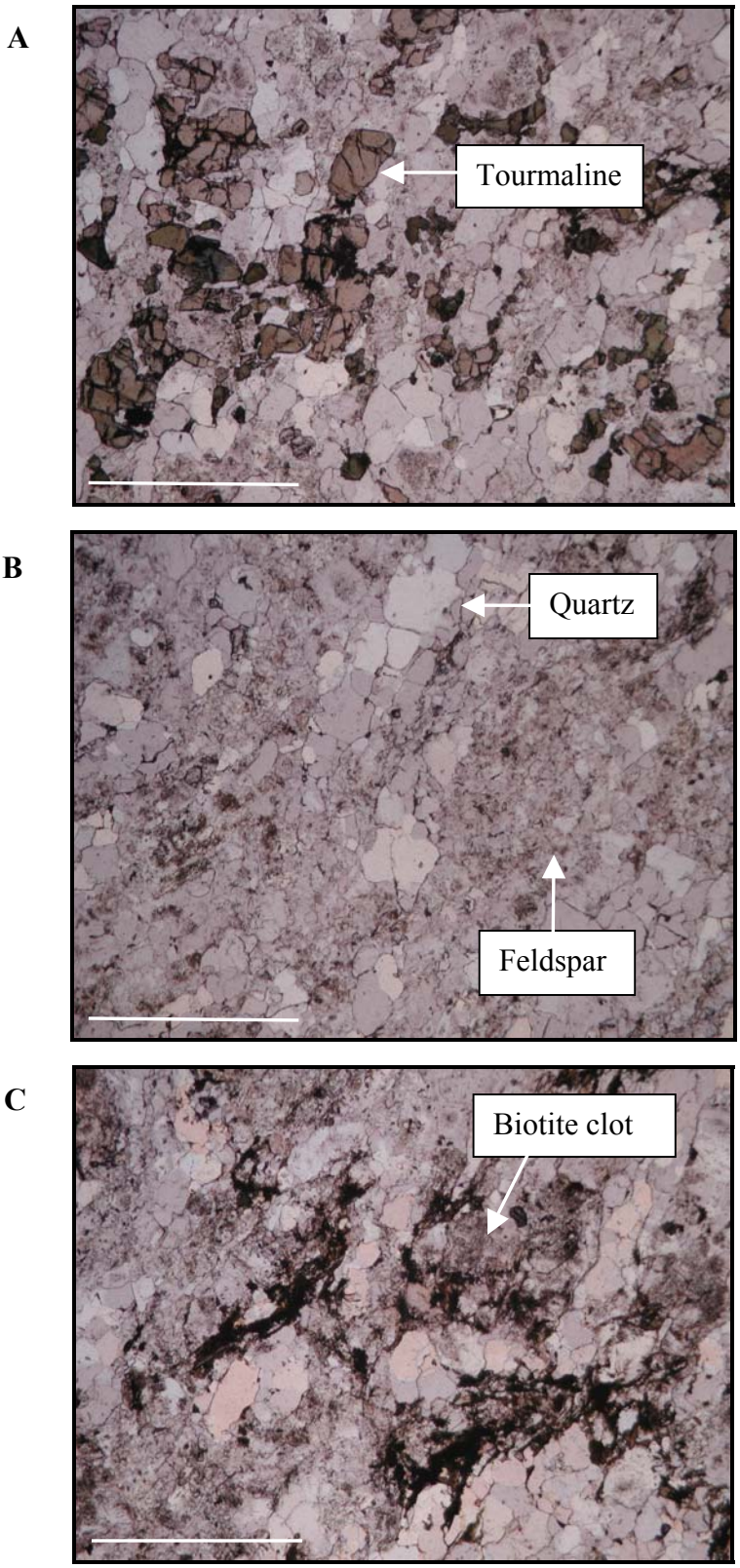

Figure 4.5: A) Tourmaline in the nodule core zone; B) Quartz and feldspars in the halo zone; C) Biotite clots of the host granite zone. Plane-polarized light; scale bar is 1mm.

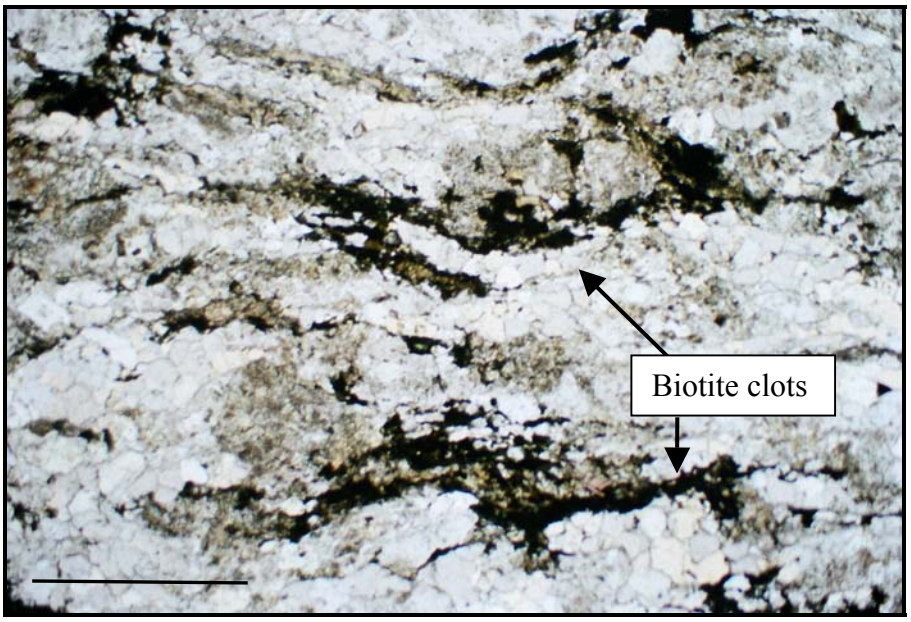

Figure 4.6: Photomicrograph of host granite zone (sample 130321) containing biotite clots that define a moderate foliation throughout the groundmass. Polycrystalline quartz aggregates and feldspar comprise the groundmass. Plane-polarized light, scale bar represents 1mm.

length, and albite crystals 0.5mm in length. Albite crystals are tabular and range from 0.5-4mm, and are intergrown with microcline and quartz crystals throughout the groundmass. They are highly included with muscovite and sericite flakes 0.03-0.5mm in length, which probably indicate alteration. This gives the albite a "dusty" appearance. Albite also occurs as phenocrysts in porphyritic phases of the Scrubber Granite.

Biotite flakes ranging from 0.1-0.5mm in length occur along with muscovite, sericite, opaque minerals and clay minerals to form 0.3-4mm elongate clots. These clots appear to overprint the major mineralogy of the groundmass including quartz and feldspar, defining a foliation of varying degrees throughout the host granite (Figure 4.6). Clots contain 70% biotite, 20% muscovite/sericite, 5% clay minerals and 5% opaque minerals; hematite is also present in some clots. Muscovite flakes ranging from 0.2-1mm in length occur in biotite clots and as discrete flakes randomly dispersed throughout the groundmass. Sericite and opaque minerals occur as sub-microscopic to 0.02mm grains within clots. Clays occur as sub-microscopic, sub-opaque brown-black minerals.

4.3.2 Leucocratic halo zone

Leucocratic halo zones are mineralogically similar throughout the Scrubber Granite, and are texturally comparable (i.e. similar grain size and grain contacts) to the adjacent host granite. The halo commonly contains 60% quartz, 20% albite, 12% microcline, ± 5% biotite, and 3% muscovite. Quartz crystals range from 0.1-1.2mm in diameter, forming polycrystalline mosaic aggregates that are intergrown with albite and microcline, and tend to parallel any foliation in the rock. Quartz is moderately included with apatite, zircon and monazite crystals 0.01-0.02mm in diameter.

Tabular albite crystals 0.5-1.2mm in length are randomly distributed throughout the groundmass where they are intergrown with quartz aggregates and microcline crystals. They are highly included with muscovite and sericite flakes 0.05-0.7mm in length, indicating moderate alteration. Microcline crystals are sub-rounded to tabular in form and range from 0.3-2.8mm in length. They are randomly distributed throughout the groundmass, and are intergrown with quartz aggregates and albite. Microcline crystals are moderately included with muscovite flakes 0.03-0.2mm in length and albite crystals 0.5mm in diameter.

Although regarded as "leucocratic" due to the absence of biotite and other dark mineral phases, some halo zones contain varying amounts of biotite clots, occasionally up to 10% (Figure 4.7). These clots are mineralogically and texturally similar to those of the host granite zone.

4.3.3 Tourmaline-rich core zone

The tourmaline-rich core zone commonly contains 60% tourmaline (abbreviated Tur following Kretz, 1993), 30% quartz, 10% albite and trace amounts of microcline. Similar in texture to the host granite and leucocratic halo zones, the core zone is comprised of 0.1-0.7mm polycrystalline quartz mosaics that are intergrown with tourmaline and feldspars, and infill fractures in tourmaline crystals. Tabular albite crystals 0.8-1.7mm in length are intergrown with quartz aggregates and microcline crystals. Albite contains many inclusions such as 0.05mm muscovite flakes, sub-microscopic sericite, indicating alteration, and 0.08mm quartz crystals. Microcline crystals are rare in nodule cores; where present, these 0.2-4mm sub-rounded crystals are

A

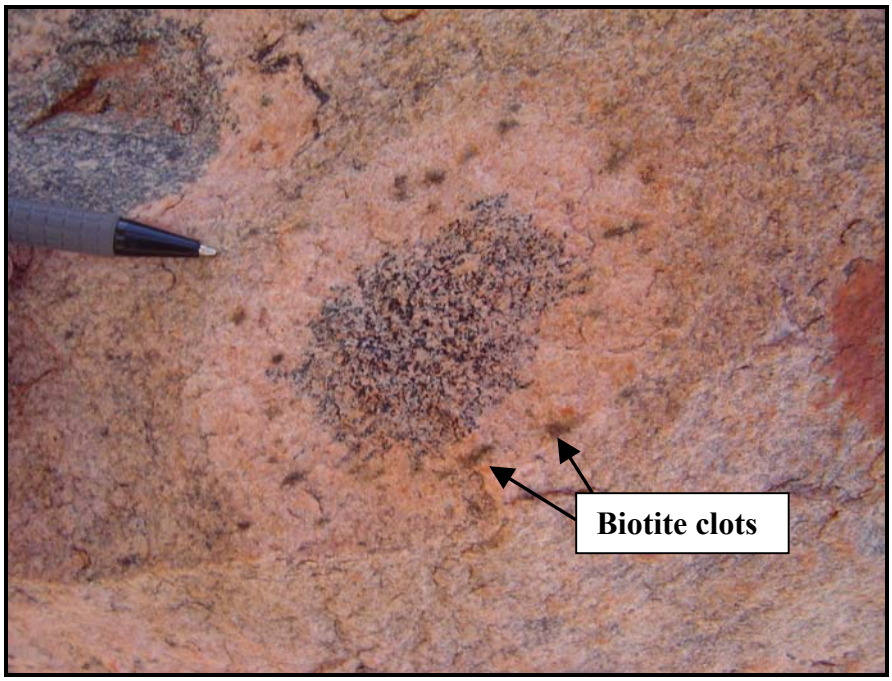

B

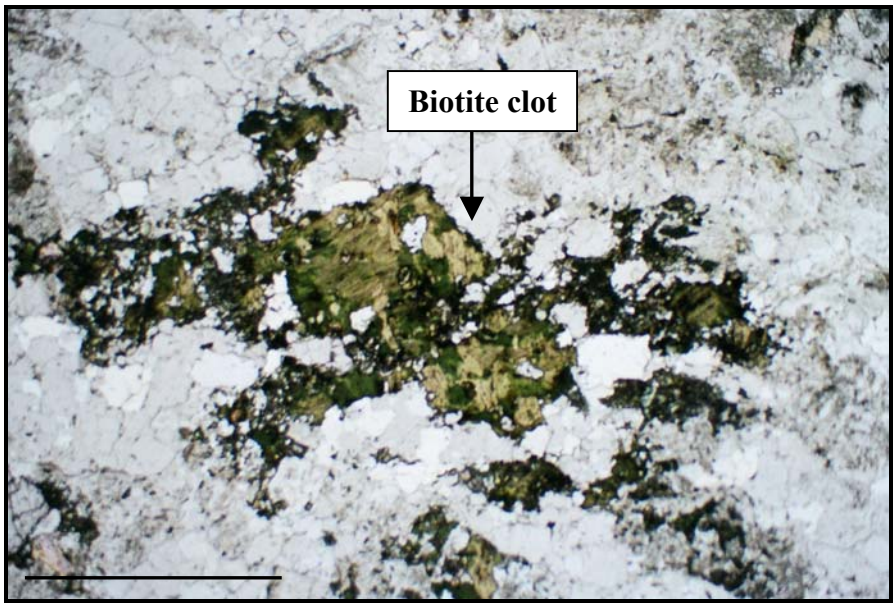

Figure 4.7: A) Macroscopic view of biotite clots in halo material (stop 156a); B) photomicrograph of biotite/muscovite/sericite/opaque mineral clot in a halo zone, surrounded by polycrystalline quartz aggregates and feldspar crystals. Plane-polarized light, scale bar represents 1mm.

intergrown with albite crystals and quartz aggregates. Tourmaline crystals present in the core zones of nodules and veins are typically unzoned and exhibit several textural habits. Tourmaline most frequently occurs as randomly distributed, fractured, irregular aggregates lacking crystal shape, or as sub-rounded to sub-equant crystals that are slightly rhombohedral in form. These crystals are green-brown in plane polarized light, and range from 0.1 to >2mm in diameter. However, in several nodule morphologies, including the starburst nodules, tourmaline occurs as dense clusters of interlocking prismatic needles extending up to 1cm in length. These crystals show a marked pleochroism, ranging from green-brown to purple. Irregular to sub-equant tourmaline crystals may occur along with these prismatic counterparts in nodule and vein core zones. In the dense rosette of the rosette nodules, tourmaline occurs as massive aggregates. Occasionally, tourmaline crystals appear to be altered along crystal boundaries and within fractures.

Although some of these differing textural habits may arise from the angle at which the crystals were cut, they will be discussed separately as they demonstrate different features of the tourmaline crystals. The following section reviews the textural diversity observed in tourmaline crystals of the Scrubber Granite and its associations with other mineral phases.

4.3.3.1 Irregular tourmaline crystals

Patchy or blebby non-prismatic tourmalines in the core zone are termed “irregular” tourmaline crystals. Ranging from 0.1-2mm in length, these crystals are commonly encompassed by polycrystalline quartz aggregates and embayed by dusty albite crystals, which contributes to their irregular or patchy appearance (Figure 4.8). Fractures within tourmaline crystals are commonly infilled by quartz, REE carbonates, and occasionally by hematite, as seen in Figure 4.9. Generally, tourmaline displays irregular grain contacts with feldspar and quartz crystals (Figure 4.10).

Irregular tourmaline crystals occur along with prismatic and sub-rounded to sub-equant tourmaline crystals in nodule cores.

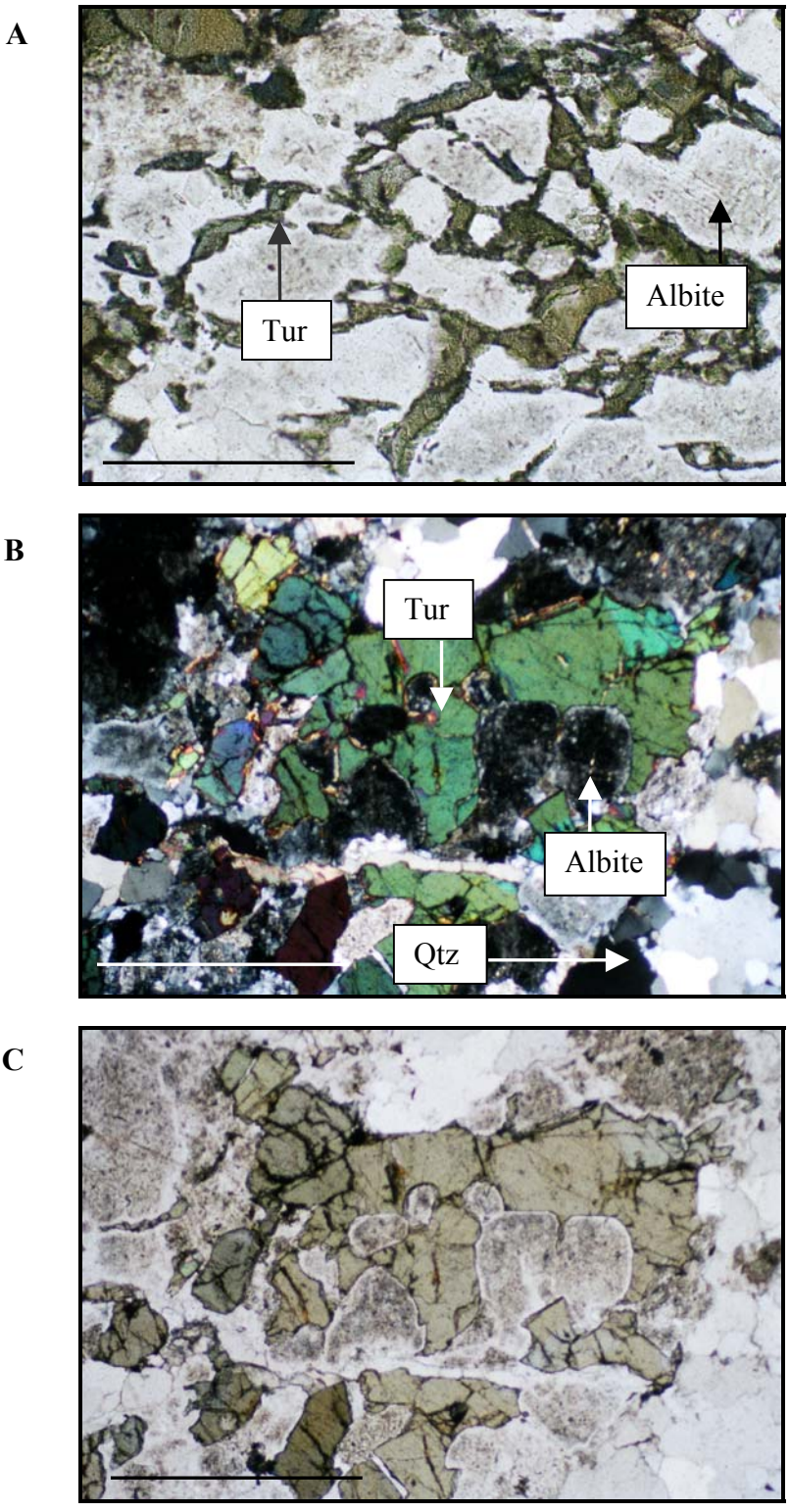

Figure 4.8: A) Irregular, patchy tourmaline (Tur) crystals associated with dusty albite crystals; plane polarized light; B) irregular tourmaline crystals intergrown with quartz aggregates (Qtz) and embayed by albite crystals; cross polarized light; C) same as B, in plane polarized light; scale bar represents 1mm (all photos from sample 130315).

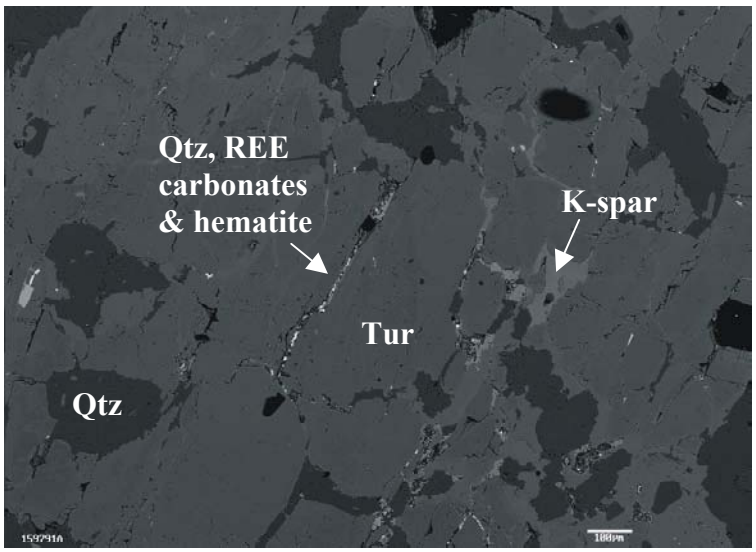

Figure 4.9: Back scattered electron photomicrograph of tourmaline (Tur) in the center, with fracture fill (quartz, REE carbonates and hematite) and alkali feldspar (K-spar) and quartz (Qtz) around it. Sample 159791A; scale bar represents 100μm.

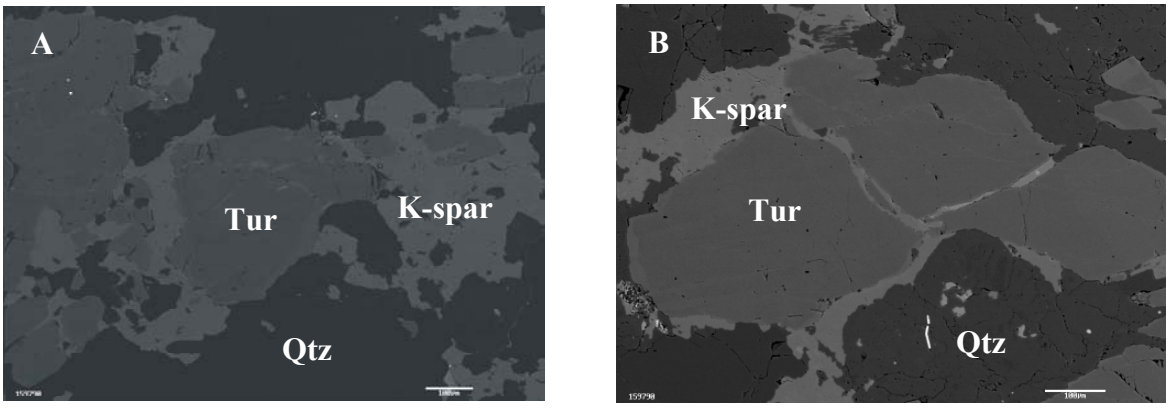

Figure 4.10: A) and B) Back scattered electron photomicrograph of tourmaline (Tur), alkali feldspar (K-spar) and quartz (Qtz) in sample 159790; scale bar represents 100 μm.

4.3.3.2 Sub-rounded to sub-equant tourmaline crystals

Tourmaline crystals commonly occur as sub-rounded to sub-equant crystals in the core region. Ranging from 0.02-1.3mm in diameter, these tourmalines are typically

the smallest of tourmaline crystals, and are encompassed by polycrystalline quartz aggregates (Figure 4.11). Unlike their irregular counterparts, sub-rounded to sub-equant tourmaline crystals are rarely embayed by albite crystals, and occur along with irregular, prismatic, and massive tourmaline crystals in nodule cores and in tourmaline veins (Figure 4.12).

4.3.3.3 Prismatic tourmaline crystals

Prismatic or bladed tourmaline crystals range from 0.1 to >1cm in length in nodule cores. They are surrounded by polycrystalline quartz aggregates and may include albite and quartz crystals (Figure 4.13). Fractures within tourmaline are infilled by quartz crystals. Prismatic tourmaline crystals are associated with sub-rounded to sub-equant crystals (see Figure 4.13a) and with irregular and massive tourmaline crystals.

4.3.3.4 Massive tourmaline

Massive tourmaline, dense aggregates of large, occasionally prismatic, fractured crystals, occurs in the dense rosette zone of the tourmaline rosette nodules. Surrounding the dense rosette are sub-rounded to sub-equant tourmaline crystals of the nodule core. The latter are associated with polycrystalline quartz aggregates and dusty albite crystals (Figure 4.14). Massive tourmaline may encompass albite and quartz crystals; tourmaline fractures are infilled by quartz.

4.3.3.5 Altered tourmaline

A number of tourmaline crystals from various nodule types exhibit weak to moderate alteration in the form of red-brown to black sub-opaque to opaque material along grain boundaries and within fractures (Figure 4.15A and B). This material is similar to the sub-opaque mineral assemblage associated with biotite clots of the host granite and halo zones. However, biotite is not associated with this dark material in the core zone. Tourmaline and biotite are rarely adjacent to one another, with the exception of the proto-nodules, where tourmaline and biotite are in close spatial association due to the lack of halo material separating the core and host granite zones (Figure 4.15B).

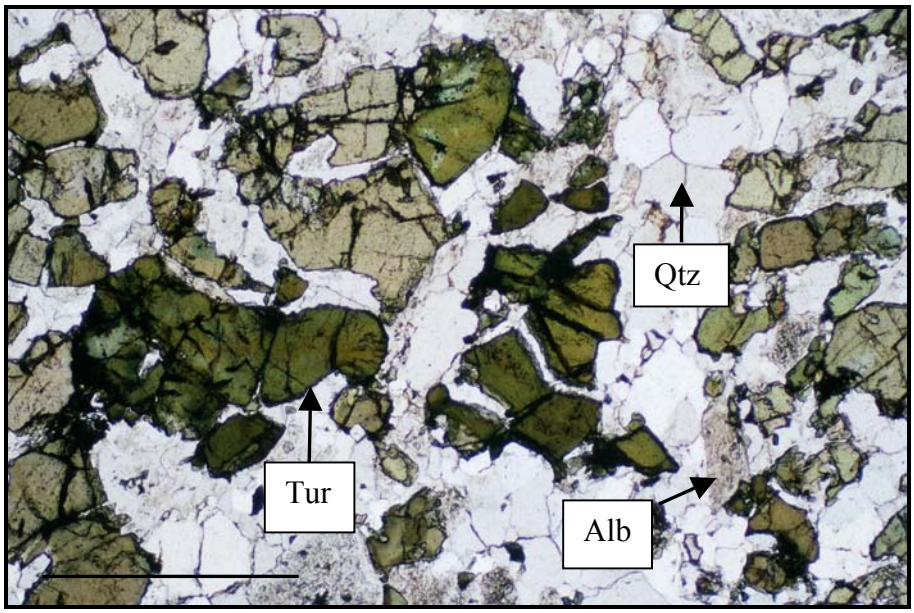

Figure 4.11: Sub-rounded tourmaline crystals (Tur) in sample 130318 (flower shaped nodule). Tourmaline is intergrown with quartz aggregates (Qtz) and dusty albite crystals (Alb). Plane polarized light; scale bar represents 1mm.

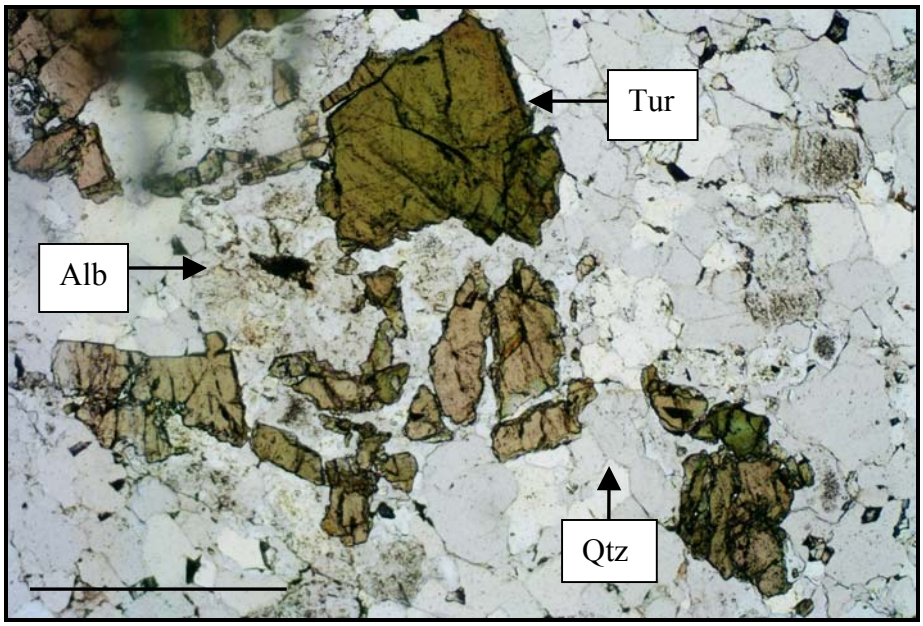

Figure 4.12: This photomicrograph is from a tourmaline vein (130323), which displays the same sub-rounded tourmaline texture and mineral associations as nodule cores. Plane polarized light; scale bar represents 1mm.

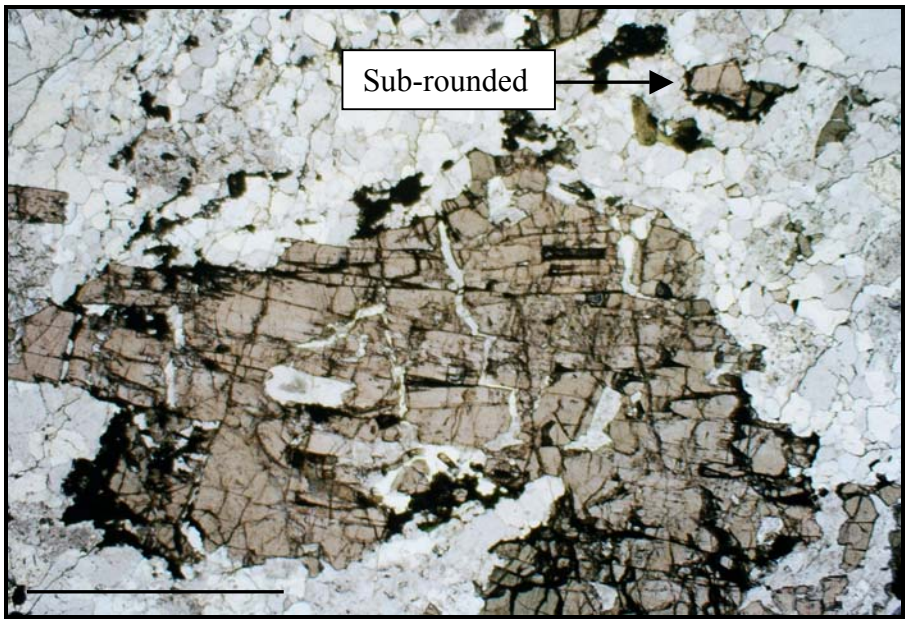

Figure 4.13: Bladed tourmaline crystals in the core zone of sample 130316, adjacent to sub-rounded crystals. Plane polarized light; scale bar represents 1mm.

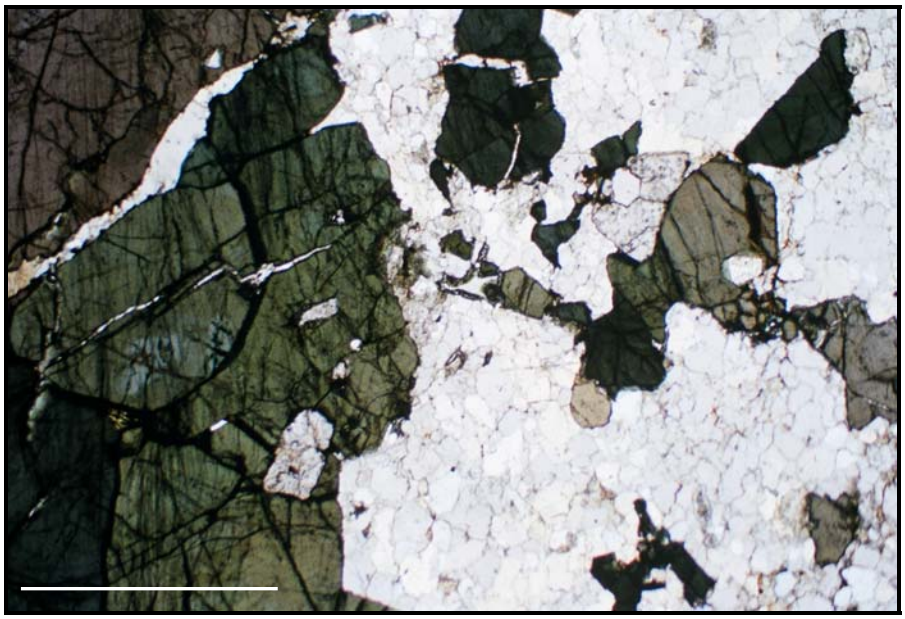

Figure 4.14: This photomicrograph of sample 130319 shows the massive tourmaline of the dense rosette to the left, and the sub-equant tourmaline of the surrounding nodule core to the right. Plane polarized light; scale bar represents 1mm.

A

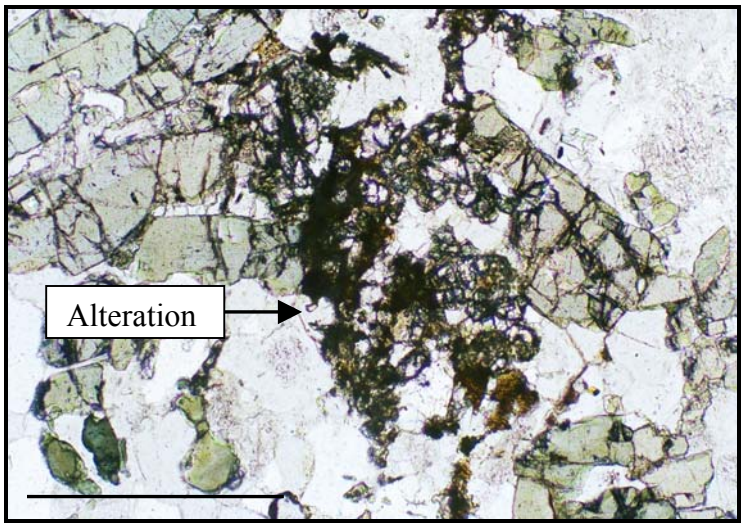

B

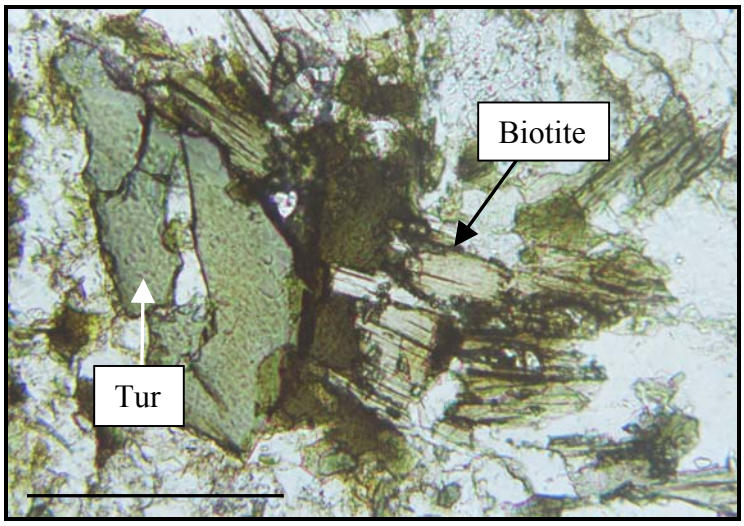

Figure 4.15: A) Altered tourmaline crystals of sample 130318; B) tourmaline in contact with biotite clot in a proto-nodule (sample 130322). Plane polarized light; scale bar represents 1mm.

4.4 CHEMISTRY OF THE MINERALOGIC ZONES

4.4.1 Introduction

Examining the mineralogic and textural characteristics of the host granite, leucocratic halo and tourmaline-rich core zones of the Scrubber Granite is an integral part of this study, as it reveals information relating to the physical development of tourmaline (e.g. intergranular textural relationships) as well as information that ultimately relates to the

chemistry of the fluid from which the tourmaline crystallized (e.g. minerals present in the core zone). However, a more detailed account of fluid chemistry is provided by the chemical examination of each mineralogic zone.

Whole rock analyses of the various mineralogic zones from six Scrubber Granite samples were completed. Major and trace element concentrations were measured using x-ray fluorescence (XRF) and inductively coupled plasma mass spectrometry (ICP-MS). Mass balance calculations were completed using this data to determine which elemental phases were gained or lost across the zones. Appendices D.2-D.4 summarize the analytical techniques involved in these processes.

Determining the chemistry of tourmaline crystals in the Scrubber Granite is also important, as this reveals what elements were necessary for the precipitation of tourmaline. Results of electron microprobe analysis of individual tourmaline crystals are presented in Section 4.6. These results are used to categorize the tourmaline on an Al-Fe-Mg ternary diagram and to calculate chemical formulae.

4.4.2 Whole rock data

Whole rock analyses were completed on isolated rock chips of the various mineralogical zones in the following samples: 1) spherical nodule (130315); 2) starburst nodule (130316); 3) flower nodule (130318); 4) massive granite (130321); 5) tourmaline vein (130323); and 6) nodule from porphyritic granite (130324). These samples were chosen as they contained the necessary volume of each mineralogic zone required for sampling and analysis, and were deemed representative of the nodule types. Mineralogical and textural similarities between nodules suggest that any nodule from the Scrubber Granite would likely yield similar whole rock chemical results. Rock chips are representative of the bulk mineralogic zone they were extracted from, and contamination from neighboring zones was avoided during sampling. Samples of each zone were extracted using a rock saw, and were powdered for chemical analysis.

Major and trace element concentrations in the host, halo and core zones of samples 130315, 130316 and 130318 were examined, as well as an additional inner granite zone in sample 130318 (see Figure 4.4). An isolated, massive granite (sample 130321) was examined for chemical comparison with granite zones immediately

adjacent to nodules or veins. The tourmaline-rich zone of the vein sample 130323 was too thin to attain a reasonably sized sample for analysis, so only the halo and host granite were examined. Similarly, only the core and host granite were analyzed in sample 130324, as the volume of halo material was insufficient for testing. Major and trace element concentrations of the various zones in these samples are given in Tables D.1 and D.2 in Appendix D.

Major and trace element data for the core, halo and host zones of samples 130315 (spherical nodule), 130316 (starburst nodule) and 130318 (flower nodule) are presented diagrammatically in the following sections for discussion purposes. These samples were chosen as all three zones were chemically analyzed, and they are representative of all core, halo and host major and trace element data (see Tables D.1 and D.2).

4.4.2.1 Major element concentrations

Core zones from samples 130315, 130316 and 130318 have similar major element concentration trends (see Figure 4.16 and Table D.1 in Appendix D). They commonly contain similar SiO_2 and Al_2O_3 concentrations, higher MgO, Fe_2O_3, MnO, TiO_2 and P_2O_5 concentrations, and lower Na_2O and K_2O concentrations relative to the host. Differences in chemical concentrations between zones are directly related to slight differences in mineralogy; differences between the host and core are related to the lack of abundant feldspars in the core and the lack of tourmaline in the host. The higher concentration of magnesium, iron and possibly manganese in the core can be directly attributed to the presence of tourmaline. The relatively higher concentration of phosphorous could possibly be due to an abundance of phosphate minerals (apatite and monazite) in the core relative to the host. The relative depletion in sodium and potassium in the core relative to the host is likely due to the lower concentration of Na- and K-rich mineral phases such as albite, microcline and biotite.

Halo zones from samples 130315, 130316 and 130318 have similar major element concentration trends. Relative to the host, they have comparable SiO_2, Al_2O_3, Na_2O, K_2O and P_2O_5 concentrations and lower MgO, Fe_2O_3, MnO and TiO_2 concentrations. The similarities between the host and halo element concentrations can

be attributed to the similar abundance of quartz, feldspars, and the relative depletion of the aforementioned elements can be attributed to the lack of abundant biotite clots in the halo relative to the host granite.

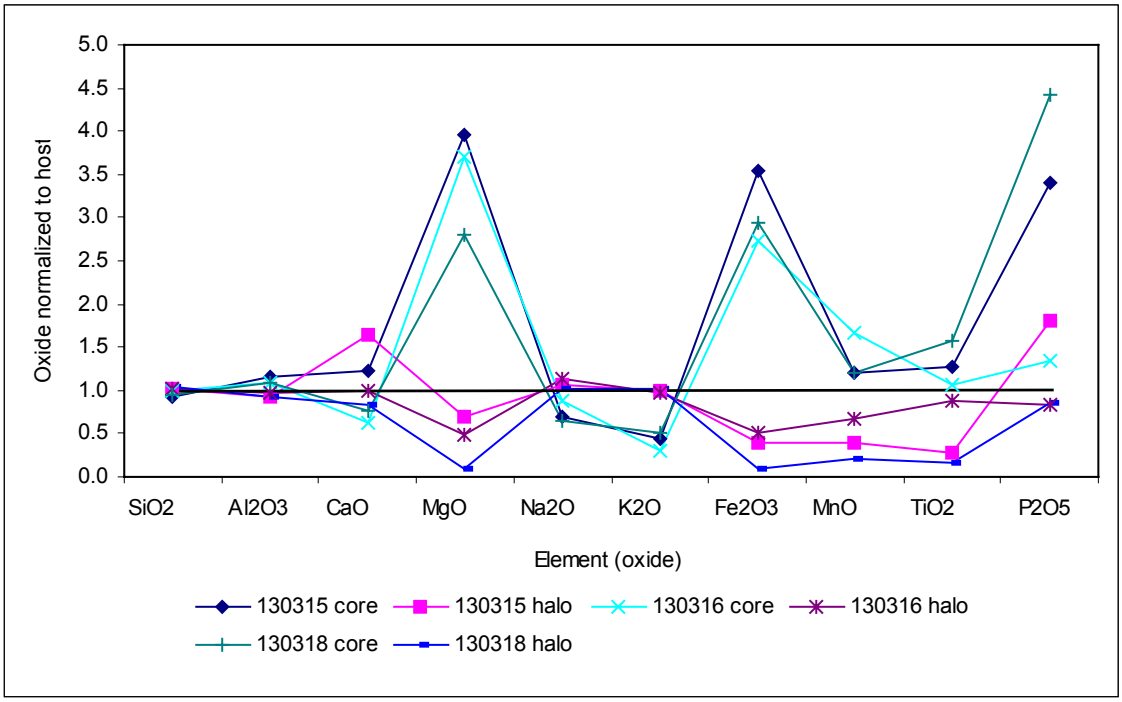

Figure 4.16: Major element oxide concentrations of core, halo and host zones in samples 130315, 130316 and 130318, normalized to the host.

4.4.2.2 Trace element concentrations

Core zones in samples 130315, 130316 and 130318 have similar trace element concentration trends (Figure 4.17; Tables D.1 and D.2). Relative to the host, the core has comparable Zr, Hf and Th concentrations, higher B and Sc concentrations, and lower Rb, Sr, Y, Nb, Ba, and Ta concentrations. As most trace elements do not usually form their own mineral phases, differences in trace element concentrations across the three zones are often related to trace element substitutions for select major elements in mineral phases.

The core and host have similar zirconium and hafnium concentrations due to the relatively uniform distribution of zircon crystals throughout the Scrubber Granite. The higher boron concentration in the core is attributable to the abundance of tourmaline.

The relative depletion in Rb and Sr relative to the host is expected, as these elements tend to substitute for K in biotite and microcline, mineral phases that are sparse to absent in the core. The depletion in Ba is perhaps due to its occasional substitution for Ca and Na and its role in the sericitization of mineral phases more abundant in the halo and host zones such as microcline and plagioclase (Lesher et al., 1986).

The halo zones from samples 130315, 130316 and 130318 have similar trace element concentration trends. Relative to the host, these samples generally have similar Sr, Zr, Ba, Hf, Ta and Th concentrations, higher B concentrations, and lower Sc, Rb, Y, and Nb concentrations. The high boron content can be attributed to the occasional and sparse occurrence of tourmaline in the halo zones. Overall, the host contains a higher concentration of trace elements relative to the halo.

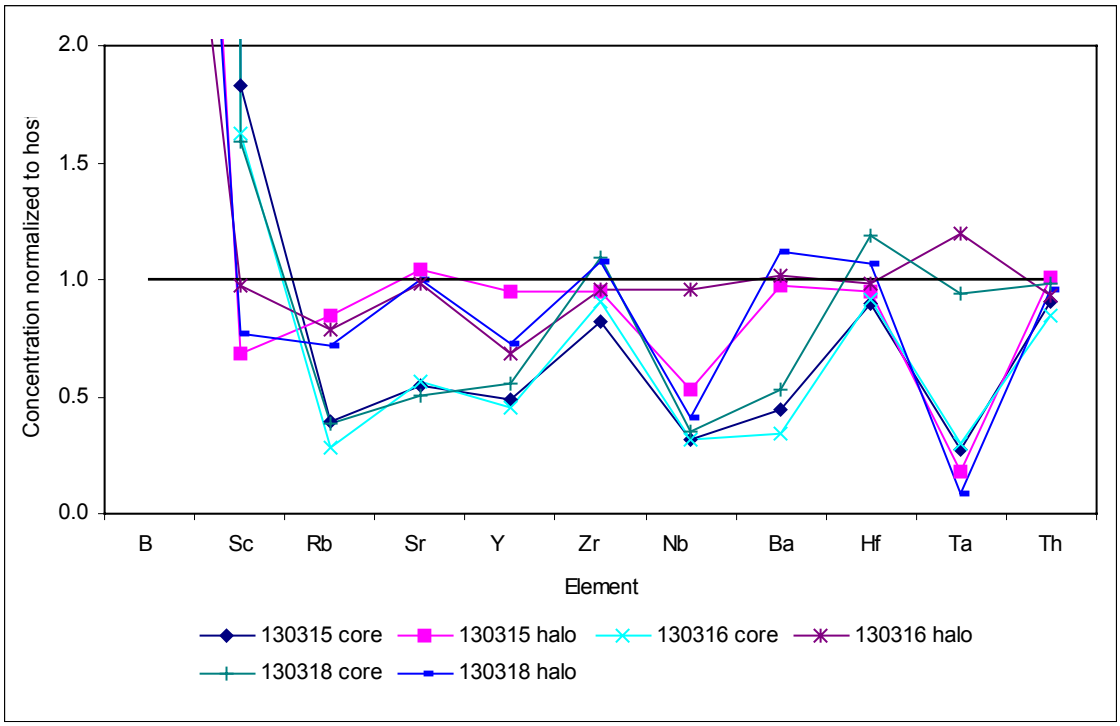

Figure 4.17: Trace element data of the core, halo and host zones of samples 130315, 130316 and 130318, normalized to the host. Note: boron concentration in the core is 385 times greater than the host in 130315, 360 times greater in 130316, and 563 times greater in sample 130318; boron concentration in the halo is 7.5 times greater than the host in sample 130315, 4.3 times greater in sample 130316 and 6.7 times greater in sample 130318.

Chondrite-normalized plots of core, halo and host rare earth element concentrations in samples 130315, 130316 and 130318 are provided in Figures 4.18A, B and C, respectively. All mineralogic zones in these samples display an LREE-enriched pattern, with a pronounced europium anomaly. Generally, the halo zones tend to have the lowest REE concentrations, and the core has the highest.

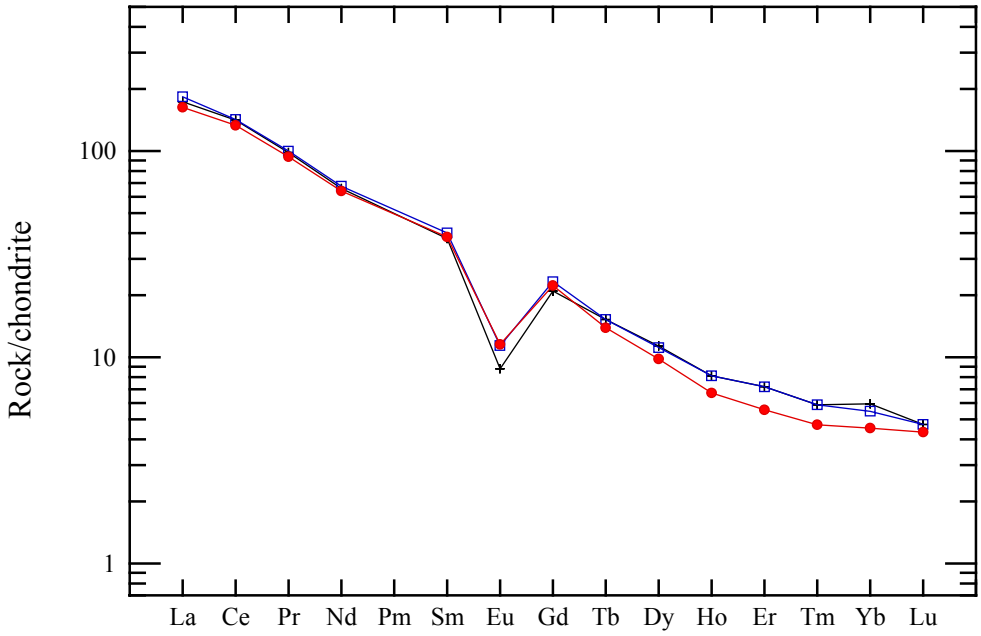

Figure 4.18A: Rare earth element chondrite-normalized plot of the core, halo and host zones of sample 130315. Crosses denote core values, open squares denote halo values, and infilled circles denote host values. Created in IgPet 2001, using chondrite values of Sun and McDonough (1989).

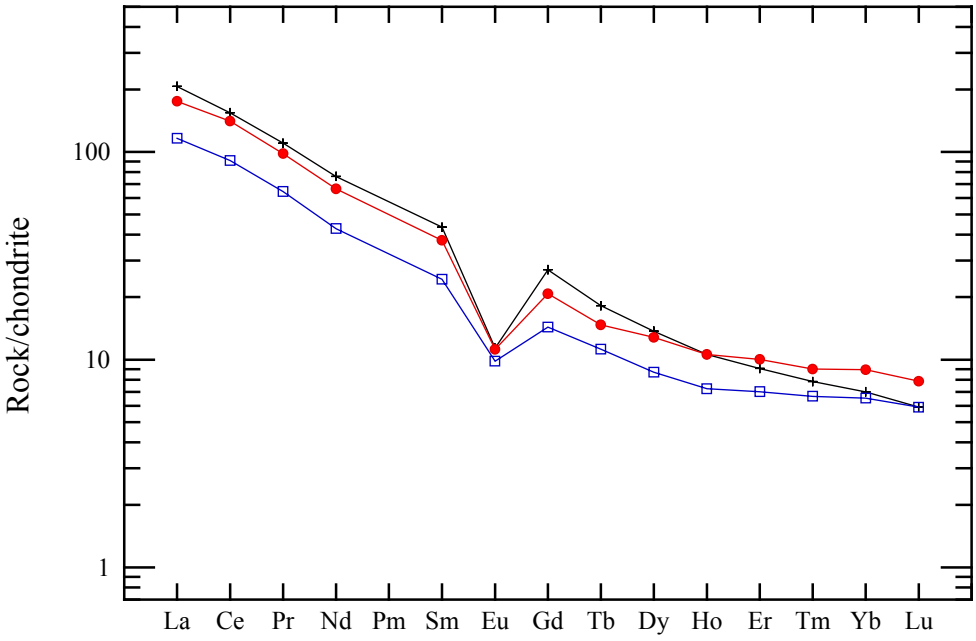

Figure 4.18B: Rare earth element chondrite-normalized plot of the core, halo and host zones of sample 130316. Crosses denote core values, open squares denote halo values, and infilled circles denote host values. Created in IgPet 2001, using chondrite values of Sun and McDonough (1989).

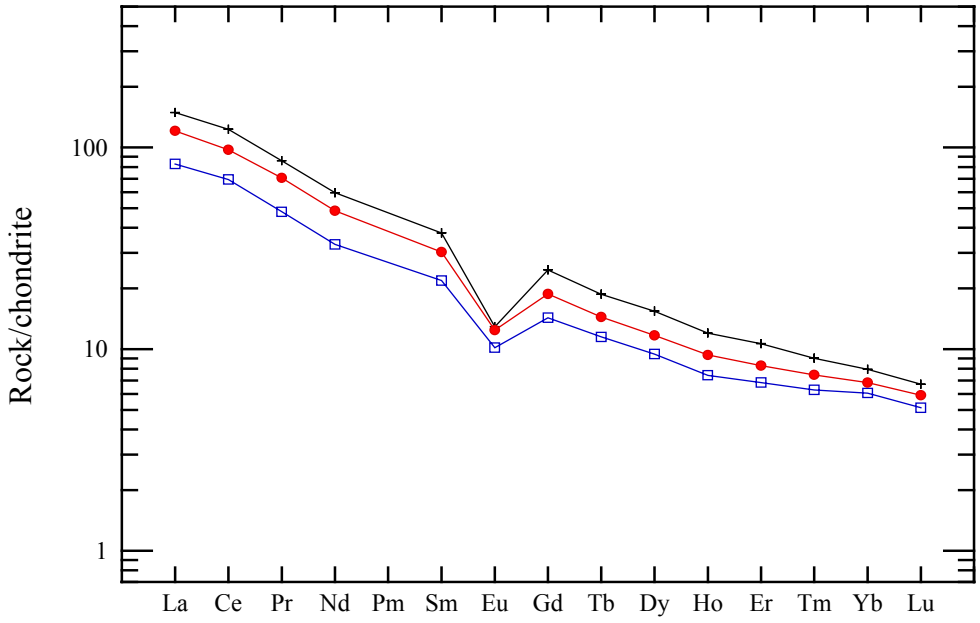

Figure 4.18C: Rare earth element chondrite-normalized plot of the core, halo and host zones of sample 130318. Crosses denote core values, open squares denote halo values, and infilled circles denote host values. Created in IgPet 2001, using chondrite values of Sun and McDonough (1989).

4.5 MASS BALANCE CALCULATIONS

As previously stated, this study requires some estimate of relative elemental concentrations among core, halo and host zones of the Scrubber Granite in order to constrain the chemical composition of the nodule-forming fluid. Gresens (1967), and other studies including Babcock (1973), Grant (1986), and Leitch and Lentz (1994), have derived a set of equations that directly relate compositional variations to mass changes. Conventional mass balance calculations are concerned with the chemical losses and gains that occur during the alteration of a parent rock (Leitch and Lentz, 1994).

In the following discussions, the 'unaltered' mineralogic zone is termed the parent rock, and the relatively 'altered' zone is termed the product. These terms are used herein to maintain the terminology established in the literature, and do not imply that nodule formation was an alteration process. The relative assignment of these terms depends on the parent-product pair of interest; for example, when comparing host and core zones, the host has been assigned as the parent and the core as the product. Mass balance calculations are employed in this study to solve for relative changes in rock chemistry between mineralogic zones.

4.5.1 The Gresens' method

The Gresens' (1967) mass balance calculation method is summarized in this section, following the presentation of the basic mass balance equation. Gresens' equation is:

$$X_n = W^B - W^A = w \{[(F_v)(X^B)(S^B/S^A)] - X^A\} \quad (4.1)$$

Where
- X_n is the weight % change in component n;
- W^A, W^B are the weight % of component n in parent rock A and product rock B;
- w is the initial mass of parent rock in grams;
- F_v is the volume factor, the ratio of volume of product rock to parent rock (in weight %);
- X^A, X^B are weight % proportions of component n in parent rock A and product rock B, calculated from chemical analyses, and
- S^A, S^B are specific gravities of parent and product rock, measured on representative rock chips.

Thus, the mass change is calculated by subtracting the weight percent of the element in the product from that in the parent ($W^B - W^A$) for each parent-product pair. In the above equation, w is commonly set to 100g so that if X^A and X^B are in weight percent, X_n is in weight percent change of component n. X^A and X^B values for each element can be determined from chemical results given in weight % oxide; trace element results must be converted from ppm to %. Since variation in specific gravity (S^A, S^B) is usually minor, (commonly less than 5%), it is not necessary to measure specific gravities if only gross changes in chemical composition are sought (Leitch and Lentz, 1994). Therefore, the S^B/S^A ratio was set to one. However, as tourmaline has a specific gravity of 3.2, it was decided to test the suitability of using a S^B/S^A ratio of unity by varying the specific gravity of the various parent-product pairs based on the relative proportions of tourmaline, quartz and feldspar. Ratios of slightly above (1.1) and below unity (0.96) were substituted into equation 4.1. These values affected the magnitude of previous results obtained using $S^B/S^A = 1$, but not the relative increases or decreases in element concentration between zones. The volume factor F_v is the ratio of the parent rock volume to the altered rock volume. This ratio is calculated using those elements thought to be immobile, such as the oxides TiO_2 and Al_2O_3 or elements such as Zr, Y, and Nb (see section 4.5.1.1) (Leitch and Lentz, 1994). If the oxide considered to be immobile is Al_2O_3 then the mass ratio is X^A_{Al2O3}/X^B_{Al2O3}. Substituting this factor for F_v in equation 4.1 yields:

$$X_n = W^B - W^A = w\ \{[(X^A_{Al2O3}/X^B_{Al2O3})\ (X^B)\ (S^B/S^A)] - X^A\} \qquad (4.2)$$

X^A_{Al2O3}/X^B_{Al2O3} is the mass ratio of Al_2O_3 in parent rock A and product B, used directly from chemical analyses, assuming Al_2O_3 is immobile. Once the F_v of an immobile element is calculated for each parent-product pair, this can be applied to the mobile oxides or elements to get real mass gains and losses. The volume factor is thus a correction factor. Leitch and Lentz (1994) summarize this process by stating that "mass balancing recalculates the immobile component back to its original composition and multiplies the mobile component by the X^A_{Al2O3}/X^B_{Al2O3} ratio".

Substituting values for w, F_v, X^A, X^B and S^A, S^B into equation 4.1 yields values for X_n, the change in mass proportion of component or element n. The interpretation of these values, which can be positive or negative, involves an appreciation for the

apparent changes in mobile and immobile element masses during mass additions (positive X_n values) and mass subtractions (negative X_n values). Since this equation is essentially product mass minus parent mass, positive values indicate an increase in the element's mass in the product, and negative values indicate a decrease in the element's mass in the product.

Interpretation of positive and negative mass balance values in this study is slightly different from that of the common hydrothermal alteration study that employs mass balance calculations to determine what has been added to or lost from the system via development of hydrothermal veins. This study employed mass balance calculations to identify relative changes in element concentrations among the various zones with no assumption that changes were a result of hydrothermal alteration. For example, a mass increase in iron in the core zone relative to the host does not necessarily indicate that the iron migrated from the host to the core. Changes in element mass between zones and how it relates to nodule development are discussed further in Chapter 7.

4.5.1.1 Establishing an immobile element

Gresens (1967) made the fundamental assumption that one or more components are immobile during the alteration of a parent rock. In order to complete mass balance calculations, an immobile element must be identified, as these elements are used as correction factors (see equation 4.2). Based on previous mass balance studies (see discussion below), Al and Zr were deemed immobile in the mass balance calculations in this study.

MacLean and Kranidiotis (1987) and MacLean (1988) have demonstrated that Al and Zr were highly immobile elements during hydrothermal alteration of volcanic host rocks in the Phelps Dodge massive sulfide deposit. These elements were also deemed immobile at Matagami (MacLean, 1984), Kidd Creek (Campbell et al., 1984) and Noranda (Gibson et al., 1983). Grant (1986), in his paper providing an alternate solution to Gresens' mass balance calculations, also assumes that aluminum has remained immobile in his hypothetical discussion. Furthermore, MacLean (1990) uses Al_2O_3 and Zr to establish immobile element fractionation lines, and Barrett and

MacLean (1991) demonstrated how the strong effects of alteration can be examined using the "highly immobile Ti-Zr-Al group of elements". Thus, Al and Zr, proven to be immobile, will be used to calculate mass changes between mineralogic zones.

4.5.1.2 Example Calculation

Table 4.2 presents data used in a sample mass balance calculation using equation 4.2 and assuming Al_2O_3 immobility for sample 130315 (spherical nodule). The parent (A) is the host granite zone and the product (B) is the halo zone. The following steps are followed in completing mass balance calculations:

1. Determine mass fraction values for element concentrations given in weight percent oxide by dividing the chemical results by 100, and multiplying by the atomic weight of the elements divided by the molecular weight of the oxide. Convert trace elements from ppm to percent, and then follow the above steps.
2. Determine Fv for each parent-product pair, using immobile element.
3. Using equation 4.2, determine weight percent change in element.

Thus, the weight % change in element Si is:

Step 1: Parent (A) = 0.7433 (28.08/60.08) = 0.3474
Product (B) = 0.7511 (28.08/60.08) = 0.3511

Step 2: $F_v = X^A_{Al2O3}/X^B_{Al2O3} = 0.0738/0.0676 = 1.09$

Step 3: $X_{Si} = w\ \{[(F_v)\ (X^B)\ (S^B/S^A)] - X^A\}$
$X_{Si} = 100\ \{[(1.09)\ (0.3511)\ (1)] - 0.3474\}$
$X_{Si} = 3.53$

Table 4.2: Mass balance calculation for sample 130315.

Element	Analyses Parent Amount (Host)	Analyses Product Amount (Halo)	X^A Element Mass Proportion	X^B Element Mass Proportion	X_n Relative Change (%)
SiO_2	74.33	75.11	0.3474	0.3511	3.53
Al_2O_3	13.94	12.78	0.0738	0.0676	-0.01
CaO	1.33	2.18	0.0095	0.0156	0.75
MgO	0.30	0.21	0.0018	0.0013	-0.04
Na_2O	3.18	3.35	0.0236	0.0249	0.36
K2O	4.5	4.45	0.0374	0.0369	0.28
Fe_2O_3	1.43	0.57	0.0100	0.0040	-0.56
MnO	0.05	0.02	0.0004	0.0002	-0.02
TiO_2	0.15	0.04	0.0009	0.0002	-0.07
P_2O_5	0.05	0.09	0.0002	0.0004	0.02
Fv = X^A_{Al2O3}/X^B_{Al2O3} = 1.09 for all calculations.					

The above mass balance calculations were carried out for several parent-product pairs in the samples analyzed for their whole rock major and trace element concentrations, including 1) host-halo, 2) halo-core, and 3) host-core. Additional calculations were completed for samples containing more than three mineralogic zones (e.g. flower nodule sample 130318, due to the additional inner granite zone) or less than three, in cases where all zones could not be sampled (e.g. tourmaline vein sample 130323).

4.5.2 Results

Complete mass balance results for major and trace elements are presented in Appendix D.4. Aluminum was assumed to be immobile in major element calculations, and zirconium was assumed to be immobile in trace element calculations; as both phases are immobile, similar results would have been obtained if only one was used in all calculations (see discussion in section 4.5.1.1). Results of mass balance calculations for host-halo, halo-core, and host-core parent-product pairs completed on sample 130315 are summarized in the following sections. This sample was selected for discussion purposes as it is representative of most nodule results; relative gains or losses in major and trace elements between nodule types is the same, and absolute differences are due to local compositional variations. In Figures 4.19 to 4.21, positive values indicate an apparent increase of the elemental concentration in the product, and negative values indicate an apparent decrease in the elemental concentration in the product (see Table 4.3). Table 4.4 summarizes the major element gains and losses in the nodule-forming fluid.

Table 4.3: Meaning of positive and negative parent-product pairs

Parent product pair	Value	Zone of element concentration
Host halo	Positive	Halo
	Negative	Host
Halo core	Positive	Core
	Negative	Halo
Host core	Positive	Core
	Negative	Host

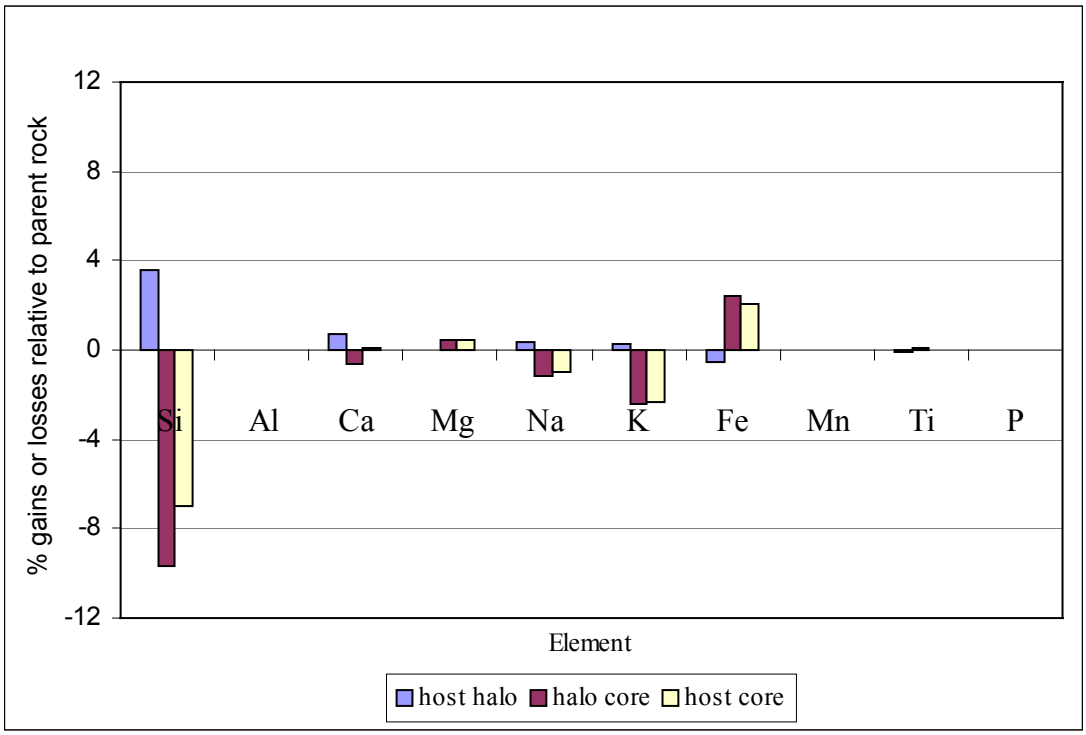

Figure 4.19: Major element mass balance results for sample 130315.

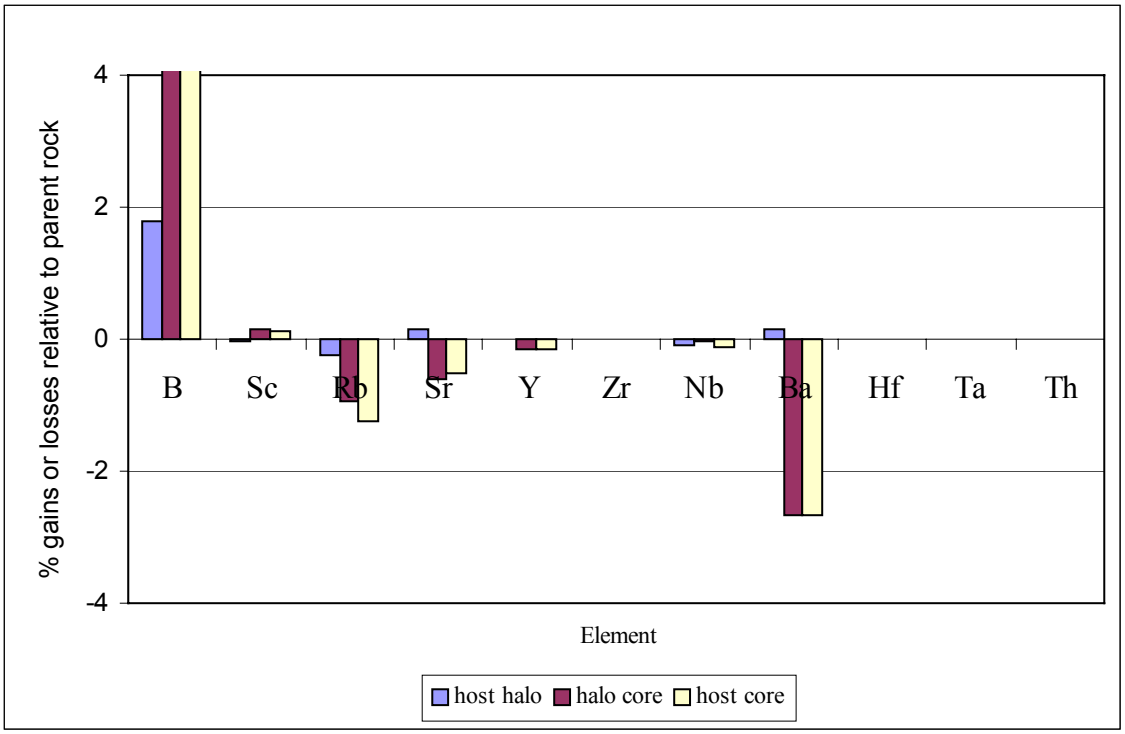

Figure 4.20: Trace element mass balance results for sample 130315. Note: core contains 114% more boron relative to halo, and 122% more relative to host.

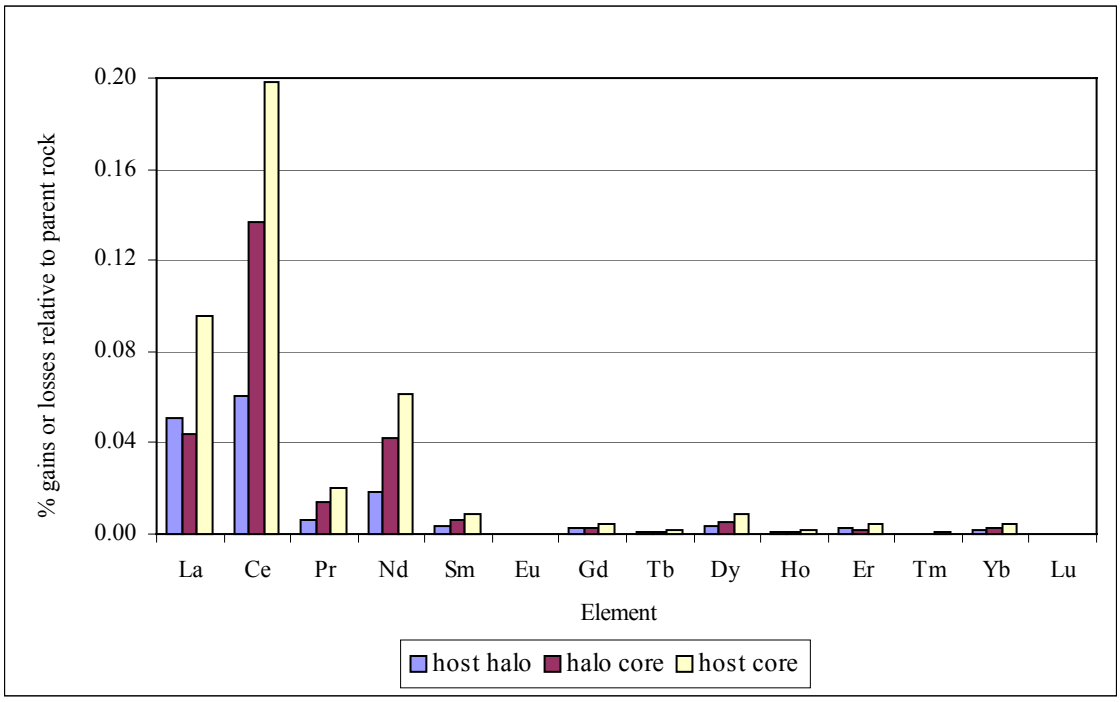

Figure 4.21: Rare earth element mass balance results for 130315.

Table 4.4: Mass balance results for 130315.

Elements concentrated in nodule-forming fluid relative to host	Mg, Fe, B, Sc, Th, La, Ce, Pr, Nd, Sm, Gd, Tb, Dy, Ho, Er, Tm, Yb, Lu
Elements concentrated in the halo relative to core and host	Si, Ca, Na, K
Elements concentrated in the host relative to the fluid	Rb, Sr, Y, Nb, Ba, Ta
Immobile elements	Al, Ti, Mn, P, Zr, Hf, Eu

Results of mass balance calculations presented in Table 4.4 for sample 130315 can be compared with the observed mineralogy in the various zones to confirm the proposed elemental gains or losses. Elements preferentially concentrated in the core, magnesium, iron and boron, are important constituents of tourmaline. In addition, scandium and the rare earth elements (LREE in particular) are also concentrated in the core relative to the

host. The concentration of silicon in the halo was anticipated, due to its leucocratic nature caused by the higher abundance of quartz and decrease in iron-bearing minerals in this zone. The concentration of calcium is most likely due to an abundance of feldspars in the halo zone. The preferred concentration of sodium and potassium in the host relative to the halo, and the halo relative to the core, is related to the abundance of albite, microcline, muscovite, and occasionally biotite. The trace elements Rb, Sr and Ba have similar ionic radii and ionic charge, thus behaving in a similar fashion geochemically. Their presence in the host granite as opposed to the fluid phase indicates that they have behaved compatibly, substituting for Na, K or Ca in mineral phases such as feldspars and micas.

4.6 CHEMISTRY OF TOURMALINE CRYSTALS

As tourmaline is an integral component of nodules, the chemical composition of tourmaline was determined to clarify the elements required for the crystallization of tourmaline from the nodule-forming fluids. In addition, this allows for the comparison with tourmaline from other geological environments that may provide constraints on the origin of the Scrubber Granite tourmalines.

4.6.1 Tourmaline composition and classification

Microprobe analyses of ten unzoned tourmaline crystals and one zoned crystal in spherical nodules are presented in Tables 4.5 and 4.6 (see Appendix D.5 for analytical techniques). These samples were chosen as they were deemed representative of most nodules in the Scrubber Granite.

The electron microprobe at the U of S does not have appropriate crystal spectrometers to measure boron. Thus, as boron is the only cation to be in regular triangular coordination, it is assumed that there are 3 boron atoms per formula unit coordinating with 9 oxygens to produce $(BO_3)_3$ (Tsang and Ghose, 1973). The remaining oxygens (31 total minus 9 associated with boron = 22 oxygens) were used to calculate the number of cations per formula unit. These calculations parallel those by Henry and Guidotti (1985). The total Fe content is reported as FeO, based on recommendations by Bouvier et al., 1972.

Table 4.5: Composition of representative tourmaline grains in unzoned tourmaline nodules.

	Crystals										
Wt. %	1	2	3	4	5	6	7	8	9	10	Avg.
SiO_2	35.77	34.78	34.98	34.79	34.84	34.29	35.67	35.46	35.14	35.68	35.14
TiO_2	0.58	0.57	0.49	0.60	0.68	0.62	0.78	0.43	0.49	0.60	0.58
Al_2O_3	31.63	31.25	31.14	31.49	31.35	32.62	32.10	33.71	33.60	34.14	32.30
FeO*	13.07	13.09	13.47	12.52	13.39	12.60	12.49	11.74	11.51	12.15	12.60
MgO	3.59	3.70	3.26	2.78	2.37	2.63	2.84	2.63	3.68	3.13	3.06
MnO	0.22	0.14	0.13	0.13	0.09	0.14	0.19	0.18	0.14	0.13	0.15
CaO	0.44	0.48	0.40	0.45	0.44	0.34	0.34	0.35	0.41	0.28	0.39
Na_2O	2.08	2.15	2.12	2.05	1.96	1.91	2.10	1.91	2.03	2.04	2.04
K_2O	0.00	0.00	0.00	0.00	0.00	0.00	0.00	0.00	0.00	0.00	0.00
F	0.00	0.00	0.00	0.00	0.00	0.00	0.00	0.00	0.00	0.00	0.00
Total	87.39	86.16	86.03	84.82	85.14	85.15	86.59	86.42	87.00	88.19	86.29
	Number of atoms on the basis of 22 oxygens										
B**	3.00	3.00	3.00	3.00	3.00	3.00	3.00	3.00	3.00	3.00	3.00
Si	5.34	5.28	5.33	5.34	5.35	5.24	5.36	5.30	5.22	5.24	5.30
Ti	0.07	0.07	0.06	0.07	0.08	0.07	0.09	0.05	0.05	0.07	0.07
Al	5.57	5.59	5.59	5.70	5.67	5.87	5.68	5.93	5.88	5.91	5.74
Fe^{2+}	1.63	1.66	1.72	1.61	1.72	1.61	1.57	1.47	1.43	1.49	1.59
Mg	0.80	0.84	0.74	0.64	0.54	0.60	0.64	0.59	0.82	0.69	0.69
Mn	0.03	0.02	0.02	0.02	0.01	0.02	0.02	0.02	0.02	0.02	0.02
Ca	0.07	0.08	0.07	0.07	0.07	0.06	0.05	0.06	0.07	0.04	0.06
Na	0.60	0.63	0.63	0.61	0.58	0.57	0.61	0.55	0.58	0.58	0.59
K	0.00	0.00	0.00	0.00	0.00	0.00	0.00	0.00	0.00	0.00	0.00
F	0.00	0.00	0.00	0.00	0.00	0.00	0.00	0.00	0.00	0.00	0.00

*Total Fe calculated as FeO
**B assumed to be stoichiometric
Note: Crystals 1, 2, 3 = sample 159791E; crystals 4, 5, 6, 7, 8 = sample 159791A; crystals 9, 10 = sample 159790. Samples courtesy of the GSWA.

4.6.2 Chemical zonation in tourmaline

The majority of tourmaline crystals examined in this study were unzoned. However, optical and slight chemical zonation was observed in a few samples, such as the tourmaline crystal pictured in Figure 4.22 and 4.23. Results of a microprobe linescan across the zoned region of the tourmaline crystal in Figure 4.23 are given in Table 4.6. Zoning commonly indicates changing fluid composition during tourmaline crystallization; however, linescan microprobe results are similar to those of the unzoned tourmalines in Table 4.5. In Figures 4.22 and 4.23, the light areas corresponds to denser more Fe-rich zones that emit more electrons when excited, thus appearing brighter. Darker areas represent less dense, relatively Fe-poor zones that do not emit as many electrons.

Table 4.6: Composition of linescan points across a zoned tourmaline crystal in sample159791E.

	Points										
Wt. %	1	2	3	4	5	6	7	8	9	10	Avg.
SiO_2	33.36	32.75	33.47	33.48	33.08	33.44	34.41	33.86	33.07	35.23	33.62
TiO_2	0.76	0.34	0.60	0.57	0.45	0.38	0.26	0.49	0.54	0.56	0.49
Al_2O_3	30.19	29.61	29.65	29.78	29.91	31.30	30.98	30.83	30.38	30.88	30.35
FeO*	15.04	14.97	13.65	14.81	15.86	16.59	15.98	15.68	15.31	13.14	15.10
MgO	2.16	2.50	3.59	2.84	2.16	1.50	1.69	1.88	1.85	3.49	2.37
MnO	0.22	0.19	0.25	0.14	0.21	0.17	0.18	0.16	0.23	0.09	0.18
CaO	0.46	0.48	0.57	0.50	0.48	0.49	0.48	0.48	0.44	0.52	0.49
Na_2O	2.00	2.21	2.64	2.12	2.01	1.95	2.18	2.09	1.97	2.18	2.14
K_2O	0.00	0.00	0.53	0.00	0.00	0.00	0.00	0.00	0.03	0.00	0.28
F	0.00	0.00	0.00	0.00	0.00	0.00	0.00	0.00	0.00	0.00	0.00
Total	84.22	83.06	85.47	84.25	84.2	85.86	86.25	85.51	83.95	86.11	84.89
	Number of atoms on the basis of 22 oxygens										
	1	2	3	4	5	6	7	8	9	10	Avg.
B**	3.00	3.00	3.00	3.00	3.00	3.00	3.00	3.00	3.00	3.00	3.00
Si	5.26	5.24	5.23	5.27	5.24	5.20	5.31	5.26	5.24	5.35	5.26
Ti	0.09	0.04	0.07	0.07	0.05	0.04	0.03	0.06	0.06	0.06	0.06
Al	5.61	5.59	5.46	5.52	5.59	5.74	5.63	5.65	5.67	5.53	5.59
Fe	1.98	2.00	1.78	1.95	2.10	2.16	2.06	2.04	2.03	1.67	1.97
Mg	0.51	0.60	0.84	0.67	0.51	0.35	0.39	0.44	0.44	0.79	0.55
Mn	0.03	0.03	0.03	0.02	0.03	0.02	0.02	0.02	0.03	0.01	0.02
Ca	0.08	0.08	0.10	0.08	0.08	0.08	0.08	0.08	0.07	0.08	0.08
Na	0.61	0.69	0.80	0.65	0.62	0.59	0.65	0.63	0.61	0.64	0.65
K	0.00	0.00	0.11	0.00	0.00	0.00	0.00	0.00	0.01	0.00	0.06
F	0.00	0.00	0.00	0.00	0.00	0.00	0.00	0.00	0.00	0.00	0.00

*Total Fe calculated as FeO
**B assumed to be stoichiometric

Although microprobe analyses cannot provide sufficient data to completely characterize site occupancies in the tourmaline structure, it appears that the composition of the tourmalines conforms to a schorl. This is supported by chemical formula calculations based on in Tables 4.5 and 4.6, and by the Al-Fe-Mg plot of average zoned and unzoned tourmalines (Figure 4.24). The average chemical formula of these tourmalines is $Na_{0.6}(Fe^{2+}, Mg, Mn)_{2.4}Al_{5.7}B_3Si_{5.3}(O,OH)_{30}(OH,F)$.

From Figure 4.24, it is apparent that tourmalines from the Scrubber Granite as well as from the Seagull Batholith are similar to pegmatite tourmalines from Dyar et al. (1999). Similarities between tourmalines from nodules and those from pegmatites are relevant to discussions in Chapter 7.

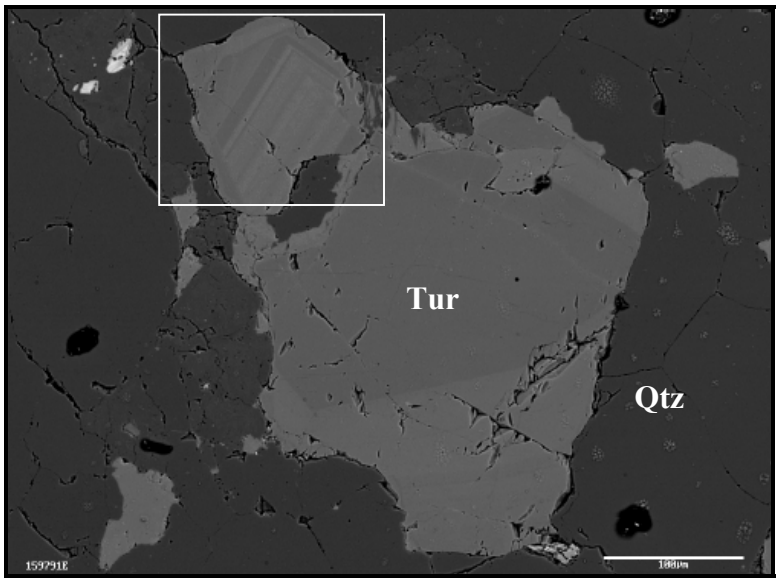

Figure 4.22: Back-scattered electron image of zoned tourmaline (Tur) crystal surrounded by quartz (Qtz) from sample 159791E. Scale bar represents 100μm. White box shows area displayed in Figure 4.23.

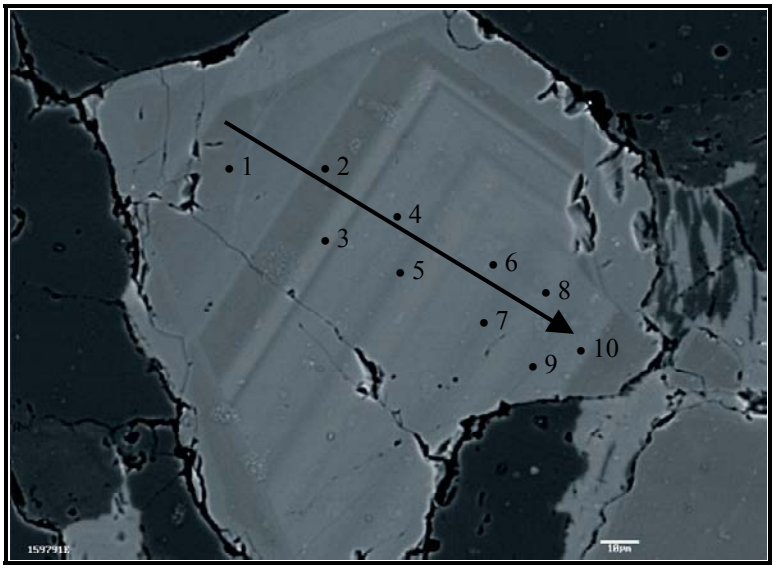

Figure 4.23: Back-scattered electron image of zoned region of tourmaline crystal, showing approximate point locations along the linescan. Scale bar represents 10μm.

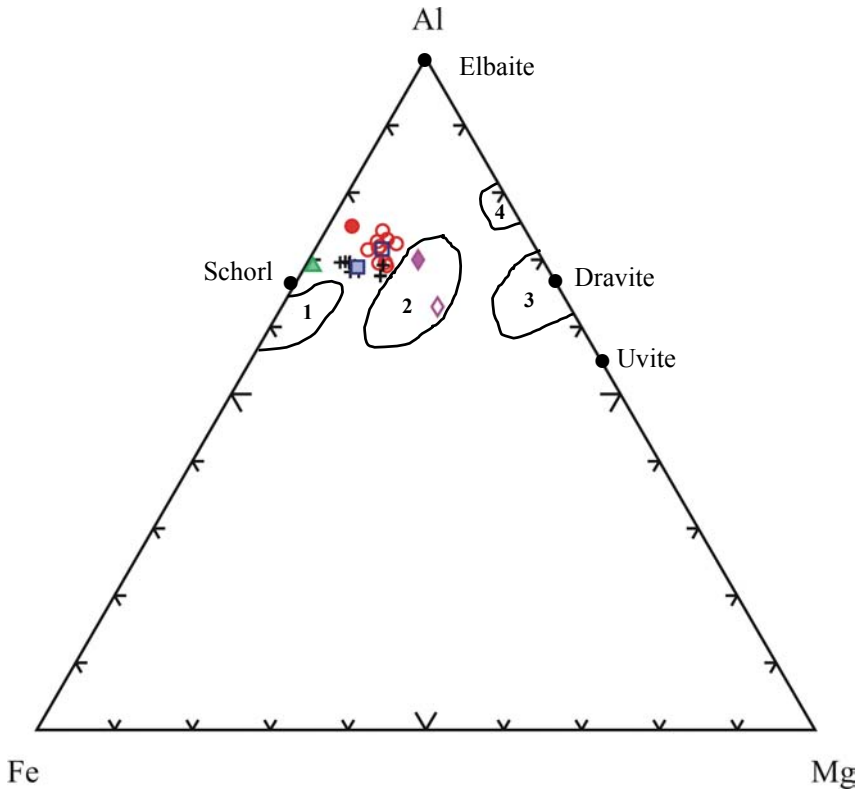

Figure 4.24: Al-Fe-Mg diagram (following parameters used by Jiang et al., 1999) showing the composition of Scrubber Granite unzoned tourmaline crystals (open circles) and the average of that data (open square), linescan points across a zoned tourmaline crystal (crosses) and the average of that data (filled square), tourmalines in nodules of the Seagull Batholith (filled triangle; Sinclair and Richardson, 1992) and the Rooiberg granite (open diamond; Smithies, 1988). Tourmalines from mesothermal gold deposits (filled diamond; King, 1990) and pegmatites (filled circle; Dyar et al., 1999) were also included on this diagram. Numbered fields represent compositions from (1) granitic tin-tungsten environments, (2) mesothermal gold deposits, (3) base metal sulfide deposits, and (4) unconformity hosted uranium deposits (King, 1990 and references therein).

4.7 CHAPTER SUMMARY

The following summary statements can be made based on the observations discussed in this chapter:

1. The Scrubber Granite is comprised of three mineralogic zones: host granite, leucocratic halo, and tourmaline-rich core. These zones are texturally similar;
2. Tourmaline exhibits several textures in various nodule types, including massive, prismatic, irregular and sub-rounded, and is occasionally moderately altered;

3. Whole rock major and trace element analyses of host, halo and core zones demonstrated that the differences in mineralogy, including the presence of tourmaline in the cores and the higher percentage of biotite and feldspar in the halo and host, affected the element concentrations;
4. Samples 130315, 130316 and 130318 are LREE-enriched, and display a pronounced europium anomaly; halo zones tend to have the lowest concentrations of REE, and core regions have the highest;
5. In order to complete mass balance calculations, Al and Zr were assumed to be the immobile element phases;
6. Elements concentrated in the core (i.e. nodule-forming fluid) include Mg, Fe, B, Sc, Th, La, Ce, Pr, Nd, Sm, Gd, Tb, Dy, Ho, Er, Tm, Yb and Lu. Elements concentrated in the halo relative to core and host include Si, Ca, Na, and K. Elements concentrated in the host relative to core and halo are Rb, Sr, Y, Nb, Ba and Ta; immobile elements are Al, Ti, Mn, P, Zr, Hf and Eu;
7. Zoned and unzoned tourmaline crystals have similar chemical data and can be classified as schorl. Scrubber Granite tourmaline has an average chemical formula of $Na_{0.6}(Fe^{2+}, Mg, Mn)_{2.4}\,Al_{5.7}B_3Si_{5.3}(O,OH)_{30}(OH,F)$;
8. Tourmalines from nodules in the Scrubber Granite and the Seagull Batholith have similar Al-Fe-Mg concentrations as the pegmatite tourmaline plotted in Figure 4.24; and
9. Although mass balance calculations estimated the concentration of elements in the nodule-forming fluid relative to other zones, the ingredients necessary for tourmaline precipitation, according to the above formula, must have been present.

CHAPTER 5
FLUID INCLUSION MICROTHERMOMETRY

5.1 INTRODUCTION

Fluid inclusions, minute quantities of liquid (± gas) trapped in minerals, can provide a valuable key to understanding the physical and chemical processes by which crystals grow in nature (Shepherd et al., 1985). Although generally microscopic (2-20μm), fluid inclusions represent actual samples of ancient fluid existing at some time in the geologic history of a rock (Roedder, 1984). The temperature, density and composition of the fluid from which the enclosing mineral originated can be determined using microthermometry, or microscopic heating and cooling studies of phase transitions in such inclusions.

There are varied fluid inclusion assemblages contained within most mineral samples, including primary, secondary, and pseudosecondary inclusions (Roedder, 1984). Of interest in this study are inclusions that are primary in origin. When crystals grow in a fluid medium of any kind, any condition that disturbs the growth of an otherwise microscopically perfect crystal can result in the trapping of small portions of the fluid in the solid crystal, generating a primary inclusion (Shepherd et al., 1985). This trapped solution represents the actual fluid from which the mineral grew. Shepherd et al. (1985) outlined the following criteria for deeming an inclusion as primary in origin:

1. Inclusions are parallel to growth zones or crystal faces;
2. Inclusions occur in a three-dimensional random distribution;
3. Inclusions are isolated, occurring at distances > 5 times the inclusion diameter away from adjacent inclusions; and
4. Inclusions have a large size relative to the host crystal.

Primary fluid inclusions contained in tourmaline crystals of the Scrubber Granite are an integral part of this study, as they can be used to estimate the composition and minimum temperature of the fluid reservoir from which tourmaline precipitated. Fluid inclusion microthermometric analyses were completed on two samples from the Scrubber Granite: 1) a tourmaline vein (sample 130323); and 2) a starburst nodule (sample 130316). The starburst nodule sample was selected due to its relatively coarse crystal size (see Figure 4.2), in anticipation of larger fluid inclusions. The tourmaline vein sample was chosen to determine whether tourmaline in nodules and veins crystallized under similar conditions. The actual vein sampled for this study is shown in Figure 3.15a.

Wafers, or thick sections, used in this fluid inclusion study were produced from the tourmaline-rich zones of the above samples. Prior to analysis, wafers were broken into thumbnail-sized "chips" small enough to fit on the fluid inclusion stage. Chips were numbered for reference, and petrographically examined to identify those containing the largest primary inclusions. Large (>30μm in diameter), isolated inclusions randomly distributed throughout the crystal were deemed primary in origin. Appendix D.6 summarizes the analytical techniques used in this study.

In both the starburst nodule and tourmaline vein, tourmaline crystals contain moderate amounts of 30-75μm, two-phase (liquid + vapor at room temperature) primary fluid inclusions. Conversely, adjacent quartz crystals contained sparse inclusions, which were too small for analysis. Thus, all microthermometric measurements were completed on primary fluid inclusions in tourmaline crystals. Histograms of all low- and high-temperature data collected from samples 130316 and 130323 are presented in section 5.3.

5.2 FLUID INCLUSION ANALYSES

5.2.1 Tourmaline vein

Extensive microthermometric analyses were carried out on primary fluid inclusions within tourmaline crystals in chip 3b of tourmaline vein sample 130323. These irregular-shaped inclusions are approximately 50μm in diameter, and contain a liquid phase and vapor bubble at room temperature (25˚C) (Figure 5.1). The degree of fill is

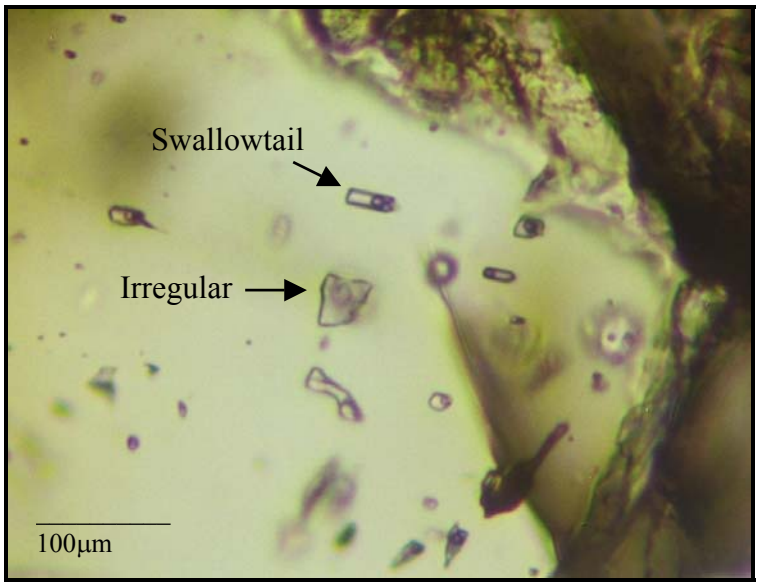

Figure 5.1: Primary fluid inclusions in tourmaline crystal of chip 3b from tourmaline vein sample 130323. Inclusions are approximately 35 to 50μm in diameter. Note swallowtail and irregular inclusions.

roughly 0.90, or 90% liquid. Therefore, inclusions are considered to be "liquid-rich", as fluid takes up >50% of the phase volume (Shepherd et al., 1985). Vapor bubbles contract on cooling, indicating that these are H_2O-rich or aqueous inclusions, as opposed to CO_2-rich. In addition, no other gas appears on cooling, confirming the absence of CO_2, which has a lower liquid-vapor eutectic.

Average microthermometric measurements of the irregular inclusion pictured in Figure 5.1 are summarized in the following sections. This inclusion was selected as it is representative of the primary inclusion assemblage in sample 130323. Data collected from all inclusions analyzed are provided in Appendix D.6.

5.2.1.1 Freezing data

The irregular inclusion was cooled to approximately -110˚C during consecutive heating and cooling runs. The nucleation temperature (T_n) in the fluid was recognized on cooling by the sudden contraction of the vapor bubble at approximately -62.0˚C. Upon warming at an average rate of 4˚C per minute, the eutectic temperature (T_e) for this

inclusion was measured at -46.2˚C; the actual onset of first melting probably occurs at some temperature below this value (Roedder, 1984). This low T_e, below that of pure H_2O-NaCl inclusions with T_e= -21.2˚C, indicates that this inclusion is not composed strictly of sodium chloride. Additional salts likely to depress the eutectic temperature to such a degree include $CaCl_2$ (H_2O-NaCl-$CaCl_2$ T_e = -52.0˚C). The presence of this low T_e chloride could obscure the identification of salts with higher eutectic temperatures, including $MgCl_2$ (H_2O-NaCl-$MgCl_2$ T_e = -35.0˚C) and KCl (H_2O-KCl T_e= -10.6˚C). The eutectic was recognized by the first appearance of slight graininess within the inclusion, indicating first melting (Crawford, 1981).

With continued heating at a similar rate, the temperature of final melting of the salt hydrate phase (T_m salt) was estimated at approximately -27.5˚C. This phase change was recognized by a lack of graininess within the inclusion and the subsequent recrystallization of ice into larger crystals. Although the T_m salt may not be an imperative measurement in all fluid inclusion analyses, Shepherd et al. (1985, p. 74) suggest that "…by measuring the final melting temperatures for both ice (T_m ice) and hydrate (T_m salt), the composition of the fluid can be expressed more fully than for ice alone. Thus, by using eutectic, ice and hydrate melting temperatures, thermometric analysis becomes a valuable semi-quantitative technique".

The final melting point of ice (T_m ice) was measured at -10.2˚C, with excellent reproducibility both within this inclusion and with other inclusions in sample 130323. This phase change was recognized by the complete rounding out of the bubble meniscus upon final melting of all ice crystals. The large size of the vapor bubble in this inclusion made the estimation of T_m ice easier and more reliable.

The following generalizations can be made based on the cooling data from this fluid inclusion and from other inclusions in sample 130323:

1. These are aqueous (H_2O-rich), two-phase, liquid-rich inclusions (liquid >50%), comprised of a liquid and vapor phase at room temperature (25˚C).
2. Due to the low T_e (-46.2˚C), these inclusions must contain other salts in addition to NaCl. The most probable is $CaCl_2$; however, $MgCl_2$ and KCl could also be present.
3. These inclusions are most closely represented by the H_2O-NaCl-$CaCl_2$ system.

5.2.1.2 Heating data

After the cooling data was collected, heating runs were carried out. The inclusion was heated from room temperature (25˚C) to 200˚C at a warming rate of 5˚C/minute. The inclusion was then warmed at a much slower rate (1˚C/minute) in anticipation of homogenization (this heating regime was established after several runs). The nature of homogenization in all inclusions from 130323 was into the liquid phase (L + V→ L); vapor bubbles gradually reduced in size until they completely disappeared at the homogenization temperature (T_h). In some inclusions, the vapor bubble wiggled back and forth as the inclusion approached homogenization.

Although freezing data collected from sample 130323 was comparable between individual inclusions, heating data collected from these inclusions was not as consistent. The temperature of homogenization for the large, irregular inclusion was 454.4˚C, whereas the T_h for the swallowtail inclusion (Figure 5.1) was 283.7˚C. The heating and cooling data (reproducible to ±1˚C) for the irregular fluid inclusion are summarized in Table 5.1.

Table 5.1: Microthermometric data for the irregular inclusion of sample 130323.

Symbol	Measurement	Temperature
T_n	Nucleation temperature	-62.0˚C
T_e	Eutectic temperature	-46.2˚C
T_m salt	Final melting of salt hydrate	-27.5˚C
T_m ice	Final melting of ice	-10.2˚C
T_h	Homogenization temperature	+454.4˚C

5.2.1.3 Inclusion composition

Bodnar (2003) has presented the following equation for determining the salinity of H_2O-NaCl solutions using freezing point depression:

$$\text{Salinity (wt \%)} = 0.00 + 1.78\,\theta - 0.0442\,\theta^2 + 0.000557\,\theta^3 \qquad (5.1)$$

where θ is the negative of the freezing point depression in degrees Celsius. According to this equation, with a freezing point depression of -10.2˚C, the irregular inclusion would have a salinity of 14.1 weight percent. This calculated salinity can be compared

with that observed at a T_m ice of -10.2˚C on an H_2O-NaCl temperature vs. salinity diagram (Figure 5.2). The last solid phase to disappear at this temperature is ice, as the inclusion lacks characteristics that would indicate hydrohalite as the final solid to melt. These characteristics, according to Bodnar (2003), include the sluggish melting of hydrohalite, which may persist metastably for several minutes to hours at temperatures above 0.1˚C, and the more granular appearance of this chloride relative to ice. Thus, the appearance and response in the rate of melting of the solid during heating has indicated that ice is the last phase to melt.

The T_m ice of -10.2˚C indicates that this inclusion has a salinity of approximately 14 weight percent according to Figure 5.2, which agrees well with the calculated value. However, is the H_2O-NaCl salinity equation and corresponding diagram accurate for estimating the salinity of inclusions represented by the H_2O-NaCl-$CaCl_2$ system?

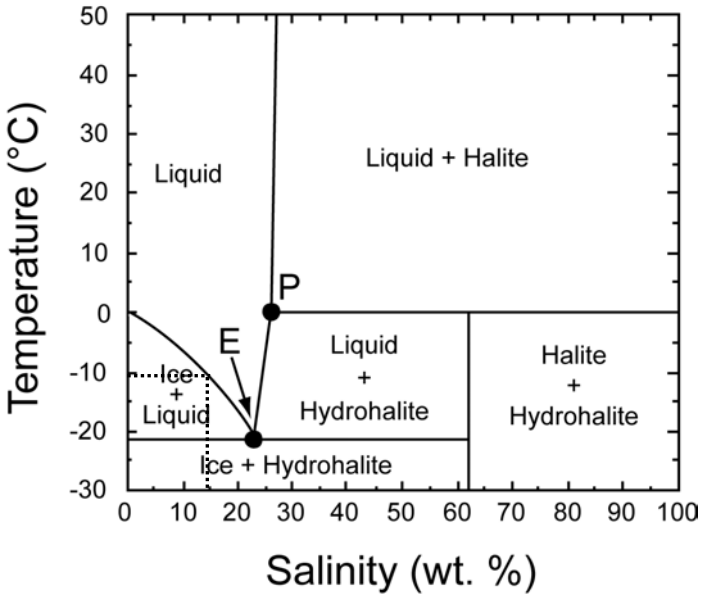

Figure 5.2: Vapor-saturated phase relations in the H_2O-NaCl system at low temperatures. E = eutectic (-21.2˚C, 23.2 wt % NaCl); P = peritectic (0.1˚C, 26.3 wt % NaCl) (Bodnar, 2003). Dashed lines represent 14 weight % salinity at –10.2˚C.

According to Bodnar (2003), most two-phase (liquid + vapor) inclusions in the H_2O-NaCl-$CaCl_2$ system freeze to form ice, hydrohalite and antarcticite ($CaCl_2 \bullet 6H_2O$). In this system, eutectic melting (T_e) is first observed at -52.0˚C during heating (Figure

5.3). Antarcticite will disappear at the eutectic, leaving fine-grained ice and hydrohalite in the liquid phase. As heating continues, the liquid composition follows the hydrohalite-ice cotectic until the hydrohalite phase disappears (T_m salt). The melting path then proceeds into the "ice" field and moves toward the ice apex with continued heating. The bulk composition of the inclusion is defined by the intersection of the melting path with the appropriate isotherm (T_m ice) in the ice field.

The irregular inclusion in chip 3b has a eutectic temperature of -46.2˚C, a T_m salt (hydrohalite) of -27.5˚C, and a T_m ice of -10.2˚C. The bulk composition of this inclusion can be estimated using Figure 5.3 (Bodnar, 2003). Antarcticite melts at -46.2˚C. With continued heating the inclusion follows the hydrohalite-ice cotectic until the hydrohalite phase disappears at -27.5˚C. From this point on the cotectic, the inclusion follows a path into the ice field along an imaginary line drawn from the -27.5˚C point on the cotectic to the apex of the ice corner. The inclusion will have a bulk composition corresponding to the intersection of this melting path with the -10.2˚C isotherm. Assuming that the inclusion composition is most closely approximated by the H_2O-NaCl-$CaCl_2$ system, the bulk composition can be estimated at 86 weight % H_2O, 7 weight % NaCl, and 7 weight % $CaCl_2$.

The estimation of salinity using the H_2O-NaCl equation produced a bulk salinity of 14.1 weight percent NaCl equivalent. This is similar to what was estimated using the H_2O-NaCl-$CaCl_2$ system (7 wt % NaCl + 7 wt % $CaCl_2$ = 14 weight percent salinity). Thus, since there is no salinity equation for the H_2O-NaCl-$CaCl_2$ system, the H_2O-NaCl equation is appropriate for calculating salinity in this inclusion and other primary inclusions in this sample.

5.2.1.4 Inclusion density estimates

Roedder (1984) suggests, "…if the relative volumes of the liquid and gas phases are determined at room temperature and if the salinity is known, the density of the originally homogeneous fluid can be estimated". This is a two-phase, aqueous (H_2O-rich) inclusion with a 0.90 degree of fill, and a salinity of approximately 14 weight percent NaCl equivalent. Using Figure 5.4 as a guide, the density of the fluid at room temperature (25˚C) is approximately 1.0 g/cm^3.

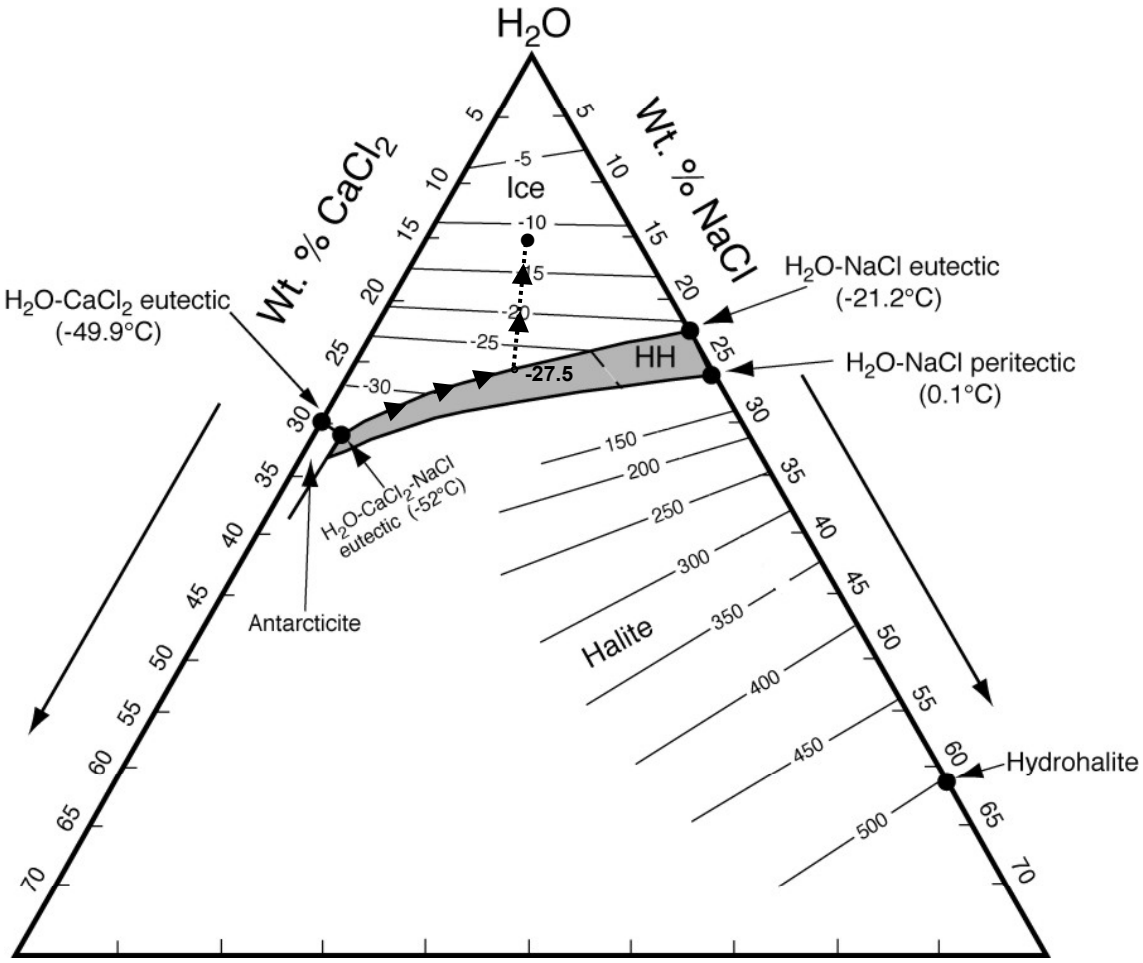

Figure 5.3: The H_2O-NaCl-$CaCl_2$ system showing isotherms (in degrees Celsius) of halite solubility and ice melting (Bodnar, 2003). The irregular inclusion in 130323 follows the melting path indicated by arrowheads. Circle at –10.2°C indicates bulk composition of inclusion.

The degree of fill (F) is related to the total density of the inclusion (ρ_{TOT}) at a certain temperature by the following expression:

$$\rho_{TOT} = \rho_L F + \rho_V (1-F), \tag{5.2}$$

where ρ_L is the density of the liquid phase, and ρ_V is the density of the vapor phase (Shepherd et al., 1985). In most cases it is acceptable to assume that the density of the vapor phase is zero, thus:

$$\rho_{TOT} = \rho_L F \tag{5.3}$$

The values for ρ_L for a salt solution vary linearly with the salt concentration. As previously estimated from Figure 5.4, the density of the fluid at 25˚C is 1.0g/cm^3. Using the above equation, the total density of the inclusion at room temperature becomes 1.0 (0.90) = 0.9g/cm^3.

Inclusion density can also be estimated using temperature-density diagrams, in which the salinity, temperature and nature of homogenization must be known (Figure 5.5). The 14 weight percent salinity irregular inclusion homogenizes into the liquid phase at 454.4˚C. By approximating a 14 weight percent salinity between the 10 and 15 weight percent NaCl lines in Figure 5.5, the density of the irregular inclusion at T_h is roughly 0.6g/cm^3.

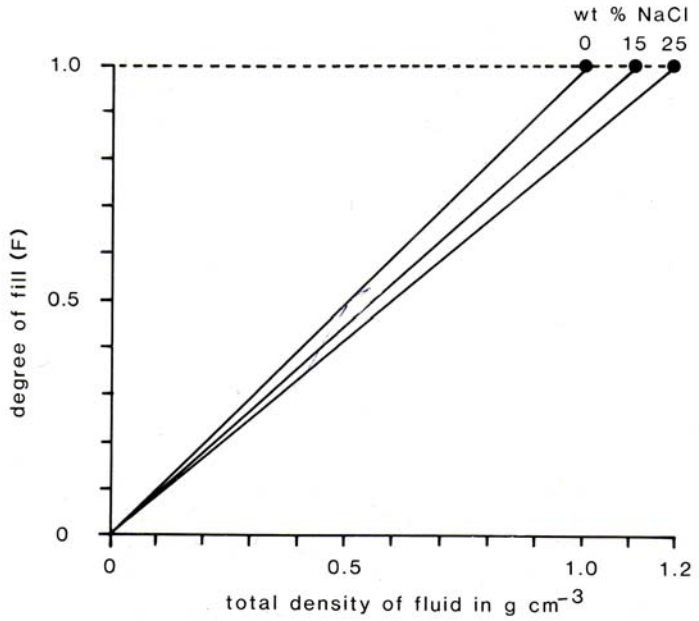

Figure 5.4: Relationship between degree of fill (F) at 25°C and the total density of the inclusion contents for different NaCl solutions (Shepherd et al., 1985).

5.2.1.5 Inclusion density calculations

Although the above diagrams are useful for estimating inclusion density, it is desirable to calculate specific densities for various salinities and temperatures. Potter and Brown (1977) have compiled density data for vapor-saturated 1 to 30 weight percent NaCl solutions (odd salinity values only) from 0˚C to 475˚C. A density equation for a 14 weight percent NaCl equivalent solution was established by averaging their 13 and 15

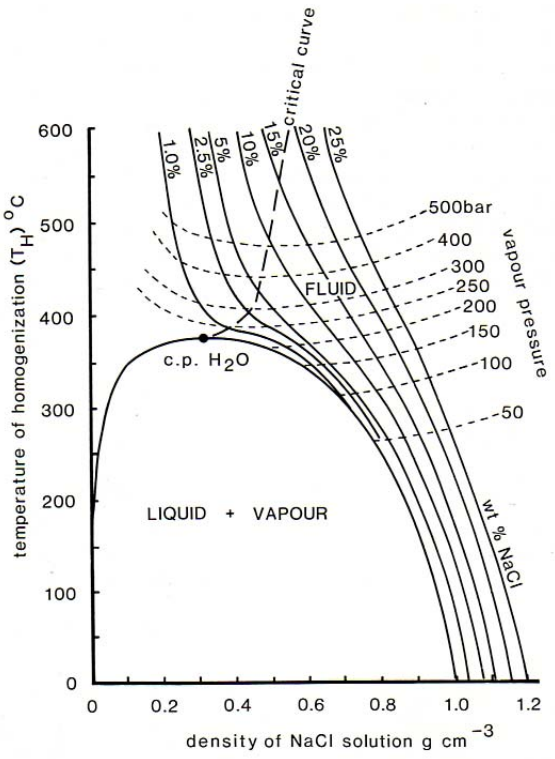

Figure 5.5: Temperature-density diagram showing the relationship between T_h, density, weight percent NaCl solution, and vapor pressure of the solution at T_h (Shepherd et al., 1985).

weight percent solution density data (see Appendix D.6). The 14 weight percent NaCl solution data were plotted on a temperature vs. density chart, and a second order polynomial regression line was fit to the data (Figure 5.6). The equation of this trend line is as follows:

$$y = -1037.8\,x^2 + 907.72x + 291.03 \qquad (5.4)$$

where y is the temperature and x is the density in g/cm^3. For any temperature, a density can be calculated using this equation.

Using the above regression line equation for a 14 weight percent NaCl solution, the density of the fluid in the irregular inclusion at a homogenization temperature of 454.4˚C can be calculated. Applying the quadratic equation to solve for x, the density of the inclusion at the homogenization temperature is $0.6 g/cm^3$. This density calculation is precisely what was estimated using Figure 5.5. Inclusion density can also

be evaluated at room temperature using equation 5.4 (y = 25˚C). The calculated value of 1.1g/cm^3 agrees well with that estimated using Figure 5.4.

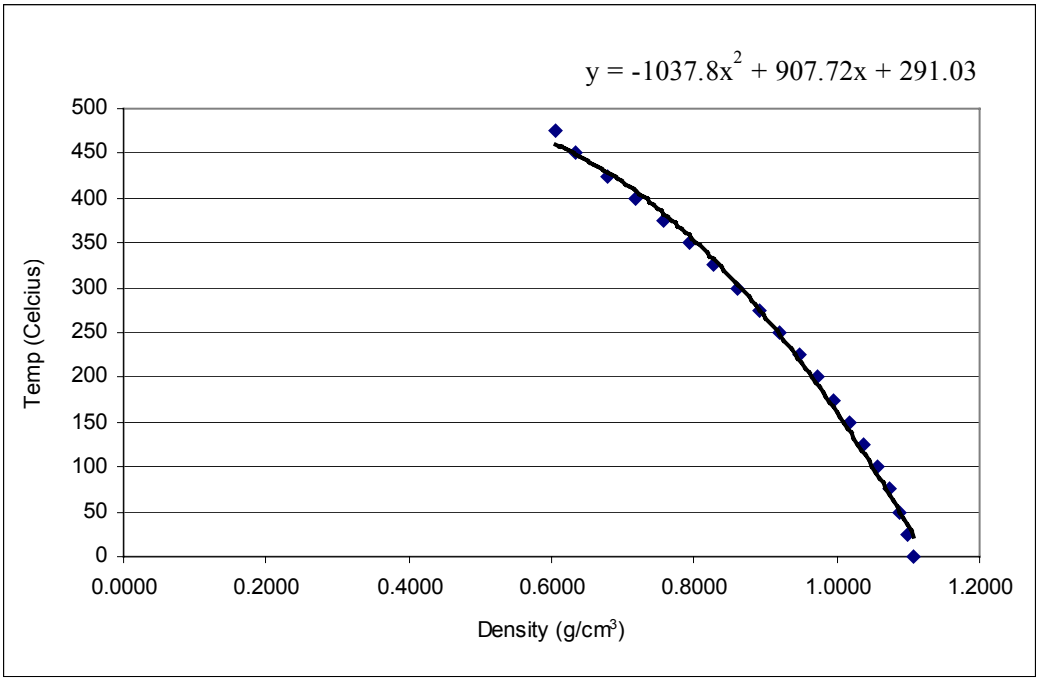

Figure 5.6: Temperature vs. density diagram for a 14 weight percent NaCl solution estimated from Potter and Brown's (1977) data for 13 and 15 weight percent NaCl solutions.

5.2.2 Starburst nodule

Extensive microthermometric analyses were carried out on tourmaline fluid inclusions in chips 2 and 11 of starburst nodule sample 130316. Primary inclusions examined in these chips are large (30-75μm) and irregular, containing a liquid and vapor phase at room temperature (25˚C) (Figure 5.5). Degree of fill is estimated at 0.85, or 85% liquid. The average microthermometric data for the large inclusion indicated in Figure 5.7 are summarized in the following sections. This inclusion was selected as it is representative of all primary inclusions in 130316, and because it yielded the most reproducible temperatures.

Figure 5.7: Fluid inclusions in tourmaline crystal of chip 11 from sample 130316. Arrow indicates the large two-phase inclusion, approximately 75μm in diameter.

5.2.2.1 Freezing data

The large inclusion from chip 11 was cooled to approximately -110˚C during consecutive cooling and heating runs. The nucleation temperature (T_n) was observed on cooling at -64.8˚C, indicated by the sudden contraction of the vapor bubble as the surrounding fluid began to freeze (Roedder, 1984). Cooling continued to approximately -100˚C. The inclusion was then warmed to -75˚C at a rate of 5˚C/minute, after which the heating rate was slowed to 1˚C/minute in anticipation of reaching the eutectic temperature. Recognized by the onset of graininess in the inclusion fluid, the eutectic was measured at -49.9˚C. This low eutectic again indicates the presence of other salts in addition to NaCl, including $CaCl_2$ and possibly $MgCl_2$ and KCl. The final melting temperature of the salt hydrate (T_m salt) was recognized by the disappearance of this graininess at -26.5˚C. Marked by the complete rounding out of the vapor bubble, the final melting point of ice (T_m ice) was measured at -10.6˚C.

5.2.2.2 Heating data

Upon completion of the freezing runs, the large inclusion was heated from room temperature to 200˚C at a warming rate of 5˚C/minute. In anticipation of homogenization, the heating rate was then reduced to 1˚C/minute (this heating regime

was established after several runs). Homogenization into the liquid phase in the large inclusion occurred at 330.0˚C. Results of the microthermometric analyses from the large inclusion of sample 130316 are summarized in Table 5.2 (reproducible to ±1˚C).

Table 5.2: Microthermometric data for the large inclusion in sample 130316.

Symbol	Measurement	Temperature
T_n	Nucleation temperature	-64.8˚C
T_e	Eutectic temperature	-49.9˚C
T_m salt	Melting of salt hydrate	-26.5˚C
T_m ice	Melting of ice	-10.6˚C
T_h	Homogenization temperature	+330.0˚C

5.2.2.3 Inclusion composition

Using the equation presented by Bodnar (2003) for determining salinity in H_2O-NaCl solutions (equation 5.1), the large inclusion, with a freezing point depression of -10.6˚C, has a salinity of 14.6 weight percent. An estimated salinity from Figure 5.2 is in good agreement with the calculated value at roughly 15 weight percent NaCl equivalent. However, the same question arises: can H_2O-NaCl systematics accurately determine the salinity of this inclusion, which is most closely represented by the H_2O-NaCl-$CaCl_2$ system?

The accuracy of the H_2O-NaCl salinity estimates can be verified by comparing them with the salinity obtained using Figure 5.8 (upper portion of Figure 5.3). Upon the disappearance of antarcticite at the eutectic temperature of -49.9˚C, the inclusion follows the hydrohalite-ice cotectic until the hydrohalite phase melts at -26.5˚C (T_m salt). Drawing a line from this point on the cotectic to the apex of the ice corner, the inclusion has a bulk composition corresponding to the intersection of the melting path with the -10.6˚C isotherm. Thus, the inclusion has a rough composition of 85 weight percent H_2O, 8 weight percent NaCl, and 7 weight percent $CaCl_2$, yielding an overall salinity of 15 weight percent (8 + 7 weight percent salts). This salinity is comparable to that obtained using H_2O-NaCl systematics, at 14.6 weight percent. Therefore, since there is no salinity equation for the H_2O-NaCl-$CaCl_2$ system, the salinity of this inclusion can be calculated using H_2O-NaCl systematics.

5.2.2.4 Inclusion density estimates

The relationship between degree of fill (0.85) and the salinity (roughly 15 weight percent) of this inclusion can be used to estimate density at room temperature using Figure 5.4. According to this diagram, these inclusions have a density of roughly 0.95g/cm^3. Using this estimation along with a 0.85 degree of fill in equation 5.3, the total density of the inclusions becomes 0.8g/cm^3.

Temperature vs. density diagrams, such as Figure 5.5, are an alternate technique for estimating inclusion density. At room temperature (25˚C), this inclusion has an approximate density of 1.1g/cm^3; the density decreases to 0.8g/cm^3 at the 330.0˚C homogenization temperature.

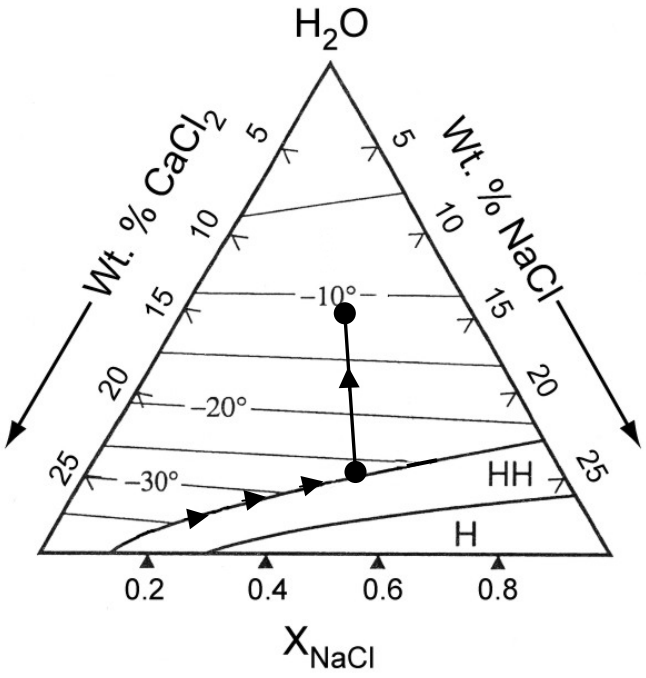

Figure 5.8: Isotherms in degrees Celsius of the ice liquidus at 1 atmosphere pressure in the H_2O-NaCl-$CaCl_2$ system (Bodnar, 2003). The large inclusion from sample 130316 follows path marked by arrowheads; bulk composition corresponds to point at –10.6˚C.

5.2.2.5 Inclusion density calculations

Potter and Brown's (1977) data for NaCl solutions can again be used to estimate density in the large inclusion of 130316. After assessing the estimated and calculated salinities, it was determined that Potter and Brown's (1977) 15 weight percent NaCl solution data would yield the most accurate density determination in this inclusion. Their data was

plotted on a temperature vs. density chart, and a second order polynomial regression line was fit to the data (Figure 5.9). The equation of the trendline is:

$$y = -1164.7x^2 + 1152.1x + 184.19 \quad (5.5)$$

where y is the temperature and x is the density in g/cm^3. At the homogenization temperature (330.0˚C) of the large inclusion, the density is 0.8g/cm^3, which is precisely what was estimated in the previous section. At room temperature, the inclusion has a density of 1.1g/cm^3, which also agrees with estimates made.

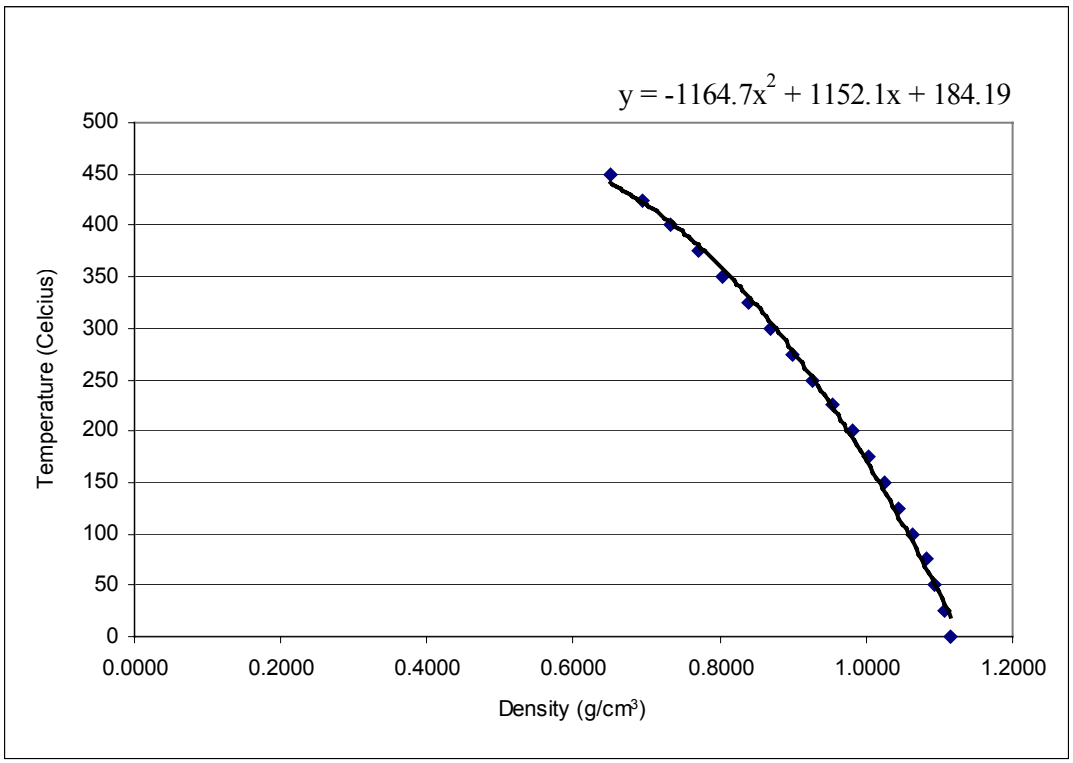

Figure 5.9: Temperature vs. density diagram for a 15 weight percent NaCl solution plotted using Potter and Brown's (1977) density data.

5.3 HISTOGRAMS

The following histograms (Figures 5.10 and 5.11) contain all low-temperature and high-temperature data for samples 130316 and 130323. All inclusion measurements are summarized in Tables D.4 and D.5 in Appendix D.

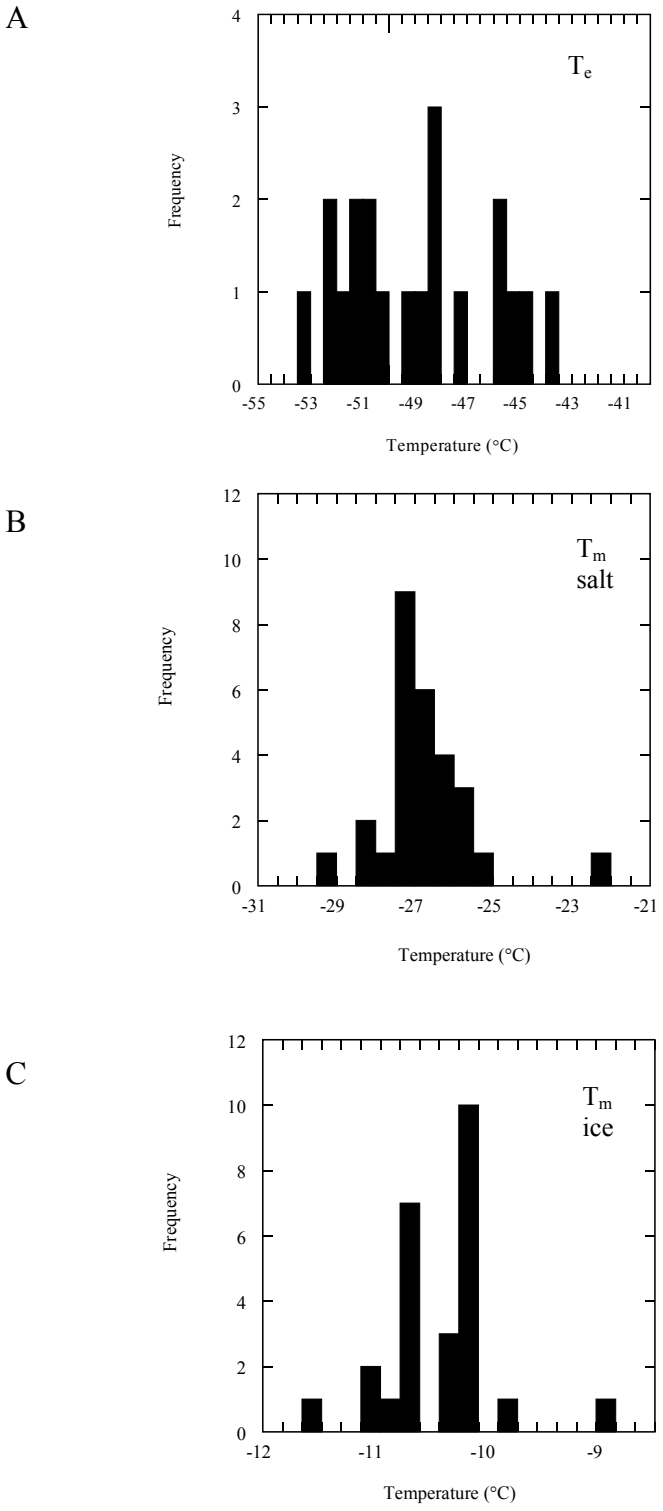

Figure 5.10: Low-temperature measurements of primary inclusions in tourmaline from samples 130316 and 130323. A) Eutectic temperature; B) Final melting temperature of salt hydrate; and C) Final melting temperature of ice.

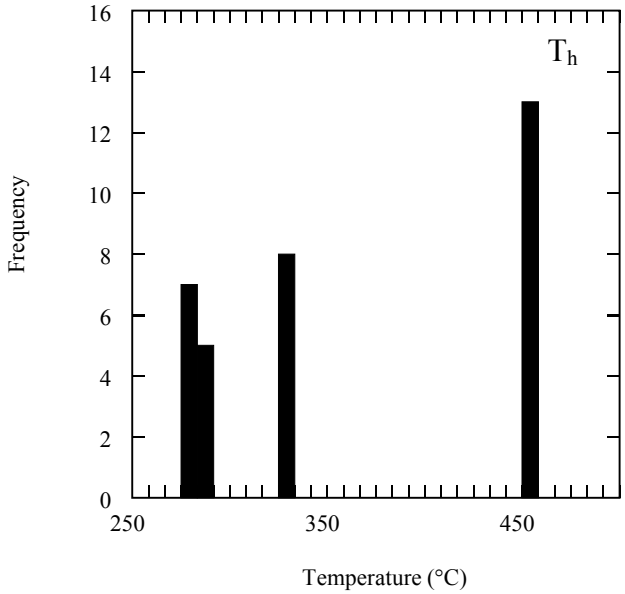

Figure 5.11: Homogenization temperatures of primary inclusions in tourmaline from samples 130316 and 130323.

5.4 CHAPTER SUMMARY

Fluid inclusion microthermometric analyses were completed on large, two-phase primary inclusions within tourmaline crystals from sample 130323, a tourmaline vein, and sample 130316, a starburst nodule. The occasional small size and moderate abundance of most tourmaline fluid inclusions in these samples was a limiting factor on the quantity of microthermometric measurements that could be made. Thus, analyses were completed on a small population of large primary inclusions in certain chips.

Inclusions in both samples displayed similar microthermometric properties, including comparable nucleation temperatures, eutectic temperatures, and temperatures of first melting of the salt hydrate and ice phases. Homogenization temperatures were variable within and between inclusions from 130323 and 130316. The following table summarizes these data as well as the salinity and density values for the tourmaline vein and starburst nodule samples.

Table 5.3: Typical fluid inclusion data for samples 130323 and 130316.

Sample Number	Degree Of Fill	T_n (°C)	T_e (°C)	T_m salt (°C)	T_m ice (°C)	T_h (°C)	Salinity (Wt % NaCl Equiv.)	Density (g/cm^3) at 25°C	Density (g/cm^3) at T_h
Irregular inclusion 130323	0.90	-62.0	-46.2	-27.5	-10.2	454.4	14.1	1.1	0.6
Large inclusion 130316	0.85	-64.8	-49.9	-26.5	-10.6	330.0	14.6	1.1	0.8

The following statements can be made regarding the nature of the fluid reservoir from which tourmaline precipitated in the starburst nodule and tourmaline vein:

1. This fluid has a salinity of 14 to 15 weight percent NaCl equivalent;
2. The fluid composition can be summarized as follows: $H_2O > NaCl \geq CaCl_2 > (\pm) MgCl_2 \geq (\pm)$ KCl. Thus, these inclusions are most closely represented by the H_2O-NaCl-$CaCl_2$ system. Additionally, the elemental components necessary for the precipitation of tourmaline (schorl variety) must have been present in the fluid reservoir, namely Na, Fe, Mn, Al, B, Si, OH and F. However, the presence of these components cannot be assessed through microthermometric analysis;
3. Homogenization temperatures indicate that the fluid reservoir had a temperature of at least 250˚C to 460˚C when the tourmaline was crystallizing;
4. Fluid density, which may affect element diffusion and crystal growth, was found to be roughly $1.0 g/cm^3$ at room temperature, and decreased with increasing temperature at various T_h. The lowest density measurement is $0.6 g/cm^3$; and
5. Due to similar microthermometric results, the starburst nodule and tourmaline vein may have crystallized under similar conditions, possibly from similar fluid reservoirs. However, the vein analyzed herein is not typical of most vein morphologies (compare Figure 3.15A with 3.15B and C). Therefore, it cannot be assumed that all tourmaline veins in the Scrubber Granite crystallized from a similar fluid reservoir as the nodules, especially since most veins and veinlets overprint nodule textures.

CHAPTER 6
STABLE AND RADIOGENIC ISOTOPE GEOCHEMISTRY OF TOURMALINE

6.1 INTRODUCTION

Isotope geochemistry, the study of the abundance ratios of stable and radiogenic isotopes of major and trace elements in rocks, is an important component of this investigation into the origin of tourmaline nodules in the Scrubber Granite. Isotope studies can elucidate a number of geologic problems and processes, such as age and evolution of rocks, temperatures of geological processes, and the origin of natural waters and magmas (Hoefs, 1997). The stable isotopic compositions of oxygen (^{18}O and ^{16}O) and hydrogen (D and H), and the radiogenic isotopic compositions of neodymium (^{143}Nd and ^{144}Nd) and samarium (^{147}Sm) in tourmaline separates from various samples of the Scrubber Granite is the focus of this chapter. Of the minerals occurring in the nodules and veins, the stable and radiogenic isotopic signatures in tourmaline were measured as it is the mineral of interest in this study, and because of its highly refractory nature (i.e. its resistance to decomposition by heat, pressure, or chemical attack), thus maintaining original isotopic characteristics (King, 1990).

Stable isotope abundance ratios of oxygen and hydrogen in tourmaline separates can be used to model or estimate the temperature of tourmaline crystallization from a fluid reservoir, the oxygen and hydrogen isotopic composition of this fluid, and the possible fluid type. Radiogenic isotope abundance ratios of neodymium and samarium in tourmaline separates will aid in constraining possible nodule-forming fluid sources.

Tourmaline was separated from the core zones of the following Scrubber Granite samples: 1) spherical nodule (sample 130315); 2) starburst nodule (130316); 3) flower-shaped nodule (130318); 4) dense core of the tourmaline rosette nodule (130319); 5) the outer nodule core of the tourmaline rosette nodule (130319); 6)

irregular nodule (130320); 7) tourmaline vein (130323); and 8) nodule from porphyritic granite (130324). Tourmaline separates from the dense core of the tourmaline rosette nodule will be referred to as sample 130319a, and tourmaline from the outer nodule core as sample 130319b. The mineral separation process is summarized in Appendix D.7.

6.2 STABLE ISOTOPE SYSTEMATICS

Most naturally occurring elements have more than one stable isotope, a non-radiogenic variety of an element that has the same number of protons and electrons, but has a different number of neutrons in the nucleus (Valley et al., 1986). A different number of neutrons cause the atomic weight, or mass number, of isotopes to vary, which in turn causes isotopes of the same element to behave differently, having different densities, vapor pressures, and boiling points (Hoefs, 1997). Such differences result in the separation or 'fractionation' of isotopes during geologic processes, including isotopic exchange reactions or physical processes such as melting and crystallization.

Stable isotope ratios are measured relative to a standard and are expressed in parts per thousand, or parts per mil (‰). The isotope ratio is expressed as a δ (delta) value. In this study, the isotopic composition of oxygen and hydrogen are expressed as per mil differences of $^{18}O/^{16}O$ and D/H ratios relative to a standard called SMOW (Standard Mean Ocean Water):

Oxygen isotopic composition:

$$\delta^{18}O = \left(\frac{(^{18}O/^{16}O)_{sample} - (^{18}O/^{16}O)_{SMOW}}{(^{18}O/^{16}O)_{SMOW}} \right) x1000 \qquad (6.1)$$

Hydrogen isotopic composition:

$$\delta D = \left(\frac{(D/H)_{sample} - (D/H)_{SMOW}}{(D/H)_{SMOW}} \right) x1000 \qquad (6.2)$$

Positive values of $\delta^{18}O$ and δD calculated from equations 6.1 and 6.2 indicate enrichment of a sample in ^{18}O and D relative to SMOW; negative values indicate depletion of those isotopes in the sample relative to the standard.

Oxygen and hydrogen are among the most important elements in which natural variations of isotopic compositions have been observed (Hoefs, 1997). As these

elements are often main components of geologically important fluids, stable isotope analysis provides a means to study these fluids and fluid-rock interactions. Oxygen and hydrogen isotopic compositions of tourmaline separates from sample core zones are presented in Table 6.1. The results will be discussed and interpreted in the following sections.

Table 6.1: Oxygen and hydrogen isotope compositions of tourmaline separates (‰).

Sample	Nodule Type	$\delta^{18}O_{(SMOW)}$	$\delta D_{(SMOW)}$
130315	Spherical nodule	7.9	-16.9
130316	Starburst nodule	8.0	-21.6
130318	Flower-shaped nodule	8.9	-23.4
130319a	Dense core of tourmaline rosette nodule	7.7	-21.0
130319b	Outer core of tourmaline rosette nodule	7.8	-29.6
130320	Irregular nodule	9.7	-16.4
130323	Tourmaline vein	9.6	-24.7
130324	Nodule from porphyritic granite	9.8	-27.1

6.3 COUPLED OXYGEN AND HYDROGEN ISOTOPE STUDIES

Integrated oxygen and hydrogen isotope studies provide researchers with a powerful means of characterizing fluids that have interacted with minerals and rocks of interest. This section presents how oxygen and hydrogen isotopic data from Scrubber Granite tourmaline separates will be used to:

1) Model the temperature of the fluid from which tourmaline crystallized, or temperature of final isotopic equilibration between tourmaline and water*;
2) Estimate the fluid oxygen and hydrogen isotopic composition; and
3) Estimate the possible fluid type.

It is desirable to constrain fluid characteristics as these properties may indicate which physical and chemical processes were involved in the generation of tourmaline nodules in the Scrubber Granite, which is the goal of this study.

* The terms "water" and "fluid" are used synonymously to describe the reservoir from which tourmaline originated, with no reference to the nature of this generation.

6.3.1 Modeling of fluid temperature and isotopic composition

In order to estimate the temperature and isotopic composition of the fluid reservoir from which the tourmaline crystallized, oxygen and hydrogen isotopic abundance ratios of the tourmaline separates were measured (see Table 6.1). These $\delta^{18}O$ and δD values for tourmalines can be used to calculate corresponding $\delta^{18}O$ and δD for the fluid reservoir at various temperatures. With this approach, both the fluid composition ($\delta^{18}O$ and δD of the fluid) and the fluid temperature can be estimated simultaneously.

Subsequent to this modeling, the most geologically appropriate range of temperatures and compositions is selected. This process is based on petrographic and analytical data (such as fluid inclusion studies), as well as comparisons with other geothermometric studies. The use of oxygen and hydrogen isotope abundance ratios in a mineral to constrain a temperature or range of temperatures at which the mineral crystallized from a fluid reservoir is termed "geothermometry". Geothermometry also indirectly estimates the fluid composition and can aid in the identification of fluid type. The theory behind oxygen and hydrogen geothermometry is summarized in the following sections.

6.3.1.1 Oxygen isotope geothermometers

When two solid phases (minerals) have equilibrated oxygen with a common reservoir at a specific temperature, the difference in their $\delta^{18}O$ values measured relative to the same standard is a function of temperature (Faure, 1986). Thus, the isotope composition of oxygen in rock-forming minerals can be used to determine the temperature of isotopic equilibration, or temperature of crystallization. This isotope thermometer is based on three assumptions:

1. The exchange reactions must have reached equilibrium;
2. The isotopic compositions were not altered subsequent to the establishment of equilibrium; and
3. The temperature dependence of the fractionation factors is known from experimental determinations (Faure, 1986).

The fractionation factor, α, for isotope exchange between minerals, is a linear function of $1/T^2$, where T is in degrees Kelvin (Hoefs, 1987). For example, consider the fractionation of oxygen for the quartz-water (QW) and calcite-water (CW) system (from Clayton et al., 1972 and O'Neil et al., 1969, respectively). The relationship between α and T for quartz is:

$$1000 \ln \alpha_{QW} = 3.38 (10^6/T^2) - 3.40 \quad (6.3)$$

while for calcite it is:

$$1000 \ln \alpha_{CW} = 2.78 (10^6/T^2) - 3.40 \quad (6.4)$$

By subtracting the first equation from the second, we get:

$$1000 \ln \alpha_{QW} - 1000 \ln \alpha_{CW} = 0.60 (10^6/T^2), \text{ or} \quad (6.5)$$

$$\delta_Q - \delta_C = \Delta_{QC} = 0.60 (10^6/T^2) \quad (6.6)$$

As shown in equation 6.6, the difference in the $\delta^{18}O$ values in quartz and calcite (Δ_{QC}) is approximately equal to the 1000 ln α_{QW} – 1000 ln α_{CW} expression in equation 6.5. Additionally, these equations show how the difference in $\delta^{18}O$ values of coexisting quartz and calcite is inversely proportional to the square of the temperature at which these two minerals equilibrated oxygen with the same reservoir (Faure, 1986). Thus, the above fractionation factor equations, and other such equations for various mineral pairs, are thermometers from which temperature can be determined.

Although it is desirable to complete geothermometric calculations using isotope ratios from a mineral pair as described above, only tourmaline separates were analyzed for their oxygen and hydrogen isotopic compositions. The use of tourmaline and quartz as a mineral pair, the two most prominent minerals in nodule cores, was negated by the cursory assumption from initial fluid inclusion investigations that the sparse distribution and small size of quartz fluid inclusions relative to those in tourmaline indicated that tourmaline and quartz were not in textural equilibrium.

Nonetheless, the oxygen isotope composition of tourmaline is representative of the crystallization temperature and the temperature of the fluid from which it formed. In this case, it was decided to model the temperature and fluid compositions using the tourmaline-water fractionation curves for oxygen and hydrogen developed by Zheng (1993) and Kotzer et al. (1993), respectively.

The oxygen isotope fractionation factor for tourmaline-water derived by Zheng (1993) deals with mathematical relationships between atoms in mineral crystals, and involves aspects such as vibrational frequencies and their isotopic shifts. Calculated fractionations are in good agreement with known experimental and empirical calibrations. Zheng (1993) has derived the following equation for tourmaline-water (TW) oxygen isotope fractionation:

$$1000 \ln \alpha_{(TW)} = \delta^{18}O_T - \delta^{18}O_W = 4.21\ (10^6/T^2) - 6.99(10^3/T) + 2.14 \qquad (6.7)$$

Since the $\delta^{18}O_T$ ($\delta^{18}O$ in tourmaline separates) has been measured in various samples from the Scrubber Granite, either the $\delta^{18}O_W$ ($\delta^{18}O$ in the fluid) or T, temperature (in degrees Kelvin) can be solved for using equation 6.7 if one parameter is given an assigned value. Thus, at an assigned temperature, $\delta^{18}O_W$ can be determined; conversely, at an assigned $\delta^{18}O_W$ value, temperature can be determined.

A range of fluid temperatures was used to contour the possible range of $\delta^{18}O_W$ values for tourmaline. The minimum temperature used was 250˚C, constrained by the lowest homogenization temperature observed in the fluid inclusion studies of tourmaline crystals (see Chapter 5). The maximum temperature used was 800˚C as tourmaline begins to breakdown around this temperature range, depending on the chemistry of the fluid phase (London et al., 1996; London, 1999; Wolf and London, 1997; Holtz and Johannes, 1991).

For example, using the oxygen isotope data measured from tourmaline separates in sample 130315, and assigning a temperature of 400˚C (673˚K), the following $\delta^{18}O_W$ can be calculated using equation 6.7:

$$\delta^{18}O_T - \delta^{18}O_W = 4.21\ (10^6/T^2) - 6.99(10^3/T) + 2.14$$
$$7.9‰ - \delta^{18}O_W = 4.21\ (10^6/673^2) - 6.99(10^3/673) + 2.14$$
$$7.9‰ - \delta^{18}O_W = 1.05$$
$$-\delta^{18}O_W = 1.05 - 7.9$$
$$\delta^{18}O_W = 6.9‰$$

Because tourmaline is relatively resistant to alteration, its $^{18}O/^{16}O$ ratios should reflect the isotopic composition and temperature of the fluids from which it formed (Kotzer et al., 1993). Thus, at 400˚C, the tourmaline, having a $\delta^{18}O_T$ = 7.9‰, would be in equilibrium with a fluid reservoir having a $\delta^{18}O_W$ of 6.9‰.

6.3.1.2 Hydrogen isotope geothermometers

Hydrogen-isotope ratio abundances can also be used as geothermometers, in a similar fashion as previously summarized for oxygen isotopes. Kotzer et al. (1993) have devised the following empirical (based on observation or experiment) hydrogen isotope fractionation factor for tourmaline-water at temperatures between 300 and 600˚C:

$$1000 \ln \alpha_{(TW)} = \delta D_T - \delta D_W = -27.2 \, (10^6/T^2) + 28.1 \qquad (6.8)$$

Kotzer et al. (1993) have estimated that the error in temperatures estimated from equation 6.10 is ± 50ºC, given the uncertainties in the measurement of δD_T values. By substituting the measured δD_T values (see Table 6.1) into equation 6.8, the δD_W value can be solved for within the selected temperature range (250-800˚C). An example calculation using data from sample 130315 is presented, at a temperature of 400˚C (673˚K):

$$\delta D_T - \delta D_W = -27.2 \, (10^6/T^2) + 28.1$$
$$-16.9 - \delta D_W = -27.2 \, (10^6/673^2) + 28.1$$
$$-16.9 - \delta D_W = -31.95$$
$$-\delta D_W = -31.95 + 16.9$$
$$\delta D_W = 15.1‰$$

Thus, at a temperature of 400˚C, the tourmaline, having a δD_T of –16.9‰, is in isotopic equilibrium with a fluid reservoir having a δD_W of 15.1‰. The above calculations for oxygen and hydrogen isotope fractionation between tourmaline and water have been completed using all sample data presented in Table 6.1, in 50˚C increments at temperatures between 250 and 800˚C (523 to 1073˚K). Results of this temperature modeling for sample 130315 is summarized in Table 6.2. Complete results for all samples are presented in Appendix D.8.

Although a broad range of practical temperatures was chosen to complete these calculations, geologically realistic temperatures and corresponding $\delta^{18}O_W$ and δD_W values for this fluid can be further constrained. This data was plotted on a typical δD vs. ^{18}O plot (Figure 6.1).

Table 6.2: Oxygen and hydrogen isotope ratio values for water in sample 130315.

Temperature (˚C)	$\delta^{18}O_W$ (‰) (Zheng, 1993)	δD_W (‰) (Kotzer et al., 1993)
250	3.7	54.4
300	5.1	37.8
350	6.1	25.1
400	6.9	15.1
450	7.4	7.0
500	7.8	0.5
550	8.0	-4.8
600	8.2	-9.3
650	8.4	-13.1
700	8.5	-16.3
750	8.6	-19.0
800	8.6	-21.4

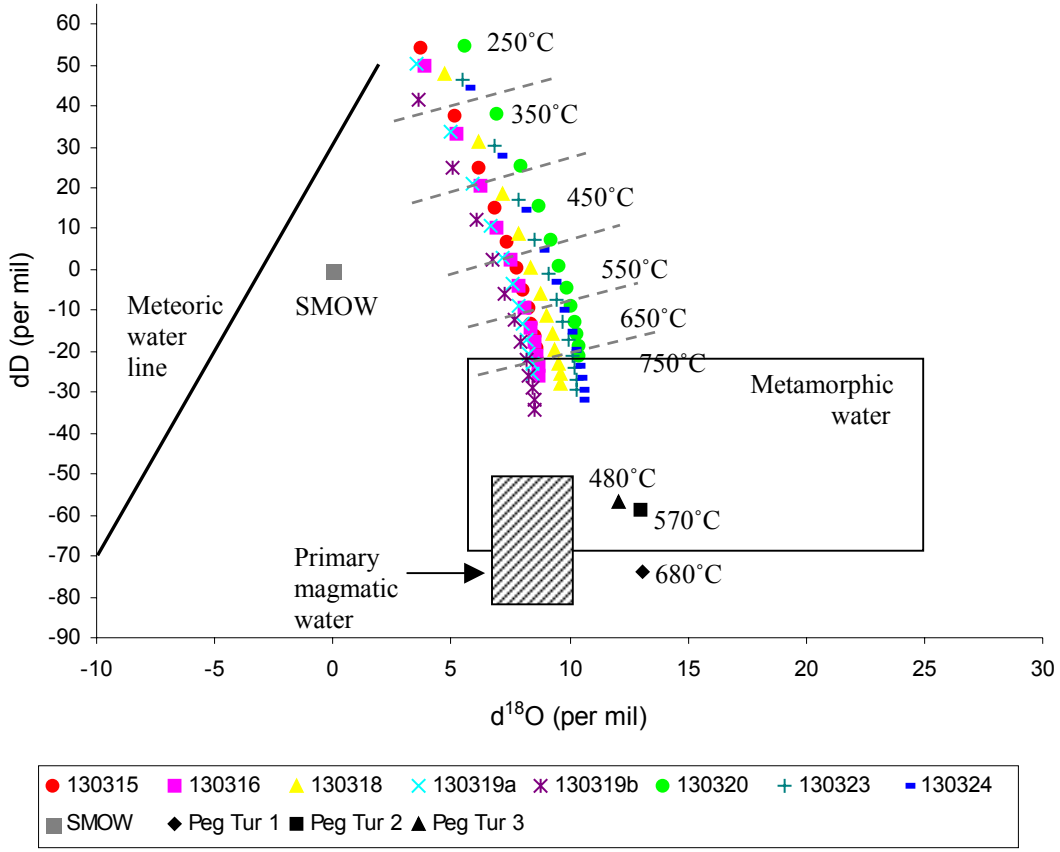

Figure 6.1: Plot of δD vs. $\delta^{18}O$ for various waters (modified from Hoefs, 1997). Data in each sample set from the Scrubber Granite (samples 130315-130324) represents fluid isotopic compositions at various temperatures, approximated by dashed lines. The lowest data point for each sample set represents 800˚C, and the highest point represents 250˚C. Pegmatite data from Dyar et al. (1999).

6.3.2 Estimating crystallization temperatures and fluid type

In Figure 6.1, the $\delta^{18}O_W$ data points for the Scrubber Granite tourmaline fall within a defined range of +3.7 to +10.5‰ for temperatures between 250 and 800˚C, in the approximate range of the magmatic water field. Conversely, δD_W data points are quite variable, between –34.1 and +54.4‰ for the same temperature range; the only natural waters that have δD values this positive are unusual meteoric waters that can have δD values up to +50‰ (Hoefs, 1997).

As it is highly unlikely that nodules crystallized from meteoric waters with extremely high δD values, and because homogenization temperatures indicate that crystallization took place above 280 to 460˚C, the low temperature data (250-400˚C) can be ruled out. Nodules probably crystallized between 450 and 700˚C.

For comparison purposes, tourmaline data from pegmatites studied by Dyar et al. (1999) are plotted in Figure 6.1, and are labeled with their respective crystallization temperatures. Dyar et al. (1999) completed a stable isotope study on tourmaline separates from the rare element Black Mountain pegmatite in Maine, U.S.A. The $\delta^{18}O_W$ and δD_W values of the tourmalines from these pegmatites were calculated using oxygen and hydrogen data in Dyar et al. (1999) at crystallization temperatures determined in this study using the tourmaline-quartz fractionation factors of Kotzer et al. (1993). The crystallization temperatures of these pegmatite tourmalines indicate that nodules probably also crystallized at higher temperatures.

Estimating the fluid type is difficult to constrain with this diagram, as the Scrubber Granite tourmalines plot outside most natural water fields. If the nodule-forming fluid was derived from the crystallizing Scrubber Granite magma, then perhaps the oxygen and hydrogen isotopes fractionated during crystallization of the host, causing the late-stage nodule-forming fluid to be lighter with respect to oxygen isotopes and heavier with respect to hydrogen isotopes.

6.4 RADIOGENIC ISOTOPE SYSTEMATICS

Radiogenic isotope systematics involve the premise of radioactivity: the spontaneous decomposition of the atoms of an unstable element (isotope) to form atoms of another stable element (isotope) (Faure, 1986). Decomposition, or decay, may form more than

one element until stability is attained. Radioactivity is a property of certain atoms and the rate of decay of an unstable parent nuclide to a stable daughter nuclide is constant for a give element, and is proportional to the number of atoms present.

Among the elements having radiogenic isotopes is neodymium (Nd), which forms from the decay of parent nuclide samarium (Sm). The change in the isotopic composition of these elements through time is described by the following radioactive decay equation:

$$(D/R)_P = (D/R)_I + P/R\ (e^{\lambda t}-1) \qquad (6.9)$$

Where $(D/R)_P$ is the present day ratio of the number of atoms of the daughter isotope D to a reference isotope R of the daughter element;
$(D/R)_I$ is the initial daughter/reference isotope ratio;
P/R is the present day ratio of the parent isotope to the daughter;
t is time; and
λ is the decay constant for the parent isotope P (Faure, 1986).

This equation demonstrates that the magnitude of the shift in the D/R ratio of a given decay pair (i.e. ^{147}Sm-^{143}Nd) that occurs over a certain period of time is a function of the rate of decay of the parent and the P/R ratio. The latter ratio is proportional to the weight ratio of the parent element to the daughter element.

Results of a Sm-Nd isotopic study of tourmaline separates from various samples of the Scrubber Granite are presented in Table 6.3. The results will be used in the following sections.

Table 6.3: Sm-Nd isotopic data of tourmaline separates.

Sample	Sm (ppm)	Nd (ppm)	$^{147}Sm/^{144}Nd$ measured	$^{143}Nd/^{144}Nd$ measured	Epsilon Nd at 1.8Ga
130315	20.4	75.1	0.1646	0.511203	-20.6
130316	17.2	59.9	0.1736	0.511187	-22.3
130318	19.2	57.4	0.2018	0.511291	-27.5
130319a	26.8	101.1	0.1601	0.511326	-17.2
130319b	35.4	137.6	0.1556	0.511331	-16.1
130320	17.3	59.3	0.1765	0.511297	-21.5
130323	44.4	158.4	0.1694	0.511322	-19.4
130324	25.5	90.8	0.1699	0.511284	-20.3
Analytical Uncertainty			0.6%	0.005%	

The value for CHUR at present time used in the calculation of Epsilon Nd are as follows: $^{143}Nd/^{144}Nd$ is 0.512638 (Goldstein et al., 1984) and $^{147}Sm/^{144}Nd$ is 0.1967 (Jacobsen and Wasserburg, 1980).

6.4.1 Sm-Nd isotope geochemistry and geochronology

Samarium and neodymium are light rare earth elements that occur in many rock-forming minerals, where they replace major ions. In the following equation for the decay of ^{147}Sm to ^{143}Nd, ^{144}Nd is used as the reference isotope because the number of atoms of ^{144}Nd in a unit weight of rock or mineral does not change as long as the system remains closed to Nd. The decay constant value is 6.54×10^{-12}/y. The radioactive decay equation for Sm-Nd is:

$$(^{143}Nd/^{144}Nd)_P = (^{143}Nd/^{144}Nd)_I + {}^{147}Sm/^{144}Nd\,(e^{\lambda t} - 1) \qquad (6.10)$$

Due to the very similar chemical properties of Sm and Nd, large ranges of Sm/Nd in natural rocks are rare. During fractionation processes, such as fractional crystallization of a magma, Nd is slightly more incompatible relative to Sm, causing increases in the concentrations of Nd and decreases in the Sm/Nd ratio in the melt phase. This is due to the slightly larger ionic radius of Nd, causing it to form weaker ionic bonds, which break more easily relative to Sm (DePaolo, 1988). Thus, with more differentiation, the Sm/Nd ratio decreases further in the resulting magmas or fluids.

6.4.2 Nd isotope evolution: CHUR and εNd

The isotopic evolution of Nd in the Earth is described in terms of a model called CHUR, the chondritic uniform reservoir (DePaolo and Wasserburg, 1976). This assumes that Nd has evolved in a uniform reservoir whose Sm/Nd ratio is equal to that of chondritic meteorites. This model is based on the fact that Sm and Nd did not undergo substantial fractionation during formation of the planets. Partial melting to form magma results in the magma, or partial melts, having higher Nd concentrations and lower Sm/Nd ratios. This in turn results in lower $^{143}Nd/^{144}Nd$ ratios over time, relative to the source, as there is not as much ^{147}Sm to decay to ^{143}Nd. Conversely, the residual source from which the magma was generated has a higher Sm/Nd ratio and thus develops a higher $^{143}Nd/^{144}Nd$ ratio.

Because Sm and Nd have very similar chemical properties and undergo only slight relative fractionation during crystal-liquid processes, departures of $^{143}Nd/^{144}Nd$ from the CHUR evolution line are small. DePaolo and Wasserburg (1976) developed a

notation whereby initial $^{143}Nd/^{144}Nd$ isotope ratios could be represented in parts per 10^4 deviation from the CHUR evolution line, termed epsilon units (ε Nd). This notation is defined as:

$$\varepsilon Nd\ (T) = [\ \{(^{143}Nd/^{144}Nd)_{sample} / (^{143}Nd/^{144}Nd)_{CHUR}\}-1] \times 10^4 \qquad (6.11)$$

A positive epsilon value indicates that the rocks were derived from residual solids in the reservoir after magma had been withdrawn at an earlier time. A negative epsilon value indicates that the rocks were derived from sources that had a lower Sm/Nd ratio than CHUR (partial melts).

6.4.3 Scrubber Granite εNd evolution diagram

Epsilon Nd values of Scrubber Granite tourmaline separates along with Scrubber Granite whole rock εNd values are plotted on an evolution diagram (Figure 6.2). As the Scrubber Granite intrudes both the Dumbie Granodiorite and the Halfway Gneiss, and is underlain by the Archean Yilgarn Craton, εNd values associated with these rock units were also included. Epsilon Nd values at present time and at the time of crystallization for the Scrubber Granite whole rock, Dumbie Granodiorite, Halfway Gneiss and Yilgarn Craton were provided by Steve Sheppard, GSWA (pers. comm.). It is expected that the source of the nodule-forming fluid will have εNd values similar to those of the tourmaline separates.

In order to construct this figure, epsilon neodymium values for the tourmaline separates must be calculated at present time and at the time of crystallization (i.e. age of the rock). According to Occhipinti et al. (2001), the Scrubber Granite crystallized at approximately 1.8Ga. Epsilon Nd calculations are completed using the $^{147}Sm/^{144}Nd$ and $^{143}Nd/^{144}Nd$ ratios measured in the separates.

Based on textural interpretations from previous chapters, it was anticipated that the tourmalines would have similar neodymium ratios as the Scrubber Granite whole rock. However, it is apparent that tourmaline separates have εNd values that are much lower than those of the possible fluid reservoirs, including the Scrubber Granite whole rock. The tourmaline εNd values can be interpreted in several ways:

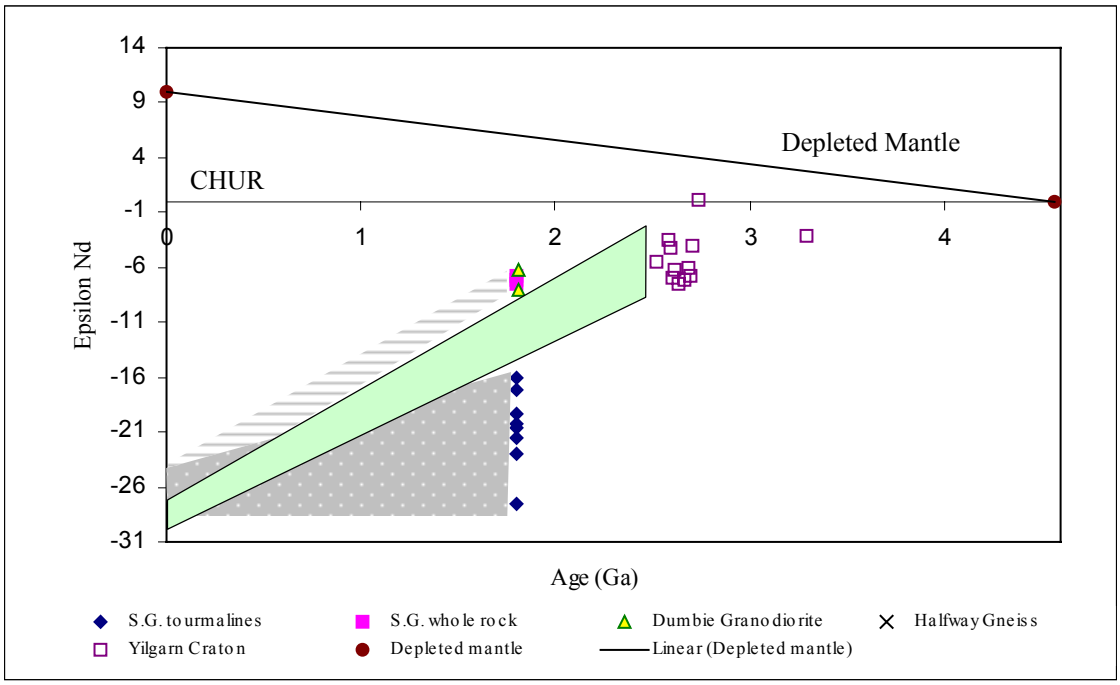

Figure 6.2: Epsilon Nd diagram of Scrubber Granite (S.G.) tourmaline separates, Scrubber Granite whole rock, Dumbie Granodiorite, Halfway Gneiss, Yilgarn Craton, and depleted mantle (Scrubber Granite whole rock data and data from other rock units provided by Steve Sheppard, GSWA, pers. comm.). All data relative to La Jolla = 0.511860. Present day value of CHUR = 0.512638. Model ages calculated assuming a linear evolution over the age of the earth, from εNd = 0 at 4.57 Ga to εNd = +10 at present day, that is present-day $^{143}Nd/^{144}Nd_{DM}$ = 0.513144 and $^{147}Sm/^{144}Nd_{DM}$ = 0.2136. Striped region represents Scrubber Granite whole rock evolution lines; stippled region represents tourmaline separates evolution lines; green region represents Yilgarn Craton evolution lines.

1) The nodule-forming fluid was externally derived from outside the Scrubber Granite;
2) The nodule-forming fluid was a mixture of a late-stage Scrubber Granite volatile phase and an external fluid; or
3) The nodule-forming fluid was derived from the crystallizing Scrubber Granite magma and the isotopic composition of the tourmaline crystals were affected by a later event, in which isotopic exchange occurred. Based on the trend of the isotopic evolution lines in Figure 6.2, it is possible that fluid that interacted extensively with Yilgarn Craton rocks may have been responsible for resetting the isotope systematics of the tourmaline at ca. 1.5Ga or younger.

The first scenario is difficult to imagine, given the physical characteristics of the Scrubber Granite tourmaline nodules; how would an external fluid source migrate into the Scrubber Granite and form the spherical to irregular nodule morphologies observed in this pluton?

Although there are limited Nd isotope studies in this part of Western Australia, at present there is no known rock reservoir with which a fluid would have interacted to develop the Nd isotopic composition of the tourmalines obtained in this study. More work is required to determine whether an external fluid was available at 1.8 Ga to mix with a Scrubber Granite volatile phase.

The third scenario is the most plausible, as it involves the exsolution of the nodule-forming fluid from the crystallizing Scrubber Granite magma, with later isotopic exchange with a fluid. This exchange may have occurred around 1.5Ga or earlier, perhaps during an "unnamed" event that took place after the Capricorn Orogeny (Cawood and Tyler, 2004; see Chapter 2). However, the exact timing of this isotopic resetting is not known.

6.5 CHAPTER SUMMARY

The following paragraphs summarize the results of stable and radiogenic isotope analyses completed on tourmaline separates:

1. Using oxygen and hydrogen tourmaline-water fractionation factors and the measured $\delta^{18}O$ and δD values in the tourmaline, the oxygen and hydrogen isotopic composition of the fluid reservoir was measured over a temperature range of 250-800˚C. The lower limit of this range was constrained by the minimum homogenization temperature and the upper limit was constrained by the stability of tourmaline, which begins to breakdown around 700-800˚C. The fluid in isotopic equilibrium with tourmaline had $\delta^{18}O$ values ranging from +3.7 to +10.5‰ and δD values ranging from –34.1 to + 54.4‰. On a typical $\delta^{18}O$ vs. δD diagram (Figure 6.1), these data plot above the suggested magmatic water field; pegmatite tourmalines plotted for comparison also plot outside this field. As the low temperature δD values for the Scrubber Granite tourmalines are geologically unrealistic, the temperature of crystallization is most likely between

450 and 700˚C; homogenization temperatures also indicate crystallization at higher temperatures.

2. It was anticipated that samarium-neodymium systematics would constrain the source of the fluid reservoir from which the tourmaline crystallized. Epsilon Nd values of the tourmaline separates at 1.8 Ga were compared to whole rock εNd values of the Scrubber Granite, Dumbie Granodiorite, Halfway Gneiss and Yilgarn Craton at their respective crystallization ages; the most likely source of the nodule-forming fluid would presumably have similar εNd values as the tourmaline separates. However, the Nd isotopic ratio of the tourmaline separates are more negative than the Scrubber Granite whole rock values and values of other possible fluid reservoirs. Several scenarios could give rise to these tourmaline values: 1) the nodule-forming fluid was externally derived from outside the Scrubber Granite; 2) the nodule-forming fluid was a mixture of a late-stage Scrubber Granite volatile phase and an external fluid; or 3) the isotopic compositions of tourmaline crystals were affected by a later event, in which isotopic exchange occurred. The third scenario is the most plausible, as it entails the exsolution of the nodule-forming fluid from the Scrubber Granite magma, a theory that is more conducive to explaining nodule morphology. Therefore, as the tourmaline crystals have possibly not remained closed systems, the discrepancy in the Scrubber Granite tourmaline and whole rock εNd values does not necessarily discredit the presumption that the nodule-forming fluid may have originated from the crystallizing Scrubber Granite magma.

CHAPTER 7

THE ORIGIN OF TOURMALINE NODULES IN THE SCRUBBER GRANITE

7.1 INTRODUCTION

Field relationships, mineralogical and textural features, and geochemical, fluid inclusion and isotopic data from tourmaline nodules of the Scrubber Granite were presented in preceding chapters. The present chapter develops an argument for the generation of tourmaline nodules in the Scrubber Granite based on these data. Throughout this discussion, reference to and comparison with tourmaline nodules documented in other localities and nodule formation theories associated with these studies will be carried out where appropriate.

This chapter begins with a physical comparison between the field observations in the Scrubber Granite and those documented at other nodule localities. The mineralogical and textural similarities are then discussed, followed by an overview of nodule-forming fluid characteristics. Finally, a hypothesis, including a nodule-formation sequence of events, is presented for the genesis of the Scrubber Granite tourmaline nodules.

7.2 FIELD OBSERVATIONS

Tourmaline nodules are variably distributed throughout massive, porphyritic, foliated and sheared phases of the Scrubber Granite. Although certain regions are devoid of nodules, abundant nodules (>8 nodules/m^2) are present in other areas; these two extremes are occasionally juxtaposed next to one another, and there are also regions containing sparse (<4 nodules/m^2) to moderate (≥4 nodules/m^2) nodules. Spherical, elongate, rosette, irregular, flower/doughnut-shaped, horseshoe/C-shaped and starburst nodules are commonly characterized by a tourmaline-rich core surrounded by a leucocratic halo, and are mineralogically similar throughout the granite with regional

variations in crystal size. Nodule trains, tubes and swarms, as well as tourmaline veins, pegmatites and sparse inclusions of other rock types were also documented in the Scrubber Granite.

Nodules of the Scrubber Granite are strikingly similar to tourmaline nodules documented in other localities, particularly those of the Cnydas Granite in South Africa (Jankowitz, 1987; Hugh Smithies, GSWA, pers. comm). Although most tourmaline nodules in the literature are documented only as spherical entities, the Cnydas Granite also contains "ring structures" (doughnut-shaped nodules in Scrubber Granite terms) and elongate nodules, making this a critical pluton for comparison. Tourmaline nodules of another South African granite, the Cape Granite Suite (Rozendaal and Bruwer, 1995; Rozendaal et al., 1995), as well as spherical nodules in Czechoslovakian leucogranites (Nemec, 1975) and nodules of the Seagull Batholith in the Yukon Territory (Sinclair and Richardson, 1992; Samson and Sinclair, 1992) also resemble those of the Scrubber Granite. Himalayan leucogranites (LeFort, 1991) display spherical nodules as well as nodule trains and swarms, making this an important study for comparison with the Scrubber Granite as few nodule-bearing plutons contain these features. The occurrence of tourmaline veins and pegmatites in these nodule-bearing plutons is also important to note, as these features have been used by other researchers to support nodule formation theories.

South African leucogranites contain various outcroppings of tourmaline nodules, some of which are associated with hydrothermal alteration and Sn-Zn-(W) mineralization, such as the nodules of the Cape Granite Suite (Rozendaal and Bruwer, 1995). Similar nodules occur in the Cnydas Granite of the northern Cape Province, where they may be related to the Van Rooi's Vley Sn-W mineralization (Jankowitz, 1987).

The recognition of physical similarities between the Scrubber Granite and those of other nodule-bearing plutons is important as this affirms that theories proposed to explain the genesis of Scrubber Granite nodules can most likely explain the genesis of tourmaline nodules observed elsewhere. It is important that any theory proposed for the generation of the Scrubber Granite tourmaline nodules be applicable to all morphologic types.

7.2.1 Physical similarities with nodules in other localities

Regardless of their spatial association with Sn-W mineralization, tourmaline nodules in South African granitic suites are remarkably similar to those documented in the current study, as shown in Figures 7.1 and 7.2. An excerpt from the field descriptions of Jankowitz (1987, p. 38), translated to English by David Martin at the Geological Survey of Western Australia, confirms the similarities between nodules of the Cnydas Granite and those of the Scrubber Granite:

> It is a fine to medium grained, leucocratic granite that weathers to an orange color, particularly where it is sheared. Two phases are recognized, with one characterized by tourmaline nodules and veins, and the other by the absence of tourmaline. The two phases are essentially the same, but the latter is enriched in plagioclase and mafic minerals and is usually covered with desert varnish.
>
> The tourmaline-rich nodules vary in size from about 2 to 50cm, are rounded to subrounded, but also form ring structures in which granitic material is trapped. Tourmaline veins of varying widths are present in the granite and are lined by leucocratic margins. The veins die out in places and individual nodules are then present, showing that the veins and nodules are genetically linked, and that the veins possibly acted as feeders for the boron-rich gases and fluids.
>
> Varying local concentrations of very coarse-grained euhedral microcline phenocrysts (megacrysts) are also present and are usually situated close to tourmaline nodules. This possibly represents a later-stage 'internal pegmatite phase' of crystallization where enough melt was available and whereby the boron-rich fluids also accumulated.
>
> The granite is fine- to medium-grained and intensely sheared. The tourmaline nodules are elongated in a vertical to sub-vertical direction within the shear zones with subordinate lateral elongation. The lineation indicates a greater vertical to lateral displacement during the Cnydas Shear deformation.

The Cnydas Granite is largely comprised of spherical nodules (Figure 7.1A and B), but also contains nodule ring structures that trap host granite (Figure 7.2), and nodule trains (Figure 7.3).

Jankowitz (1987) stated that veins must act as feeders to the nodules, due to their apparent spatial association; he also states that there may be a late-stage pegmatite phase, where B-rich fluids may have accumulated. However, his views on the source of the fluid are not clear; are the fluids derived externally and then added to the internal pegmatite system, or is the fluid derived internally from the crystallizing magma?

Regardless, Jankowitz (1987) proposed that the nodules were genetically linked to tourmaline veins, but did not explain their spherical, ring or train-like morphologies.

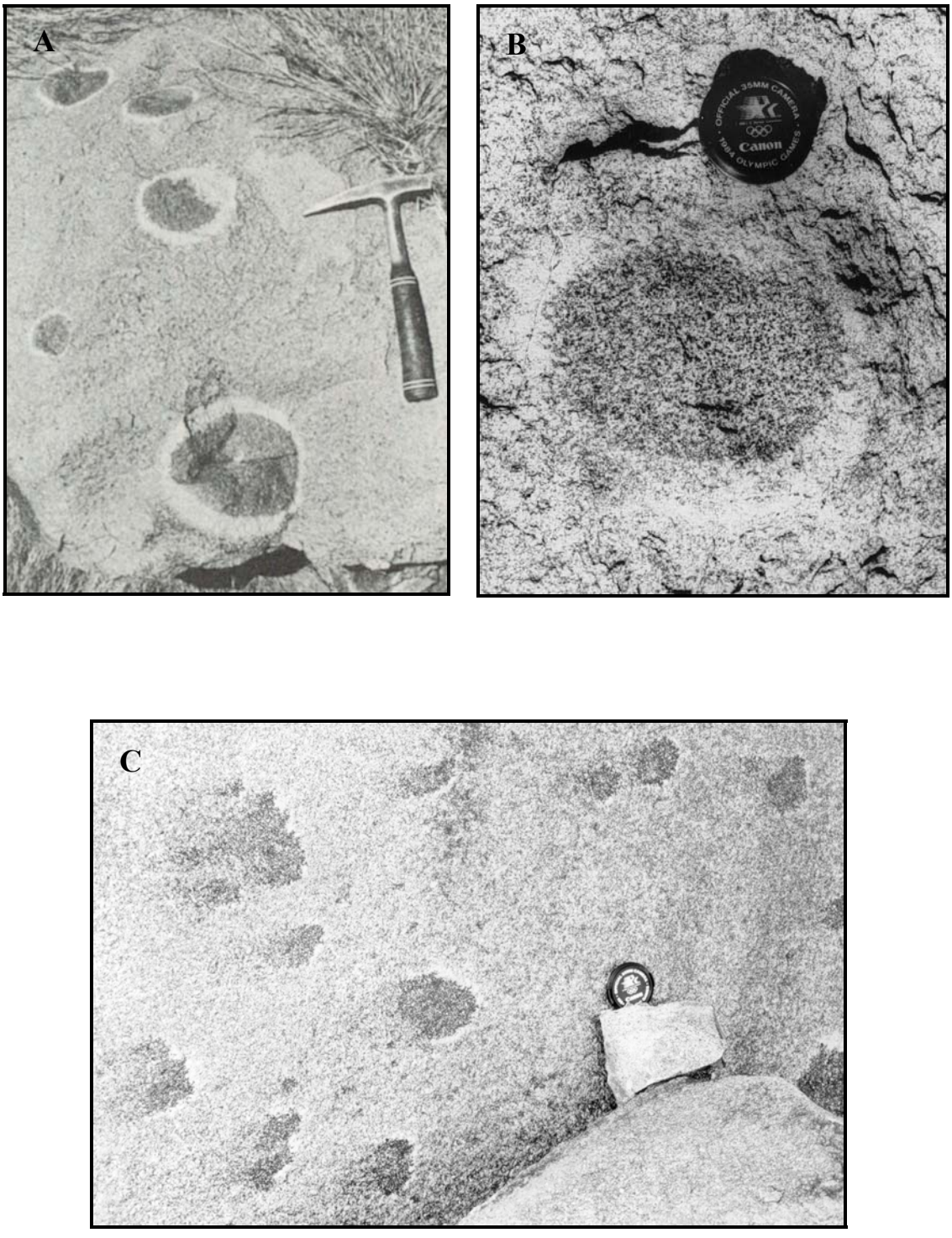

Figure 7.1: A) and B) Spherical nodules in the Cnydas granite; C) Spherical nodules in the Cnydas granite that do not have defined halos on left side of nodules (A from Jankowitz, 1987; B and C courtesy of Hugh Smithies, GSWA, pers. comm.).

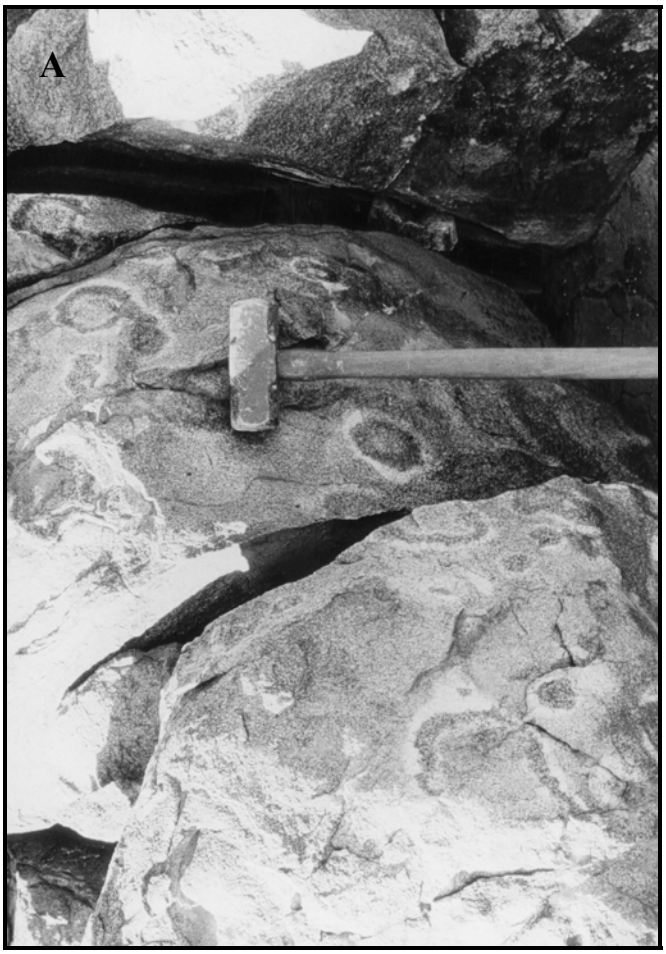

Figure 7.2: A) and B) Doughnut-shaped nodules of the Cnydas granite in South Africa; photos courtesy of Hugh Smithies, GSWA (pers. comm.).

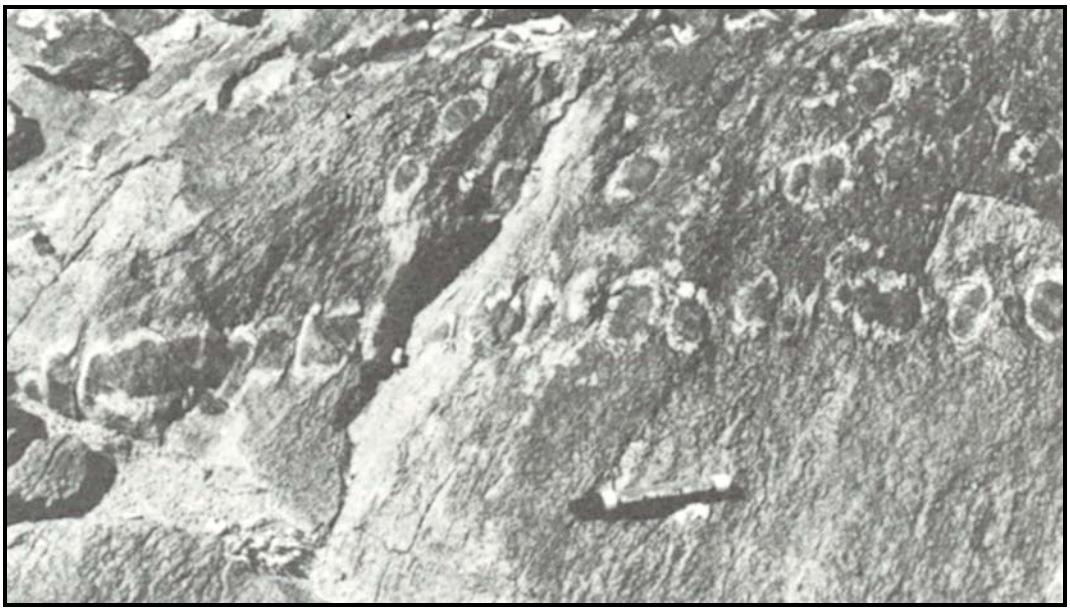

Figure 7.3: Alignment of nodules forming a nodule train, running horizontally in this photo from the Cnydas Granite, South Africa; adjacent to the nodule train are randomly dispersed spherical nodules (from Jankowitz, 1987).

Rozendaal and Bruwer (1995) considered the origin of tourmaline nodules in the Neoproterozoic Cape Granite Suite of South Africa, based on the following field observations (p. 150):

> Granite texture and probably also mineralogy were not controlling factors with respect to [nodule] distribution, as suggested by the diversity of textural types of rocks that host the nodules. They therefore are not confined to a particular granite and have been found in several juxtaposed, texturally contrasting phases. The nodules also pseudomorph granite textures, i.e. coarse-grained granites host coarse-grained nodules. Evidence of structural control is shown by narrow, crosscutting, tourmaline-bearing fractures that contain nodules arranged like beads on a string. The above relations support an interpretation of late-magmatic hydrothermal fluids superimposed on a variety of crystalline granites, producing nodular replacement features. The distribution of the fluids was structurally controlled, even though fractures are not clearly evident in many of the nodule localities. In those areas, hairline fractures, grain-boundary migration or infiltration and diffusion along grain boundaries are considered to have controlled the fluid movement. The mechanism responsible for their spherical shape is not fully understood, but could relate to point nucleation at the end of dendritically arranged micro-fractures or possibly to the tendency, in some environments, for tourmaline to crystallize as rosettes.

Other field relations to note in the Cape Granite Suite include the apparent concentration of nodules in the roof zones of granites (Rozendaal and Bruwer, 1995). Nodules are considered to result from late-stage volatile-rich (B, F) hydrothermal fluids that replace their host rock through various metasomatic reactions. However, this summary fails to pin point the origin of the fluids; are they derived externally or internally? Just as Jankowitz (1987) failed to explain possible controls on the morphology of nodules, Rozendaal and Bruwer (1995) also fail to fully explain the mechanism(s) controlling the spherical nature of nodules.

Rozendaal et al. (1995), in their summary paper discussing the use of tourmaline nodules as indicators of mineralization in the Cape Granite Suite, state that the nodules form as a result of hydrothermal alteration of the crystallized granite. This more closely pin points the fluid source as external, as opposed to the "magmatic-hydrothermal" fluid described by Rozendaal and Bruwer (1995) in the above quote, which could presumably be derived from either the Cape Granite magma, or an external source.

Nemec (1975), in his study of tourmaline nodules in leucocratic granites of the Czech Republic, suggests that the nodules as well as their halos originated through metasomatic replacement, or "tourmalinization" of the host granite. Boron-bearing fluids imported into the rocks in connection with pegmatite injections were thought to initiate these metasomatic processes. Nemec (1975) performed whole rock chemical analyses of host granite, core and halo zones, and came up with the following chemical equations based on components lost and gained in the generation of nodules:

K-feldspar + boron + iron + water = tourmaline + quartz + potassium + acid

Thus, in the nodule core, the tourmalinization of granite consisted mostly of the replacement of potassium feldspar. According to Nemec (1975), the components set free by this reaction (quartz, potassium and acid) migrated into the adjacent rock, producing the breakdown of biotite and the generation of the leucocratic halo. The development of tourmaline in the core would require a considerable import of boron, aluminum and iron, and an export of silica. Nemec (1975) suggests that the boron may have been brought into the system via pegmatitic fluids, thus supporting an external fluid source theory. These fluids are thought to have leached iron from the rocks it

percolated through, and, according to Nemec (1975), iron would continue to be enriched until tourmaline was precipitated. However, would this not have produced a linear, vein-like feature, as opposed to a spherical nodule? Nemec (1975) concentrates on the chemistry of the nodules, and does not fully consider their physical attributes.

LeFort (1991), in his study of tourmaline nodules in Miocene Himalayan leucogranites, suggests that these nodules result from metasomatic circulation of a late boron-rich phase formed during the crystallization of the boron-rich magma. He also states that these textures are not the last granitic material to crystallize, as pegmatites and aplites often crosscut them (top of Figure 7.4A). Thus, LeFort (1991) believes that the fluid is internally derived from the host magma, which is assumed to be boron-rich due to the presence of prismatic crystals of tourmaline in the groundmass. His mechanism for the formation of the nodules parallels that of Rozendaal and Bruwer (1995) and Jankowitz (1987); they collectively propose that veins feed, or drive nodule formation. LeFort (1991) also fails to explain the morphology of the nodules.

Sinclair and Richardson (1992) documented tourmaline nodules of the 100 Ma Seagull Batholith in the Yukon Territory (Figure 7.5). They propose that nodules are magmatic-hydrothermal features related to the separation and entrapment of aqueous, B-rich fluids within coexisting granitic magma. According to Sinclair and Richardson (1992), various aspects of the Seagull Batholith support this theory, namely:

1. Nodules are concentrated at the top of the batholith, irrespective of country rock;
2. Nodules decrease in abundance and tourmaline content with depth;
3. Nodules are typically spherical in shape; and
4. The absence of structural features related to nodule form or distribution.

In general, nodules of the Seagull Batholith are spherical to ovoid in shape, and occasionally, two or more nodules are joined to form larger, more irregular bodies. Sinclair and Richardson (1992) state that tourmaline-bearing fractures or quartz-tourmaline veins locally crosscut nodules, but that most nodules are spatially unrelated

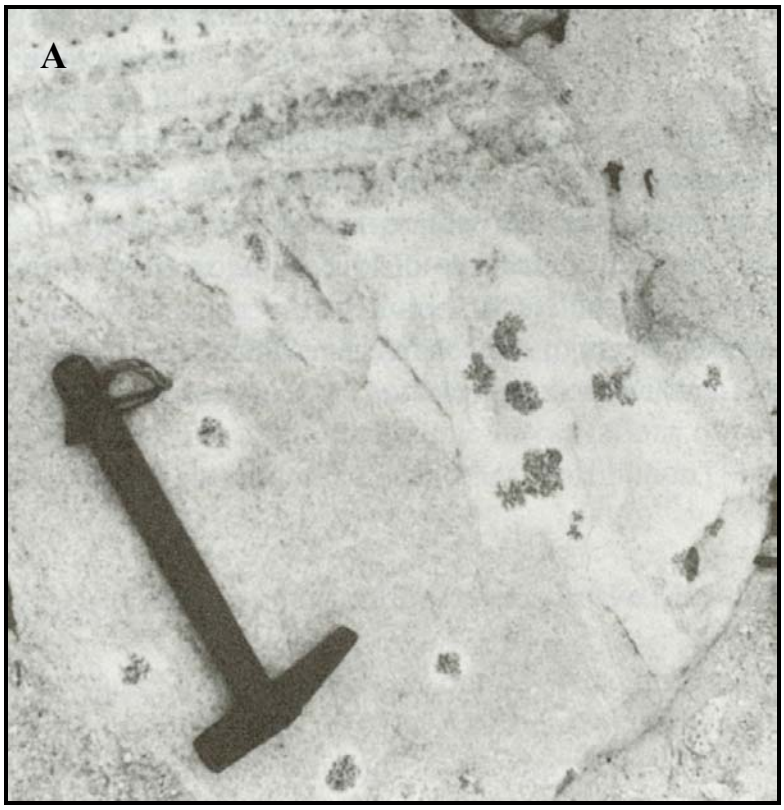

Figure 7.4: A) Tourmaline nodules from the Himalayas; B) Nodule train, also from the Himalayas. Photos from LeFort (1991).

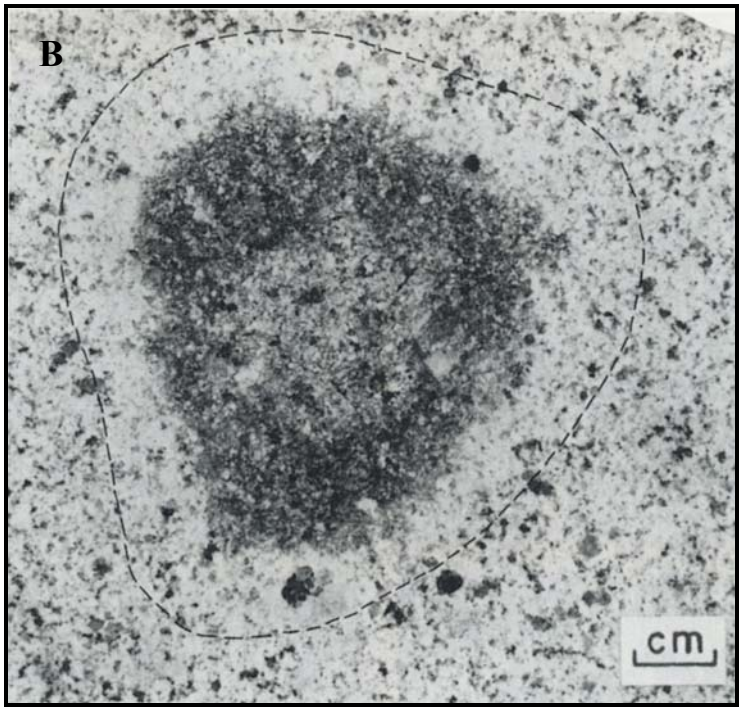

Figure 7.5: A) Outcrop of tourmaline nodules in the Seagull Batholith (hammer for scale); B) Tourmaline nodule from the Seagull Batholith, displaying zones (dashed line represented margin of leucocratic halo). Photos from Sinclair and Richardson (1992).

to these features. Nodules extend over several hundred meters below the upper contact of the batholith, and nodules at depth contain less tourmaline and lack miarolitic cavities that occur in many nodules near the top of the batholith. According to Sinclair and Richardson (1992), nodules consist of several concentric zones: 1) a 1 to 2cm leucocratic halo of biotite-free granite that surrounds each nodule; 2) a dark outer zone 1 to 5cm wide comprised mostly of quartz and tourmaline; and 3) a more leucocratic 1 to 2cm inner zone consisting of quartz, microcline, albite and tourmaline. In most cases, the dark outer zone extends to the center of the nodule, and the inner leucocratic zone is absent. In some nodules, the dark outer zone surrounds a central miarolitic cavity lined with crystals of quartz, tourmaline, and occasionally, topaz (Sinclair and Richardson, 1992).

Sinclair and Richardson (1992) make the following statements regarding tourmaline nodule formation (p. 932):

> The textural features within the [nodules] are probably due to the interaction of crystal-bearing melt and aqueous, B-, F- and Fe-rich fluid that was trapped as the surrounding melt solidified. Primary fluid inclusions in quartz, tourmaline and fluorite in the [nodules] have salinities ranging from 8 to 42 equivalent wt. % NaCl + $CaCl_2$, indicating that the fluids are also Cl-rich. Initially, the melt and fluid trapped in the [nodules] may have been in equilibrium, but as they cooled, disequilibrium ensued. Reaction between the aqueous fluid and minerals already crystallized within the [nodules] resulted in the extensive replacement of feldspar by tourmaline in the outer zone [of the nodule]. In some [nodules], this replacement essentially reached completion, and excess B in the fluid precipitated as crystals of tourmaline in miarolitic cavities in the center of the [nodules]. In [nodules] in which replacement was less extensive, an inner zone formed in which tourmaline occurs as discrete grains associated with quartz, microcline and albite, and within granophyric intergrowths of quartz and alkali feldspar.
>
> The leucocratic halo that surrounds each [nodule] is distinguished from the adjacent granite solely by the absence of biotite. No indication of pre-existing biotite is evident; the absence of biotite in the halo is probably due to a deficiency of Fe in the melt that crystallized around the [nodule]-forming fluid. The deficiency of Fe may have been related, at least in part, to partitioning of Fe from the melt into the [nodule]-forming fluid.

Thus, the separation of a late-stage boron-rich fluid from the crystallizing Seagull magma may have produced nodules containing miarolitic cavities in the roof zone and crystalline nodules at depth in the batholith.

7.2.2 Summary of physical similarities and related origin theories

Rozendaal and Bruwer's (1995) post-magmatic replacement theory is based on spatial and temporal relationships of the nodules, with no emphasis on or consideration of the physical nature of the nodules. They simply state, "the mechanism responsible for their spherical shape is not fully understood". Perhaps Rozendaal and Bruwer (1995) are preoccupied with the apparent association of tourmaline nodules and veins with the nearby Sn-W mineralization. Did the spatial association of these features lead Rozendaal and Bruwer (1995) to assume that post-magmatic hydrothermal fluids also produced the nodules?

Rozendaal and Bruwer (1995) do, however, consider the distribution of the nodules in the Cape Granite Suite, stating "their distribution is possibly controlled by fluid movement along micro-fractures". However, there is a general lack of tourmaline veins observed in their field photos, as in the Scrubber Granite, relative to the number of nodules per unit area. How many veins or micro-veins are necessary to nourish the development of abundant nodules observed in granitic plutons? What volume of fluid is required to form a nodule? These questions must be addressed in these hypotheses.

According to Rozendaal et. al. (1995), the structural control on nodule formation is evidenced by "narrow, cross-cutting tourmaline veins with nodules arranged like beads on a string". However, in their published field photos, nodules appear as discrete, spherical entities, similar to nodules of the Scrubber Granite. In the Scrubber Granite, nodules only occasionally appear as nodule trains (i.e. this is the exception, not the rule), and are infrequently associated with tourmaline veins; when spatially associated, veins clearly overprint nodule textures. Additionally, nodule trains in the Scrubber Granite consist of aligned individual spherical nodules, and do not appear as linear (vein-like) entities, as one might expect if they are originating from a structural feature. The nodule train of the Cnydas Granite (Figure 7.3) is also comprised of spherical nodules that are contained by individual halo zones, and are not vein-like in appearance, even though Jankowitz (1987) states that veins in the Cnydas Granite are feeders for nodules.

Jankowitz (1987) does not provide an interpretation of the ring structures (doughnut-shaped nodules) in the Cnydas Granite. It is difficult to envision how these

nodules could evolve from his vein-based theory. Nemec (1975) also suggests a structural control in the "tourmalinization" of leucogranites. Again, it is unlikely that a spherical texture could develop from a linear fluid injection. Although LeFort (1991) supports an internally derived fluid source, i.e. the boron-rich fluid is a late-stage derivative of the crystallizing magma, he also suggests that the fluid migrates through the crystal mush via vein-like structures.

Sinclair and Richardson's (1992) nodule formation theory considers both nodule morphology and texture. They believe that nodules were derived from an immiscible, boron-rich aqueous fluid phase that separated from the crystallizing Seagull Batholith magma, which was subsequently entrapped in the magma-crystal mush, preventing the fluid from exiting the system. Gaseous pockets of immiscible fluid would possibly have a spherical to ovoid form; these aqueous pockets, presumably less dense than the surrounding crystallizing magma, would rise to the upper portion of the batholith. Here, at a critical degree of crystallization, the gaseous pockets would not be able to rise through the crystal mush, at which point the pockets would become entrapped and crystallize to form nodule textures.

The idea of an aqueous, immiscible fluid phase separating from the crystallizing host magma eventually crystallizing to form nodules directly addresses the issues of nodule morphology, the lack of tourmaline crystallized in the groundmass of the Scrubber Granite, and the lack of tourmaline veins associated with nodule formation. This "pocket-based" theory is favored in the current study as a good starting point from which to explain the genesis of the Scrubber Granite tourmaline nodules.

7.3 MINERALOGICAL AND TEXTURAL CONSIDERATIONS

Three mineralogic zones have been identified in the Scrubber Granite: 1) host granite; 2) leucocratic halo; and 3) tourmaline-rich nodule cores; aspects of these zones that are pertinent to formation hypotheses in other studies are discussed herein.

Halo zones surrounding nodule cores in the Scrubber Granite often contain biotite clots. Biotite flakes do not exhibit evidence of chemical breakdown, such as alteration to chlorite. Biotite is in close spatial association with tourmaline crystals in

proto-nodules, which generally lack halo zones; here, biotite again lacks evidence of alteration or breakdown. Conversely, biotite flakes are absent in the halo zones of the Cnydas Granite, an observation that, according to Jankowitz (1987), indicates that biotite adjacent to nodule cores were destroyed during the crystallization of tourmaline in nodule cores, an idea borrowed from Nemec (1975). In other words, they suggest that tourmaline crystallizes in nodule cores at the expense of biotite in the host granite; this process is thought to produce the leucocratic, biotite-free halo zones. Ideally, if biotite was being "used up" to provide the necessary ingredients for the crystallization of tourmaline, there would be textural evidence of this process. Textural and mineralogical observations of biotite clots do not support this hypothesis; additionally, there is a moderate amount of nodules that contain biotite clots in the halo zone. The destruction of biotite as the source of iron for the crystallization of tourmaline in nodule cores and the generation of the leucocratic halo is not favored in the current study.

Scrubber Granite nodule core zones are comprised of tourmaline, quartz, albite and occasionally microcline. Microscopically, tourmaline commonly occurs as irregular aggregates, but also occurs as subrounded, prismatic and massive crystals, and occasionally shows signs of alteration. Grain boundary contacts between tourmaline and feldspar grains are important to focus on, as previous researchers have suggested that tourmaline is replacing feldspars in the core (Nemec, 1975; Jankowitz, 1987).

In the core zone of the Scrubber Granite nodules, tourmaline displays various textural relationships with feldspars. Irregular tourmaline crystals are embayed by albite crystals, and generally display irregular grain contacts with quartz and feldspar. Subrounded tourmalines are intergrown with quartz and feldspars. Prismatic tourmaline crystals are typically surrounded by quartz crystals and occasionally enclose albite and quartz. Massive tourmaline occurs in the dense aggregates of the tourmaline rosette nodules, where it may enclose albite and quartz crystals. The irregular grain contacts between tourmaline and other mineral phases in nodules may indicate that replacement may have taken place. However, this does not necessarily indicate that nodules are "replacement features" of a crystallized granite, but that nodules may incorporate portions of the crystal mush from the surrounding host during the separation of the late-stage nodule-forming fluid. These crystals may be replaced by mineral phases

crystallizing from the fluid, including tourmaline. This may also explain the similar crystal size and texture across the three mineralogic zones in the Scrubber Granite, which was assumed to indicate replacement of previously crystallized granite to form leucocratic halos and nodule cores by Rozendaal and Bruwer (1995), who stated that "…the grain size and texture of the host rock is pseudomorphed by the nodule, i.e. coarse-grained granites host coarse-grained nodules".

7.4 FLUID CHARACTERISTICS

Fluid inclusion and geochemical studies of tourmaline crystals, as well as stable and radiogenic isotope analyses of tourmaline separates constrained the following characteristics of the nodule-forming fluid:

1. H_2O-NaCl-$CaCl_2$ fluid with 14 to 15 weight % salinity;
2. Temperatures between 450˚C and 700˚C;
3. Oxygen and hydrogen isotopic composition of +7.2 to +10.4‰ and +7.0 to -29.0‰, respectively, at the above temperature range;
4. More negative εNd values relative to the Scrubber Granite whole rock; and
5. A concentration of the following elements: Mg, Fe, B, Sc, Th and REE (see Figure 7.6).

Thus, the fluid can be summarized as a late-stage aqueous fluid that contains major and trace element phases necessary to precipitate tourmaline. However, some elemental exchanges may have taken place during fluid crystallization, forming the leucocratic halo between the core and surrounding (partially) crystallized granite.

Figure 7.6 outlines the relative element concentrations as determined from mass balance calculations, and does not indicate all elements present in each zone. The elements necessary for the crystallization of all mineral phases present in the host, halo and core were obviously in these regions. In Figure 7.6, it is assumed that the elements present in the host granite are inherent from the host magma, and the elements in the halo are similar to those of the host, with the exception that it is devoid of abundant melanocratic mineral phases (e.g. biotite). Elements in the core are assumed to have been preferentially incorporated into the residual fluid, and are not a result of the migration of elements from the host or halo zones.

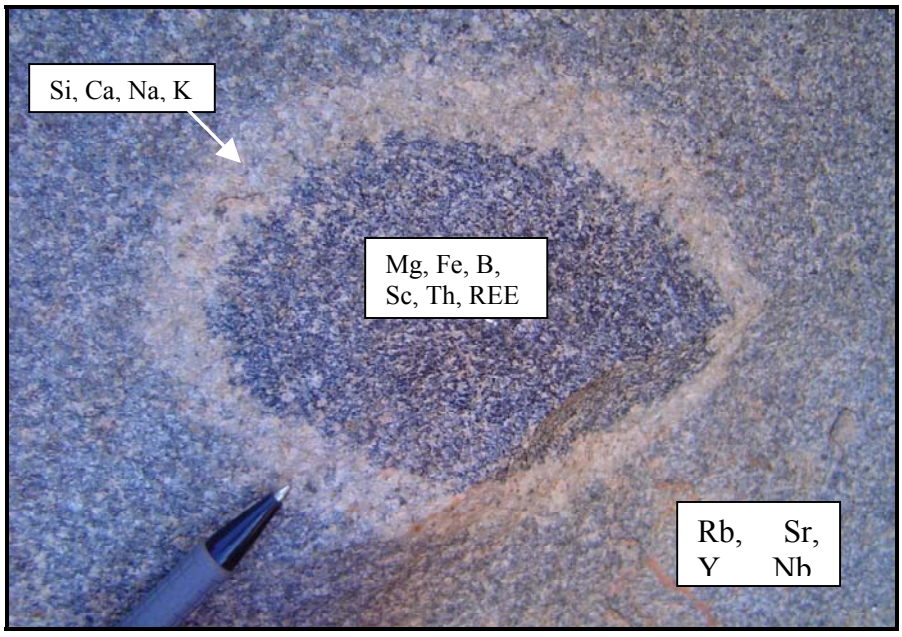

Figure 7.6: Schematic diagram of relative element concentrations (in boxes) determined in mass balance calculations.

7.5 FORMATION OF A LATE-STAGE FLUID

This study favors the "pocket-based" nodule formation theory proposed by Sinclair and Richardson (1992) and Samson and Sinclair (1992) for the Seagull Batholith as a reference point from which to start. The physical similarities between tourmaline nodules of the Scrubber Granite and those of the Seagull Batholith is important, as the latter contains an important nodule physical attribute that must be explained in any all-encompassing nodule formation theory: the presence of miarolitic cavities. The fact that miarolitic cavities, features typically associated with pegmatites (e.g. London, 1986) and occasionally with leucogranites (e.g. Candela and Blevin, 1995) are present inside nodules of the roof zone in the Seagull Batholith provides a strong case for a common formation process among nodules, miarolitic cavities and pegmatitic fluids. The formation of nodules can thus be modeled after the formation processes related to pegmatite and miarolitic cavity development. Several studies by London (1986, 1988, 1989, 1992) among others will help to constrain pegmatite crystallization processes; key papers by Candela and Blevin (1995) and Candela (1991)

examine the formation of miarolitic granites and the genesis and separation of an aqueous phase from plutonic environments, respectively.

An underlying issue with existing nodule formation theories involves the lack of a nodule formation sequence of events. Formation processes of pegmatites and miarolitic granites will help to constrain the following parameters of the nodule formation:

1. Temperature of initial granitic magma crystallization;
2. Temperature of initial fluid separation from granitic magma;
3. Degree of crystallization associated with #2;
4. Temperature of final crystallization of the granite;
5. Temperature of initial fluid crystallization; and
6. Final temperature of complete crystallization of granite and nodule.

Also of aid in the above modeling will be the fluid inclusion homogenization temperatures, which provide a minimum crystallization temperature for the nodule fluid (see Chapter 5), and stable isotope data, which helped to constrain the likely crystallization temperatures of tourmaline crystals (see Chapter 6). The following sections summarize the parameters of pegmatite fluid development, miarolitic cavity formation, the formation hypothesis and a sequence of events for the formation of nodules.

7.5.1 Temperature of pegmatite fluid generation

London (1992) states that "in seeking to explain what state or processes makes pegmatites as opposed to texturally and compositionally homogeneous granites, Jahns and Burnham (1969) proposed that it is the presence of an aqueous vapor phase, together with silicate melt, that is essential to pegmatite formation". In other words, he is attributing the transition from granitic to pegmatitic textures to the exsolution of an aqueous vapor phase from a saturated melt. At what temperature does the vapor phase exsolved; i.e. at what temperature does the melt become water-saturated?

In his fluid inclusion studies, London (1986) found evidence for magmatic compositions down to approximately 475˚C. This lower limit of "pegmatite-producing magmas" was confirmed by experiments with the Macusani glass (London et al., 1989),

whose solidus lies at 450˚C at 200MPa. Thus, the solidus of the granitic melt can be set at between 475 and 450˚C.

Temperature conditions of pegmatite formation were constrained by London (1986), who defined solidi for the Tanco pegmatite and miarolitic rare-element pegmatites in Afghanistan and California near 475˚C and pressures of approximately 250 MPa for both types of pegmatite. These parameters were constrained by combining phase relations of the lithium aluminosilicates with fluid inclusion data.

7.5.2 Miarolitic cavities and the separation of volatile phases

London (1986), in his discussion of miarolitic cavities in pegmatites, has constrained the conditions of pocket (miarole) formation to 425-475˚C and pressures of 2400-2800bars; he states that this P-T range is similar to the late-stage crystallization of pockets in the Tanco pegmatite. London (1986) believes this signifies that compositionally similar miarolitic and rare element pegmatites may crystallize under similar P-T conditions.

London (1986) ponders the cause of miarolitic pocket formation, and states that "in view of the conclusion that miarolitic and massive pegmatites crystallize at similar P-T conditions, the presence or absence of pegmatitic pockets appears to be controlled by the timing and extent of volatile exsolution from silicate melt". The abundance of tourmaline in pegmatitic miaroles is thought to reflect high concentrations of boron in late-stage pegmatitic fluids and London (1986) states that this provides an important clue for understanding pocket formation.

As tourmaline commonly does not crystallize throughout the "groundmass" of pegmatite systems, this results in high boron contents in late-stage fluids; London (1986) states that the accumulation of boron through fractional crystallization in the absence of tourmaline enhances the solubility (retention) of H_2O in late-stage fluids. The exsolution of H_2O from these fluids (upon the crystallization of tourmaline) provides favorable conditions for pocket (miarolitic cavity) formation. London (1986) also states that pocket formation can occur anywhere in the pegmatite and is not restricted to the site of tourmaline crystallization.

Candela and Blevin (1995), in their study of the miarolitic Ruby Creek monzogranite of Eastern Australia, suggest that the occurrence of "undercooling textures, miaroles and a fractionated composition suggests that the rocks are the product of the rise of buoyant bubble + crystal + melt plumes that result from Rayleigh-Taylor instabilities in the volatile phase-bearing crystallization interval". These buoyant plumes would transport volatiles toward the top of the chamber.

In their consideration of pressures and depths associated with miarolitic granites, Candela and Blevin (1995) discuss the general occurrence of miaroles near the roof zone of plutons, suggesting that they are a near-surface phenomenon developing at pressures less than 2 to 3 kbars.

In a related study, Candela (1991) examines the physics governing magmatic aqueous phase evolution (vapor phase exsolution) and emplacement in upper regions of felsic magma chambers. In this discussion, he summarizes a process in which magmatic H_2O exsolution occurs at <<20% crystallization (at high initial magmatic H_2O concentrations or low pressures), inducing the rise of plumes laden with bubbles (± crystals). He suggests that H_2O will accumulate within a marginal boundary layer or crystallization interval within magma chambers.

The primary process in the crystallization of a magma body is the irreversible loss of heat to the surroundings; heat passes out of the magma at the margins of the body, and crystallization is focused in these regions (Candela, 1991). Over time, the solidus moves toward the interior of the magma chamber, defining a moving margin. As this crystallization ensues, the evolved melt is either convected away from the crystallization interface, and mixes with the bulk melt, or becomes trapped in the immobile crystal mush and does not mix with the bulk melt.

Vapor saturation in these cooling systems is the result of either a pressure decrease (first boiling) or the crystallization of anhydrous phases (second or resurgent boiling) or both. Candela (1991) states that in the case of second boiling, H_2O saturation will occur ahead of the inward advancing solidus, or occur late and in spatially segregated areas, with H_2O back diffusing from the crystallization interval into the remaining body of the liquid.

Candela (1991) states that the controls on the rate of crystallization need to be defined so that the behavior of H_2O in the region of crystallization can be determined. After several equation manipulations, which is beyond the scope of this study, Candela (1991) concludes that the rate of diffusion of H_2O into the residual melt is insignificant relative to the rate of crystallization, and H_2O either accumulates in the crystallization interval or at the crystal-melt interface. Candela (1991) then goes on to discuss consequences of boundary zone vapor saturation in a crystallization interval. The following quote from Candela (1991) summarizes this process:

> As the leading edge of the crystallization interval advances into the magma after the nucleation incubation period, the percent crystallization at the wall steadily climbs. At some time, depending on the depth and the initial H_2O concentration in the melt, a critical fraction of liquid remaining is reached at the wall such that vapor saturation is achieved. As crystallization proceeds, the [vapor exsolution progress] front advances inward behind the [critical fraction of liquid remaining] front. The H_2O-saturated melt is confined to the crystallization interval. Even though the presence of vapor bubbles reduces the bulk density of the crystallization interval relative to its surroundings, a few tens of percent (by volume) of bubbles plus crystals greatly reduce the probability of flow of the melt + vapor + crystal mixture because of the increased viscosity….If the vapor-liquid-crystal region is modeled as a simple cubic lattice with the aqueous fluids as the potentially percolating phase, advection of the fluid upward may be considered possible when the volume fraction of the aqueous phase in the crystallization interval reached approximately 0.31 (31%). The flux of H_2O at critical percolation may be low; however, as the volume fraction increases beyond the critical percolation threshold, the advective flux (driven by buoyancy and the positive pressure gradient produced by vapor exsolution, and allowed by the ability of the melt and the vapor to flow into the region vacated by advecting fluid) will increase rapidly (a type of gravitationally driven filter pressing of vapor).
>
> Critical percolation begins at the wall and sweeps inward behind the zone of vapor bubble nucleation. It is followed by the solidus. The zone of percolation occurs between the solidus and a surface characterized by the critical value of the vapor exsolution progress variable at which percolation commences. For an idealized, hypothetical hemispherical magma chamber, this zone of percolation is a hemispherical shell that moves inward and thickens with time, as does the crystallization interval. The rate of increase of the volume fraction of vapor is significantly retarded as the volume of the vapor phase exceeds 0.31 because of the upward advection of the vapor from the system. This large volume change is not experienced by the whole magma chamber but only by the hemispherical shell of percolation, which is centimeters to meters thick.

Candela (1991) states that the critical factor determining the behavior of a given system is the rate of change of the density of the crystal-melt-vapor system as crystallization proceeds. This rate is controlled by the timing of vapor evolution (which in turn is controlled by the concentration of water in the magma) and by the density of the aqueous phase (which in turn is controlled by pressure and to a lesser extent by temperature). For magmas with high water concentration values, vapor saturation occurs early and significant buoyancy is achieved at relatively low viscosity (crystallinity). In this case, plumes may rise from a sub-vertical border zone. This theory has been diagrammatically summarized by Candela (1991) in Figure 7.7.

Given that the probability of eruption of a granitic melt is significantly decreased for crystallization >20%, vapor evolution probably occurs at a degree of crystallinity >20% for this mechanism to be operative (Candela, 1991). The conditions imperative to this model include an emplacement depth of no more than 2 or 3 km, as emplacements at 3 or 4kms would not allow the first bubbles to form until approximately 25% crystallization occurred. The high viscosities realized in felsic systems with greater than 20% crystals might preclude plume rise under these conditions.

In summary, Candela (1991) states that the achievement of critical percolation (i.e. aqueous phase exsolution) within a crystallization interval is possible if the initial H_2O concentration of the magma is above a minimum value for a given pressure (Figure 7.8) and if the system is at a pressure of less than 2 kbar. In systems with high enough H_2O concentrations for a given intrusion pressure or in cases where crystal nucleation occurs dominantly along the walls of the chamber, plumes of bubble-laden melt may raft to the top of the magma chamber. Candela (1991) states that this may account for the delivery of magmatic aqueous fluids from large portions of magma chambers to the upper portions, where mineralized zones can form.

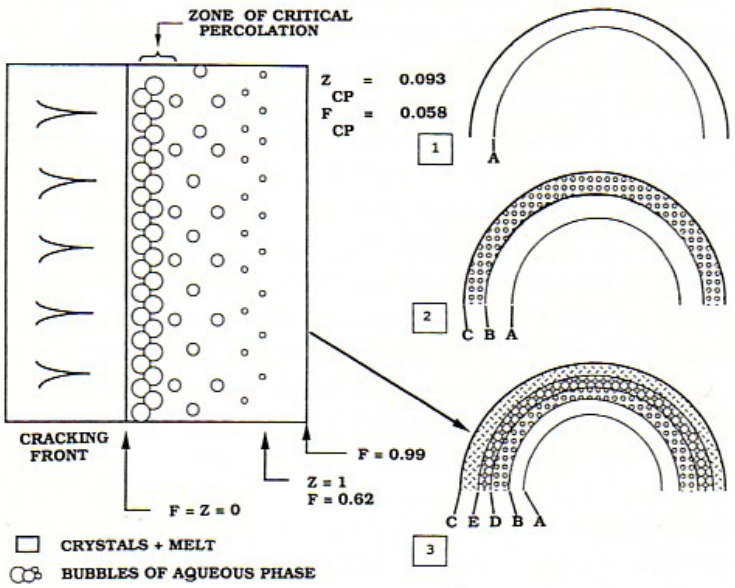

Figure 7.7: Idealized illustration of the production of a cluster of vapor bubbles at critical percolation. F is the crystallization progress, which varies from 1 (100% liquid) to 0 (100% solid); Z is vapor exsolution progress, which progresses toward zero as vapor is exsolved. Numbers in this figure are for initial [H_2O] of 2.5%, and a H_2O saturation of 4%. Three stages in the formation of a crystallization interval upon intrusion are shown in the right portion of the figure; A is the leading edge of the crystallization interval, B is the leading edge of the zone of aqueous phase saturation, C is the magma/country rock contact, D is the leading edge of the zone of percolation, and E is the solidus (from Candela, 1991).

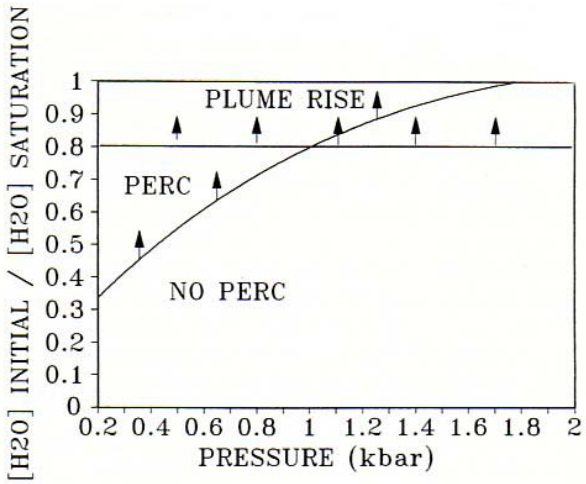

Figure 7.8: Curved line indicates, for a given pressure, the minimum ratio of the initial to the magmatic H_2O concentration at saturation at which a cluster of vapor bubbles will allow the upward advection of magmatic H_2O (PERC = percolation, or volatile phase exsolution). Arrows indicate regions of the graph favoring large-scale upward transport of the magmatic aqueous phase (from Candela, 1991).

7.6 FORMATION HYPOTHESIS

It is proposed that the nodules formed from an aqueous fluid phase that separated from the crystallizing Scrubber magma, similar to the theories put forth by Samson and Sinclair (1992) and Sinclair and Richardson (1992). The globular to blebby nature of most nodules (see Figures 3.4A, B and 3.7C) further promotes the pre-solid state formation of tourmaline nodules. The task is to now propose a nodule formation sequence of events, modeled after several studies on pegmatites, miarolitic granites and the general crystallization of granitic magmas.

7.6.1 Sequence of nodule formation

The following schematic diagram (Figure 7.9) summarizes the possible temperatures, degree of crystallization and timing of the separation of the aqueous volatile phase associated with the generation of nodules. These parameters have been given approximate temperature ranges, and some degree of overlap between stages may occur. The associated stages of formation are described below:

Stage 1: Uniform granitic magma

In order to assess the approximate initial temperature of the Scrubber Granite magma, several experimental and field-based studies have been examined. Nabelek et al. (1992), in their study of the generation and crystallization conditions of the peraluminous Harney Peak leucogranite of South Dakota, state that the tourmaline-bearing granite was largely generated from a metasedimentary source at pressures of 5 to 6 Kbar, temperatures between 800 and 850˚C, and water-undersaturated conditions (i.e. $a H_2O$ less than unity).

Crystallization experiments conducted by Clemens and Wall (1981) on peraluminous granitic magmas were carried out at pressures of 1-7 kbar, temperatures in the range of 700-900˚C, and water activities ($a H_2O$) of 0.1-1.0. Several other workers, including Scaillet et al. (1995) and London (1992) suggest initial leucogranitic magmatic temperatures of >800˚C and between 900 and 950˚C, respectively. Thus, a temperature range of 800 to 950˚C has been selected for the initial temperature of the Scrubber Granite, as this includes most suggested temperatures in the literature.

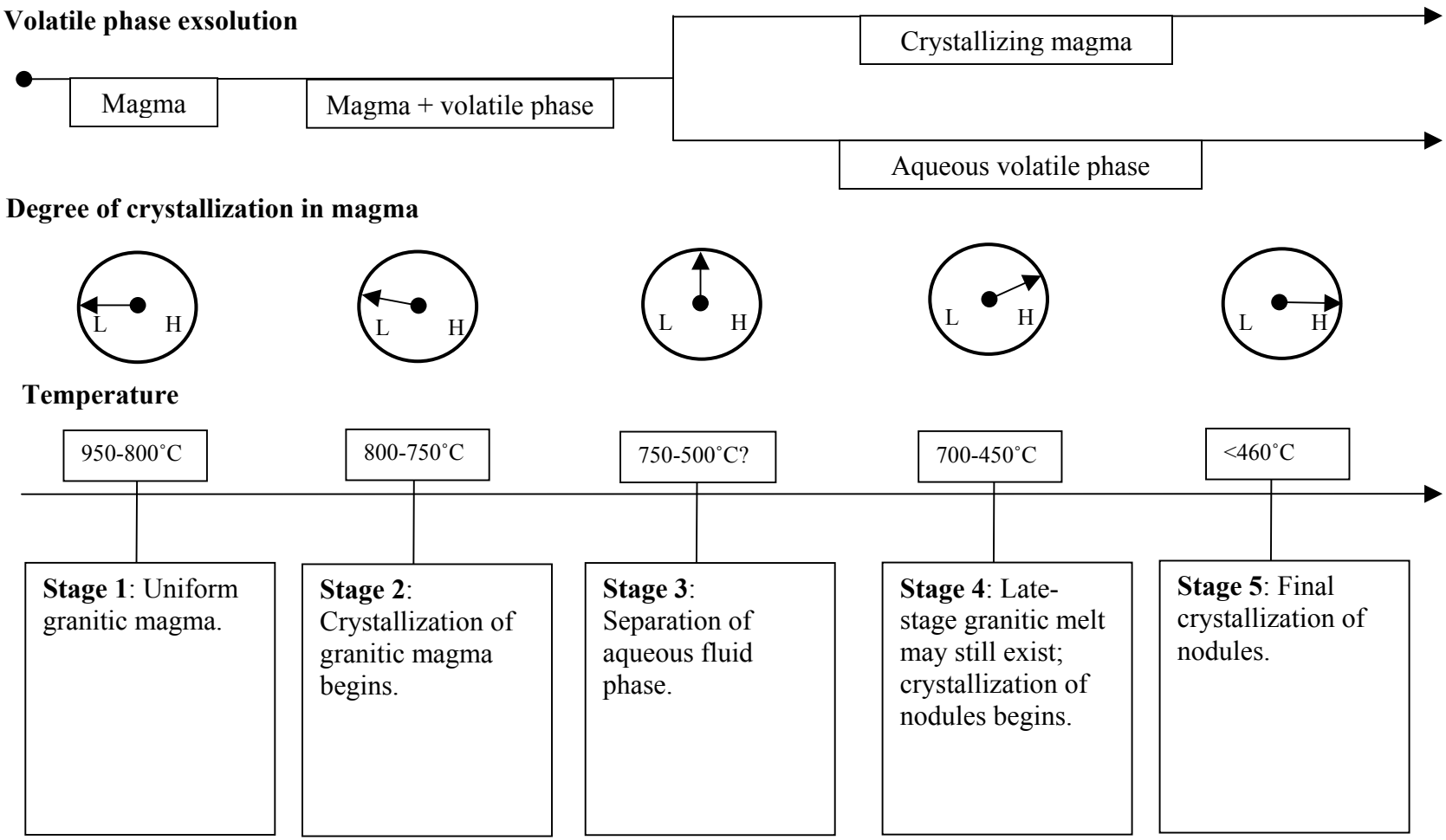

Figure 7.9: Sequence of events in the formation of tourmaline nodules in the Scrubber Granite. See text for details.

Stage 2: Crystallization of granitic magma begins

Upon the generation of a granitic magma, the lower density melt will begin its ascent to higher levels of the crust (Nabelek et al., 1992). During the ascent, the magma will begin to cool and crystallize as it encounters relatively cooler country rock. As anhydrous mineral phases are precipitated from the magma, the aH_2O in the magma will increase. Crystallization is thought to begin around the lower boundary of the uniform granite magma stage (800˚C) and possibly at slightly lower temperatures (750˚C).

Stage 3: Separation (exsolution) of aqueous fluid phase

Following the hypothesis proposed by Candela (1991), at <<20% crystallization (for magmas with high initial magmatic H_2O concentrations or low pressures), or at least at a 20% degree of crystallization (for magmas less H_2O enriched), there is an exsolution of the volatile phase within the crystallization interval or at the crystal-melt interface of the magma chamber. As crystallization continues, and as the concentration of the volatile phase in the crystallization interval increases, rise of the fluid pockets (bubbles ± crystals ± melt) upward is possible after the volume fraction of the volatile phase reaches approximately 31% (the critical percolation threshold). This continues until the Scrubber Granite has reached complete crystallization. Candela (1991) does not assign any temperature restraints to this process; the temperature range associated with this nodule formation stage in Figure 7.9 is confined by stages 2 and 4.

Stage 4: Late-stage granitic melt may still exist; crystallization of nodules begins

According to Manning (1981) and Pichavant and Manning (1984), late-stage granitic melts may exist at temperatures as low as 450 to 500˚C. Tourmaline fluid inclusions from the Scrubber Granite had temperatures of homogenization between 282 and 456˚C, yielding the minimum temperatures at which crystallization took place. The crystallization of nodules may have commenced at higher temperatures. From stable isotope studies (Chapter 6), the temperature of crystallization of tourmalines was confined to 450-700˚C, confined by unrealistic low temperature stable isotope data and

the higher temperature pegmatite tourmaline data of Dyar et al. (1999). Thus, crystallization may occur over this temperature range.

Stage 5: Final crystallization of nodules (constrained by T_h temperatures)

As crystallization of the Scrubber Granite magma nears a critical point at which nearly all aqueous fluid has been separated from the crystallizing magma, the pockets are nearing complete crystallization. This temperature range is roughly constrained by the homogenization temperatures discussed above, giving a temperature range of roughly 280 to 450˚C for the minimum crystallization temperature.

7.6.2 Formation of various nodule morphologies

Possible controlling factors on the size and shape of the residual fluid pockets are summarized as follows (see Figure 7.10):

As the aqueous, volatile-rich pockets are presumably less dense than the surrounding crystallizing magma, they will rise through the magma chamber. However, the rise and crystallization of these pockets (bubbles) can be restricted by surrounding crystals in the crystallization interval; thus, the degree of crystallization in a discrete zone of the magma chamber may influence the overall shape of the nodule, depending on how it impedes the ascent of the bubble. Spherical nodules may represent volatile pockets that were surrounded by a crystal mush with a lower degree of crystallization, allowing the preferred globular shape to take form. Starburst nodules also formed the preferred spherical shape, and are characterized by dendritic to prismatic tourmaline crystals that extend out into the leucocratic halo regions.

Dense rosettes of tourmaline in spherical rosette nodules probably represent the last phase of crystallization within the fluid pocket, and may be similar to miarolitic cavities observed in the Seagull Batholith (Sinclair and Richardson, 1992; Samson and Sinclair, 1992). Although the tourmaline rosette nodules of the Scrubber Granite do not texturally resemble miarolitic cavities (i.e. do not contain void spaces filled with coarse crystals), the formation processes may be similar.

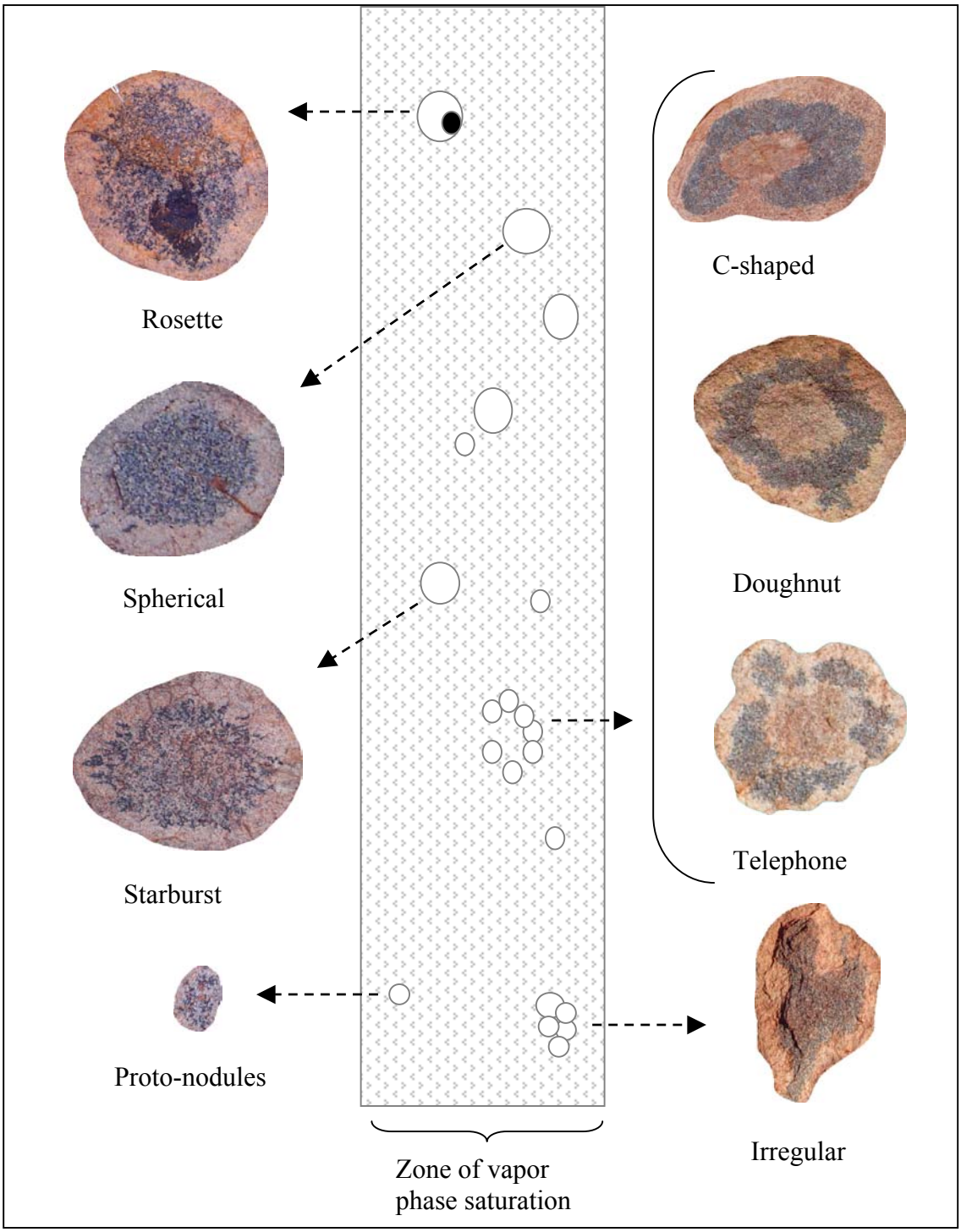

Figure 7.10: Relating the volatile phase exsolution model to the various nodule morphologies observed in the Scrubber Granite: spherical, tourmaline rosette, starburst, proto-nodules, C-shaped, or horseshoe, doughnut or flower-shaped, telephone-dial nodules, and irregular nodules.

Nodules of C-shaped/horseshoe, doughnut/flower-shaped and telephone dial morphologies may have formed by similar processes. Perhaps small spherical fluid pockets began to coalesce in a spherical array. Pockets that completely merged around a central region of host granite represent doughnut/flower-shaped nodules. C-shaped or horseshoe nodules represent pockets that merged in a semicircular fashion, thus only partially enclosing host granite zone, and the telephone dial nodules could represent the coalescence of pockets that did not successfully merge, thus forming a spherical array of individual nodules surrounded by separate halo zones. Other nodule textures in the Scrubber Granite support this theory of individual nodule pockets merging before or syn-crystallization, including the 'dumb-bell' shaped nodules in the center of Figure 1.1, merging starburst nodules in Figure 3.11B, and the nodule 'swarms' of Figure 3.14A and B.

Irregular nodules may represent pockets that were impeded from forming the preferred spherical shape due to a high degree of host granite crystallization immediately surrounding the pocket. These nodules could also represent volatile pockets that merged in an unusual fashion, giving rise to irregular nodule shapes. Proto-nodules possibly owe their small size to the small volatile pocket they formed from and lack of significant coalescence with surrounding pockets.

7.7 CLOSING STATEMENTS

Based on field observations, mineralogy, texture, and the results of whole rock and tourmaline chemistry, fluid inclusion microthermometry and stable and radiogenic isotope analyses, it is concluded that the tourmaline nodules of the Scrubber Granite formed from a late-stage B-rich volatile fluid phase that separated from the crystallizing magma. This volatile phase exsolved as buoyant bubbles, or pockets, from which the tourmaline nodules crystallized. This hypothesis is perhaps more encompassing than previous studies and is applicable to other nodule localities due to the focus on explaining the physical nature of the nodules.

Several common themes arose throughout the author's investigation into the occurrence and formation of nodules, miarolitic cavities and pegmatites. These features

are all typically associated with peraluminous, leucogranitic rocks that are occasionally associated with Sn-W or other mineralization, are shallowly emplaced (<2 or 3 km below surface), and are thus associated with low pressures (2 to 3 kbar). The formation and separation of a late-stage aqueous volatile phase from a crystallizing magma is a widely accepted geologic phenomenon; however, parameters associated with this event such as temperature, degree of crystallization, pressures and affect of host magma composition are poorly constrained in the literature.

REFERENCES

Babcock, R.S. 1973. Computational models of metasomatic processes. Lithos **6**, 279-290.

Barrett, T.J. and MacLean, W.H. 1991. Chemical, mass, and oxygen isotope changes during extreme hydrothermal alteration of an Archean rhyolite, Noranda, Quebec. Economic Geology **86**, 406-414.

Benard, F., Moutou, P, and Pichavant, M. 1985. Phase relations of tourmaline leucogranites and the significance of tourmaline in silicic magmas. Journal of Geology **93**, 271-291.

Bodnar,R.J. 2003. Introduction to fluid inclusions. In: Samson, I., Anderson, A., and Marshall, D. (eds.), Fluid inclusions: analysis and interpretation. Mineralogical Association of Canada Short course **32**, 1-9.

Bouvier, J.L., Sen Gupta, J.G., and Abbey, S. 1972. Use of an "automatic sulfur titrator" in rock and mineral analysis: determination of sulphur, total carbon and ferrous iron. Geological Survey of Canada Paper **72**-31.

Campbell, I.H., Lesher, C.M., Coad, P., Franklin, J.M., Gorton, M.P. and Thurston, P.C. 1984. Rare-earth element mobility in alteration pipes below massive Cu-Zn sulfide deposits. Chemical Geology **45**, 181-202.

Candela, P.A. 1991. Physics of aqueous phase evolution in plutonic environments. American Mineralogist **76**, 1081-1091.

Candela, P.A., and Blevin, P.L. 1995. Do some miarolitic granites preserve evidence of magmatic volatile phase permeability? Economic Geology **90**, 2310-2316.

Cawood, P.A. and Tyler, I.M. 2004. Assembling and reactivating the Proterozoic Capricorn Orogen: lithotectonic elements, orogenies, and significance. In: Assembling the Palaeoproterozoic Capricorn Orogen. Precambrian Research. **128/3-4**, 201-219.

Clayton, R.N., O'Neil, J.R., and Mayeda, T.K. 1972. Oxygen isotope exchange between quartz and water. Journal of Geophysical Research **77**, 3057-3067.

Clemens, J.D. and Wall, V.J. 1981. Origin and crystallization of some peraluminous (S-type) granitic magmas. Canadian Mineralogist **19**, 111-131.

Crawford, M.L. 1981. Phase equilibria in aqueous fluid inclusions. In: L.S. Hollister and M.L. Crawford (eds.), Short Course in Fluid Inclusions: Application to Petrology **6**, Mineralogical Association of Canada.

DePaolo, D.J. 1998. Neodymium isotope geochemistry. An introduction. Springer-Verlag. New York, N.Y. 187 pgs.

DePaolo, D.J., and Wasserburg, G.J. 1976. Nd isotopic variations and petrogenetic models. Geophysics Research Letters **3**, 249-252.

Dickin, A. 1995. Radiogenic isotope geology. Cambridge University Press. New York, N.Y. 490 pgs.

Dyar, M.D., Guidotti, C.V., Core, D.P, Wearn., K.M., Wise, M.A., Francis, C.A., Johnson, K., Brady, J.B., Robertson, J.D., and Cross, L.R. 1999. Stable isotope and crystal chemistry of tourmaline across pegmatite-country rock boundaries at Black Mountain and Mount Mica, southwestern Maine, U.S.A. European Journal of Mineralogy **11**, 281-294.

Etheridge, M.A., Rutland, R.W.R., and Wyborn, L.A.I. 1987. Orogenesis and tectonic process in the early to middle Proterozoic of Northern Australia. In: Kroner, A. (ed.), Proerozoic lithospheric evolution. Geodynamics Series **17**, 131-147.

Evans, D.A.D., Sircombe, K.N., Wingate, M.T.D., Doyle, M., McCarthy, M., Pidgeon, R.T., and Van Niekerk, H.S. 2003. Revised geochronology of magmatism in the western Capricorn Orogen at 1805-1785Ma: diachroneity of the Pilbara-Yilgarn collision. Australian Journal of Earth Sciences **50**, 853-864.

Faure, G. 1986. Principles of isotope geology. 2nd Edition, John Wiley and Sons, Inc. New York, 464 pgs.

Farmer, G.L. and D.J. DePaolo. 1997. Sources of Hydrothermal Components: Heavy Isotopes. In: Barnes, H.L. (ed.), The Geochemistry of Hydrothermal Ore Deposits, 3rd edition, Wiley Interscience, 31-61.

Gee, R.D. 1979. Structure and tectonic style of the Western Australian shield. Tectonophysics **58**, 327-369.

Gibson, H.L., Watkinson, D.H, and Comba, C.D.A. 1983. Silicification: hydrothermal alteration of an Archean geothermal system within the Amulet rhyolite formation, Noranda, Quebec. Economic Geology **78**, 954-971.

Goldstein, S., O'Nions, R.K. and Hamilton, P.J. 1984. A Sm-Nd study of atmospheric dusts and particulates from major river systems. Earth and Planetary Science Letters **70**, 221-236.

Grant, J.A. 1986. The isocon diagram-a simple solution to Gresens' equation for metasomatic alteration. Economic Geology **81**, 1976-1982.

Gresens, R.L. 1967. Composition-volume relationships of metasomatism. Chemical Geology **2**, 47-65.

Henry, D.J., and Guidotti, C.V. 1985. Tourmaline as a petrogenetic indicator mineral: an example from the staurolite-grade metapelites of NW Maine. American Mineralogist **70**, 1-15.

Hoefs, J. 1987. Stable isotope geochemistry. 3rd edition. Springer-Verlag, Berlin. 241 pgs.

Hoefs, J. 1997. Stable isotope geochemistry. 4th edition. Springer-Verlag, Berlin. 241 pgs.

Holtz, F., and Johannes, W. 1991. Effect of tourmaline on melt fraction and composition of first melts in quartzofeldspathic gneiss. European Journal of Mineralogy **3**, 527-536.

Jacobsen, S.B. and Wasserburg, G.J. 1980. Sm-Nd isotopic evolution of chondrites. Earth and Planetary Science Letters **50**, 139-155.

Jahns, R.H., and Burnham, C.W. 1969. Experimental studies of pegmatite genesis. I. A model for the derivation and crystallization of granitic pegmatites. Economic Geology **64**, 843-864.

Jankowitz, J.C. 1987. Petrochemistry of the Cnydas Subsuite. Bulletin of the Geological Survey no.87, Department of Mineral and Energy Affairs, Republic of South Africa, 38-44.

Jiang, S.Y., Han, F., Shen, J.Z., and Plamer, M.R. 1999. Chemical and Rb-Sr, Sm-Nd systematics of tourmaline from the Dashang Sn-polymetallic ore deposit, Guangxi Province, P.R.China. Chemical Geology **157**, 49-67.

King, R.W. 1990. Tourmaline from mesothermal gold deposits of the Superior Province, Canada. Textural, chemical and isotopic relationships. PhD. Thesis, 228 pgs. University of Saskatchewan, Saskatoon, Saskatchewan.

Kotzer, T.G., Kyser, T.K., King, R.W., and Kerrich, R. 1993. An empirical oxygen- and hydrogen-isotope geothermometer for quartz-tourmaline and tourmaline-water. Geochimica et Cosmochimica Acta **57**, 3421-3426.

Kretz, R. 1983. Symbols for rock-forming minerals. American Mineralogist **68**, 277-279.

LeFort, P. 1991. Enclaves of the Miocene Himalayan leucogranites. In: Enclaves and granite petrology. Didier and Barbain (eds.), 35-47.

Leitch, C.H.B, and Lentz, D.R. 1994. The Gresens approach to mass balance constraints of alteration systems: methods, pitfalls, examples. In: Lentz, D.R., ed., Alteration and alteration processes associated with ore-forming systems. Geological Association of Canada, Short Course Notes **11**, 161-192.

Lesher, C.M., Goodwin, A.M., Campbell, I.H., and Gorton, M.P. 1986. Trace element geochemistry of ore-associated and barren, felsic metavolcanic rocks in the Superior Province. Canadian Journal of Earth Sciences **23**, 222-237.

London, D. 1999. Stability of tourmaline in peraluminous granite systems: the boron cycle from anatexis to hydrothermal aureoles. European Journal of Mineralogy **11**, 253-262.

London, D. 1992. The application of experimental petrology to the genesis and crystallization of granitic pegmatites. Canadian Mineralogist **30**, 499-540.

London, D. 1986. Formation of tourmaline-rich gem pockets in miarolitic pegmatites. American Mineralogist, **71**, 396-405.

London, D., Morgan, G.B., and Wolf, M.B. 1996. Boron in granitic rocks and their contact aureoles. In: Grew, E.S., and Anovitz, L.M. (eds.), Boron Mineralogy, petrology and geochemistry. Reviews in Mineralogy **33**, 299-325.

London, D., Hervig, R.L., and Morgan, G.B. 1988. Melt-vapor solubilities and element partitioning in peraluminous granite-pegmatite systems: experimental results with Macusani glass at 200MPa. Contributions to Mineralogy and Petrology **99**, 360-373.

London, D., Morgan, G.B., and Hervig, R.L. 1989. Vapor saturated experiments with Macusani glass + H2O at 200 MPa, and the internal differentiation of granitic pegmatites. Contributions to Mineralogy and Petrology **102**, 1-17.

MacLean, W.H. 1990. Mass change calculations in altered rock series. Mineralium Deposita **25**, 44-49.

MacLean, W.H. 1988. Rare earth elements mobility at constant inter-REE ratios in the alteration zone at the Phelps Dodge massive sulfide deposit, Matagami, Quebec. Mineralium Deposita **23**, 231-238.

MacLean, W.H. 1984. Geology and ore deposits of the Matagami District. Canadian Institute of Mining and Metallurgy Special Volume **34**, 483-495.

MacLean, W.H., and Kranidiotis, P. 1987. Immobile elements as monitors of mass transfer in hydrothermal alteration: Phelps Dodge massive sulfide deposit, Matagami, Quebec. Economic Geology **82**, 951-962.

Manning, D.A.C. 1981. The effect of fluorine on liquidus phase relationships in the system Qz-Ab-Or with excess water at 1 kb. Contributions to Mineralogy and Petrology **76**, 206-215.

Martin, D.McB., and Thorne, A.M. 2004. Tectonic setting and basin evolution of the Bangemall Supergroup in the northwestern Capricorn Orogen. Precambrian Geology **128** 3-4 385-409.

Myers, J.S., Shaw, R.D., and Tyler, I.M. 1996. Tectonic evolution of Proterozoic Australia. Tectonics **15**, 6, 1431-1446.

Nabelek, P.I., Russ-Nabelek, C., and Denison, J.R. 1992. The generation and crystallization conditions of the Proterozoic Harney Peak Leucogranite, Black Hills, South Dakota, USA: petrologic and geochemical constraints. Contributions to Mineralogy and Petrology **110**, 173-191.

Nemec, D. 1975. Genesis of tourmaline spots in leucocratic granites. Neues Jahrbuch Mineralogic Monatshefte **7**, 308-317.

Occhipinti, S.A., and Sheppard, S. 2001. Geology of the Glenburgh 1:100 000 sheet. Western Australia Geological Survey. 1: 100 000 Geological Series Explanatory Notes, 37 pgs.

Occhipinti, S.A., Sheppard, S., Passchier, C., Tyler, I.M., and Nelson, D.R. 2004. Palaeoproterozoic crustal accretion and collision in the southern Capricorn Orogen: the Glenburgh Orogeny. *In* Assembling the Palaeoproterozoic Capricorn Orogen. Precambrian Research **128/3-4**, 237-255.

Occhipinti, S.A., Sheppard, S., Myers, J.S., Tyler, I.M., and D.R. Nelson. 2001. Archaean and Palaeoproterozoic geology of the Narryer Terrane (Yilgarn Craton) and the southern Gascoyne Complex (Capricorn Orogen) Western Australia- a field guide. Western Australia Geological Survey. Record 2001/8, 70 pgs.

Occhipinti, S.A., Sheppard, S., Nelson, D.R., Myers, J.S., and Tyler, I.M. 1998. Syntectonic granite in the southern margin of the Palaeoproterozoic Capricorn Orogen, Western Australia. Australian Journal of Earth Sciences **45**, 509-512.

O'Neil, J.R., Clayton, R.N., and Mayeda, T.K. 1969. Oxygen isotope fractionation in divalent metal carbonates. Journal of Chemical Physics **51**, 5547-5558.

Pan, Y., Fleet, M.E., and Barnett, R.L. 1994. Rare-earth mineralogy and geochemistry of the Mattagami Lake volcanogenic massive sulfide deposit, Quebec. Canadian Mineralogist **32**, 133-147.

Pitchavant, M., and Manning, D. 1984. Petrogenesis of tourmaline granites and topaz granites; the contribution of experimental data. Physics of the Earth and Planetary Interiors **35**, 31-50.

Potter, R.W., and Brown, D.L. 1977. The volumetric properties of aqueous sodium chloride solutions from 0 to 500˚C at pressures up to 2000 bars based on a regression of available data in the literature. Preliminary Steam Tables for NaCl solutions. USGS Bulletin 1421-C.

Roedder, E. 1984. Fluid Inclusions. Reviews in Mineralogy **12**. Bookcrafters, Inc., 644 pgs.

Rollinson, H. 1995. Using geochemical data: evaluation, presentation, interpretation. Longman Group UK Limited, England, 352 pgs.

Rozendaal, A. and Bruwer, L. 1995. Tourmaline nodules: indicators of hydrothermal alteration and Sn-An-(W) mineralization in the Cape Granite Suite, South Africa. Journal of African Earth Sciences **21/1**, 141-155.

Rozendaal, A., Bruwer, L., and Scheepers, R. 1995. Tourmaline nodules as indicators of Sn-Zn-(W) mineralization in the Cape Granite Suite, South Africa. Mineral Deposits, Pasava, Kribek & Zak (eds.), 511-513.

Rutland, R.W.R. 1973. Tectonic evolution of the continental crust in Australia. In: Tarling, D.H. and Runcorn, S.K. (eds.), Continental drift, seafloor spreading and plate tectonics: implications for the Earth Sciences, 1003-1025.

Samson, I.M., and Sinclair, W.D. 1992. Magmatic hydrothermal fluids and the origin of quartz-tourmaline orbicles in the Seagull Batholith, Yukon Territory. Canadian Mineralogist **30,** 937-954.

Scaillet, B., Pichavant, M., and Roux, J. 1995. Experimental crystallization of leucogranite magmas. Journal of Petrology **36**, 3, 663-705.

Sinclair, D.W., and Richardson, J.M. 1992. Quartz-tourmaline orbicules in the Seagull Batholith, Yukon Territory. Canadian Mineralogist **30**, 923-935.

Shepherd, T.J., Rankin, A.H., and Alderton, D.H.M. 1985. A Practical Guide to Fluid Inclusion Studies. Chapman and Hall, New York, 239 pgs.

Sheppard, S. 2004. Unraveling the complexity of the Gascoyne Complex. Western Australia Geological Survey Record 2004/S, 26-28.

Sheppard, S., Occhipinti, S.A., and Tyler, I.M. 2003. The relationship between tectonism and composition of granitoid magmas, Yarlarweelor Gneiss Complex, Western Australia. Lithos **66**, 133-154.

Smithies, R.H. 1988. The geology and alteration/mineralization of the Van Rooi's Vley W/Sn deposit, Namaqua Metamorphic Complex, South Africa. M.Sc. thesis, 123 pgs. Rhodes University, Grahamstown, South Africa.

Sun, S.S. and McDonough, W.F. 1989. Chemical and isotopic systematics of oceanic basalts: implications for mantle composition and processes. In: Saunders A.D. and Norry M.J. (eds.), Magmatism in ocean basins. Geological Society of London Special Publication **42**, 313-345.

Taylor, R.P., Ikingura, J.R., Fallick, A.E., Huang, Yiming, and Watkinson, D.H. 1992. Stable isotope compositions of tourmalines from granites and related hydrothermal rocks of the Karagwe-Ankolean belt, northern Tanzania. Chemical Geology (Isotope Geoscience Section) **94**, 215-227.

Tsang, T. and Ghose, S. 1973. Nuclear magnetic resonance of ^{1}H, ^{7}Li, ^{11}B, ^{23}Na and ^{27}Al in tourmaline (elbaite). American Mineralogist **58**, 224-229.

Tyler, I.M., and Thorne, A.M. 1990. The northern margin of the Capricorn Orogen, Western Australia-an example of an Early Proterozoic collision zone. Journal of Structural Geology **12**, 5/6, 685-701.

Williams, S.J. 1986. Geology of the Gascoyne Province Western Australia. Geological Survey of Western Australia Report **15**.

Wolf, M.B., and London, D. 1997. Boron in granitic magmas: stability of tourmaline in equilibrium with biotite and cordierite. Contributions to Mineralogy and Petrology **130**, 12-30.

Valley, J.W., Taylor, H.P. Jr., O'Neil, J.R. *eds*. 1986. Stable isotopes in high temperature geological processes. Mineralogical Society of America. Reviews in Mineralogy **16**, 570 pgs.

Zheng, Y.F. 1993. Calculation of oxygen isotope fractionation in hydroxyl-bearing silicates. Earth and Planetary Science Letters **120**, 247-263.

APPENDIX A
STOP LOCATION INFORMATION

Easting	Northing	Stop No.	Sample No.	Nodule Abundance	Nature of Granite	Strike/dip
392342	7228626	1	130301	S	nodular granite	160/NA
392331	7228581	2		N	granite	155/NA
392314	7228624	3	130302	M	nodular granite	150/NA
392302	7228648	4		N	granite	150/NA
392282	7228667	5		A	nodular granite	150/NA
392275	7228692	6		M	nodular granite	155/NA
392242	7228721	7		S	nodular granite	160/NA
392221	7228700	8		S	nodular granite	
392290	7228601	9		A	nodular granite	
392219	7228486	10	130303	A	nodular granite	
392219	7228486	10	130317*	A	nodular granite	
392219	7228486	10	130320*	A	nodular granite	140/NA
392158	7228566	11	130322*	A	nodular granite	125/NA
392158	7228566	11	130323*	A	nodular granite	
392188	7228610	12		M	nodular granite	150/NA
392203	7228620	13		S	nodular granite	
392211	7228611	14		A	nodular granite	
392231	7228557	15		A	nodular granite	
392295	7228468	16		A	nodular granite	
392344	7228494	17		M	nodular granite	
392363	7228552	18		S	nodular granite	
392364	7228413	19		S	nodular granite	
392336	7228361	20		M	nodular granite	
392291	7228390	21		M	nodular granite	
392267	7228342	22		S	nodular granite	150/81SW
392340	7228356	23		M	nodular granite	
392417	7228364	24		A	nodular granite	
392331	7228367	25		S	nodular granite	
392208	7228338	26		S	nodular granite	
392179	7228299	27	130324*	M	porphyritic granite	155/84SW
392131	7228308	28		M	porphyritic granite	150/87SW
392112	7228296	29		M	porphyritic granite	150/87SW
391974	7228240	30	130321*	N	granite	
391914	7228233	31		M	nodular granite	150/NA
391854	7228223	32		N	granite	

Easting	Northing	Stop No.	Sample No.	Nodule Abundance	Nature of Granite	Strike/dip
391804	7228191	33		N	granite	
391753	7228161	34		N	granite	
391622	7228047	35		M	nodular granite	
392101	7228436	36		M	porph. nodular granite	150/87SW
392038	7228397	37		A	porph. nodular granite	150/87SW
392012	7228332	38		N	porph. granite	
391987	7228423	39		S	porph. nodular granite	140/84SW
392161	7228447	40		M	nodular granite	
392404	7228462	41		N	granite	
392425	7228414	42		S	nodular granite	
392440	7228263	43		S	nodular granite	150/NA
392447	7228194	44		S	nodular granite	
392180	7228132	45		S	nodular granite	155/80SW
392196	7228023	46		M	nodular granite	
391984	7227875	47		N	granite	
391752	7228064	48		N	granite	140/80SW
391868	7228110	49		N	granite	
391699	7228385	50		S	nodular granite	150/75SW
391390	7228254	51		S	nodular granite	
391432	7228376	52		N	granite (coarse)	
391455	7228406	53		S	nodular granite	
391394	7228538	54		N	granite	
391465	7228724	55		N	porphyritic granite	
391493	7228789	56		N	granite	
391699	7228880	57		M	nodular granite	
391847	7229013	58		M	nodular granite	
391880	7228495	59		M	nodular granite	140/88SW
391939	7228545	60		N	porphyritic granite	145/84SW
391949	7228586	61		N	porphyritic granite	145/87SW
391969	7228666	62		M	porph. nodular granite	
392090	7228714	63		M	porph. nodular granite	
392060	7228874	64		M	porph. nodular granite	
391968	7228820	65	130318*	A	nodular granite	150/87SW
391850	7229010	66		M	nodular granite	150/86SW
391742	7228867	67		M	porph. nodular granite	145/87SW
391201	7228792	68		N	porph. granite	135/90
391233	7228736	69		N	porph. granite	135/85SW
391238	7228679	70		S	porph. nodular granite	140/NA
391223	7228659	71		N	porphyritic granite	135/NA

Easting	Northing	Stop No.	Sample No.	Nodule Abundance	Nature of Granite	Strike/dip
391171	7228677	72		S	porph. nodular granite	135/85SW
391222	7228504	73		N	granite	
391256	7228442	74		N	granite	
391155	7228448	75		N	intense silicification	
391294	7228528	76		N	granite	135/90
391395	7228631	77		N	granite	135/90
391581	7228824	78		S	nodular granite	140/87SW
391610	7228763	79		A	porph. nodular granite	140/80SW
391622	7228741	80		M	porph. nodular granite	140/80SW
391663	7228740	81		A	nodular granite	140/80SW
391422	7228575	82		N	granite	145/84SW
391484	7228514	83		N	granite	145/84SW
391547	7228634	84		N	granite	145/87SW
391609	7228744	85		N	granite	
391803	7228910	86		M	porph. nodular granite	155/85SW
391829	7228962	87		A	nodular granite	140/85SW
391843	7228909	88		A	weathered out nodules	140/84SW
391921	7228883	89		A	nodular granite	145/84SW
391972	7228815	90		A	nodular granite	140/NA
391963	7228755	91		S	nodular granite	
391969	7228714	92	130304	A	weathered out nodules	
391969	7228714	92	130305	A	weathered out nodules	
391969	7228714	92	130308	A	weathered out nodules	
391969	7228714	92	130309	A	weathered out nodules	
391937	7228604	93		M	porph. nodular granite	145/85SW
391531	7228735	94		N	porphyritic granite	145/83SW
391348	7228774	95		N	granite	
393268	7227054	96		N	granite	135/NA
393216	7226977	97		N	granite	135/NA
393177	7226975	98		N	granite	135/NA
393067	7226870	99		N	granite	155/76SW
393027	7226832	100		N	granite	145/SW
392991	7226876	101		S	nodular granite	
393010	7226919	102		N	granite	145/81SW
393034	7226960	103		M	nodular granite	145/82SW
393053	7226989	104		M	nodular granite	
393225	7227081	105		M	nodular granite	115/NA
393237	7227154	106		A	nodular granite	140/NA
393104	7227182	107		S	nodular granite	

Easting	Northing	Stop No.	Sample No.	Nodule Abundance	Nature of Granite	Strike/dip
393191	7227245	108		A	nodular granite	140/NA
393160	7227292	109		A	nodular granite	140/NA
393168	7227356	110		A	nodular granite	130/NA
393150	7227469	111		A	nodular granite	155/90
393268	7227360	112		M	nodular granite	155/90
393245	7227165	113	130319*	M	nodular granite	135/78SW
393245	7227165	113	130315*	M	nodular granite	135/78SW
393213	7227196	114		M	nodular granite	135/78SW
393228	7227181	115		M	nodular granite	135/78SW
393373	7227348	116		S	nodular granite	145/74SW
393262	7227227	117		A	nodular granite	130/80SW
393387	7227490	118		N	granite	145/82SW
393357	7227608	119		N	granite	145/88SW
393173	7227584	120		M	nodular granite	140/83SW
393065	7227593	121		N	granite	145/85SW
393066	7227537	122		M	nodular granite	145/85SW
393034	7227308	123	130310	A	nodular granite	
392897	7227396	124		M	nodular granite	140/NA
392675	7227131	125		N	granite	
392675	7227142	126		S	nodular granite	
392354	7227200	127		S	nodular granite	155/NA
392440	7227357	128		M	nodular granite	140/85SW
392577	7227480	129		S	nodular granite	
392776	7227580	130		A	nodular granite	130/NA
392872	7227438	131		N	granite	
393192	7227713	132		N	granite	135/90
393007	7227920	133		S	nodular granite	145/90
392976	7228062	134		N	granite	145/71SW
392884	7228061	135		M	nodular granite	135/NA
392734	7227978	136		N	granite	
392686	7227934	137		A	nodular granite	135/NA
392719	7227823	138		M	nodular granite	150/NA
392798	7227723	139		M	nodular granite	
392937	7227758	140		M	nodular granite	145/NA
393195	7227596	141		S	nodular granite	145/NA
393728	7227068	142		N	granite	
393737	7226953	143		N	granite	
393819	7227003	144		S	nodular granite	140/NA
393835	7226934	145		N	granite	

Easting	Northing	Stop No.	Sample No.	Nodule Abundance	Nature of Granite	Strike/dip
393912	7226957	146		N	granite	
393822	7226808	147		N	granite	
393726	7226809	148		N	granite	
393644	7226561	149		N	granite	
393929	7226610	150		N	granite	
393912	7226408	151		N	massive granite	140/78SW
393986	7226504	152		N	massive granite	
394163	7226699	153		N	massive granite	
394193	7226751	154		M	nodular granite	
394069	7226787	155		N	massive granite	
394328	7226685	156		A	nodular granite	145/71SW
394362	7226513	157		N	granite	
394330	7226501	158		M	nodular granite	
394364	7226399	159		N	granite	
394295	7226304	160		N	granite	130/73SW
394386	7226284	161		S	nodular granite	
394543	7226199	162		S	nodular granite	
394530	7226324	163		N	granite	135/90
394426	7226569	164		N	granite	
394363	7226886	165		N	gneiss	135/78SW
394599	7226901	166		N	gneiss	135/78SW
394548	7226725	167		N	coarse granitoid	
394650	7226998	168		N	felsic igneous	
394652	7227126	169		N	coarse granitoid	
394585	7227090	170		N	metapelite	
394580	7227037	171		N	felsic igneous	
394603	7227065	172	130311	N	felsic igneous	
391012	7228452	173	130312	N	felsic igneous	
391006	7228454	174	130313	N	felsic igneous	
390978	7228433	175	130314	N	felsic igneous	
390818	7228566	176		N	felsic igneous	
390941	7228556	177		N	felsic igneous	
392241	7228521	178		S	nodular granite	
391793	7228211	179		N	granite	150/78SW
391737	7228144	180		A	nodular granite	145/78SW
391654	7228098	181		S	nodular granite	
391620	7228057	182		A	nodular granite	
391618	7228035	183	130316*	A	nodular granite	
391690	7227951	184		A	nodular granite	

Extra Samples from GSWA

Easting	Northing	Stop No.	Sample No.	Nodule Abundance	Nature of Granite	Strike/dip
N/A	N/A	N/A	159790	N/A	N/A	N/A
			159791A	N/A	N/A	N/A
			159791E	N/A	N/A	N/A

* = Sample from blast site
N/A = No data available
S = Sparse nodules
M = Moderate nodules
A = Abundant nodules

Note: Samples 130307 and 130308 are of a granodiorite from outside the Scrubber Granite region.

APPENDIX B

MAPS OF THE SCRUBBER GRANITE

The following maps of the Scrubber Granite were generated in ArcView GIS 3.3. The outline of the three lobes of the Scrubber Granite and the position of all stop locations were compiled by the GSWA. Using these files as a template, the author has created several map layers highlighting data collected in the field, including sample locations, structural features, and nodule distribution, abundance, morphology and size.

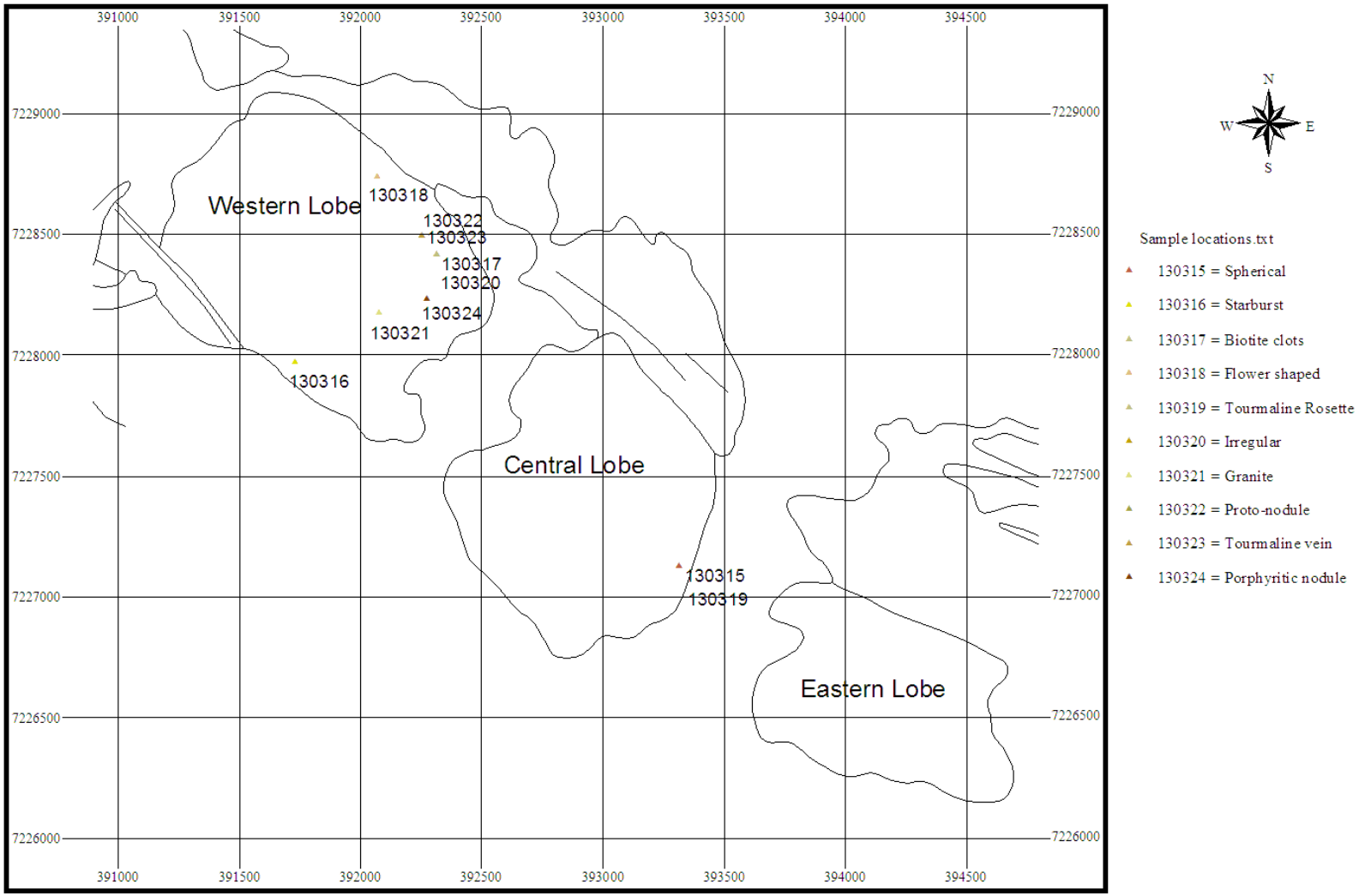

Figure B.1: Sample locations across the three lobes of the Scrubber Granite.

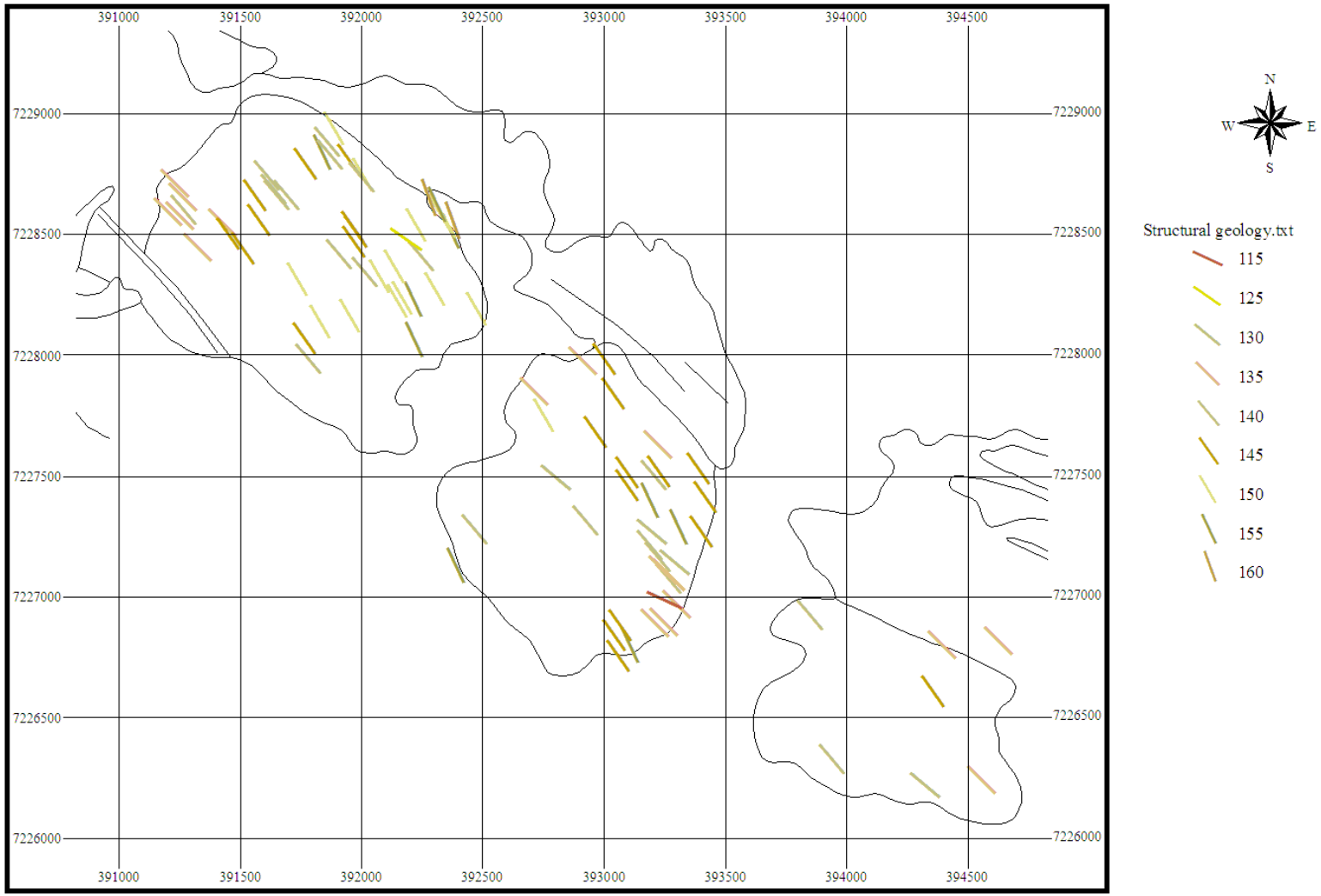

Figure B.2: Alignment of nodules, veins, shear zones and foliations. Legend indicates alignment direction in degrees.

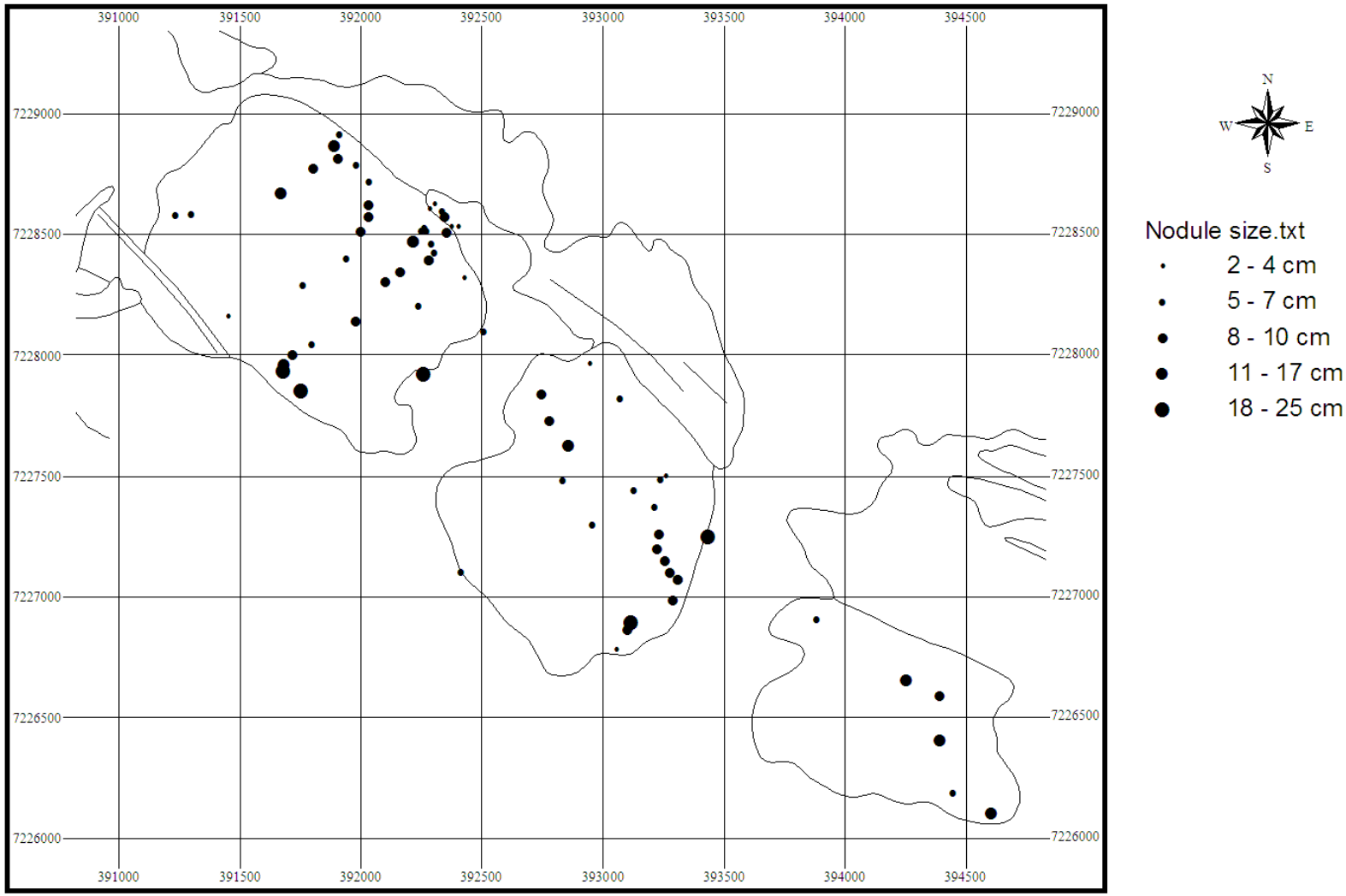

Figure B.3: Variation in nodule size across the Scrubber Granite.

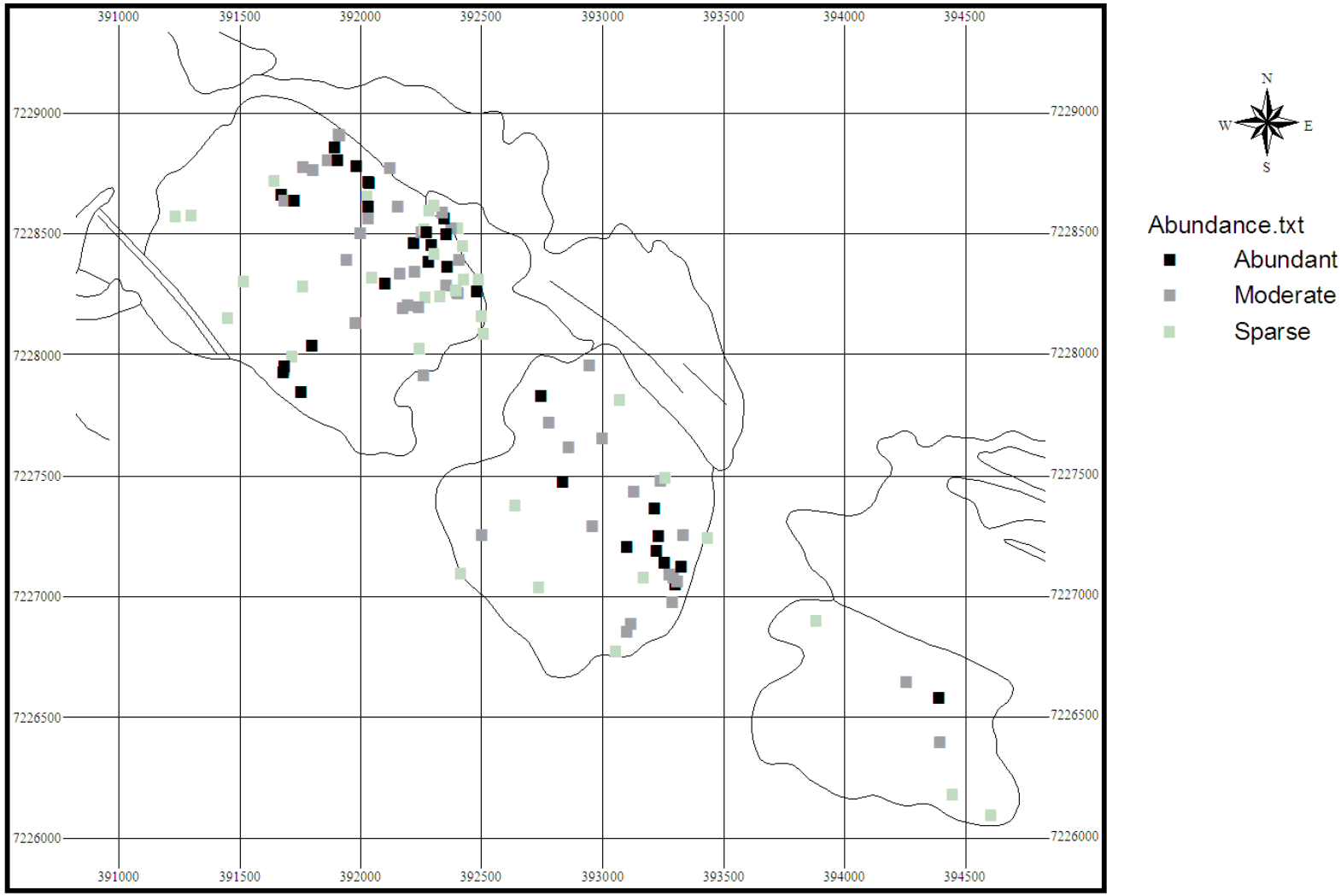

Figure B.4: Nodule abundance across the Scrubber Granite.

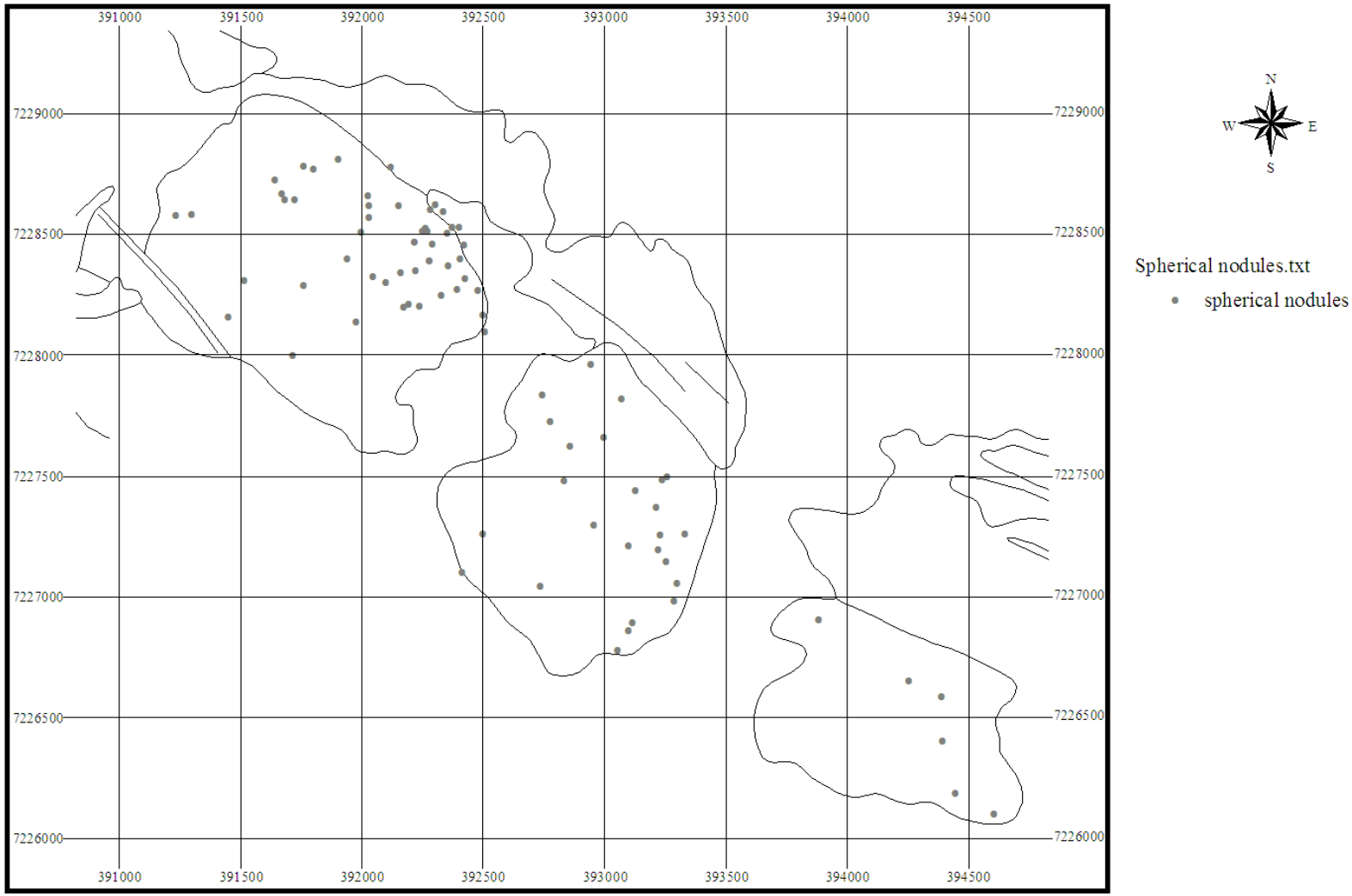

Figure B.5: Distribution of spherical to elongate nodules across the Scrubber Granite.

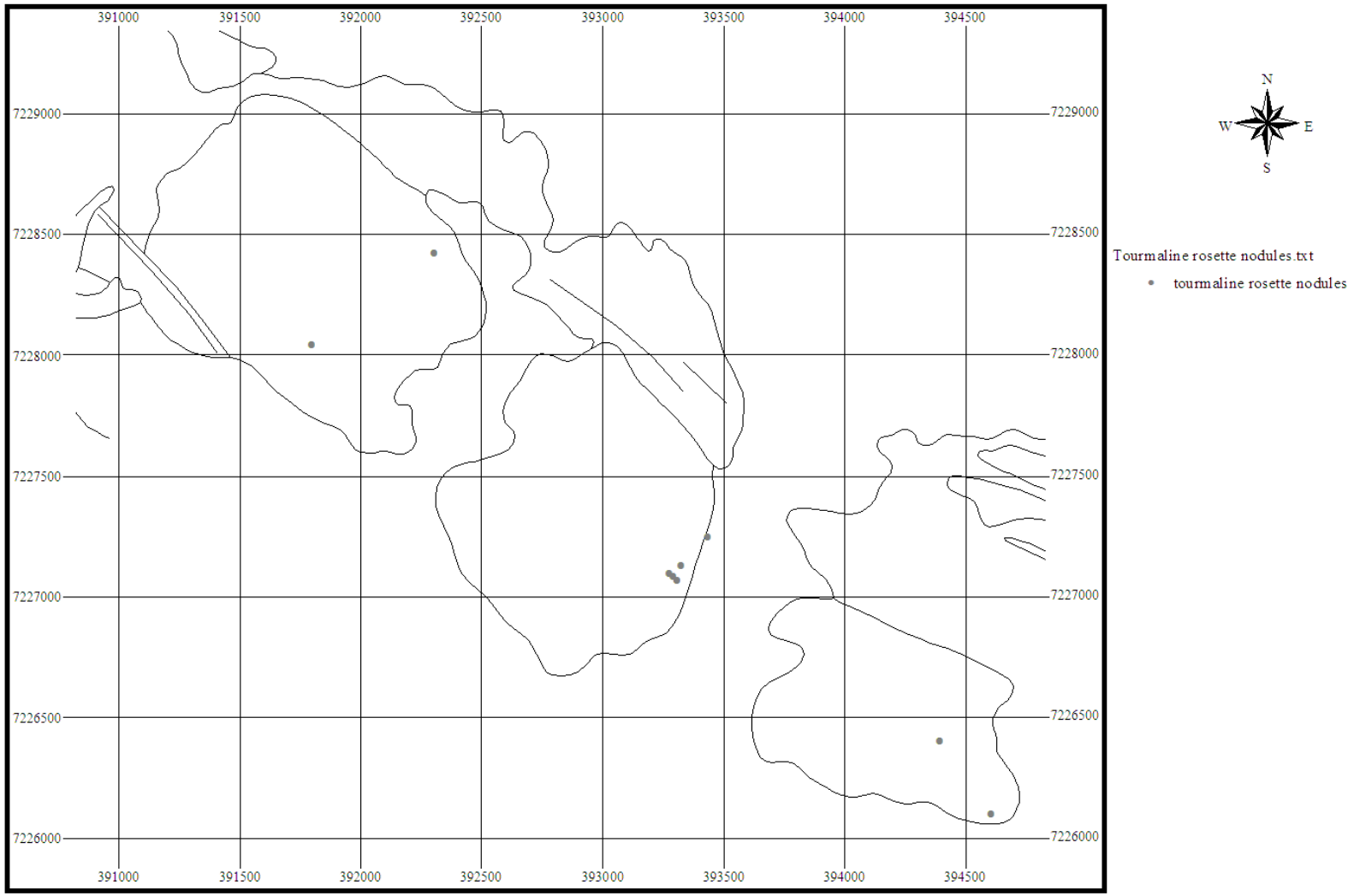

Figure B.6: Distribution of tourmaline rosette nodules across the Scrubber Granite.

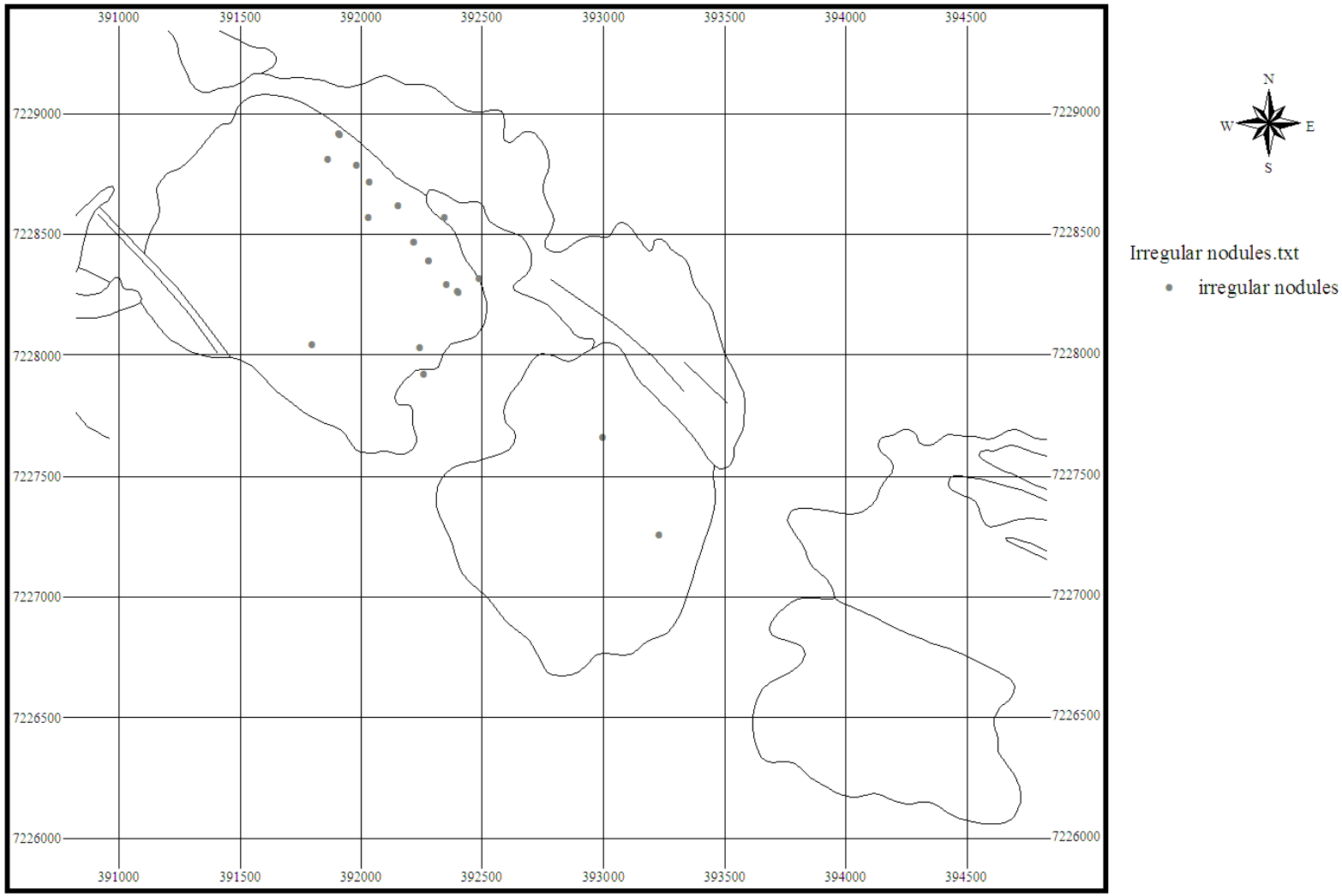

Figure B.7: Distribution of irregular nodules across the Scrubber Granite.

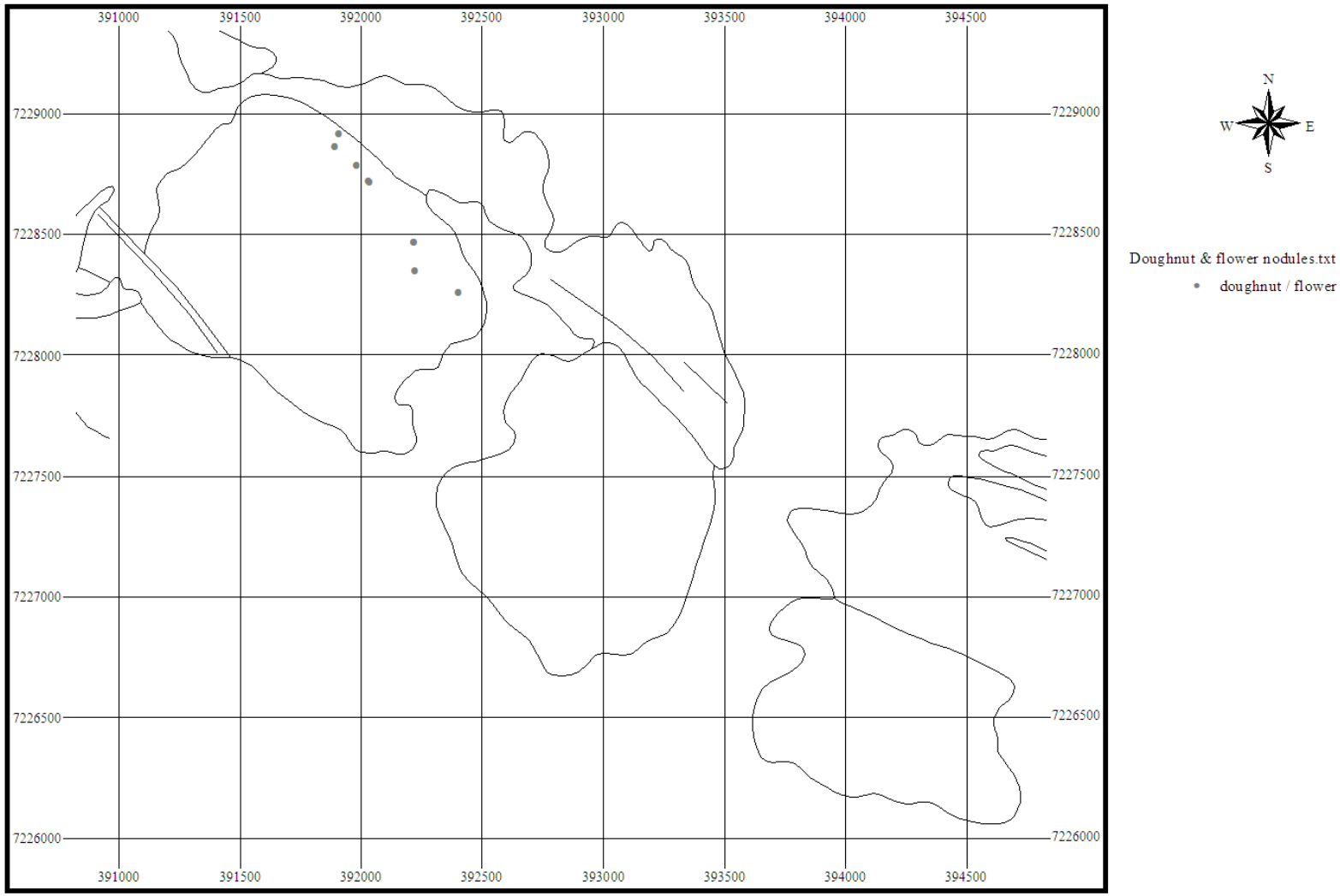

Figure B.8: Distribution of doughnut and flower-shaped nodules across the Scrubber Granite.

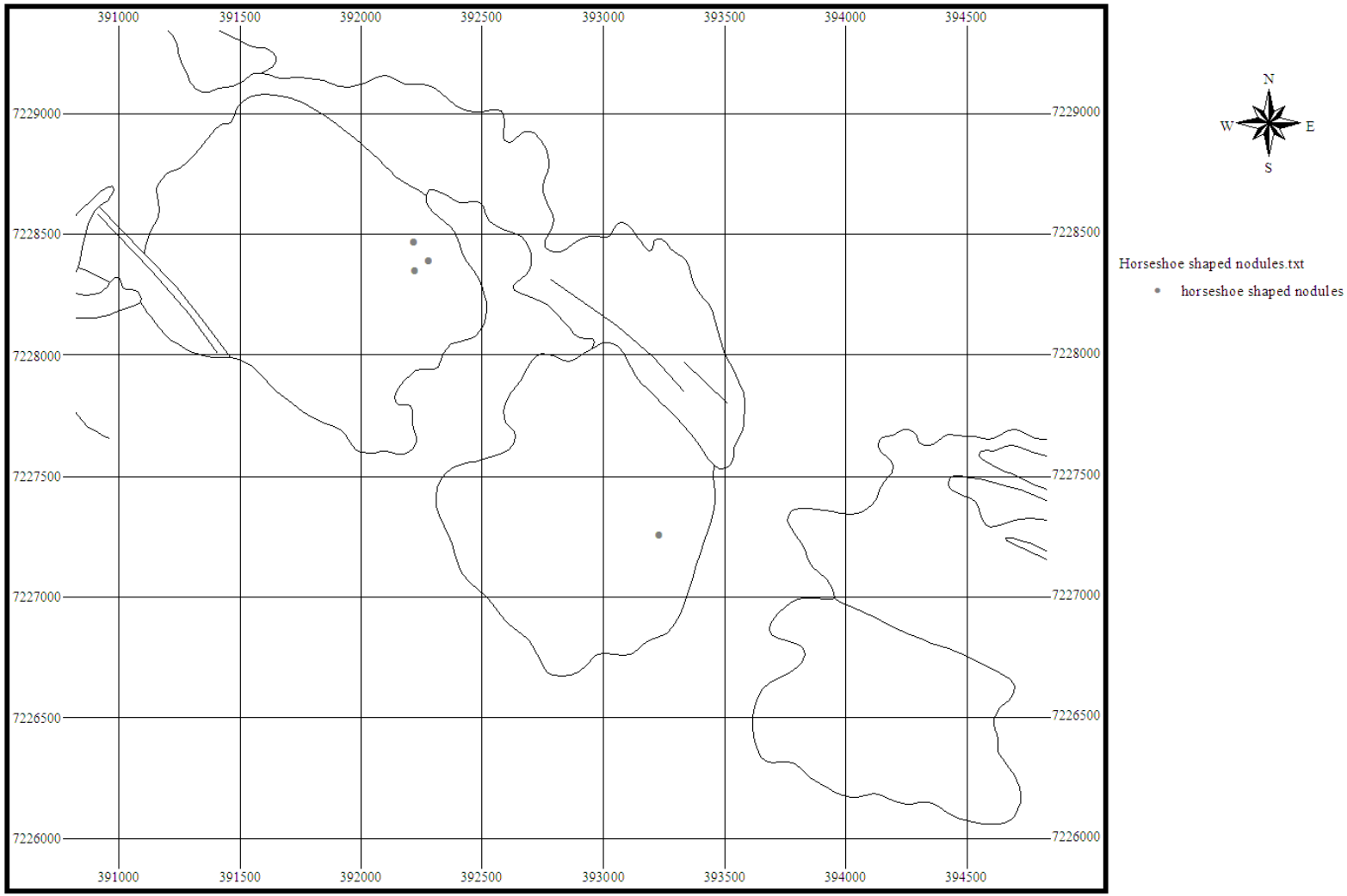

Figure B.9: Distribution of horseshoe and C-shaped nodules across the Scrubber Granite.

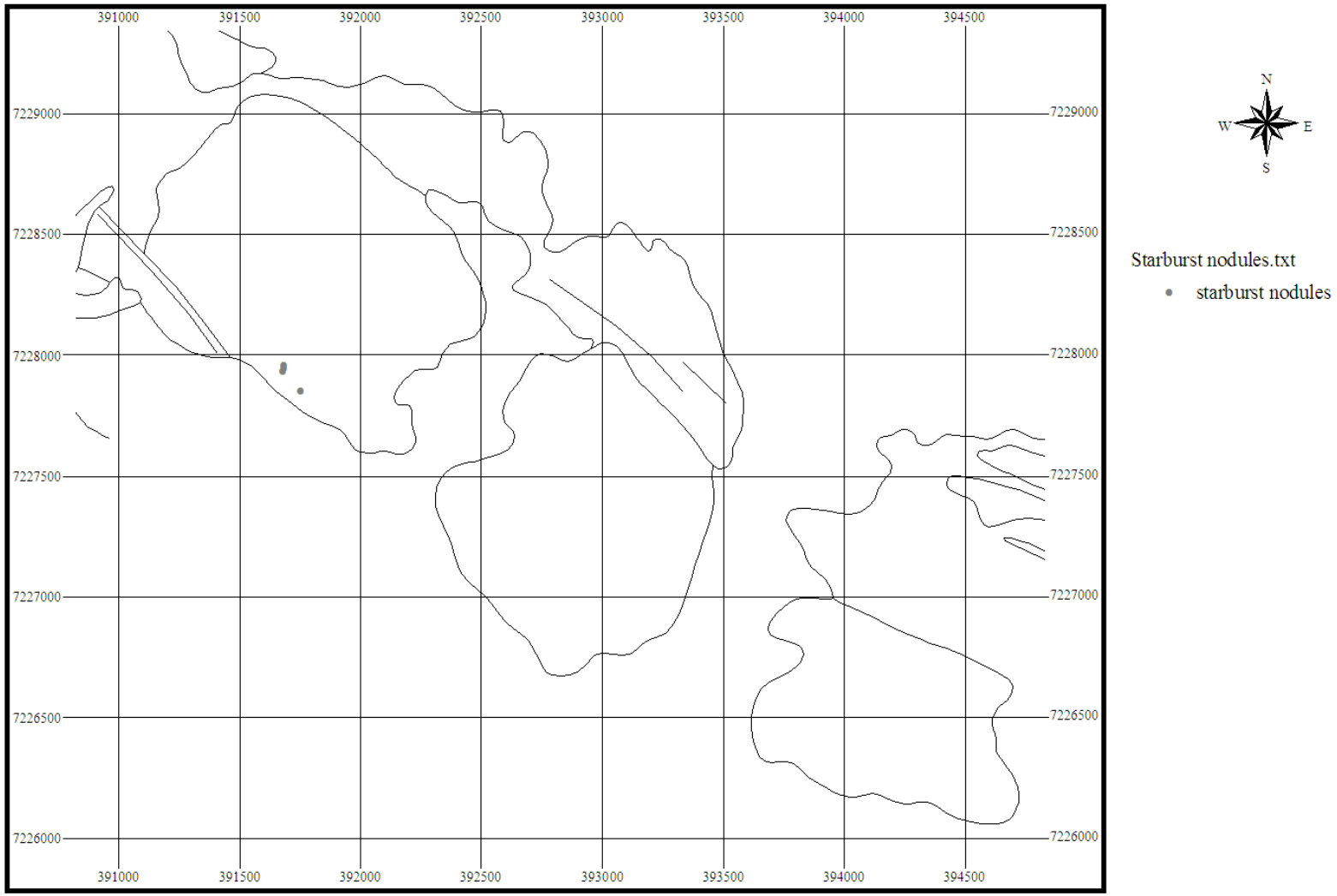

Figure B.10: Distribution of starburst nodules across the Scrubber Granite.

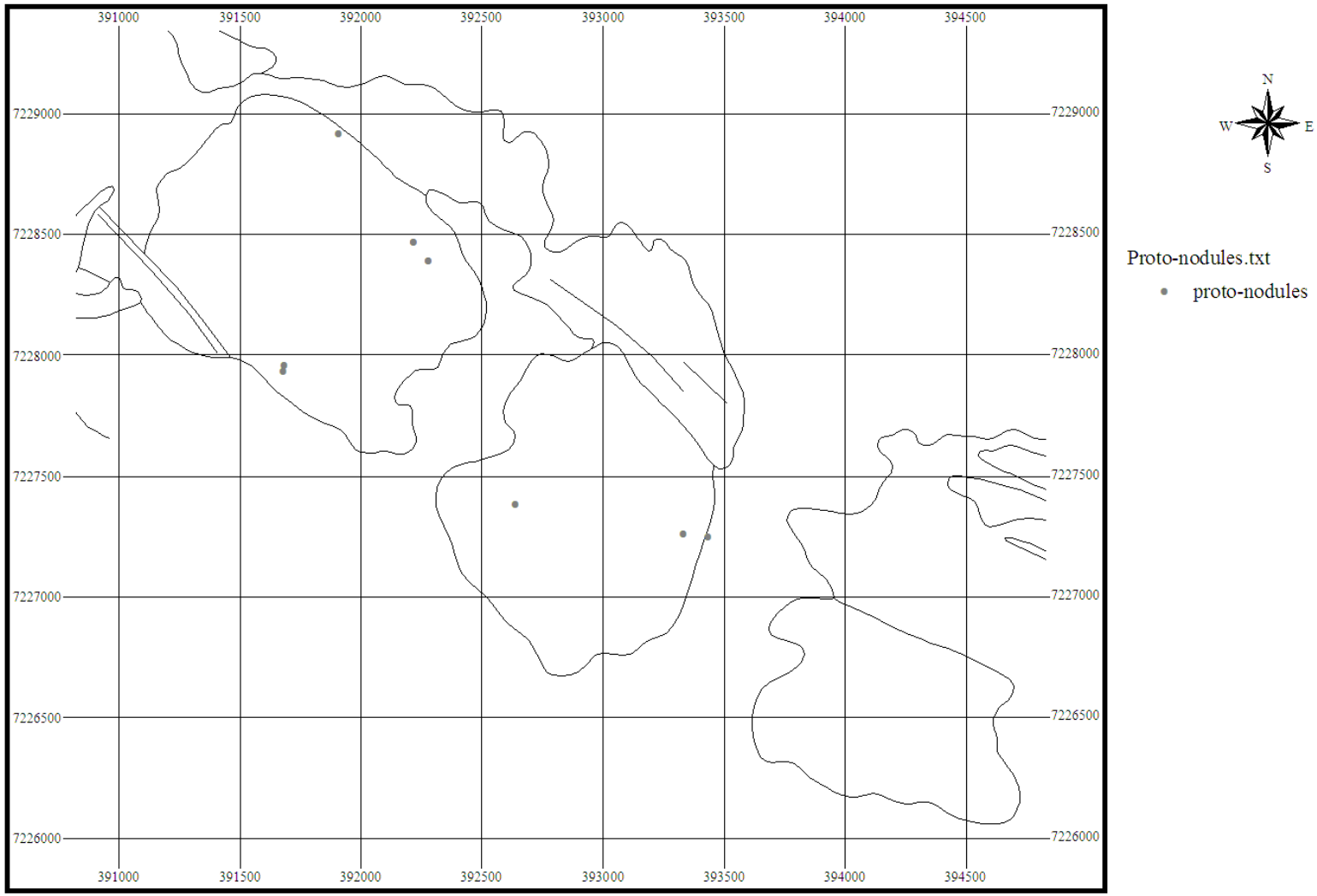

Figure B.11: Distribution of proto-nodules across the Scrubber Granite.

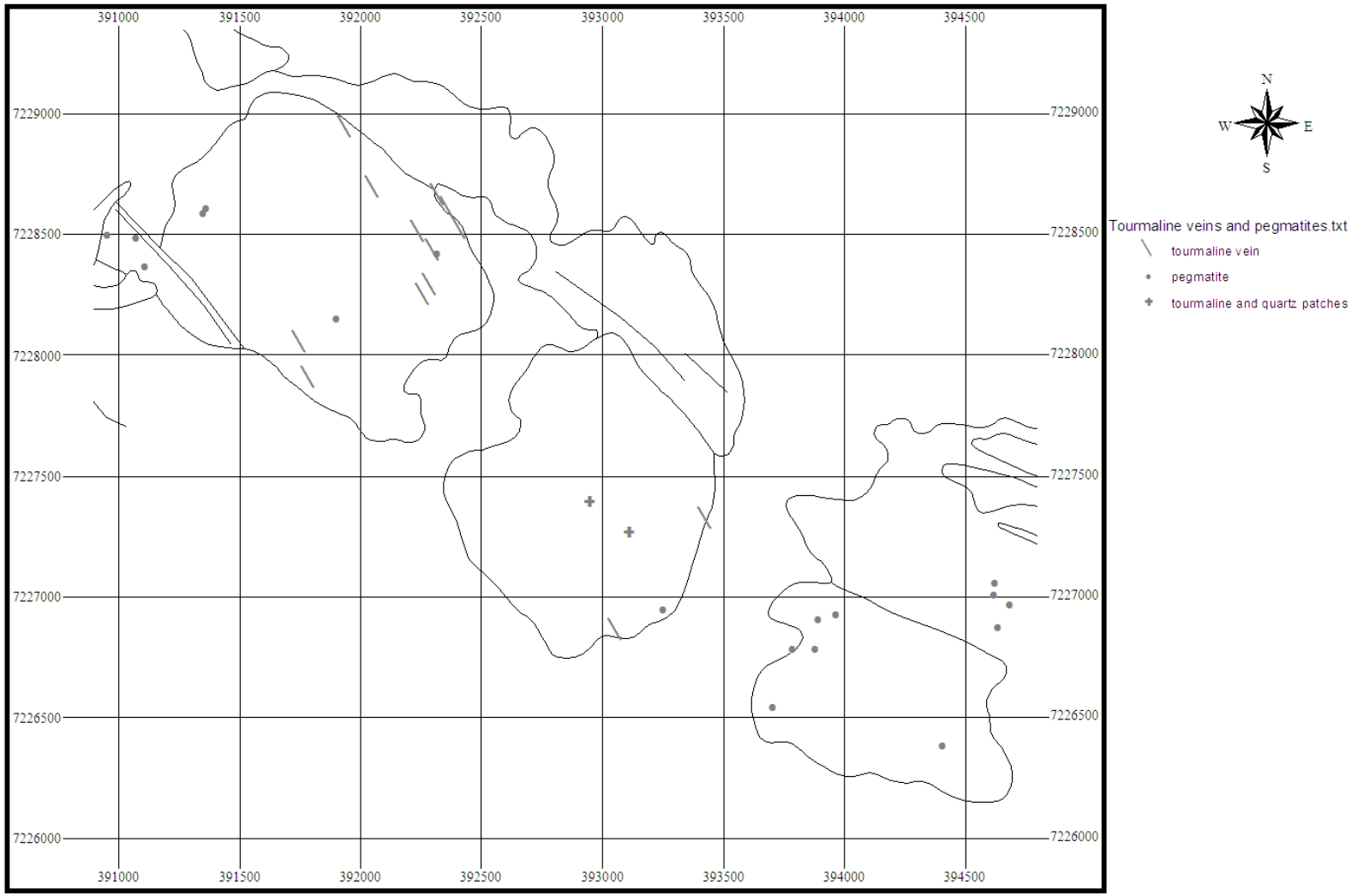

Figure B.12: Distribution of tourmaline veins, pegmatites, and quartz-tourmaline patches across the Scrubber Granite.

APPENDIX C

PETROGRAPHIC DESCRIPTIONS

130315- Spherical nodule with halo clots

Hand Specimen Description

This massive granite host rock contains a spherical nodule that is approximately 5cm in diameter. The halo material is approximately 2.5cm thick, and contains biotite clots 0.1 to 0.5cm in length. A weak foliation is visible, defined by biotite clots in the host granite and halo regions. Irregular tourmaline crystals in the core zone are aligned parallel to this foliation.

Mineralogy

HOST GRANITE	%	HALO	%	CORE	%
Quartz	60	Quartz	55	Quartz	55
Microcline	20	Microcline	20	Tourmaline	30
Albite	10	Albite	10	Albite	8
Biotite	8	Biotite	8	Microcline	5
Accessory phases*	2	Muscovite/sericite	5	Accessory phases*	2
Opaques	tr	Accessory phases*	2	Biotite	tr
				Muscovite	tr

*Monazite, apatite and zircon are included in quartz crystals throughout all zones.
This is a polished thin section. Opaque minerals did not reflect light.
tr = trace amounts

Mineral Descriptions

HOST GRANITE

Quartz — Quartz crystals vary from 0.10–0.80mm in diameter. They form interlocking polycrystalline aggregates that display a mosaic texture. Quartz aggregates occur adjacent to microcline, albite and muscovite, and are roughly parallel to the weak foliation. Quartz crystals are moderately included with monazite, apatite and zircon grains ranging from 0.02-0.1mm in diameter.

Microcline — Microcline crystals range from 0.4-3.20mm in length and are tabular in form. They are in intergrown with albite and quartz crystals. Microcline crystals are moderately included with muscovite flakes 0.03–0.2mm in length and albite crystals 0.5mm in diameter. These crystals are randomly distributed throughout the groundmass.

Albite — Albite crystals are tabular and range from 0.8-1.80mm in length. They are intergrown with microcline and quartz crystals. Albite crystals are highly included with muscovite flakes 0.03-0.5mm in length. These crystals are randomly distributed throughout the groundmass.

Biotite — Biotite flakes define a weak foliation throughout the host rock. They are a green-brown color in plane-polarized light. Individual flakes range from 0.1-0.5mm in length, and form 0.3-4.00mm clots with muscovite/sericite throughout the groundmass. Clots contain 80% biotite and 20% muscovite/sericite, and appear to overprint the quartz aggregates and feldspars in the groundmass.

Muscovite/ sericite — Muscovite/sericite flakes range from 0.02-0.6mm in length. They occur in clots along with biotite flakes, and also occur as inclusions in albite crystals.

Opaques — Opaque mineral grains range from 0.05-0.10mm in diameter. The grains are disseminated throughout the rock, and show no reflectance under reflected light.

HALO

Quartz — Quartz crystals range from 0.10-1.20mm in diameter. They form interlocking polycrystalline aggregates that display a mosaic texture. These aggregates occur adjacent to microcline, albite and biotite clots, and are roughly parallel to the weak foliation. Quartz crystals are moderately included with monazite, apatite and zircon grains ranging from 0.02-0.1mm in diameter.

Microcline — Microcline crystals range from 0.3-2.80mm in length, and are roughly tabular in form. They are in intergrown with albite and quartz crystals. Microcline crystals are moderately included with muscovite flakes 0.03–0.2mm in length and albite crystals 0.5mm in diameter. Microcline is randomly distributed throughout the groundmass.

Albite — Albite crystals are tabular and range from 0.5–1.20mm in length. They are highly included with muscovite flakes 0.05-0.7mm in length. Albite crystals are randomly distributed throughout the groundmass.

Biotite — Biotite flakes define a weak foliation throughout the halo zone. They are a green-brown color in plane-polarized light. Individual flakes range from 0.1-0.5mm in length; they form 1.00-5.00mm clots with muscovite/sericite throughout the groundmass. Clots contain 80% biotite and 20% muscovite/sericite, and appear to overprint the quartz aggregates and feldspars in the groundmass.

Muscovite/ sericite — Muscovite/sericite flakes range from 0.02 to 0.6mm in length. They occur in clots along with biotite flakes, and also occur as inclusions in albite crystals.

CORE

Quartz	Quartz crystals range from 0.08-2.00mm in diameter. They form interlocking polycrystalline aggregates that display a mosaic texture. These aggregates occur adjacent to microcline, albite and tourmaline crystals, and are roughly parallel to the weak foliation. Quartz crystals are moderately included with monazite, apatite and zircon grains ranging from 0.02-0.1mm in diameter.
Tourmaline	Tourmaline crystals are irregular and blebby in nature. Irregular masses range from 0.10-2.00mm in length. They occur in association with albite and quartz crystals. Impingements of quartz and albite occur in these irregular crystals. Tourmaline is green in plane polarized light.
Albite	Albite crystals range from 0.6-1.20mm in length. They form interlocking crystals with quartz and microcline, and also occur in direct contact with tourmaline.
Microcline	Microcline crystals are tabular and range from 0.4-1.60mm in length. They form interlocking crystals with albite, quartz and tourmaline.
Biotite	Biotite flakes 0.05-0.10mm in length occur as polycrystalline clots sparsely disseminated throughout the core. They are surrounded by quartz and feldspar grains.
Muscovite	Muscovite flakes are 0.2mm in length. Individual flakes are sparsely disseminated throughout the core between quartz crystals.

Texture

This rock has a weak foliation defined by elongated biotite/muscovite/sericite clots in the host granite and halo zones. Irregular tourmaline stringers are aligned parallel to this foliation in the core zone. Throughout the rock, quartz grains form polycrystalline aggregates that roughly parallel the foliation and are associated with all major minerals phases. Accessory phases including monazite, apatite and zircon are included in quartz crystals in all mineralogic zones.

Alteration

Biotite/muscovite/sericite clots appear to overprint quartz and feldspar crystals. The clots may be post-crystallization, but pre-deformation, as they are elongate and form a weak foliation in the rock.

130316- Starburst nodule

Hand Specimen Description

This massive granite host rock contains a starburst nodule that is approximately 7cm in diameter. The halo material is approximately 3cm thick, and contains biotite clots 1-3mm in diameter. These clots, along with irregular tourmaline crystals in the core, define a weak foliation throughout the rock. Tourmaline in the core is irregular and blebby to semi-prismatic. This polished thin section does not contain host granite, as it would not fit within the slide boundaries. Thus, only halo and core zones are examined.

Mineralogy

HALO	%
Quartz	45
Albite	25
Microcline	20
Biotite	6
Muscovite/sericite	2
Opaques	2
Accessory phases*	tr

CORE	%
Tourmaline	50
Quartz	35
Albite	12
Muscovite/sericite	2
Opaques	1
Accessory phases*	tr

*Monazite, apatite and zircon are included in quartz crystals throughout all zones.
This is a polished thin section. Opaque minerals did not reflect light.
tr = trace amounts

Mineral Descriptions

HALO

Quartz — Quartz crystals vary from 0.10–0.70mm in diameter. They form interlocking polycrystalline aggregates that display a mosaic texture. Quartz aggregates occur adjacent to microcline, albite and muscovite, and are roughly parallel to the weak foliation. Quartz crystals are moderately included with monazite, apatite and zircon grains ranging from 0.02-0.1mm in diameter.

Albite — Albite crystals are tabular and range from 0.75-4.00mm in length. They are intergrown with microcline and quartz crystals. Albite crystals are highly included with 0.05mm muscovite flakes, sericite, and 0.08mm quartz crystals.

Microcline — Microcline crystals range from 1.00-3.10mm in length and are tabular in form. They are in intergrown with albite and quartz crystals. Microcline crystals are moderately included with albite and quartz crystals roughly 0.5mm in diameter.

Biotite — Biotite flakes, along with other minerals, define a weak foliation throughout the halo zone. They are a green-brown color in plane-polarized light. Individual flakes range from 0.2-0.75mm in length; they form 1.00-5.00mm clots with muscovite/sericite and opaque minerals throughout the groundmass. Clots contain 80% biotite, 15% muscovite/sericite, and 5% opaques, and appear to overprint the quartz aggregates and feldspars in the groundmass.

Muscovite/ sericite — Muscovite/sericite flakes range from 0.02 to 0.65mm in length. They occur in clots along with biotite flakes and opaques, and also occur as inclusions in albite crystals. Muscovite also occurs as individual 0.1-0.2mm flakes dispersed throughout the halo material.

Opaques — Opaque mineral grains range from 0.05-0.10mm in diameter. These grains are associated with biotite, muscovite and sericite, forming clots that overprint the major mineral assemblage.

CORE

Tourmaline — Tourmaline crystals in the core zone are irregular and also display some bladed, prismatic crystals. Irregular crystals ranging from 0.10-2.00mm in length form masses up to 1.5cm in size. Bladed crystals range from 1.00-4.00mm in length. They are associated with albite and quartz crystals. Tourmaline is green in plane polarized light. Some crystals are altered around the edges to sericite, muscovite, and opaques (± hematite).

Quartz — Quartz crystals range from 0.10-0.7mm in diameter. They form interlocking polycrystalline aggregates that display a mosaic texture. These aggregates occur adjacent to microcline, albite and tourmaline crystals, and are roughly parallel to the weak foliation. Quartz crystals are moderately included with monazite, apatite and zircon grains ranging from 0.02-0.1mm in diameter.

Albite — Albite crystals are tabular and range from 0.3-1.70mm in length. They are intergrown with microcline and quartz crystals. Albite crystals are highly included with muscovite flakes 0.05-0.7mm in length.

Muscovite/ sericite — Muscovite/sericite flakes range from 0.02 to 0.65mm in length. They occur along with opaque minerals in alteration clots associated with tourmaline crystals.

Opaques — Opaque mineral grains (± hematite) range from 0.05-0.10mm in diameter. These grains are associated with muscovite and sericite, forming alteration clots associated with tourmaline crystals.

Textures

This rock has a weak foliation defined by elongated biotite/muscovite/sericite clots in the halo zone. Irregular tourmaline stringers are aligned parallel to this foliation in the core zone. Bladed, prismatic tourmaline crystals are also present in the core zone, and show evidence of alteration. Throughout the rock, quartz grains form polycrystalline aggregates that roughly parallel the foliation and are associated with all major minerals phases. There is a lack of microcline in the core. Accessory phases including monazite, apatite and zircon are included in quartz crystals in all mineralogic zones.

Alteration

Biotite/muscovite/sericite clots appear to overprint quartz and feldspar crystals in the halo zone. The clots may be post-crystallization, but pre-deformation, as they are elongate and form a weak foliation in the rock. Tourmaline crystals in the core are altered to a sericite/muscovite/opaque mineral assemblage around the edges that appears colorless to black-brown in plane light. Opaque minerals do not reflect light, and may include hematite.

130317- Biotite clots in host granite

Hand specimen description

This massive granite host rock contains abundant biotite clots throughout the groundmass, ranging from 2-6mm in length. Host granite is texturally similar to other host granite regions lacking abundant biotite clots. This rock has a moderate foliation defined by these clots. There are no nodules contained in this polished thin section, although there are nodules in close proximity to this sample location.

Mineralogy

HOST GRANITE	%
Quartz	55
Albite	15
Biotite	15
Microcline	10
Muscovite/sericite	5
Accessory phases*	tr

*Monazite, apatite and zircon are included in quartz crystals throughout all zones.
This is a polished thin section. Opaque minerals did not reflect light.
tr = trace amounts

Mineral Descriptions

HOST GRANITE

Quartz — Quartz crystals vary from 0.07–0.70mm in diameter. They form interlocking polycrystalline aggregates that display a mosaic texture. Quartz aggregates occur adjacent to microcline, albite and muscovite, and are roughly parallel to the weak foliation. Quartz crystals are moderately included with monazite, apatite and zircon grains ranging from 0.02-0.1mm in diameter.

Albite — Albite crystals are tabular and range from 0.75-1.3mm in length. They are intergrown with microcline and quartz crystals. Albite crystals are highly included with muscovite flakes and quartz crystals.

Biotite — Biotite flakes define a weak foliation throughout the halo zone. They are a green-brown color in plane-polarized light. Individual flakes range from 0.2-0.75mm in length; they form 1.00-5.00mm clots with muscovite/sericite throughout the groundmass. Clots contain 80% biotite and 20% muscovite/sericite, and appear to overprint the quartz aggregates and feldspars in the groundmass.

Microcline	Microcline crystals range from 0.5-3.10mm in length and are tabular in form. They are in intergrown with albite and quartz crystals. Microcline crystals are moderately included with albite and quartz crystals roughly 0.5mm in diameter.
Muscovite/ sericite	Muscovite/sericite flakes range from 0.02 to 0.65mm in length. They occur in clots along with biotite flakes, and also occur as inclusions in albite crystals.

Textures

Biotite, muscovite, sericite and opaque minerals (hematite) define a moderate foliation in this rock. Quartz grains form polycrystalline aggregates that roughly parallel the foliation and are associated with all major mineral phases.

Alteration

The biotite/muscovite/sericite/opaque mineral clots appear to overprint quartz and feldspar crystals throughout the groundmass.

130318- Flower nodule

Hand Specimen Description

This granitic rock contains a flower nodule roughly 15cm in diameter that is comprised of various mineralogic zones. Host granite surrounds the nodule, halo material encompasses the flower shaped tourmaline-rich core, and there is an inner granite zone mineralogically and texturally similar to the outer host granite. The outer and inner host granite displays a moderate foliation, defined by elongated biotite clots. The halo zone is roughly 0.8-1.00mm thick, and contains sparse biotite clots. This polished thin section includes the outer host granite, both halo zones, tourmaline-rich core, and inner host granite. This sample is quite fine-grained relative to other nodule types (ex. starburst).

Mineralogy

HOST GRANITE (Outer and inner zones)	%	HALO	%	CORE	%
Quartz	60	Quartz	65	Tourmaline	50
Albite	15	Albite	20	Quartz	39
Biotite	10	Microcline	10	Albite	10
Muscovite/sericite	8	Biotite	2	Accessory phases*	1
Microcline	2	Muscovite/sericite	2	Biotite	tr
Accessory phases*	1	Accessory phases*	1	Muscovite	tr

*Monazite, apatite and zircon are included in quartz crystals throughout all zones.
This is a polished thin section. Opaque minerals did not reflect light.
tr = trace amounts

Mineral Descriptions

HOST GRANITE (Outer and inner zones)

Quartz — Quartz crystals vary from 0.04–0.65mm in diameter. They form interlocking polycrystalline aggregates that display a mosaic texture. Quartz aggregates occur adjacent to microcline, albite and muscovite, and are roughly parallel to the weak foliation. Quartz crystals are moderately included with monazite, apatite and zircon grains ranging from 0.02-0.1mm in diameter.

Albite — Albite crystals are tabular and range from 0.5-1.50mm in length. They are intergrown with microcline and quartz crystals. Albite crystals are highly included with muscovite flakes 0.03-0.5mm in length and small quartz crystals 0.5mm in diameter. Albite is randomly distributed throughout the groundmass.

Biotite — Biotite flakes define a weak foliation throughout the host rock. They are a green-brown color in plane-polarized light. Individual flakes range from 0.2-1.3mm in length, and form 0.5-3.00mm clots with

muscovite/sericite throughout the groundmass. Clots contain 80% biotite and 20% muscovite/sericite, and appear to overprint the quartz aggregates and feldspars in the groundmass.

Muscovite/ sericite — Muscovite/sericite flakes range from 0.04-0.80mm in length. They occur in clots along with biotite flakes, and also occur as inclusions in albite crystals. Muscovite also occurs as individual aggregates of flakes between quartz crystals.

Microcline — Microcline crystals range from 0.4-1.00mm in length and are tabular in form. They are in intergrown with albite and quartz crystals. Microcline crystals are highly included with muscovite flakes 0.03–0.2mm in length and quartz crystals 0.5mm in diameter. These crystals are randomly distributed throughout the groundmass.

HALO

Quartz — Quartz crystals range from 0.04-0.90mm in diameter. They form interlocking polycrystalline aggregates that display a mosaic texture. These aggregates occur adjacent to microcline, albite and biotite clots, and are roughly parallel to the weak foliation. Quartz crystals are moderately included with monazite, apatite and zircon grains ranging from 0.02-0.1mm in diameter.

Albite — Albite crystals are tabular and range from 0.09–1.30mm in length. They are highly included with muscovite flakes <0.01mm in length. Albite crystals are randomly distributed throughout the groundmass.

Microcline — Microcline crystals range from 0.2-0.80mm in length, and are roughly tabular in form. They are in intergrown with albite and quartz crystals. Microcline crystals are moderately included with muscovite flakes 0.03–0.2mm in length and albite crystals 0.5mm in diameter. Microcline is randomly distributed throughout the groundmass.

Biotite — Biotite flakes define a weak foliation throughout the halo zone. They are a green-brown color in plane-polarized light. Individual flakes range from 0.1-0.5mm in length; they form 1.00-2.00mm clots with muscovite/sericite throughout the groundmass. Clots contain 80% biotite and 20% muscovite/sericite, and appear to overprint the quartz aggregates and feldspars in the groundmass.

Muscovite/ sericite — Muscovite/sericite flakes range from 0.02 to 0.6mm in length. They occur in clots along with biotite flakes, and also occur as inclusions in albite crystals.

CORE

Tourmaline	Tourmaline crystals in the core zone display prismatic to sub-equant crystals. Crystals range from 0.02 to 1.3mm in length, and are associated with albite and quartz crystals. Tourmaline is green in plane polarized light. Some crystals are altered around the edges to sericite, muscovite and opaques (± hematite).
Quartz	Quartz crystals range from 0.03-0.9mm in diameter. They form interlocking polycrystalline aggregates that display a mosaic texture. These aggregates occur adjacent to microcline, albite and tourmaline crystals, and are roughly parallel to the weak foliation. Quartz crystals are moderately included with monazite, apatite and zircon grains ranging from 0.02-0.1mm in diameter.
Albite	Albite crystals range from 0.6-1.20mm in length. They form interlocking crystals with quartz and microcline, and also occur in direct contact with tourmaline.
Biotite	Biotite flakes 0.05-0.10mm in length occur as polycrystalline clots sparsely disseminated throughout the core. They are surrounded by quartz and feldspar grains.
Muscovite	Muscovite flakes are 0.2mm in length. Individual flakes are sparsely disseminated throughout the core between quartz crystals.

Textures

This rock is quite fine-grained relative to other nodule types described. There are several mineralogic zones present in this rock that contains a flower nodule: 1) host granite; 2) halo; 3) core; 4) halo; and 5) inner host granite. The host granite surrounding the nodule is mineralogically and texturally similar to the inner host granite. The two halo zones are identical (~1.5cm thick), and the core zone contains fine-grained tourmaline crystals. Biotite/muscovite/sericite clots define a moderate foliation throughout the granite and halo zones; tourmaline in the core zone is aligned parallel to the foliation. Throughout the rock, quartz grains form polycrystalline aggregates that roughly parallel the foliation and are associated with all major minerals phases. Accessory phases including monazite, apatite and zircon are included in quartz crystals in all mineralogic zones.

Alteration

Biotite/muscovite/sericite/opaque mineral clots appear to overprint quartz and feldspar crystals in the halo zone. Tourmaline in the core shows slight alteration around crystal edges to a sericite/muscovite/opaque mineral assemblage that appears colorless to black-brown in plane light. Opaque minerals do not reflect light, and may include hematite.

130319-Tourmaline rosette nodule

Hand Specimen Description

This rock contains a spherical nodule 8cm in diameter. This nodule contains a dense rosette in the center of the core region composed of densely packed irregular to prismatic tourmaline crystals 0.5-5mm in length. The halo zone is approximately 2.5cm thick, and contains sparse biotite clots, which define a weak foliation through the rock. This polished thin section does not contain host granite, as it would not fit within the slide boundaries. Thus, only halo and core zones are examined.

Mineralogy

HALO	%	CORE	%	DENSE CORE	%
Quartz	55	Tourmaline	50	Tourmaline	95
Albite	20	Quartz	35	Quartz	5
Microcline	15	Albite	14		
Biotite	7	Accessory phases*	1		
Muscovite/sericite	2	Muscovite/sericite	tr		
Opaques	1	Opaques	tr		
Accessory phases*	tr				

*Monazite, apatite and zircon are included in quartz crystals throughout all zones.
This is a polished thin section. Opaque minerals did not reflect light.
tr = trace amounts

Mineral Descriptions

HALO

Quartz — Quartz crystals vary from 0.02–2.20mm in diameter. They form interlocking polycrystalline aggregates that display a mosaic texture. Quartz aggregates occur adjacent to microcline, albite and muscovite, and are roughly parallel to the weak foliation. Quartz crystals are moderately included with monazite, apatite and zircon grains ranging from 0.02-0.1mm in diameter.

Albite — Albite crystals are tabular and range from 0.2-1.00mm in length. They are intergrown with microcline and quartz crystals. Albite crystals are highly included with muscovite flakes and quartz crystals.

Microcline — Microcline crystals range from 0.2-2.00mm in length and are tabular in form. They are in intergrown with albite and quartz crystals. Microcline crystals are moderately included with albite and quartz crystals roughly 0.5mm in diameter.

Biotite — Biotite flakes define a weak foliation throughout the halo zone.

They are a green-brown color in plane-polarized light. Individual flakes range from 0.2-0.75mm in length; they form 1.00-1.50mm clots with muscovite/sericite throughout the groundmass. Clots contain 80% biotite, 15% muscovite/sericite, and 5% opaques, and appear to overprint the quartz aggregates and feldspars in the groundmass.

Muscovite/ sericite — Muscovite/sericite flakes range from 0.2 to 2.00mm in length. They occur in clots along with biotite flakes, and also occur as inclusions in albite crystals.

Opaques — Opaque mineral grains range from 0.05-0.10mm in diameter. These grains are associated with biotite, muscovite and sericite, forming clots that overprint the major mineral assemblage.

CORE

Tourmaline — Tourmaline crystals in the core zone are irregular to prismatic. Irregular masses range from 0.2-2.00mm in length, and prismatic crystals range from 1.00-3.00mm in length. Both are aligned roughly parallel to the weak foliation in the halo. They are associated with albite and quartz crystals. Tourmaline is green in plane polarized light. Some crystals exhibit dark alteration zones along their perimeters consisting of sericite, muscovite, and opaque (± hematite) minerals.

Quartz — Quartz crystals range from 0.07-0.7mm in diameter. They form interlocking polycrystalline aggregates that display a mosaic texture. These aggregates occur adjacent to microcline, albite and tourmaline crystals, and are roughly parallel to the weak foliation. Quartz crystals are moderately included with monazite, apatite and zircon grains ranging from 0.02-0.1mm in diameter.

Albite — Albite crystals are tabular and range from 0.2-0.35mm in length. They are intergrown with microcline and quartz crystals. Albite crystals are highly included with muscovite flakes 0.05-0.7mm in length.

Muscovite/ sericite — Muscovite/sericite flakes range from 0.02 to 0.65mm in length. They occur along with opaque minerals in alteration clots associated with tourmaline crystals.

Opaques — Opaque mineral grains (± hematite) range from 0.05-0.10mm in diameter. These grains are associated with muscovite and sericite, forming alteration clots associated with tourmaline crystals.

DENSE CORE

Tourmaline	Tourmaline comprising the dense core zone is fractured and massive, with occasional bladed to prismatic crystals ranging from 1.00-4.00mm in length. The tourmaline masses are green in plane polarized light.
Quartz	Quartz, ranging from 0.02-0.05mm in diameter, infills fractured tourmaline in the dense core.

Textures

This rock has a weak foliation defined by elongated biotite/muscovite/sericite/opaque clots in the halo zone. Irregular and prismatic tourmaline crystals in the core are aligned parallel to this foliation, and show evidence of alteration. There is a dense rosette of massive to prismatic tourmaline in the central region of the core zone. Throughout the rock, quartz grains form polycrystalline aggregates that roughly parallel the foliation and are associated with all major minerals phases. Accessory phases including monazite, apatite and zircon are included in quartz crystals in all mineralogic zones. There is a lack of microcline in the core.

Alteration

Biotite/muscovite/sericite/opaque mineral clots appear to overprint quartz and feldspar crystals in the halo zone. Tourmaline in the core shows slight alteration around crystal edges to a sericite/muscovite/opaque mineral assemblage that appears colorless to black-brown in plane light. Opaque minerals do not reflect light, and may include hematite.

130320- Irregular Nodules

Hand Specimen Description

This rock contains an irregular nodule 6cm in diameter. It is surrounded by host granite, and is enclosed in halo material 0.5-1.5cm thick. The host granite contains biotite clots that define a weak foliation. Tourmaline in the nodule forms radiating arms comprised of prismatic crystals that extend into the halo material. The central area of the nodule from which the tourmaline radiates is comprised of irregular to sub-equant crystals. The polished thin section contains host granite, halo and core of the irregular nodule.

Mineralogy

HOST	%	HALO	%	CORE	%
Quartz	65	Quartz	75	Tourmaline	95
Albite	15	Albite	22	Quartz	5
Biotite	8	Microcline	2	Accessory phases*	tr
Muscovite/sericite	6	Accessory phases*	1		
Microcline	5				
Opaques	1				
Accessory phases*	tr				

*Monazite, apatite and zircon are included in quartz crystals throughout all zones.
This is a polished thin section. Opaque minerals did not reflect light.
tr = trace amounts

Mineral Descriptions

HOST

Quartz — Quartz crystals vary from 0.02–1.00mm in diameter. They form interlocking polycrystalline aggregates that display a mosaic texture. Quartz aggregates occur adjacent to microcline, albite and muscovite, and are roughly parallel to the weak foliation. Quartz crystals are moderately included with monazite, apatite and zircon grains ranging from 0.02-0.1mm in diameter.

Albite — Albite crystals are tabular and range from 0.3-0.8mm in length. They are intergrown with microcline and quartz crystals. Albite crystals are highly included with muscovite flakes and accessory phases.

Biotite — Biotite flakes define a weak foliation throughout the halo zone. They are green in plane-polarized light. Individual flakes range from 0.4-0.65mm in length; they form 1.00-1.50mm clots with muscovite/sericite throughout the groundmass. Clots contain 80% biotite, 15% muscovite/sericite, and 5% opaques, and appear to overprint the quartz aggregates and feldspars in the groundmass.

Muscovite/ sericite — Muscovite/sericite flakes range from 0.18 to 0.5mm in length. They occur in clots along with biotite flakes, and also occur as inclusions in albite crystals.

Microcline — Microcline crystals range from 0.3-0.5mm in length and are tabular in form. They are in intergrown with albite and quartz crystals. Microcline crystals are moderately included with albite and quartz crystals roughly 0.5mm in diameter.

Opaques — Opaque mineral grains range from 0.05-0.10mm in diameter. These grains are associated with biotite, muscovite and sericite, forming clots that overprint the major mineral assemblage.

HALO

Quartz — Quartz crystals range from 0.18-0.5mm in diameter. They form interlocking polycrystalline aggregates that display a mosaic texture. These aggregates occur adjacent to microcline, albite and tourmaline crystals, and are roughly parallel to the weak foliation. Quartz crystals are moderately included with monazite, apatite and zircon grains ranging from 0.02-0.1mm in diameter.

Albite — Albite crystals are tabular and range from 0.4-0.5mm in length. They are intergrown with microcline and quartz crystals. Albite crystals are highly included with muscovite flakes 0.05-0.7mm in length.

Microcline — Microcline crystals range from 0.4-0.65mm in length and are tabular in form. They are in intergrown with albite and quartz crystals. Microcline crystals are moderately included with albite and quartz crystals roughly 0.5mm in diameter.

CORE

Tourmaline — Tourmaline crystals in the core zone are irregular to prismatic. Irregular masses are highly fractured and range from 0.2-3.00mm in length. Prismatic crystals range from 1.00-9.00mm in length. Both are aligned roughly parallel to the weak foliation in the halo. They are associated with albite and quartz crystals. Tourmaline is green in plane polarized light. Some crystals exhibit dark alteration zones along their perimeters consisting of sericite, muscovite, and opaque (± hematite) minerals.

Quartz	Quartz crystals range from 0.07-0.9mm in diameter. They form interlocking polycrystalline aggregates that display a mosaic texture. These aggregates occur adjacent to microcline, albite and tourmaline crystals, and are roughly parallel to the weak foliation. They also infill fractures in the tourmaline. Quartz crystals are moderately included with monazite, apatite and zircon grains ranging from 0.02-0.1mm in diameter.

Textures

This rock contains a weak foliation defined by biotite/muscovite/sericite/opaque clots elongated throughout the groundmass. Irregular and prismatic tourmaline is roughly parallel to this foliation in the core. Tourmaline defines a radiating nodule that is irregular in shape. Throughout the rock, quartz grains form polycrystalline aggregates that roughly parallel the foliation and are associated with all major minerals phases. Accessory phases including monazite, apatite and zircon are included in quartz crystals in all mineralogic zones.

Alteration

Biotite/muscovite/sericite/opaque mineral clots appear to overprint quartz and feldspar crystals in the halo zone. Tourmaline in the core shows slight alteration around crystal edges to a sericite/muscovite/opaque mineral assemblage that appears colorless to black-brown in plane light. Opaque minerals do not reflect light, and may include hematite.

130321- Granite

Hand Specimen Description

This is a massive granite, void of nodules and phenocrysts. A moderate foliation is developed throughout the rock, defined by elongate biotite/muscovite clots 1.00-7.00mm in length. This polished thin section is comprised solely of host granite.

Mineralogy

HOST	%
Quartz	55
Albite	20
Microcline	15
Biotite	7
Muscovite/sericite	2
Opaques	1
Accessory phases*	tr

*Monazite, apatite and zircon are included in quartz crystals throughout all zones.
This is a polished thin section. Opaque minerals did not reflect light.
tr = trace amounts

Mineral Descriptions

HOST GRANITE

Quartz — Quartz crystals vary from 0.10–0.50mm in diameter. They form interlocking polycrystalline aggregates that display a mosaic texture. Quartz aggregates occur adjacent to microcline, albite and muscovite, and are roughly parallel to the weak foliation. Quartz crystals are moderately included with monazite, apatite and zircon grains ranging from 0.02-0.1mm in diameter.

Albite — Albite crystals are tabular and range from 0.3-1.00mm in length. They are intergrown with microcline and quartz crystals. Albite crystals are highly included with muscovite flakes 0.03-0.5mm in length. These crystals are randomly distributed throughout the groundmass.

Microcline — Microcline crystals range from 0.2-0.5mm in length and are tabular in form. They are in intergrown with albite and quartz crystals. Microcline crystals are moderately included with muscovite flakes 0.03–0.2mm in length and albite crystals 0.5mm in diameter. These crystals are randomly distributed throughout the groundmass.

Biotite — Biotite flakes define a weak foliation throughout the host rock. They are a green-brown color in plane-polarized light. Individual flakes

	range from 0.2-1.00mm in length, and form 1.00-7.00mm clots with muscovite/sericite throughout the groundmass. Clots contain 80% biotite and 20% muscovite/sericite, and appear to overprint the quartz aggregates and feldspars in the groundmass.
Muscovite/ sericite	Muscovite/sericite flakes range from 0.03-0.2mm in length. They occur in clots along with biotite flakes, and also occur as inclusions in albite crystals.
Opaques	Opaque mineral grains range from 0.05-0.10mm in diameter. The grains are disseminated throughout the rock, and show no reflectance under reflected light.

Textures

The textures observed in this slide of massive granite are similar to those observed in host granite associated with nodules/veins. A moderate foliation occurs throughout the groundmass, defined by elongated biotite/muscovite/sericite clots. Throughout the rock, quartz grains form polycrystalline aggregates that roughly parallel the foliation and are associated with all major minerals phases. Accessory phases including monazite, apatite and zircon are included in quartz crystals.

Alteration

Biotite/muscovite/sericite/opaque mineral clots appear to overprint quartz and feldspar throughout the granite. Opaque minerals do not reflect light, and may include hematite.

130322- Proto-nodules

Hand Specimen Description

This rock contains proto-nodules, small (0.5-1.2cm) tourmaline clots that are not surrounded by halo material. Tourmaline in the nodules is aligned roughly parallel to the weak to moderate foliation in the host granite defined by biotite/muscovite clots. Proto-nodules are in close association with these clots, as there is no halo material to separate nodule core from host granite.

Mineralogy

HOST	%	CORE	%
Quartz	60	Tourmaline	95
Albite	15	Quartz	5
Microcline	10		
Biotite	8		
Muscovite/sericite	6		
Opaques	1		
Accessory phases*	tr		

*Monazite, apatite and zircon are included in quartz crystals throughout all zones.
This is a polished thin section. Opaque minerals did not reflect light.
tr = trace amounts

Mineral Descriptions

HOST

Quartz — Quartz crystals vary from 0.04–0.65mm in diameter. They form interlocking polycrystalline aggregates that display a mosaic texture. Quartz aggregates occur adjacent to microcline, albite and muscovite, and are roughly parallel to the weak foliation. Quartz crystals are moderately included with monazite, apatite and zircon grains ranging from 0.02-0.1mm in diameter.

Albite — Albite crystals are tabular and range from 0.3-1.5mm in length. They are intergrown with microcline and quartz crystals. Albite crystals are highly included with muscovite flakes and accessory phases.

Microcline — Microcline crystals range from 0.1-0.65mm in length and are tabular in form. They are in intergrown with albite and quartz crystals. Microcline crystals are moderately included with albite and quartz crystals roughly 0.5mm in diameter.

Biotite — Biotite flakes define a weak foliation throughout the halo zone. They are green in plane-polarized light. Individual flakes range from 0.4-0.65mm in length; they form 1.00-2.10mm clots with

muscovite/sericite throughout the groundmass. Clots contain 80% biotite, 15% muscovite/sericite, and 5% opaques, and appear to overprint the quartz aggregates and feldspars in the groundmass.

Muscovite/ sericite — Muscovite/sericite flakes range from 0.10 to 0.4mm in length. They occur in clots along with biotite flakes, and also occur as inclusions in albite crystals.

Opaques — Opaque mineral grains range from 0.05-0.10mm in diameter. These grains are associated with biotite, muscovite and sericite, forming clots that overprint the major mineral assemblage.

CORE

Tourmaline — Tourmaline crystals in the core zone are irregular to prismatic. They are highly fractured and range from 0.2-2.10mm in length. These tourmaline crystals are aligned roughly parallel to the weak foliation and form clots in the host granite and are associated with albite and quartz crystals. Tourmaline is green in plane polarized light.

Quartz — Quartz crystals range from 0.1-0.4mm in diameter. They form interlocking polycrystalline aggregates that display a mosaic texture. These aggregates occur adjacent to microcline, albite and tourmaline crystals, and are roughly parallel to the weak foliation. They also infill fractures in the tourmaline. Quartz crystals are moderately included with monazite, apatite and zircon grains ranging from 0.02-0.1mm in diameter.

Textures

This rock contains a weak foliation defined by biotite/muscovite/sericite/opaque clots elongated throughout the groundmass. Irregular and prismatic tourmaline is roughly parallel to this foliation in the core. Throughout the rock, quartz grains form polycrystalline aggregates that roughly parallel the foliation and are associated with all major minerals phases. Accessory phases including monazite, apatite and zircon are included in quartz crystals in all mineralogic zones.

Alteration

Biotite/muscovite/sericite/opaque mineral clots appear to overprint quartz and feldspar crystals in the host granite. Opaque minerals do not reflect light, and may include hematite.

130323- Tourmaline Vein

Hand Specimen Description

This rock contains a 1.5cm-wide tourmaline vein, enclosed by 1cm halo material. The vein extended for over 8m in the host granite. Biotite clots define a weak foliation in the host granite that tourmaline in the vein runs roughly parallel to. This polished thin section includes a small portion of host granite, halo and tourmaline-rich vein.

Mineralogy

HOST	%	HALO	%	CORE	%
Quartz	60	Quartz	70	Tourmaline	65
Albite	20	Microcline	20	Quartz	30
Microcline	10	Albite	10	Albite	5
Biotite	8	Accessory phases*	tr	Accessory phases*	tr
Muscovite/sericite	2				
Opaques	tr				
Accessory phases*	tr				

*Monazite, apatite and zircon are included in quartz crystals throughout all zones.
This is a polished thin section. Opaque minerals did not reflect light.
tr = trace amounts

Mineral Descriptions

HOST

Quartz — Quartz crystals vary from 0.02–0.65mm in diameter. They form interlocking polycrystalline aggregates that display a mosaic texture. Quartz aggregates occur adjacent to microcline, albite and muscovite, and are roughly parallel to the weak foliation. Quartz crystals are moderately included with monazite, apatite and zircon grains ranging from 0.02-0.1mm in diameter.

Albite — Albite crystals are tabular and range from 0.12-0.55mm in length. They are intergrown with microcline and quartz crystals. Albite crystals are highly included with muscovite flakes and accessory phases.

Microcline — Microcline crystals range from 0.2-1.5mm in length and are tabular in form. They are in intergrown with albite and quartz crystals. Microcline crystals are moderately included with albite and quartz crystals roughly 0.5mm in diameter.

Biotite — Biotite flakes define a weak foliation throughout the halo zone. They are green in plane-polarized light. Individual flakes range from 0.4-0.65mm in length; they form 1.00-1.60mm clots with muscovite/sericite throughout the groundmass. Clots contain 80%

biotite, 15% muscovite/sericite, and 5% opaques, and appear to overprint the quartz aggregates and feldspars in the groundmass.

Muscovite/ sericite — Muscovite/sericite flakes range from 0.02 to 0.25mm in length. They occur in clots along with biotite flakes, and also occur as inclusions in albite crystals.

Opaques — Opaque mineral grains range from 0.05-0.10mm in diameter. These grains are associated with biotite, muscovite and sericite, forming clots that overprint the major mineral assemblage.

HALO

Quartz — Quartz crystals range from 0.08-0.3mm in diameter. They form interlocking polycrystalline aggregates that display a mosaic texture. These aggregates occur adjacent to microcline, albite and tourmaline crystals, and are roughly parallel to the weak foliation. Quartz crystals are moderately included with monazite, apatite and zircon grains ranging from 0.02-0.1mm in diameter.

Microcline — Microcline crystals range from 0.3-1.10mm in length and are tabular in form. They are in intergrown with albite and quartz crystals. Microcline crystals are moderately included with albite and quartz crystals roughly 0.5mm in diameter.

Albite — Albite crystals are tabular and range from 0.2-0.6mm in length. They are intergrown with microcline and quartz crystals. Albite crystals are highly included with muscovite flakes 0.05-0.7mm in length.

CORE

Tourmaline — Tourmaline crystals in the core zone are irregular to prismatic. They form clots 0.3 to 9mm in length, and are aligned roughly parallel to the weak foliation in the halo. They are associated with albite and quartz crystals, and include albite crystals up to 0.3mm in length. Tourmaline is green in plane polarized light. Some crystals exhibit dark alteration zones along their perimeters consisting of sericite, muscovite, and opaque (± hematite) minerals.

Quartz — Quartz crystals range from 0.02-0.3mm in diameter. They form interlocking polycrystalline aggregates that display a mosaic texture. These aggregates occur adjacent to microcline, albite and tourmaline crystals, and are roughly parallel to the weak foliation. They also

infill fractures in the tourmaline. Quartz crystals are moderately included with monazite, apatite and zircon grains ranging from 0.02-0.1mm in diameter.

Albite — Albite crystals are tabular and range from 0.3-1.1mm in length. They are intergrown with microcline and quartz crystals. Albite crystals are highly included with muscovite flakes 0.05-0.7mm in length.

Textures

This rock contains a weak foliation defined by biotite/muscovite/sericite/opaque clots elongated throughout the groundmass. Irregular and prismatic tourmaline is roughly parallel to this foliation in the core. Throughout the rock, quartz grains form polycrystalline aggregates that roughly parallel the foliation and are associated with all major minerals phases. Accessory phases including monazite, apatite and zircon are included in quartz crystals in all mineralogic zones. The halo material contains an unusual abundance of microcline.

Alteration

Biotite/muscovite/sericite/opaque mineral clots appear to overprint quartz and feldspar crystals in the halo zone. Tourmaline in the core shows slight alteration around crystal edges to a sericite/muscovite/opaque mineral assemblage that appears colorless to black-brown in plane light. Opaque minerals do not reflect light, and may include hematite.

130324- Nodule from porphyritic granite

Hand Specimen Description

This granitic rock contains an elongate 3 x 5cm nodule, in a porphyritic groundmass. The nodule has an overall grain size of 0.1mm (fine-grained), and is surrounded by a 0.5cm thick halo. A 0.5cm dense tourmaline core is at the center of the nodule. The groundmass contains biotite/muscovite clots that define a moderate foliation; the nodule and included tourmaline crystals are elongate parallel to this foliation.

Mineralogy

HOST	%	HALO	%	CORE	%	DENSE CORE	%
Quartz	60	Quartz	70	Tourmaline	50	Tourmaline	65
Albite (groundmass)	15	Albite (groundmass)	15	Quartz	32	Quartz	20
Albite (phenocrysts)	3	Albite (phenocrysts)	5	Albite	16	Albite	15
Microcline	10	Microcline	8	Microcline	2		
Biotite	8	Accessory phases*	tr	Accessory phases*	tr		
Muscovite/sericite	3						
Opaques	1						
Accessory phases*	tr						

*Monazite, apatite and zircon are included in quartz crystals throughout all zones.
This is a polished thin section. Opaque minerals did not reflect light.
tr = trace amounts

Mineral Descriptions

HOST

Quartz — Quartz crystals vary from 0.03–0.40mm in diameter. They form interlocking polycrystalline aggregates that display a mosaic texture. Quartz aggregates occur adjacent to microcline, albite and muscovite, and are roughly parallel to the weak foliation. Quartz crystals are moderately included with monazite, apatite and zircon grains ranging from 0.02-0.1mm in diameter.

Albite — Albite crystals occur in the groundmass and also as phenocrysts. The groundmass crystals are tabular and range from 0.15-0.75mm in length. They are intergrown with microcline and quartz crystals, and are highly included with muscovite flakes and accessory phases. Phenocrysts are 1.1 to 1.5mm in diameter, and are also highly included with muscovite flakes.

Microcline — Microcline crystals range from 0.1-2mm in length and are tabular in form. They are in intergrown with albite and quartz crystals. Microcline crystals are moderately included with albite and quartz crystals roughly 0.5mm in diameter.

Biotite — Biotite flakes define a weak foliation throughout the halo zone. They are green in plane-polarized light. Individual flakes range from 0.1-0.65mm in length; they form 0.5-1.00mm clots with muscovite/sericite throughout the groundmass. Clots contain 80% biotite, 15% muscovite/sericite, and 5% opaques, and appear to overprint the quartz aggregates and feldspars in the groundmass.

Muscovite/ sericite — Muscovite/sericite flakes range from 0.02 to 0.50mm in length. They occur in clots along with biotite flakes, and also occur as inclusions in albite crystals.

Opaques — Opaque mineral grains range from 0.05-0.10mm in diameter. These grains are associated with biotite, muscovite and sericite, forming clots that overprint the major mineral assemblage.

HALO

Quartz — Quartz crystals range from 0.07-0.3mm in diameter. They form interlocking polycrystalline aggregates that display a mosaic texture. These aggregates occur adjacent to microcline, albite and tourmaline crystals, and are roughly parallel to the weak foliation. Quartz crystals are moderately included with monazite, apatite and zircon grains ranging from 0.02-0.1mm in diameter.

Albite — Albite crystals occur in the groundmass and also as phenocrysts. The groundmass crystals are tabular and range from 0.10-0.25mm in length. They are intergrown with microcline and quartz crystals, and are highly included with muscovite flakes and accessory phases. Phenocrysts are 1.2 to 1.5mm in diameter, and are also highly included with muscovite flakes.

Microcline — Microcline crystals range from 0.1-0.4mm in length and are tabular in form. They are in intergrown with albite and quartz crystals. Microcline crystals are moderately included with albite and quartz crystals roughly 0.5mm in diameter.

CORE

Tourmaline — Tourmaline crystals in the core zone are irregular to sub-equant and range from 0.05 to 0.65mm in length. They are associated with albite and quartz crystals and are aligned roughly parallel to the weak foliation in the rock. Tourmaline is green in plane polarized light. Some crystals exhibit dark alteration zones along their

perimeters consisting of sericite, muscovite, and opaque (± hematite) minerals.

Quartz — Quartz crystals range from 0.08-0.2mm in diameter. They form interlocking polycrystalline aggregates that display a mosaic texture. These aggregates occur adjacent to microcline, albite and tourmaline crystals, and are roughly parallel to the weak foliation. They also infill fractures in the tourmaline. Quartz crystals are moderately included with monazite, apatite and zircon grains ranging from 0.02-0.1mm in diameter.

Albite — Albite crystals are tabular and range from 0.3-0.4mm in length. They are intergrown with microcline and quartz crystals. Albite crystals are highly included with muscovite flakes 0.05-0.7mm in length.

Microcline — Microcline crystals range from 0.2-0.4mm in length and are tabular in form. They are in intergrown with albite and quartz crystals. Microcline crystals are moderately included with albite and quartz crystals roughly 0.5mm in diameter.

DENSE CORE

Tourmaline — Tourmaline crystals in the core zone are irregular to prismatic. They form clots 0.1 to 1.3mm in length, and are aligned roughly parallel to the weak foliation in the halo. They are associated with albite and quartz crystals, and include albite crystals up to 0.3mm in length. Tourmaline is green in plane polarized light. Some crystals exhibit dark alteration zones along their perimeters consisting of sericite, muscovite, and opaque (± hematite) minerals.

Quartz — Quartz crystals range from 0.06-0.4mm in diameter. They form interlocking polycrystalline aggregates that display a mosaic texture. These aggregates occur adjacent to albite and tourmaline crystals, and are roughly parallel to the weak foliation. They also infill fractures in the tourmaline. Quartz crystals are moderately included with monazite, apatite and zircon grains ranging from 0.02-0.1mm in diameter.

Albite — Albite crystals are tabular and range from 0.1-0.5mm in length. They are intergrown with microcline and quartz crystals. Albite crystals are highly included with muscovite flakes 0.05-0.7mm in length.

Textures

This rock contains a weak foliation defined by biotite/muscovite/sericite/opaque clots elongated throughout the groundmass. Irregular and prismatic tourmaline is roughly parallel to this foliation in the core. Throughout the rock, quartz grains form polycrystalline aggregates that roughly parallel the foliation and are associated with all major minerals phases. Accessory phases including monazite, apatite and zircon are included in quartz crystals in all mineralogic zones.

Alteration

Biotite/muscovite/sericite/opaque mineral clots appear to overprint quartz and feldspar crystals in the groundmass. Opaque minerals do not reflect light, and may include hematite.

APPENDIX D

ANALYTICAL TECHNIQUES AND ASSOCIATED DATA

D.1 FIELDWORK APPROACH

Fieldwork in the Western Australian Outback was completed during two three-week stints between June and August 2003. The fieldwork approach was to collect accurate, detailed data documenting the nature of the nodules and the host granite, as well as noting any structural or textural features associated with tourmaline development.

Fieldwork commenced with the examination of Scrubber Granite air photos (courtesy of the GSWA), embarking on a few "walk-abouts" to get a feel for the extent of the pluton, and establishing a mapping strategy. Each lobe of the pluton was approached separately, although data was integrated as a whole. Individual traverses across the lobes were conducted in order to cover as much of the granite as possible. Along the traverses, outcrops displaying well-developed, diverse nodules were extensively examined. Additional traverses were carried out at the end of the mapping phase to ensure that as many nodule formations were documented as possible. In total, 184 stop locations were established across the three lobes of the Scrubber Granite and in the adjacent country rock. Stop location coordinates, sample numbers, and associated data are compiled in Appendix A.

The following are features of the Scrubber Granite commonly documented at stop locations during the mapping process:

1. Nature of host granite:
    a. Massive/porphyritic/foliated/sheared;
    b. Fine/ medium/coarse-grained;
    c. Presence of tourmaline crystals/ biotite clots/ inclusions/ nodules;
    d. Structural features (ex. mineral lineations);
2. Nodule distribution, abundance, morphology, size; association with other features;
3. Halo thickness, presence of biotite clots, abundance and size of biotite clots; and
4. Presence of other features (tourmaline veins, pegmatites, etc.) and their relationship to nodule development.

Any textural and/or structural features that could support or discredit existing nodule formation theories (ex. Nemec, 1975; LeFort, 1991; Sinclair and Richardson, 1992) were also acknowledged.

Detailed observations were documented in a notebook in the field and were entered into a digital spreadsheet at camp. General features of the Scrubber Granite

were also noted on plastic air photo overlays to create a visual display of any trends or patterns. The air photos were also used to locate oneself in the Scrubber Granite by identifying landmarks such as large outcrops or vegetation. Notes from each stop location and corresponding photos and descriptions were entered into the GSWA database in Perth, W.A. upon completion of fieldwork. From these data, the GSWA created grid files of the Scrubber Granite stop locations, which were used by the author to create the ArcView GIS 3.3 maps in Appendix B.

Figure D.1: Author mapping the Scrubber Granite in the Australian Outback (western lobe). Detailed notes were entered into a field book, and general features such as nodule abundance or structural trends were also noted on air photos.

D.1.1 Sampling technique

During the mapping process, possible sample locations were noted. Upon completion of the mapping phase, proposed sample locations were reviewed and those locations displaying the most representative, well developed, and/or remarkable features were selected for sampling. These locations are summarized in Appendix A and are displayed in Figure B.1.

Several surface grab samples were collected during the mapping process. However, "fresh" samples, or samples lacking surface weathering, were required for

geochemical and isotopic studies. Therefore, samples had to be extracted from the sub-surface. Blast sites were established at several sample locations (blasted samples are marked with an asterisk in Appendix A). At each sample site, several holes were drilled into the outcrop, and were filled with explosives; a certified GSWA employee conducted the blasting. Of the resulting rock fragments, the best samples were selected and placed in plastic bags and were recorded in a field notebook and in a GSWA sample booklet. Samples from each blast site were given a sample number from the booklet.

Excess material was removed from larger samples using a rock saw at the GSWA laboratory in Perth. Samples were placed into aluminum canisters and were shipped back to Canada. Samples arrived in Canada mid-November, 2003.

Figure D.2: Part of the weathered surface that was blown off the flower/doughnut-shaped outcrop at stop 65 during blasting. The drill hole, where explosives were packed, is evident. This blast site gave rise to sample 130318.

D.2 X-RAY FLUORESCENCE SPECTROMETRY (XRF)

Samples were sent to the XRAL Laboratory at SGS Canada Inc. in Toronto, Ontario for determination of major and trace element concentrations using x-ray fluorescence spectrometry on a fused disc prepared from a 2g sample. Results of these analyses are provided in Table D.1.

Boron was determined using the Na_2O_2 fusion procedure (peroxide fusion). In this procedure, 0.1 gram of sample is fused with 0.75 gram of Na_2O_2 in a zirconium crucible. The melt is dissolved in dilute HNO_3 and made up to 40ml; dilutions are done in plastic ware (no glass is involved). The analysis is done by ICP using matrix-matched standards.

D.3 INDUCTIVELY COUPLED PLASMA MASS SPECTROMETRY (ICP-MS)

Inductively coupled plasma mass spectrometry (ICP-MS) analysis of Scrubber Granite whole rock powders was completed in the ICP-MS Laboratory at the University of Saskatchewan, using a Perkin Elmer ELAN 5000. Powdered rock samples of individual mineralogic zones were analyzed for their trace element concentrations using the following methodology.

Approximately 0.2g of each sample was dissolved with sodium peroxide in metal crucibles. Samples were placed in an oven at 480˚C for one hour to digest, and were then washed down with deionized water. Sample slurries were placed into test tubes, and were centrifuged at 3000RPM for 10 minutes. The samples had then settled to the bottom of the test tubes, and the water was poured off. Samples were then dissolved in 2.5mL of HNO_3 and 1mL of hydrogen peroxide. After approximately 5 minutes, sample solutions changed color depending on what elements were present. Test tubes were sealed and placed in a sonic bath, after which the samples were placed in bottles with deionized water, and were analyzed. Results of the ICP-MS analyses and associated errors are provided in Table D.2.

Table D.1: Major and trace element concentrations of various zones in the Scrubber Granite as determined by XRF.

		SiO_2	Al_2O_3	CaO	MgO	Na_2O	K_2O	Fe_2O_3	MnO	TiO_2	P_2O_5	Cr_2O_3	LOI	Sum	Rb	Sr	Y	Zr	Nb	Ba	B*
Sample	**Zone**	%	%	%	%	%	%	%	%	%	%	%	%	%	ppm	ppm	ppm	ppm	ppm	ppm	ppm
130315a	Core	68.39	16.08	1.62	1.19	2.20	1.96	5.06	0.06	0.19	0.17	<0.01	1.95	98.93	92	82	20	98	6	262	10010
130315b	Halo	75.11	12.78	2.18	0.21	3.35	4.45	0.57	0.02	0.04	0.09	<0.01	1.30	100.2	200	157	39	114	10	571	195
130315c	Host	74.33	13.94	1.33	0.30	3.18	4.50	1.43	0.05	0.15	0.05	<0.01	0.75	100.2	236	151	41	120	19	586	26
130316a	Core	72.45	15.26	0.87	1.00	2.96	1.48	4.42	0.05	0.17	0.08	<0.01	1.10	99.9	82	117	26	128	7	243	7920
130316b	Halo	74.54	13.61	1.38	0.13	3.74	4.67	0.82	0.02	0.14	0.05	<0.01	0.95	100.2	225	204	39	135	21	727	94
130316c	Host	73.60	14.06	1.39	0.27	3.33	4.84	1.62	0.03	0.16	0.06	<0.01	0.65	100.2	287	207	57	141	22	716	22
130318a	Inner host	73.93	14.1	1.40	0.30	3.06	4.82	1.26	0.03	0.11	0.08	<0.01	0.95	100.2	217	138	50	103	16	616	493
130318b	Core	70.97	15.36	1.07	0.84	2.20	2.31	3.99	0.06	0.19	0.31	<0.01	1.40	98.78	81	71	26	103	6	306	8450
130318c	Halo	76.95	12.93	1.19	0.03	3.41	4.65	0.13	0.01	0.02	0.06	<0.01	0.65	100.1	151	140	34	101	7	647	100
130318d	Host	74.02	14.1	1.41	0.30	3.34	4.55	1.36	0.05	0.12	0.07	<0.01	0.65	100.1	210	140	47	94	17	577	15
130321	Host	73.02	14.05	1.41	0.36	3.20	5.01	1.75	0.03	0.19	0.06	<0.01	0.90	100.2	286	189	60	149	22	680	26
130323a	Halo	76.84	12.96	0.92	0.03	3.47	4.83	0.14	0.01	0.05	0.09	<0.01	0.65	100.1	161	193	37	88	8	627	<10
130323b	Host	74.89	14.00	1.04	0.24	3.14	4.97	1.05	0.05	0.12	0.06	<0.01	0.45	100.1	217	182	47	88	12	575	69
130324a	Core	72.54	15.66	0.91	0.79	2.83	2.44	3.58	0.04	0.15	0.07	<0.01	0.80	99.88	90	120	26	106	7	320	7550
130324b	Host	74.06	14.03	1.29	0.30	3.28	4.28	1.48	0.04	0.12	0.04	<0.01	0.80	99.86	226	182	46	106	18	524	88

* Boron concentration determined with ICP.

Table D.2: Trace element concentrations of various zones in the Scrubber Granite as determined by ICP-MS.

		Sc	Sr	Y	Zr	Nb	Ba	Hf	Ta	Th	La	Ce	Pr	Nd	Sm	Eu	Gd	Tb	Dy	Ho	Er	Tm	Yb	Lu
Sample	**Zone**	ppm	ppm	ppm	ppm	ppm	ppm	ppm	ppm	ppm	ppm	ppm	ppm	ppm	ppm	ppm	ppm	ppm	ppm	ppm	ppm	ppm	ppm	ppm
130315a	Core	17.77	87.82	11.77	81.68	1.51	230.23	3.18	0.49	26.22	41.09	86.43	9.33	30.71	5.76	0.51	4.30	0.57	2.88	0.46	1.19	0.15	1.01	0.12
130315b	Halo	6.65	154.34	12.22	95.17	2.60	558.73	3.35	0.33	29.26	43.46	87.03	9.50	31.54	6.13	0.66	4.78	0.57	2.83	0.46	1.19	0.15	0.93	0.12
130315c	Host	9.70	147.22	10.10	95.77	12.03	577.94	3.53	1.81	28.98	38.62	81.53	8.92	29.90	5.86	0.67	4.58	0.52	2.49	0.38	0.92	0.12	0.77	0.11
130316a	Core	14.60	115.27	17.11	101.87	3.36	203.26	3.51	0.52	30.27	49.07	94.54	10.47	35.59	6.65	0.66	5.57	0.68	3.48	0.60	1.50	0.20	1.19	0.15
130316b	Halo	8.73	195.77	11.58	110.06	13.42	717.28	3.76	2.10	33.23	27.60	55.68	6.13	19.96	3.73	0.57	2.95	0.42	2.21	0.41	1.16	0.17	1.11	0.15
130316c	Host	8.98	191.29	16.36	111.10	14.55	679.36	3.83	1.76	35.75	41.55	86.14	9.33	31.01	5.74	0.65	4.27	0.55	3.25	0.60	1.66	0.23	1.52	0.20
130318a	Inner host	9.30	128.82	16.74	78.65	9.45	554.82	2.84	1.42	22.20	31.29	67.63	7.47	25.79	5.36	0.83	4.80	0.63	3.41	0.58	1.56	0.22	1.33	0.16
130318b	Core	14.12	79.40	18.21	83.49	2.24	293.73	3.06	1.49	21.25	35.34	75.28	8.17	27.86	5.77	0.75	5.08	0.70	3.92	0.68	1.76	0.23	1.35	0.17
130318c	Halo	6.88	134.64	10.94	70.71	0.67	622.83	2.75	0.13	20.66	19.62	42.49	4.56	15.46	3.35	0.59	2.94	0.43	2.40	0.42	1.13	0.16	1.03	0.13
130318d	Host	8.90	131.82	14.07	69.59	10.78	535.60	2.58	1.59	21.55	28.65	59.64	6.71	22.67	4.64	0.72	3.86	0.54	2.97	0.53	1.37	0.19	1.16	0.15
130321	Host	9.91	181.90	17.65	121.74	15.08	654.54	4.06	1.76	38.06	47.23	97.23	10.63	34.70	6.34	0.73	4.94	0.64	3.67	0.66	1.79	0.26	1.70	0.20
130323a	Halo	5.92	181.46	11.31	56.09	2.29	598.78	2.06	0.63	19.39	44.21	87.18	10.07	32.68	6.59	0.71	4.78	0.61	2.93	0.46	1.09	0.14	0.84	0.09
130323b	Host	6.48	182.26	15.69	63.55	6.69	570.73	2.17	1.16	20.81	29.88	58.78	6.72	22.64	4.81	0.68	4.37	0.57	3.11	0.55	1.42	0.20	1.16	0.14
130324a	Core	11.40	123.61	14.17	76.73	2.62	277.73	2.66	0.74	27.67	39.94	80.98	8.85	28.65	5.71	0.57	4.40	0.59	3.11	0.55	1.42	0.20	1.32	0.16
130324b	Host	8.16	163.08	15.38	70.06	11.51	470.34	2.49	1.46	27.68	34.67	71.82	7.94	26.10	5.22	0.64	4.17	0.59	3.12	0.57	1.49	0.21	1.29	0.16
Errors (%)		11	6	5	6	10	2	10	31	4	2	2	3	4	5	3	3	3	4	4	4	6	6	6

D.4 MASS BALANCE WORKSHEET

Mass balance calculations were completed following the methods of Gresens (1967) using the major and trace element data from the various mineralogic zones. Table D.3 provides the results of these calculations for several parent/product pairs in each sample. Positive values indicate an apparent increase of the elemental concentration in the product, and negative values indicate an apparent decrease in the elemental concentration in the product.

Table D.3: Mass balance parent product ratios for major and trace elements.

Sample Number	130315a	130315b	130315c	130316a	130316b	130316c	130318a	130318b	130318c	130318d	130321	130323a	130324a
Parent-Product	Host-Halo	Halo-Core	Host-Core	Host-Halo	Halo-Core	Host-Core	Host-Halo	Halo-Core	Host-Core	Host-Inner Host	* Host-Host	Host-Halo	Host-Core
Si	3.56	-9.70	-7.02	1.59	-4.64	-3.20	4.62	-8.04	-4.15	-0.05	0.88	3.80	-4.23
Al	-0.00	0.00	-0.00	-0.00	0.00	0.00	-0.00	0.00	0.00	0.00	-0.00	0.00	-0.00
Ca	0.75	-0.63	0.05	0.03	-0.43	-0.41	-0.08	-0.21	-0.31	-0.01	-0.05	-0.02	-0.33
Mg	-0.03	0.44	0.44	-0.07	0.45	0.39	-0.15	0.40	0.28	0.00	-0.03	-0.11	0.25
Na	0.35	-1.19	-0.94	0.39	-0.80	-0.44	0.27	-1.15	-0.98	-0.21	0.00	0.44	-0.54
K	0.28	-2.39	-2.32	-0.01	-2.78	-2.88	0.43	-2.24	-2.01	0.22	0.39	0.20	-1.73
Fe	-0.56	2.41	2.06	-0.54	2.18	1.71	-0.85	2.25	1.61	-0.07	-0.21	-0.32	1.19
Mn	-0.01	0.01	0.00	0.00	0.01	0.01	-0.02	0.03	0.00	-0.02	0.02	-0.02	-0.00
Ti	-0.06	0.06	0.00	-0.01	0.00	-0.00	-0.05	0.08	0.03	0.00	-0.01	-0.03	0.01
P	0.02	0.01	0.04	-0.00	0.00	-0.00	0.00	0.08	0.09	0.00	-0.00	0. 01	0.00
B	1.79	114	122	0.76	82.5	87.0	0.78	81.8	76.9	4.34	0.06	-0.59	74.6
Sc	-0.03	0.14	0.11	-0.00	0.07	0.06	-0.02	0.05	0.02	-0.00	0.00	0.00	0.02
Rb	-0.25	-0.92	-1.23	-0.52	-1.38	-1.96	-0.69	-0.71	-1.36	-0.11	0.07	-0.56	-1.36
Sr	0.08	-0.52	-0.44	0.06	-0.71	-0.65	0.00	-0.67	-0.65	-0.17	0.48	0.23	-0.50
Y	0.02	0.01	0.03	-0.04	0.06	0.02	-0.03	0.04	0.01	0.00	0.06	-0.02	-0.02
Zr	0.00	0.00	0.00	0.00	0.00	0.00	0.00	0.00	0.00	0.00	0.00	0.00	0.00
Nb	-0.09	-0.00	-0.10	-0.01	-0.09	-0.10	-0.10	0.01	-0.08	-0.02	0.03	-0.04	-0.09
Ba	-0.15	-2.90	-3.07	0.44	-4.97	-4.57	0.77	-3.74	-2.90	-0.44	2.82	1.07	-2.16
La	0.05	0.04	0.09	-0.13	0.25	0.11	-0.09	0.10	0.00	-0.00	0.02	0.20	0.01
Ce	0.06	0.13	0.19	-0.29	0.46	0.16	-0.17	0.21	0.03	0.00	0.07	0.39	0.02

Pr	0.00	0.01	0.02	-0.03	0.05	0.02	-0.02	0.02	0.00	-0.00	0.01	0.04	0.00
Nd	0.01	0.04	0.06	-0.10	0.18	0.07	-0.07	0.08	0.00	0.00	0.04	0.14	0.00
Sm	0.00	0.00	0.00	-0.01	0.03	0.01	-0.01	0.01	0.00	0.00	0.01	0.02	-0.00
Eu	-0.00	-0.00	-0.00	-0.00	0.00	0.00	-0.00	0.00	-0.00	0.00	0.00	0.00	-0.00
Gd	0.00	0.00	0.00	-0.01	0.03	0.01	-0.00	0.01	0.00	0.00	0.01	0.01	-0.00
Tb	0.00	0.00	0.00	-0.00	0.00	0.00	-0.00	0.00	0.00	0.00	0.00	0.00	-0.00
Dy	0.00	0.00	0.00	-0.01	0.01	0.00	-0.00	0.00	0.00	0.00	0.01	0.00	-0.00
Ho	0.00	0.00	0.00	-0.00	0.00	0.00	-0.00	0.00	0.00	-0.00	0.00	-0.00	-0.00
Er	0.00	0.00	0.00	-0.00	0.00	-0.00	-0.00	0.00	0.00	0.00	0.00	-0.00	-0.00
Tm	0.00	0.00	0.00	-0.00	0.00	-0.00	-0.00	0.00	0.00	0.00	0.00	-0.00	-0.00
Yb	0.00	0.00	0.00	-0.00	0.00	-0.00	-0.00	0.00	-0.00	0.00	0.00	-0.00	-0.00
Lu	0.00	0.00	0.00	-0.00	0.00	-0.00	-0.00	0.00	-0.00	-0.00	0.00	-0.00	-0.00
Hf	-0.00	0.00	0.00	-0.00	0.00	0.00	0.00	-0.00	0.00	0.00	0.00	0.00	0.00
Ta	-0.01	0.00	-0.01	0.00	-0.01	-0.01	-0.01	0.01	-0.00	-0.00	0.01	-0.00	-0.00
Th	0.00	0.01	0.01	-0.02	-0.00	-0.02	-0.01	-0.02	-0.03	-0.01	-0.00	0.01	-0.02

*Parent is massive granite in sample 130321 and product the host granite in sample 130315.

D.5 ELECTRON MICROPROBE TECHNIQUES

Tourmaline crystals in various polished thin sections were analyzed by wavelength-dispersive electron microprobe methods at the University of Saskatchewan, using a JEOL-8600 electron microprobe. Corrections were made using the ZAF method. Standards used were natural minerals and synthetic compounds, including SiO_2 (Si), sillimanite (Al), rutile (Ti), chromium (Cr), fayalite (Fe), diopside (Mg), MnO (Mn), $CaSiO_3$ (Ca), albite (Na), sanidine (K), fluorite (F), and pantellerite glass (Cl). Analyses are from single tourmaline grains. Results of average electron microprobe analyses obtained on representative samples are given in Table 4.5 and 4.6 in Chapter 4.

D.6 FLUID INCLUSION MICROTHERMOMETRY

Microthermometric analyses were carried out using a U.S.G.S. gas-flow heating and cooling stage. The temperature of the stage was calibrated with respect to the melting points of inclusions in two standards (a pure CO_2 inclusion and a pure H_2O inclusion). The pure H_2O inclusion was used to set the "zero point" of the stage, or the 0˚C mark at which point H_2O melts. The pure CO_2 inclusion was used to set the "negative span" of the stage, or the –56.6˚C mark, at which point CO_2 melts.

Upon calibration of the stage, microthermometry commenced. Freezing runs were conducted before heating runs on fragments of doubly polished Scrubber Granite wafers. Errors are estimated to be on the order of ±1˚C, as the stage was calibrated within one degree Celsius of the standards. All inclusion measurements are summarized in Tables D.4 and D.5.

Potter and Brown's (1977) 15 weight percent density data for NaCl solutions was used to estimate the inclusion density at various temperatures in sample 130316. Their 13 and 15 weight percent density data was averaged to obtain 14 weight percent data to estimate the inclusion density at various temperatures in sample 130323. Table D.6 contains Potter and Brown's 13 and 15 weight percent density data, as well as the averaged 14 weight percent data used in inclusion density calculations in Chapter 5.

Table D.4: Complete microthermometric data for starburst nodule sample 130316.

Sample 130316	Observation number	T_n (°C)	T_e (°C)	T_m salt h. (°C)	T_m ice (°C)	T_h (°C)
Chip2	1		-51.2	-26.3	-9.9	
	2		-48.4	-26.4		
	3		-53.4	-26.6		
	4		-52.3	-27.2		
	5		-50.8	-26.5		
Average			-51.2	-26.6	-9.9	
Sample 130316	Observation number	T_n (°C)	T_e (°C)	T_m salt h. (°C)	T_m ice (°C)	T_h (°C)
Chip 11	1			-27.1	-10.6	330.7
	2	-62.0	-52.4	-26.6		330.6
	3			-25.6	-10.6	331.3
	4		-52.3	-26.3	-10.6	329.3
	5			-27.4	-10.3	329.9
	6		-43.7	-27.4	-10.7	330.3
	7	-65.6	-51.6	-25.5		329.7
	8	-64.8	-50.6	-29.2		328.1
	9		-48.1	-22.1		
	10		-50.2	-28.2	-10.6	
	11	-66.7	-51.1	-26.7		
	12		-49.5	-26.0		
Average		-64.8°C	-49.9°C	-26.5°C	-10.6°C	330.0°C

Table D.5: Complete microthermometric data for tourmaline vein sample 130323.

Sample 130323 Chip 3b	Observation number	T_n (°C)	T_e (°C)	T_m salt h. (°C)	T_m ice (°C)	T_h (°C)
Irregular inclusion	1				-10.2	453.6
	2				-10.2	455.5
	3				-10.4	455.7
	4		-45.8	-26.6		456.1
	5			-27.5	-10.2	456.6
	6		-45.6	-27.5	-10.3	453.5
	7	-62.0		-28.4	-10.2	454.1
	8			-27.5	-10.2	454.3
	9				-10.2	454.0
	10		-44.6	-27.5	-10.2	453.5
	11		-45.2		-10.2	454.3
	12		-48.5	-28.0	-10.2	453.1
	13		-47.2	-26.9	-10.2	453.0
Average		-62.0	-46.2	-27.5	-10.2	454.4

Sample 130323 Chip 3b	Observation number	T_n (°C)	T_e (°C)	T_m salt h. (°C)	T_m ice (°C)	T_h (°C)
Swallowtail inclusion	1		-48.4	-26.8		284.6
	2				-11.1	283.2
	3				-9.0	283.3
	4				-10.6	285.7
	5					283.2
	6			-27.4		283.3
	7					283.7
	8					284.9
	9					283.0
	10					285.7
	11					283.3
	12					282.9
Average			-48.4	-27.1	-10.2	283.7

Sample 130323 Chip 3b	Observation number	T_n (°C)	T_e (°C)	T_m salt h. (°C)	T_m ice (°C)	T_h (°C)
Triangular inclusion	1		-48.9		-11.5	
	2				-10.6	
	3				-11.0	
	4			-27.4	-10.9	
Average			-48.9	-27.4	-11.0	

Table D.6: Densities of vapor saturated NaCl solutions, g/cm^3 (data from Potter and Brown, 1977).

Temperature ˚C	13 Weight Percent	15 Weight Percent	14 Weight Percent*
0	1.1006	1.1166	1.1086
25	1.0912	1.1064	1.0988
50	1.0793	1.0942	1.0868
75	1.0663	1.0813	1.0738
100	1.0490	1.0630	1.0560
125	1.0310	1.0450	1.0380
150	1.0110	1.0250	1.0180
175	0.9890	1.0030	0.9960
200	0.9650	0.9800	0.9725
225	0.9390	0.9550	0.9470
250	0.9120	0.9280	0.9200
275	0.8820	0.9000	0.8910
300	0.8500	0.8700	0.8600
325	0.8170	0.8380	0.8275
350	0.7810	0.8050	0.7930
375	0.7440	0.7700	0.7570
400	0.7040	0.7330	0.7185
425	0.6630	0.6940	0.6785
450	0.6200	0.6500	0.6350

*Averaged from Potter and Brown's (1977) 13 and 15 weight percent data.

D.7 TOURMALINE SEPARATION TECHNIQUE

Stable and radiogenic isotope analyses were completed on tourmaline separates from the core zones of samples 130315, 130316, 130318, 130319, 130320, 130323 and 130324. The following steps were taken in the mineral separation process:

1. Tourmaline-rich core zones were extracted from hand samples using a rock saw;
2. Individual core zones were doubly wrapped in plastic bags and rock chips were manually broken down the into smaller pieces using a hammer on a hard surface;
3. Small rock chips were placed in a metal pestle and mortar, and were powdered by hitting the pestle with the hammer;
4. Rock powder was removed and placed into sieves;
5. Rock powder was sieved; larger rock fragments were broken down with mortar and pestle until all powder fell into the +0.25mm sieve; fine powder from pan was discarded;
6. Sieved rock powder was placed into vials, and were taken to the magnetic mineral separator (Frantz Isodynamic Separator);

7. Frantz was set to have a side title of 15˚, a forward tilt of 15˚, and a current of 0.45 amperes;
8. Tourmaline was magnetically separated from quartz and feldspar in the rock powder; tourmaline separates were collected in a vial.

Although some impurities (quartz and feldspar crystals) may be present in the tourmaline separates, it is assumed that the separates are approximately ≥95% pure. After separation, stable and radiogenic isotopic analysis of the tourmaline separates were completed. Analytical techniques involved in these processes are summarized in the following sections.

D.8 STABLE ISOTOPE ANALYSIS

The oxygen and hydrogen isotopic compositions of tourmaline separates were analyzed at the Stable Isotope Laboratory at Queen's University in Kingston, Ontario. These analyses were carried out on a Finnigan MAT 252 isotope ratio mass spectrometer (IRMS). Errors are ± 0.2 for the oxygen data and ± 5 for the hydrogen data. Oxygen was analyzed on a silicate extraction line using BrF_5.

Analysis of oxygen isotopes is performed on CO_2 gas. Oxygen in silicates and oxides is usually converted to CO_2 through fluorination of 10-20mg samples with BrF_5 in nickel tubes at 500-650˚C (following the technique of Clayton and Mayeda, 1963). Decomposition by carbon reduction is usually carried out at 1000-2000˚C. The oxygen is converted to CO_2 over heated graphite, and the oxygen isotopic composition of the carbon dioxide is analyzed.

Hydrogen was determined using conventional extraction techniques using depleted uranium metal. The determination of hydrogen isotopes is performed on H_2 gas. However, most of the hydrogen generated from hydroxyl-bearing minerals is liberated in the form of water by heating the samples to approximately 1500˚C. Water is trapped using liquid nitrogen and then converted to hydrogen gas by passage over hot uranium at about 750˚C (see Bigeleisen et al., 1952). Please see Tables D.7 and D.8 for complete results of $\delta^{18}O$ and δD water values all samples.

Table D.7: Oxygen isotope ratio values for water in all samples.								
Temp (˚C)	130315	130316	130318	130319a	130319b	130320	130323	130324
250	3.7	3.8	4.7	3.5	3.6	5.5	5.4	5.6
300	5.1	5.2	6.1	4.9	5.0	6.9	6.8	7.0
350	6.1	6.2	7.1	5.9	6.0	7.9	7.8	8.0
400	6.9	7.0	7.9	6.7	6.8	8.7	8.6	8.8
450	7.4	7.5	8.4	7.2	7.3	9.2	9.1	9.3
500	7.8	7.9	8.8	7.6	7.7	9.6	9.5	9.7
550	8.0	8.1	9.0	7.8	7.9	9.8	9.7	9.9
600	8.2	8.3	9.2	8.0	8.1	10.0	9.9	10.1
650	8.4	8.5	9.4	8.2	8.3	10.2	10.1	10.3
700	8.5	8.6	9.5	8.3	8.4	10.3	10.2	10.4
750	8.6	8.7	9.6	8.4	8.5	10.4	10.3	10.5
800	8.6	8.7	9.6	8.4	8.5	10.4	10.3	10.5

Table D.8: Hydrogen isotope ratio values for water in all samples.								
Temp (˚C)	130315	130316	130318	130319a	130319b	130320	130323	130324
250	54.4	49.7	47.9	50.3	41.7	54.9	46.6	44.2
300	37.8	33.1	31.3	33.7	25.1	38.3	30.0	27.6
350	25.1	20.4	18.6	21.0	12.4	25.6	17.3	14.9
400	15.1	10.4	8.6	11.0	2.4	15.6	7.3	4.9
450	7.0	2.3	0.5	2.9	-5.7	7.5	-0.8	-3.2
500	0.5	-4.2	-6.0	-3.6	-12.2	1.0	-7.3	-9.7
550	-4.8	-9.5	-11.3	-8.9	-17.5	-4.3	-12.6	-15.0
600	-9.3	-14.0	-15.8	-13.4	-22.0	-8.8	-17.1	-19.5
650	-13.1	-17.8	-19.6	-17.2	-25.8	-12.6	-20.9	-23.3
700	-16.3	-21.0	-22.8	-20.4	-29.0	-15.8	-24.1	-26.5
750	-19.0	-23.7	-25.5	-23.1	-31.7	-18.5	-26.8	-29.2
800	-21.4	-26.1	-27.9	-25.5	-34.1	-20.9	-29.2	-31.6

D.9 RADIOGENIC ISOTOPE ANALYSIS

Samarium and neodymium isotope analysis was completed at the Saskatchewan Isotope Laboratory, at the University of Saskatchewan. The following steps outline the procedure used for Sm-Nd isotope evaluation of the tourmaline separates:

1. Appropriate spike weights were added to the Teflon beaker. The spike used was ^{150} Nd/^{150} Sm SIL concentrated mix;
2. The spike was dried down;
3. 1.5 mg of tourmaline was weighed into the same beaker;
4. 1 ml concentrated nitric was added to wet the sample; this mixture sat for 1 minute to equilibrate; 5 ml conc. HF was added to the beaker; sample was swirled around; equilibrated at RT;
5. Sample was dried down to a 'wet' consistency;
6. HF /Nitric acid was added to beaker in a 5:1 concentration and was bombed for 2 minutes;
7. Sample was dried down to 1/3 volume; concentrated nitric acid was added; sample dried down to half; concentrated HCl was added; sample was dried to 1/3; concentrated HCl was added; sample was dried down completely.
8. Sample was dissolved in 1.5 M HCl;
9. Samples were run through cation columns; 6.1 M HCl recovered REE from samples;
10. REE's were run through KelF columns to recover Nd at 0.32M HCl and Sm at 0.5 M HCl;
11. All samples were dried down, dissolved in 3µl water and loaded onto appropriate filaments for mass spectrometry.